Electrochemical O2 activation by Fe and Mn porphyrins : towards electrocatalytic aerobic oxidations of organic substrates

Nikolaos Kostopoulos

Université de Paris

Ecole doctorale de Chimie physique et Chimie analytique de Paris Centre

(ED388)

Laboratoire d'Electrochimie Moléculaire

Electrochemical O_2 activation by Fe and Mn porphyrins. Towards electrocatalytic aerobic oxidations of organic substrates

Par Nikolaos Kostopoulos

Thèse de doctorat en Electrochimie

Dirigée par Elodie Anxolabéhère-Mallart

Soutenue le 5 Novembre 2021

Devant un jury composé de

M. Nicolas Plumeré	Pr	Université Technique de Munich, Allemagne	Rapporteur
Mme Jalila Simaan	Dr	Aix Marseille Université, France	Rapportrice
M. Sébastien Blanchard	MDC HDR	Sorbonne Université – Faculté des Sciences, France	Examinateur
Mme Christina-Anna Mitsopoulou	Pr	Université Nationale et Capodistrienne d'Athènes, Grèce	Examinatrice Présidente du Jury
Mme Elodie Anxolabéhère- Mallart	Dr	Université de Paris, France	Directrice
Mme Claire Fave	Dr	Université de Paris, France	Co-encadrante

Acknowledgements – Remerciements – Ευχαριστίες

I thank all the members of my PhD committee, Sébastien Blanchard, Christiana Mitsopoulou, Nicolas Plumeré, and Jalila Simaan, for accepting to evaluate my work, for their useful and constructive comments, remarks, and proposed corrections, and for the exciting discussion. I also thank them for coming to Paris, some of them from far away, despite all the restrictions due to COVID-19 pandemic.
I thank especially Christiana Mitsopoulou and Sébastien Blanchard for their guidance, kindness and support, during previous stages of my chemistry studies.

Ce travail de thèse a été réalisé au Laboratoire d'Electrochimie Moléculaire de l'Université de Paris, dirigé par Elodie Anxolabéhère-Mallart. Je la remercie de m'avoir accueillie dans le laboratoire et d'avoir encadré ma thèse. Je la remercie pour le bon travail qu'on a fait ensemble, pour sa disponibilité et son enthousiasme, mais aussi pour son soutien très important au niveau personnel et professionnel. Je lui exprime ici ma plus profonde gratitude.

Je remercie très chaleureusement Claire Fave pour avoir accepté de co-encadrer ce travail de thèse, pour nos échanges constructifs, pour sa contribution cruciale dans mon projet, pour sa bienveillance et pour son soutien.
Je souhaite aussi remercier Marc Robert, pour m'avoir accueilli dans son équipe, et pour notre collaboration dans le cadre du laboratoire, de l'équipe, et des différents projets.

Je remercie très vivement Jean-Marc Noël pour notre excellente collaboration. Sa bonne humeur et sa passion pour la science ont été une source de motivation très importante pour moi, et une force motrice majeure pour le projet. Je remercie aussi Frédéric Kanoufi pour notre collaboration et nos discussions toujours intéressantes.

Je veux remercier ici Sihem Groni, ma tata préférée, pour son support, pour sa bienveillance, son aide et son écoute dans le quotidien, pour ses petits cadeaux sucrés. Qu'elle trouve ici mes sentiments distingués. Je remercie Célia Achaibou, qui a initié et beaucoup contribué dans ce projet, pour son soutien, pour ses conseils, pour m'avoir beaucoup aidé à apprendre les techniques au début de la thèse. Je remercie également Lydia Merakeb, pour nos discussions intéressantes, pour nos manips en binôme plus-que-aventureuses, pour notre collaboration dans le cadre du projet oxydation de l'ammoniaque, et surtout pour m'avoir appris ses astuces expérimentales.

Je souhaite remercier tous les chercheurs hors du laboratoire, avec qui j'ai collaboré, en particulier Nicolas Le Poul, Emmanuel Maisonhaute, Benedikt Lassalle, et Frédéric Banse. Je les remercie pour leurs contributions dans mon projet, pour leur bienveillance, pour tout ce que j'ai appris auprès d'eux. Je remercie aussi le personnel technique du laboratoire et de l'unité avec qui j'ai collaboré, c'est-à-dire, Esther Nurbet, Alexandra Pastor, David Clainquart, et Stéphanie Lau-Truong.

Je remercie également tous les gens du laboratoire qui ont participé ou contribué dans mon travail et avec qui on a passé des moments agréables dans les murs verts du labo, et en particulier Julien Bonin, Niklas von Wolff, Orestes Rivada-Wheelaghan, François Mavré, Micaela Richezzi, Bing Ma, Min Wang, Jérémy de Freitas, Rabia Djoumer, Aude Salamé, Francesco Crisanti, Damien Tocqueville, Cédric Houze, Sercan Akbaba, Guillaume Longatte, Bianca Ceballos, Daniele Sassone, Corentin Calvet, Ruwen Wang, Hussein Hijazi, Racha Kassem, Louis Romand, Mickaël Mateos, Etienne Boutin, Grace Lowe et Tamal Chatterjee.

Enfin, je tiens à remercier Stacey Alvarez, Julian Guerrero, Dorian Joulié, Martin Kientz, Daniela Mendoza, Lydia Merakeb et Justine Pallu qui ont été non seulement des collègues mais des amis pendant ces trois ans. Qu'ils trouvent ici ma gratitude la plus profonde pour leur aide au quotidien

dans le laboratoire, pour leur écoute, pour leur amitié, pour leur soutien dans et en dehors du laboratoire. En plus, un grand merci à Daniela pour nos belles aventures à synchrotron.

Εκτός από τα μέλη της οικογένειάς μου, θέλω να ευχαριστήσω ορισμένους φίλους μου των οποίων η στήριξη ήταν πολύτιμη αυτά τα τρία δύσκολα χρόνια του διδακτορικού. Ευχαριστώ λοιπόν τους Νίκο Κωστουράκη, Σπύρο Μαθιουδάκη, Βασιλική Βαρελτζή, Ραφαήλ Ματράκα, Γιάννη Δημητριάδη, Μάρθα Αλεξίου, Άρτεμι Κωνσταντουράκη, Έλλη Βήχου, και τη Γωγώ Χριστοπούλου.

οὕτως ἀταλαίπωρος τοῖς πολλοῖς ἡ ζήτησις τῆς ἀληθείας, καὶ ἐπὶ τὰ ἑτοῖμα μᾶλλον τρέπονται.

THUCYDIDES,* *History of the Peloponnesian War*, 1.20.3

(…) this shows how little trouble most people take in their search for the truth – they happily resort to ready-made opinions.

M. HAMMOND (transl.), *Thucydides, The Peloponnesian War. Translated by Martin Hammond. With an Introduction and Noted by P. J. Rhodes* (Oxford World's Classics), Oxford – New York 2009.

***Thucydides** (/θjuːˈsɪdɪdiːz/; Greek: Θουκυδίδης [tʰuːkyːdídɛːs]; c. 460 – c. 400 BC) was an Athenian historian and general. His *ξυγγραφή* recounts the history of the Peloponnesian War which took place during the fifth-century BC between Sparta and Athens. Thucydides is considered to be the father of "scientific history" because he applied strict standards of impartiality, evidence-gathering, and analysis of cause and effect, without reference to intervention by the deities, as outlined in his introduction to his work. He has also been dubbed the father of the school of political realism, which views the political behavior of individuals and the subsequent outcomes of relations between states as ultimately mediated by, and constructed upon, fear and self-interest

Table of Contents

List of Acronyms

CV : Cyclic Voltammetry or Cyclic Voltammogram

Cys : Cysteine

DFT : Density functional theory

DMF : Dimethylformamide

DMSO : Dimethylsulfoxyde

EPR : Electronic Paramagnetic Resonance

EPT: Electron Proton Transfer

eq : equivalent

GC : Glassy Carbon

GC/MS : Gas chromatography/Mass spectrometry

His : Histidine

IR : Infra-red

K : Kelvin

LSV :Linear sweep voltammogram

m-cpba : m-chloroperoxybenzoic acid

NADPH: Reduced nicotinamide adenine dinucleotide phosphate

NMR : Nuclear Paramagnetic Resonance

PET: Proton Electron Transfer

PhIO : iodosylbenzene

ppm : Part par million

RR : Resonance Raman

SCE : Saturated Calomel Electrode

SECM : Scanning electrochemical microscopy

TOF : Turnover frequency

TON : Turn over number

Tyr : Tyrosine

UV-vis : Ultra-violet-visible

vs : versus

Activation électrochimique du dioxygène par des porphyrines de fer et de manganèse. Vers des oxydations aérobies électrocatalytiques de substrats organiques

Résumé

Le développement de catalyseurs efficaces, sélectifs et à base de métaux non nobles permettant l'utilisation de O_2 en conditions douces en lieu et place d'oxydants nocifs ou de méthodes coûteuses en énergie est un enjeu crucial dans le cadre de l'oxydation de molécules organiques. Le présent sujet repose sur une approche électrochimique originale visant à développer de nouveaux procédés d'oxydation et d'halogenation inspirés des systèmes naturels pour remplacer les procédés non durables actuellement utilisés. Les métalloenzymes de type Cytochromes P450 de la famille des oxygenases/ halogenases sont capables de réaliser des réactions d'oxydation / halogenation efficacement et sélectivement dans des conditions douces, à travers l'activation réductrice de O_2.

Après coordination de O_2 sur le site actif Fe l'activation de O_2 consiste en une succession d'étapes de réduction et protonation conduisant à la coupure de la liaison O-O et à la formation de l'espèce Fe(V)=O, hautement réactive et capable d'oxyder un substrat organique. Les porphyrines Fe et Mn ont été largement étudiées en tant que modèles du site actif de ces enzymes et plusieurs intermédiaires réactionnels ont été générés par voie chimique et caractérisé par spectroscopie, et leur réactivité a été étudiée. En s'inspirant de ces systèmes naturels, notre stratégie originale est centrée sur des approches électrochimiques et spectroscopiques complémentaires pour l'étude de l'activation de O_2 par des porphyrines de Fe et Mn. Le but ultime est de développer des procédés électrocatalytiques pour l'oxydation de substrats organiques, imitant l'activité catalytique des systèmes naturels. La réaction du M^{II} (M= Fe, Mn) des complexes Fe(F_{20}TPP)Cl, Fe(TPP)Cl, Fe(F_{20}TPP)Cl, Fe^{III}(T-(2-COOH)PP)Cl et Mn(TPP)Cl avec le dioxygène est étudiée par voltamétrie cyclique (CV), la spéctroéléctrochimie UV-Vis et la microscopie électrochimique à balayage (SECM), en absence ou en présence des acides de Bronsted ou de Lewis. Des études d'électrocatalyse sont ensuite proposées ; en électrolyse préparative, la porphyrine de fer ou de manganèse, active le dioxygène dans un potentiel réducteur, en présence d'un substrat organique, comme par exemple le cyclooctène, qui peut être oxygéné ou halogéné selon les conditions réactionnelles choisies. Enfin, des études en hétérogénéisation de catalyseur avec des matériaux peut couteux, et de spectroélectrochimie Raman Résonante sont présentées comme résultats prometteurs de ce travail.

Mots-cléfs : Porphyrine, électrocatalyse, oxygène, oxydation, spectroélectrochimie

Electrochemical O_2 activation by Fe and Mn porphyrins. Towards electrocatalytic aerobic oxidations of organic substrates

Abstract

The activation of dioxygen is at the center of current economic challenges, because oxygenation and halogenation reactions play a major role in the chemical industry. These current oxidation processes often use harmful chemical oxidants, or dioxygen under drastic temperature and pressure conditions in the presence of noble metal catalysts. This is due to the kinetic inertia of oxygen. The metalloenzymes of the Cytochrome-P450 superfamily are capable of carrying out oxidation reactions efficiently and selectively under mild conditions, through the so-called reductive activation of dioxygen. This process begins with the coordination of dioxygen on the Fe ion at the active site, and leads, through a succession of reduction and protonation steps, to the cleavage of the oxygen-oxygen bond and the formation of a high valent species, Fe^{V}= O, a highly reactive species capable of oxidizing an organic substrate. The Fe and Mn porphyrins have been widely studied as models of the active site of these enzymes; several reaction intermediates were generated chemically and characterized by spectroscopy, and their reactivity was studied. In this manuscript, we propose an alternative approach that applies electrochemistry for the generation and characterization of these species. The reaction of M^{II} (M = Fe, Mn) of Fe (F20TPP) Cl, Fe^{III}(TPP)Cl, Fe^{III}(F20TPP)Cl, Fe^{III}(T-(2-COOH)PP)Cl and Mn^{III}(TPP)Cl complexes with dioxygen is studied. by cyclic voltammetry (CV), UV-Vis spectroelectrochemistry and scanning electrochemical microscopy (SECM), in the absence or presence of Bronsted or Lewis acids. Electrocatalysis studies are then proposed; in preparative electrolysis, Fe or Mn porphyrin activates dioxygen in a reducing potential, in the presence of an organic substrate, such as cyclooctene, for example, which can be oxygenated or halogenated depending on the reaction conditions chosen. Finally, studies in catalyst heterogenization with inexpensive materials, and Resonance Raman spectroelectrochemistry are presented as promising results of this work.

Key words: Porphyrin, oxygen, electrocatalysis, oxidation, spectroelectrochemistry

Ηλεκτροχημική ενεργοποίηση του οξυγόνου με τη χρήση πορφυρινών σιδήρου και μαγγανίου. Ηλεκτροκαταλυτικές αερόβιες οξειδώσεις οργανικών υποστρωμάτων

Σύνοψη

Η ενεργοποίηση του διοξυγόνου βρίσκεται στο επίκεντρο των σημερινών οικονομικών προκλήσεων, καθώς οι αντιδράσεις οξυγόνωσης και αλογόνωσης οργανικών μορίων διαδραματίζουν καίριο ρόλο στη χημική βιομηχανία. Οι διεργασίες που χρησιμοποιούνται σήμερα περιλαμβάνουν συχνά επιβλαβή χημικά οξειδωτικά ή οξυγόνο υπό συνθήκες υψηλής θερμοκρασίας και πιέσεως παρουσία ευγενών μετάλλων ως καταλυτών διότι το οξυγόνο είναι κινητικά αδρανές. Τα μεταλλοένζυμα της υπεροικογένειας του Κυτοχρώματος-P450 δύνανται να πραγματοποιούν αντιδράσεις οξείδωσης υπό ήπιες συνθήκες, σε κύτταρα, μέσω της λεγόμενης αναγωγικής ενεργοποίησης του διοοξυγόνου. Αυτή η διεργασία ξεκινά με την πρόσδεση του διοξυγόνου στο ιόν του σιδήρου στο ενεγρό κένρο και οδηγεί, μέσω μιας διαδοχής σταδίων αναγωγής και πρωτονίωσης, στη διάσπαση του δεσμού οξυγόνου-οξυγόνου και στο σχηματισμό ενός ενδιαμέσου υψηλής οξειδωτικής βαθμίδας, του Fe^{V}=O , το οποίο είναι ισχυρό οξειδωτικό ικανό να οξειδώσει οργανικά μόρια. Πορφυρινικά σύμπλοκα του σιδήρου και του μαγγανίου, έχουν μελετηθεί ευρέως ως μοντέλα του ενεργού κέντρου αυτών των ενζύμων, και πολλά ενδιάμεσα έχουν συντεθεί χημικά, χαρακτηρισθεί φασματοσκοπικά, και μελετηθεί ως προς την δραστικότητά τους. Στην παρούσα διατριβή, προτείνουμε μια εναλλακτική προσέγγιση που εφαρμόζει την ηλεκτροχημεία για τον σχηματισμό και χαρακτηρισμό αυτών των ενδιαμέσων. Η αντίδραση των συμπλόκων Fe(F_{20}TPP)Cl, Fe^{III}(TPP)Cl, Fe^{III}(F_{20}TPP)Cl, Fe^{III}(T-(2-COOH)PP)Cl και Mn^{III}(TPP)Cl με το διοοξυγόνο μετελετάται με κυκλική βολταμετρία (CV), φασματοηλεκτροχημεία UV-Vis και ηλεκτροχημική μικροσκοπία σάρωσης (SECM), απουσία ή παρουσία οξέων Brönsted ή Lewis. Στη συνέχεια προτείνονται μελέτες ηλεκτροκατάλυσης όπου η πορφυρίνη ενεργοποιεί το διοξυγόνο υπό αναγωγικό δυναμικό, παρουσία ενός οργανικού μορίου, όπως το κυκλοοκτένιο, το οποίο μπορεί να οξυγονωθεί ή να αλογονωθεί ανάλογα με τις συνθήκες της αντίδρασης. Τέλος, ως προοπτική της παρούσας διατριβής παρουσιάζονται μελέτες για την ετερογενοποίηση καταλυτών με φθηνά υλικά και τη φασματοηλεκτροχημεία συντονισμού Raman.

General Introduction

The dioxygen, O_2, was discovered in 1774 by the English chemist Joseph Priestley. It was issued from the thermal decomposition of mercury oxide. The name oxygen (*oxygène*) was given by Antoine De Lavoisier in 1778, from the greek words *ὀξὺ* (oksý, acid) and *γεννῶ* (gennô, to generate, to give birth), because he mistakenly believed that all the acids contained an oxygen atom.

Dioxygen constitutes some 21% by volume of the earth's actual atmosphere, while a significant quantity of dioxygen is dissolved in surface waters. It is believed that some 2.4 billion years ago a "Great Oxidation Event" took place, which is linked to the activity of photosynthetic cyanobacteria, and increased the levels of dioxygen in the atmosphere over 4 orders of magnitude (reaching the 10 % of the current levels), fact that changed the course of life on earth.[1]

In an aerobic atmosphere, carbon- and hydrogen-containing compounds that are present in all living things, are thermodynamically unstable to oxidation to carbon dioxide and water. However, the direct oxidation of organic compounds by oxygen is kinetically slow: we live in a metastable world and coexist with oxygen in a kinetic trap.

The central role that dioxygen plays in the life on earth is reflected on the numerous oxygen related enzymes that Evolution has provided to Nature. One of the oldest known such enzymes is Photosystem II that oxidizes water photocatalytically to produce O_2 and is indispensable in the overall photosynthetic process. Catalases and superoxide dismutases are enzymes able to protect living cells from the Reactive Oxygen Species (ROS). In the same time, abundant in Nature are enzymes such as the well-known Cytochrome P450 (Cyt-P450) that are able to catalyze the partial and controlled activation of oxygen that leads to oxidation of organic substrates. Most of these enzymes contain a heme active site: an iron cation inside a porphyrinate ligand.

During the last decades, chemists have been trying to reproduce the remarkable reactivity of these heme enzymes using metal complexes that resemble their active site, in a so-called bio-inspired approach. In REACTE research group at LEM, the bioinspired inorganic chemistry is combined with electrochemistry. In particular, the approach that we propose in the present manuscript, includes a combination of several electrochemical techniques and spectro-electrochemistry for the preparation and characterization of intermediate species, and for the evaluation of their reactivity. The manuscript is organized in the following way:

- In **Chapter 1** we discuss the context of O_2 activation, and how this activation takes place in heme enzymes. Then we present the key works of the bio-inspired approach that include the generation, characterization, and reactivity studies of iron and manganese-oxygen porphyrin intermediates, as well as and some previous or parallel efforts to reproduce enzymatic reactivity using electrochemistry.
- **Chapter 2** introduces our electrochemical approach based on previous studies carried out at LEM on the reductive activation of O_2 using an iron porphyrin, namely the Fe(F_{20}TPP)Cl. We then extend the approach to another Fe porphyrin and to a Mn porphyrin.
- **Chapter 3** describes the electrocatalytic reduction of O_2 by the Fe(F_{20}TPP)Cl in organic medium (DMF) in presence of protons, using cyclic voltammetry (CV) and UV-Vis spectroelectrochemistry and focuses on the catalytic pathways and key intermediates involved.
- In **Chapter 4** we show SECM can be utilized to study the reductive activation of O_2 by Fe porphyrins in DMF. We focus on the thermodynamic and kinetic parameters that can be obtained from the combination of experimental data and simulations, and on the structure-reactivity relationships that are therefore established.
- **Chapter 5** is devoted to the electrochemically-driven reactivity of several metal porphyrins towards organic substrates, under various experimental conditions.
- Finally, **chapter 6** includes the ongoing efforts to extend the spectroelectrochemistry approach, and in particular preliminary work with a Resonance Raman spectroelectrochemistry set-up. It also includes first experimental work on heterogenization efforts of functional catalytic systems on electrode surfaces.

Chapter 1 :

Introduction

1.1 The dioxygen molecule

The molecule of dioxygen is paramagnetic, and its electronic ground state is a triple ($^3\Sigma_g^-$). The molecular orbital theory (MOT) suggests that in the latter state, HOMO degenerate antibonding orbitals are occupied by two unpaired electrons, as shown in Scheme 1.1. The bond order is two, (bond order in molecular orbitals theory, equals the number of bonding electrons minus the number of antibonding electrons, divided by two) and the MOT is the first theory that provided a sufficient explanation for the reason why molecular O_2 is paramagnetic, with two unpaired electrons with parallel spins in the HOMO.[2]

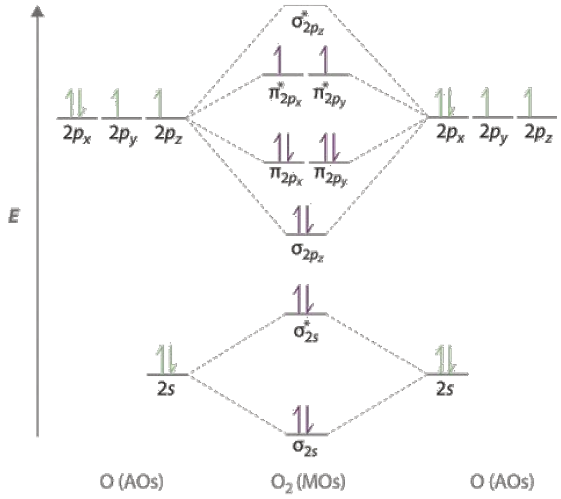

Scheme 1.1: Simplified diagram of the molecular orbitals of the electronic ground state of molecular oxygen. Two unpaired electrons occupied the HOMO.

Dioxygen is a powerful oxidant from a thermodynamic point of view, but it is kinetically inert because, its diradical character requires that it reacts with another radical (in order for the spin to be conserved) or forms a product that possesses a triplet ground state, a process that is rather rare.[3] Thus, the major reactivity pathways of dioxygen involve radicals (for instance, transition metals with unpaired electrons) or require excitation to singlet oxygen, its first excited state.

This first excited state is a singlet ($^1\Delta_g^+$); It has both π* electrons in one orbital, and it is 23 kcal mol^{-1} above the ground state. In the second excited state on the other hand, the two electrons are in separate π* orbitals, and their spins are paired, resulting in a different singlet state ($^1\Sigma_g^-$) that is 14 kcal mol^{-1} above the first excited state.

Simple one electron reduction of dioxygen leads to the superoxide ion ($O_2^{\bullet-}$) and one electron reduction of the latter leads to peroxide (O_2^{2-}). The consequence of the increased population of antibonding orbitals in reduced species, are a decrease of the O–O bond order, an increase of the O–O distance, and a decrease of the O–O stretch ($\nu_{O\text{-}O}$), compared to dioxygen. Activation of dioxygen molecule, both in biological and synthetic systems, usually starts by its binding to a rather nucleophilic metal center such as Fe^{II} or Cu^{I}. Binding involves some shift of electron density from the metal to the O_2 ligand, generally regarded as resulting in either a superoxo (one-electron reduced) and superoxide-like, or a peroxo (two-electron reduced) and peroxide-like ligand (Scheme 1.2).[4] Metal–O_2 complexes can also be synthesized by reaction with a superoxide (such as $[K]^+[O_2]^-$) or peroxide (such as $[Na]_2^+[O_2]^{2-}$) source.[4]

In the present study we will focus on Fe and Mn porphyrin oxygen species. Two main modes of coordination are known for the M-O_2 type complexes. The η_1 mode indicates a monodentate O_2 ligand (*end-on*), while η_2 (*side-on*) designates bidentate O_2 (both oxygen atoms are bound to the metal center). In these adducts, the metal (Fe or Mn) has usually an oxidation state of III or II. After cleavage of the O-O bond, M-oxo usually occur, which possess a formal O^{2-} moiety with usually a double bond between the o-atom and the metal. The oxidation state of the metal (Fe or Mn) in those cases can be either IV or V. In Scheme 1.2 some of the most common types of metal porphyrin oxygen adducts are represented, as well as the two different coordination modes of the O_2 moiety in M-O_2 type complexes.

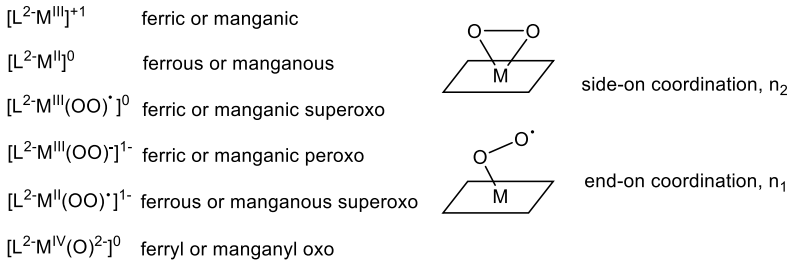

Scheme 1.2: (Left) Nomenclature for various metalloporphyrinate-oxygen adducts, followed in the present manuscript. L^{2-} designates the porphyrinate ligand. (Right) Schematic representation of the two most common coordination modes of these adducts. Square represents the porphyrinate ligand.

1.2 The importance of oxygen activation in the chemical industry

In order to pursue a sustainable future, it is required to address the chemical industry. The transition to a sustainable chemistry requires a reconceptualization of industrial processes and their products. In particular, it is necessary to reconsider not only the types of chemicals and how they are produced but also the conditions under which the reactions are carried out.[5] More sustainable technologies produce less by-products that leads to lower raw material costs, lower investment in separation, and lower disposal costs, and overall better economics.

In this context, oxidation catalysis has played and will continue to play a pivotal role mainly because oxidation is a process used in the polymer industry to produce large amounts of intermediates and monomers.[6] However, many of the oxidation reactions proceed under harsh conditions.

The synthesis of ethylene oxide, a compound produced in large quantities ($30*10^6$ tons per year in 2016) is a frequently considered example. It is utilized in different applications such as the synthesis of ethylene glycol and of various polymers. The industrial production of ethylene oxide is carried out in a mixture of ethylene and dioxygen (reaction 1.1) that react between 200°C and 300°C under pressures between 10 and 20 bar, using a silver catalyst dispersed on alumina, with a yield of 70%. The major byproduct of the reaction is CO_2 (reaction 1.2).[7]

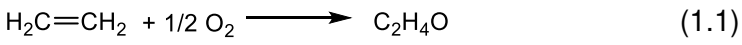

$$H_2C{=}CH_2 + 1/2\ O_2 \longrightarrow C_2H_4O \qquad (1.1)$$

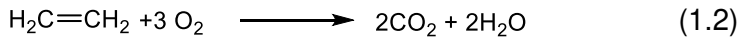

$$H_2C{=}CH_2 + 3\ O_2 \longrightarrow 2CO_2 + 2H_2O \qquad (1.2)$$

Besides efforts for improvement, this synthesis continues to operate under conditions that result in relatively low selectivity for the desired compound.

Atmospheric oxygen is by far the most important and also the cheapest oxidizing agent. Other frequently used stoichiometric oxidizing agents, such as HNO_3, H_2SO_4 and SO_3/H_2SO_4 (oleum), Cl_2, MnO_2, CrO_3, $KMnO_4$, as well as H_2O_2 and organic hydroperoxides, must first be produced by other energy consuming processes.[7] Adipic acid for example, is an important intermediate in the polymer chemistry that it is mainly used in the synthesis of nylon-6,6 , and its synthesis requires the use of HNO_3. In the last step of the synthesis, a cyclohexanol/cyclohexanone mixture (KA oil) is oxidized by nitric acid, and even thought a stoichiometric oxidant is used, catalysis by a

homogeneous catalyst containing Cu^{II} nitrate and ammonium metavanadate is also necessary (reaction 1.3).[6]

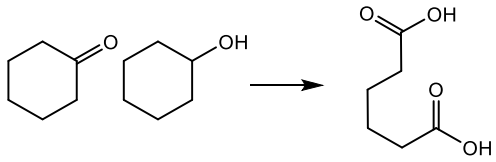

(1.3)

Metalloenzymes are a great source of inspiration for the development of more eco-friendly systems for oxidation reactions, due to the following features:

i. they work under mild conditions (physiological, inside living cells)
ii. the oxidant they use in is O_2 or H_2O_2,
iii. the side product in the reactions they catalyze is water
iv. they use non noble metals in their active sites such as Fe

In the following paragraphs, we will discuss the chemistry of these metalloenzymes, as well as some tremendous efforts of chemists to model these systems.

1.3 Enzymes for O_2 activation

In biological systems, a variety of metalloenzymes are carrying out partial and controlled O_2 reduction (vide infra), while other catalyze the complete oxygen reduction reaction:

$$O_2 + 4e^- + 4H^+ \longrightarrow 2H_2O \qquad (1.4)$$

In their active site, they contain redox active ions of transition metals such as Fe or Cu, that adopt diverse coordination environments.

Metalloenzymes catalyzing the O_2 reduction can be classified in four general categories:

- Cu oxidases and monooxygenases[1]
- Fe containing non heme oxygenases[8]
- Heme-Cu oxidases[1]
- Heme-only enzymes[1, 9-11]

We will be interested on heme enzymes, which contain an Fe porphyrin in their active site. Scheme 1.3 provides a diagram for the principal reactions catalyzed by some heme enzymes.

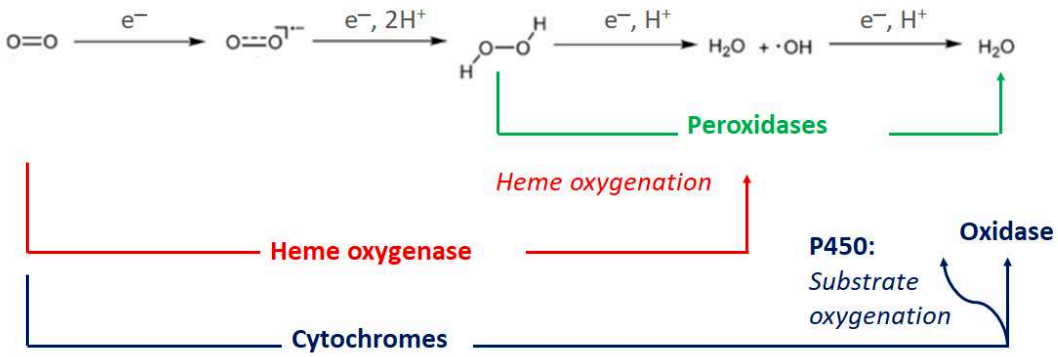

Scheme 1.3: Sequence of O_2 reduction to H_2O (in aqueous medium) and related reactivities of some representative metalloenzyme families.

Cytochrome c oxidases are Heme-Copper metalloenzymes that catalyze the complete four-electron reduction of O_2 to H_2O. The rich chemistry of these enzymes has been the subject of numerous and detailed studies over the past decades and continues to attract interest due to its relevance to fuel cell technologies.[1] However, a detailed consideration of this chemistry is out of the scope of the present manuscript.

In the present manuscript we focus on heme enzymes that perform the so-called reductive activation of O_2. This consist of a partial and controlled reduction of the oxygen molecule bound to the metal center leading to the cleavage of the O-O bond. The high-valent species which occur after the O-O bond cleavage are strong oxidants capable of oxidizing a variety of substrates, thus unraveling oxygen's potent oxidizing power.

1.3.1 Oxygen transport heme proteins

A crucial step of the catalytic cycle in heme enzymes with oxygenase reactivity is the O_2 binding to the ferrous (Fe^{II}) porphyrin, it is thus of outmost important to examine first the dioxygen transportation and storage proteins, which are hemoglobin and myoglobin respectively. They both have histidine residues in the axial position of the metal center. Figure 1.1 presents the $Fe^{II}O_2$ adducts (oxy form) of myoglobin.

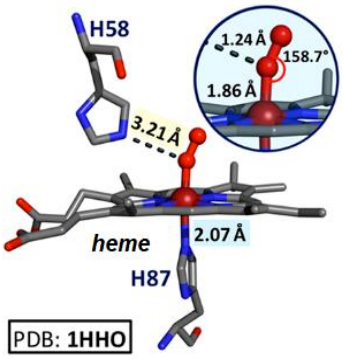

Figure 1.1: 3D representation of the distal binding pocket of the oxy-myoglobin. Reprinted with permission from ref 1. Copyright 2018 American Chemical Society.

In physiological conditions, these globin proteins are very efficient in oxygen binding and at the same time, their structure prevents further reduction of the bound dioxygen moiety that can lead to the release of deleterious ROS (reactive oxygen species).

In the deoxy form of binding sites of myoglobin and hemoglobin (where O_2 is not bound), a high spin (S=2) ferrous (Fe^{II}) center is observed with an axially coordinated histidine side-chain. Upon O_2 binding, an "in plane" (towards the porphyrin plane) movement of the Fe takes place, along with the shortening of all the Fe-N bond lengths, and the metal center is a low spin one (Fe^{III}, with S=1/2).[12]

Oxy-heme compounds, both biological and synthetic models, have been extensively studied in the last decades. Nevertheless, their electronic structure and more precisely how the metal center and O_2 share the electrons, is not fully understood and continues to be a point of discussion.[13]

In their pioneering work, Pauling and Coryell, reported in 1936 the diamagnetism of the oxy-hemoglobin adduct, and suggested that the latter's electronic structure is better represented as a $Fe^{II}(O_2)$ adduct, proposing that complete electron transfer from the Fe to the O_2 did not occur and thus the oxygen moiety in this case remains redox innocent.[14]

Several decades later, in 1964, Weiss proposed an alternative explanation for the observed diamagnetism, where the unpaired spin on the superoxide moiety (S=1/2) is antiferromagnetically coupled with the low spin Fe^{III} center (S=1/2), leading to an electronic structure that is described as $Fe^{III}(OO^{\bullet})$ (a ferric superoxo).[15] A third alternative was described by McClure for the first time,[16] and then by Goddart,[17] where the antiferromagnetic coupling occurs between an intermediate spin Fe^{II} (S=1) and a triplet dioxygen ligand (S=1), (Figure 1.2).

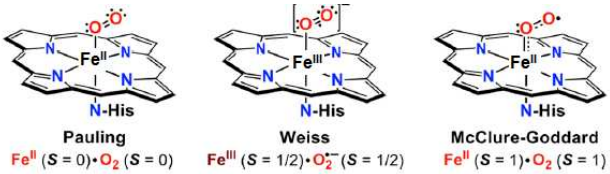

Figure 1.2: Representations of the three alternative electronic structures of the oxy-hemoglobin/myoglobin Adapted with permission from ref 1. Copyright 2018 American Chemical Society.

Recent spectroscopic and theoretical studies conducted by Sarangi and co-workers reveal that the structure of oxy-hemoglobin in solution favors the Weiss model while the solid-state crystalline state favors the Pauling model.[18]

1.3.2 Cytochrome P450 (Cyt p450)

This class of metalloenzymes is widespread in nature and amongst the most well-studied and famous ones. They mediate a large array of oxidations of organic substrates, that are crucial for aerobic life. These reactions include, hydroxylation of aliphatic and aromatic hydroxylation, olefin and arene epoxidation; alkyne oxygenation to carboxylic acid, N-/S-O- dealkylation reactions, oxidations of alcohols and aldehydes, and nitric oxide reduction.[9-10, 19] Aromatases, a subclass of Cyt-P450 enzymes, catalyze several physiological interconversions for the production of sex hormones including those in humans.[19] Some of these reactions catalyzed by Cyt-P450 are illustrated in Scheme 1.4. NADPH or nicotinamide adenine dinucleotide phosphate, is the electron donor that provides the necessary electrons to the enzyme for the O_2 activation.

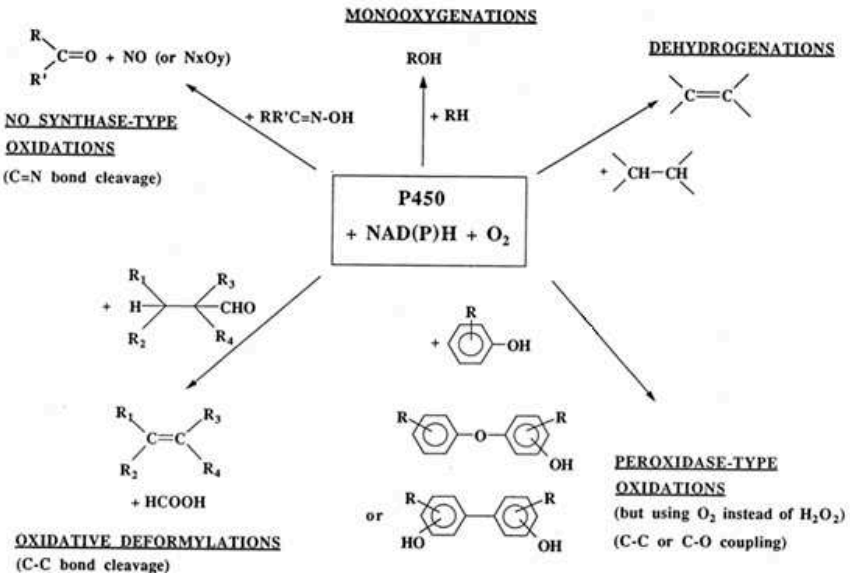

Scheme 1.4: Most common oxidation reactions catalyzed by Cyt-P450 enzymes, as described by Mansuy.[20]

In 1987, Cyt-P450$_{cam}$, was the first Cyt-P450 three-dimensional protein structure solved by X-ray crystallography[21] and since then it has been very extensively studied. It catalyzes the regiospecific and stereospecific hydroxylation of camphor, to give the 5-exohydroxycamphor, during the first step of the camphor oxidation reaction.[22]

Figure 1.3 shows the generally accepted mechanism of substrate oxidations by Cyt-P450. The resting state of Cyt-P450 contains in its active site, a ferric (Fe^{III}) metal center that is out of plane, low spin and six coordinated, with a thiolate group of a cysteine residue on the proximal side and a water molecule as sixth axial ligand on the distal site. The proximal site is known to form hydrogen bonds with side chains of several other amino acids, and these interactions are known to play a crucial role in the fine tuning of the redox potential of the metal center.[23] In the resting state, the reduction potential is usually between -0.4 and -0.17 V vs NHE for most Cyt-P450s[10] and thus rather inactive to reduction in physiological conditions, but the arrival of a hydrophobic substrate in the distal binding site, displaces the water molecule that is axial ligated, leading to the switch of the low spin Fe^{III} to a five coordinated high spin metal center.[24] This process that is entropically favored, elevates the reduction potential by several hundreds of mV (around 400 mV), that renders the one electron reduction of the Fe^{III}; more energetically favorable. This process prevents spontaneous reduction of the Fe^{III} center in absence of substrate.[22] After the one electron reduction of the metal center, the resulting high spin ferrous (Fe^{II}) center, binds O_2, giving rise to the oxy-P450

intermediate that has a reduction potential around 0 V vs NHE; between the distal oxygen atom of the $O_2^{\bullet-}$ and two new water molecules (not shown) that enter the cavity, hydrogen bond interactions are formed.[10] A second electron is then provided to the metal center by the protein, reducing the $Fe^{III}(OO^{\bullet})$ to an end-on $Fe^{III}(OO^{-})$ (ferric peroxo) that is very unstable, presumably because of the accumulation of exceeding electronic density on the metal center by two electron donating axial ligands, the thiolate and the peroxo. In spite of its instability, the species has been characterized in cryogenic temperatures (77 K) by EPR and ENDOR spectroscopies.[25]

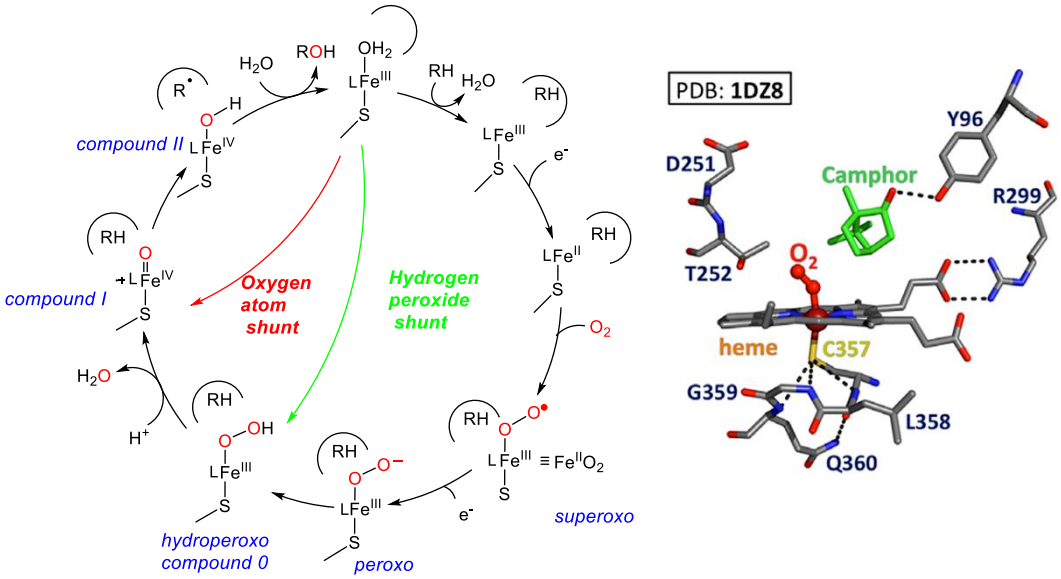

Figure 1.3: (Left) Postulated catalytic cycle for Cyt-P450 enzymes. L represents the porphyrin ligand. All species have been spectroscopically observed but the crystal structure for intermediates including peroxo and hydroperoxo Compound I and Compound II are not yet available. (Right) Close view of the oxy-Cyt P450cam highlighting the camphor substrate , the six coordinate heme center and the critical H-bonding interactions involving the proximally ligated cysteine residue. Reprinted with permission from ref 1. Copyright 2018 American Chemical Society

The ferric peroxo species, is then quickly protonated to give a hydroperoxo species ($Fe^{III}OOH$) known in the literature as compound 0. In this intermediate, the so-called push-pull machinery of the enzyme takes place: strong electron donation effects of the thiolate on the d_{z^2} orbital of the metal center and hydrogen bonding of the residues of the distal pocket on the OH moiety, lead to overall strengthening of the Fe-O and weakening of the O-O bond (see Scheme 1.5). These effects ensure the heterolytic O-O bond cleavage that occurs after a second net proton transfer to the distal oxygen atom.[1, 9, 23]

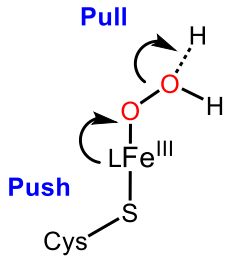

Scheme 1.5 Representation of the push-pull effect on the ferric hydroperoxo species of Cyt-P450. L represents the porphyrin ligand.

The resulting highly oxidizing species is a formal $Fe^{V}(O)$, known in the literature as Compound I. This intermediate possess a high oxidation power, demonstrated not only by its reactivity, but also by the reduction potentials of $Fe^{V}(O)$ model systems that can climb up to 1,7 V vs NHE.[26] Compound I is unstable, and it had not been isolated in high yield until recently, when Green et al. demonstrated that the enzymatic Compound I of the bacterium CYP119 can be generated, by addition of m-cpba (meta-chloroperbenzoic acid) to the ferric resting state.[27-28]

Although formally $Fe^{V}(O)$, it is now generally accepted that Compound I is better described as a Fe^{IV} metal center ferromagnetically coupled to a porphyrin π radical cation.[29-30] The now generally accepted pathway *via* which the reaction between the $Fe^{IV}(O)$ π radical cation proceeds, is known as radical rebound mechanism and has been proposed by Groves et al. for the first time in 1978,[30-31] and illustrated in Scheme 1.6.

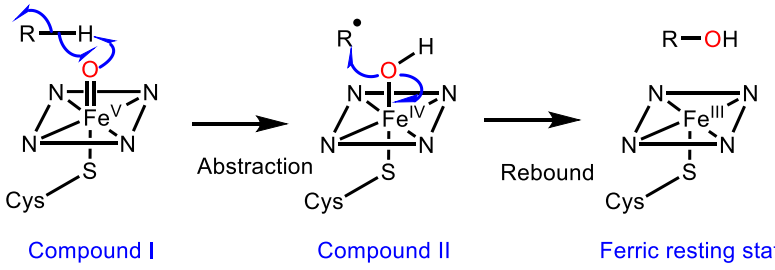

Scheme 1.6: Rebound mechanism for the oxidation reactions catalyzed by Cyt P450, proposed by Groves et al.[31]

The first step is a hydrogen atom abstraction, where Compound I accepts a hydrogen atom (H•) by homolytic cleavage of a substrate C-H bond, and gives rise to the so-called Compound II, the Fe^{IV}-OH, and a radical species $R^{\bullet\cdot}$ that remains inside the distal pocket. In the final steps these two species react to give a ferric metal center and the oxidized substrate ROH.

It is quite remarkable how such sophisticated systems have been developed by Nature, and how important is the fine tuning of the protein structure for the reactivity of the enzyme. A very illustrative observation is that when the axial base of dioxygen carrier or storage proteins are replaced with a cysteine residue, the reversible O_2-binding activity is switched to O_2 reductive activation that is testified by the observation of high valent species that occur after the O-O bond cleavage.[32]

1.3.3 Non Cyt-P450 heme proteins that catalyze oxidation reactions

The first enzymes with oxygenase activity, that do not belong to the Cyt-P450 superfamily, were discovered in 1955, by Hayaishi,[33] who discovered the tryptophan 2,3-dioxygenase, a heme protein, and Mason,[34] who discovered the tyrosinase, a copper protein. By their independent works, they demonstrated for the first time that these two enzymes catalyze the incorporation of one or two oxygen atoms in substrates, after dioxygen activation. In this paragraph, we will briefly discuss the chemistry of several non Cyt-P450 enzymes, namely heme oxygenases, dioxygenases, peroxidases, and haloperoxidases.

Heme oxygenases are enzymes that catalyzes the regiospecific degradation of the heme ring producing an oxidized species called biliverdin, free Fe^{II} ions and carbon monoxide. These enzymes play a pivotal role in many biological functions, such as iron homeostasis, cell signaling *via* the produced CO, antioxidant defense and heme catabolism. The chemistry of these enzymes possesses two unique features.

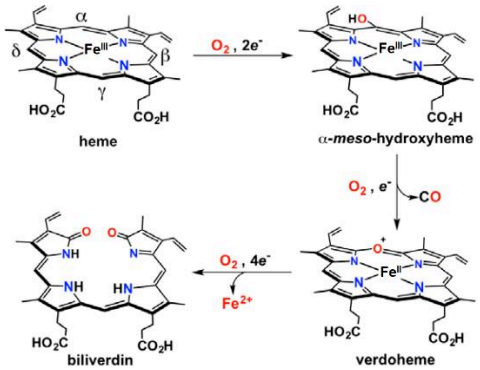

Figure 1.4: Main mechanistic steps involved in the heme degradation reaction catalyzed by heme oxygenase. Reprinted with permission from ref 1. Copyright 2018 American Chemical Society.

Firstly, it is the only enzyme where the heme group behaves as the substrate itself.[1, 35] Secondly, during the first step of the reaction, the regiospecific self-hydroxylation of α-meso position of the porphyrinate takes place, and the active species is the Compound 0 (hydroperoxo) species. This catalytically active species has been observed by EPR and ENDOR spectroscopies in cryogenic temperatures.[36]

Indoleamine 2,3 dioxygenase and Tryptophan 2,3 dioxygenase are two enzymes studied for the first time by Hayashi, [37-38] who discovered that they are able to facilitate the oxidative ring cleavage of the C^2-C^3 bond of the substrates (see Scheme 1.7 F). The catalytic cycle of these enzymes, requires only one reducing equivalent. Indeed, the Fe^{III} is reduced to Fe^{II} and the latter reacts with O_2 to give the $Fe^{III}(OO^{\bullet})$, superoxo intermediate, which is the active oxidant.

The base-catalyzed abstraction mechanism (Scheme 1.7 A and B) was the initially proposed one, but after the observation that proton of the 1-position was not necessary for the reactivity to take place, alternative proposals have been presented that include electrophilic addition (Scheme 1.7 C) and radical addition (Scheme 1.7 D) The data obtained from crystallography, mass spectrometry, mutagenesis, and computational work suggest that A and B are rather unlikely.[39] One would suggest that Fe superoxo is more of a radical species than an electrophile, so the radical mechanism would be more plausible, however this was not the case in model systems, as it will be discussed later (see paragraphs 1.4.1 and 5.1).

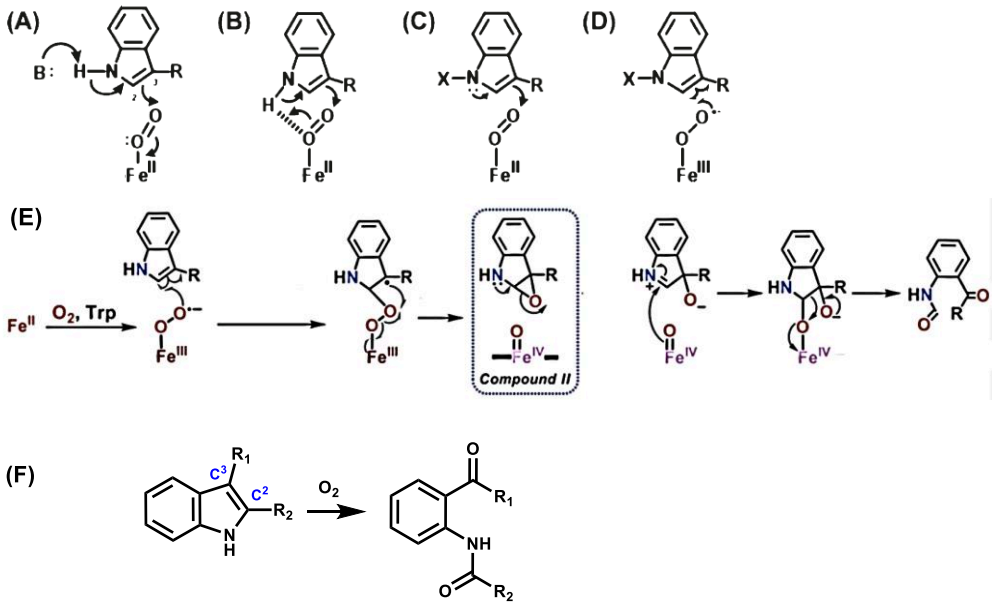

Scheme 1.7: A-D: Proposed activated complexes for the reaction of indoles in their heme active sites. E: proposed stepwise mechanism leading to the dioxygenation of the indoles, highlighting the ferryl intermediate and F: overall reaction.

Interestingly, the formation of a ferryl ($Fe^{IV}(O)$) species has been observed by Resonance Raman spectroscopy in the case of indoleamine dioxygenase,[40] suggesting that a stepwise transfer of the oxygens atoms occurs (Scheme 1.7 E), rather than a concerted two oxygen atoms addition.

Heme peroxidases catalyze the oxidation of various substrates using peroxide as the O-atom source. They are involved in several biological processes such as, prostaglandin biosynthesis, plant growth hormone metabolism, the production of thyroxine and lignin degradation. Peroxidases are found in plants, animals, and microorganisms, but the most thoroughly understood are non-mammalian heme peroxidases that are divided into three classes: intercellular (Class I), extracellular fungal (Class II), and extracellular plant peroxidases (Class III).[41]

The prosthetic group in these enzymes is the protoporphyrin IX, similar to heme containing globins and Cyt P450, and is bind to a histidine residue perpendicular to the heme. This proximal histidine forms hydrogen bonds to a conserved asparagine residue (not shown)[42] that induces a considerable anionic character at the histidine residue, promoting the push pull effect aiding the O-O bond cleavage, and reduces the $E^0_{Fe^{III}/Fe^{II}}$ stabilizing the ferric state.[43]

The catalytic mechanism is divided in three distinct steps (i) two electron reduction of H_2O_2 after the binding with the Fe^{III} resting state, that leads to the formation of Compound I, with the intermediacy of the Compound 0 (Ferric hydroperoxo) (ii) reaction of Compound I with the substrate leading to the formation of Compound II and a substrate centered radical (iii) oxidation of a second equivalent of substrate while the active site returns to its resting state. This step is the rate determining step. Interestingly, in some peroxidases, the radical cation of Compound I resides in a side chain of a distal residue (tyrosine or tryptophan) rather than in the heme. Substrates that are oxidized by peroxidases include catechols, phenols, and aromatic amines. Figure 1.5 summarizes the mechanism of the peroxidases.

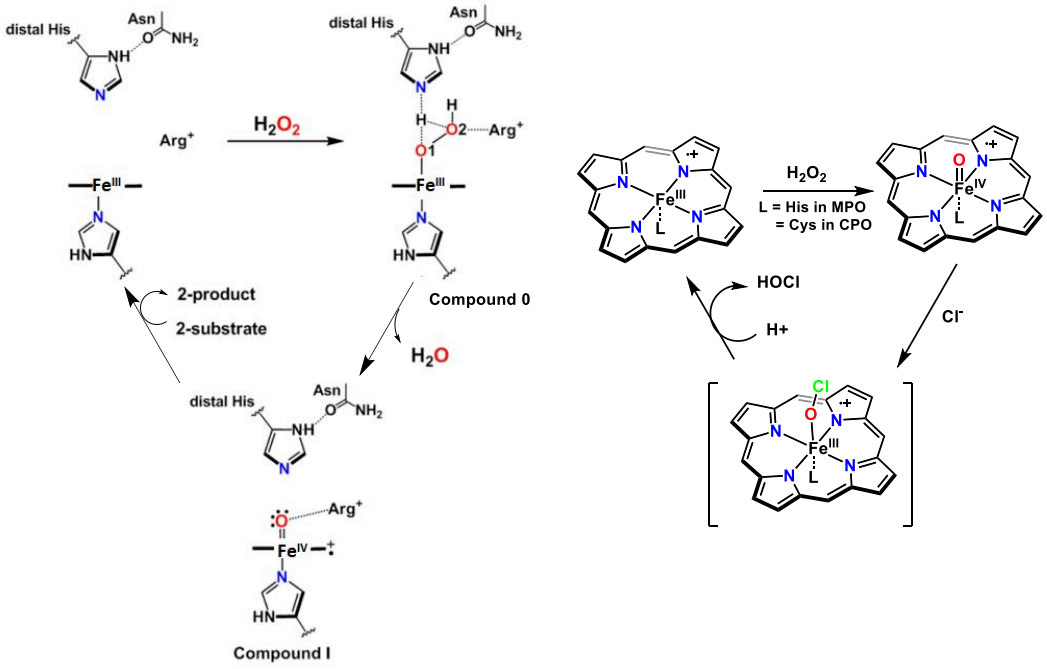

Figure 1.5: (Left) Mechanism of peroxidases.[1] (Right) mechanism of haloperoxidases as proposed in reference [44].

Similar reactivities are ascribed to ***heme haloperoxidases***, highly versatile enzymes that are able of catalyzing, among others, halogenation and dehalogenation reactions. Two heme haloperoxidases are known to date, the chloroperoxidase (CPO) and the myeloperoxidase (MPO). CPO is an enzyme that is found in caldariomyces fumago and catalyzes chlorination reactions in the biosynthesis of chlorine-containing compounds. On the other hand, MPO works as a major component of the antimicrobial system of neutrophils.[44] The chloroperoxidase can be described as a hybrid of Cyt-P450 and

peroxidases, because they contain a proximal cysteinate ligand as Cyt-P450, and a distal pocket with polar side chains reminiscent of the peroxidases.[1]

The reaction mechanisms of CPO and MPO are similar (see Figure 1.5). The reactions of the resting states of CPO and MPO with hydrogen peroxide form an $Fe^{IV}(O)$ porphyrin π radical cation species (compound I) as it is the case for peroxidases. Compound I is responsible for the oxidation of a chloride ion, to produce a postulated Fe^{III} hypochlorite that it is believed to be the active chlorinating agent. However, it has not yet been possible to spectroscopically observe it.[44]

1.4 Models of heme enzymes for O_2 activation

During the past 60 years, efforts of many bioinorganic chemists have focused on modeling the active sites of several heme enzymes. Thorough spectroscopic studies have provided crucial mechanistic information that have contributed to the understanding of the natural occurring mechanism in enzymes. Additionally, many studies aimed to reproduce the enzymatic activity by model systems and simple additives usually stoichiometric oxidants. In the present paragraph we will discuss model systems based on Fe and Mn porphyrin-oxygen intermediates, with different reduced derivatives of ligated dioxygen, ranging from ferric and manganic superoxo to compound I and II.

1.4.1 $Fe^{III}(OO^{\bullet})$ (ferric-oxy / ferric superoxo) models

$Fe^{III}(OO^{\bullet})$ can be generated by reaction of O_2 and n Fe^{II} porphyrin starting complex. Spectroscopic characterizations of the superoxo species requires low temperatures (usually around 230 K) due to its poor thermal stability. Furthermore, its stability is enhanced in aprotic environment and in complexes bearing encumbered coordination spheres. In accordance with these observations, the proposed decay pathways often include protonation or dimerization pathways.[45]

Collman et al. demonstrated spectroscopically the reversible formation of a $Fe^{III}(OO^{\bullet})$ supported on a picket fence porphyrin with methylimidazole as axial ligand, starting from Fe^{II} and O_2.[46] They also obtained its crystal structure, which is the first known crystal structure of a Fe^{III} superoxo species (see Figure 1.6).[47] The picket fence porphyrinate possesses three ortho-pivalamide phenyl groups at the meso positions of the macrocycle, that creates a hydrophobic pocket on the one side of the metal center, trans to the 5th coordination position that is occupied by the imidazole moiety. The end-on bent coordination mode of dioxygen and the O-O distances are in accordance with a ferric superoxo that fits well the model of Pauling, describing the electronic structure of oxy-hemoglobin.[48]

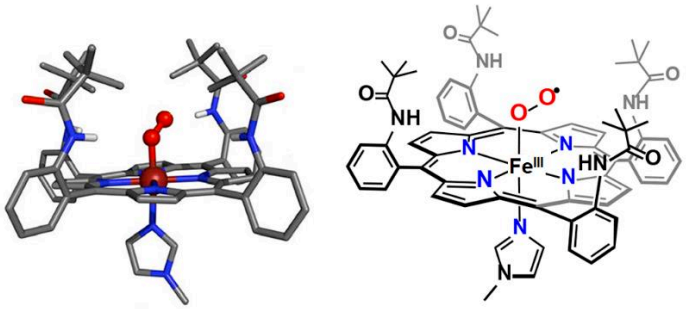

Figure 1.6: Crystal structure representation (left) and molecular structure (right) of the $Fe^{III}(OO^{\bullet})$ supported on a picket fence porphyrin as developed by Collman et al.[47]

Recently, the Scheidt[49] and the Solomon[50] groups revisited Collman's study. Scheidt et al. conducted a detailed study on the Mössbauer signatures of ferric superoxo picket fence porphyrin with three different axial N alkyl imidazole ligands, providing further details on bond distances and steric conformations of the adducts. Solomon et al. analyzed the L-edge XAS (X-ray Absorption spectroscopy) properties of the Collman complex. The detailed spectroscopic investigation in this study was combined with theoretical computations and showed that the metal oxidation state of $Fe^{III}(OO^{\bullet})$ can be between II and III pointing out that the classical oxidation state formalism may not be adequate for describing these species.

Interestingly, $Fe^{III}(OO^{\bullet})$ species are known, supported on porphyrinates that have been originally designed to model the Cyt P450 active site and thus bearded axially tethered thiolate ligand. Naruta et al. spectroscopically characterized the first such complex, using their unique twin coronet porphyrins, (see Figure 1.7), the extreme bulkiness of which protects both the superoxide moiety and the thiolate axial ligand from oxidation pathways.[51] The species in this example are generated by reaction between the ferric porphyrinate and potassium superoxide (KO_2) serving as the reducing agent, under oxygen atmosphere, in THF at 213 K. Later, the group synthesized and studied a twin twin-coronet porphyrin with tethered imidazole or pyridine as axial base, that showed a remarkably increased stability[52] (several days in toluene at room temperature, versus 1h at 253 K for thiobenzyloxy adduct, and 5h at 273 K for the thioglycolate one).

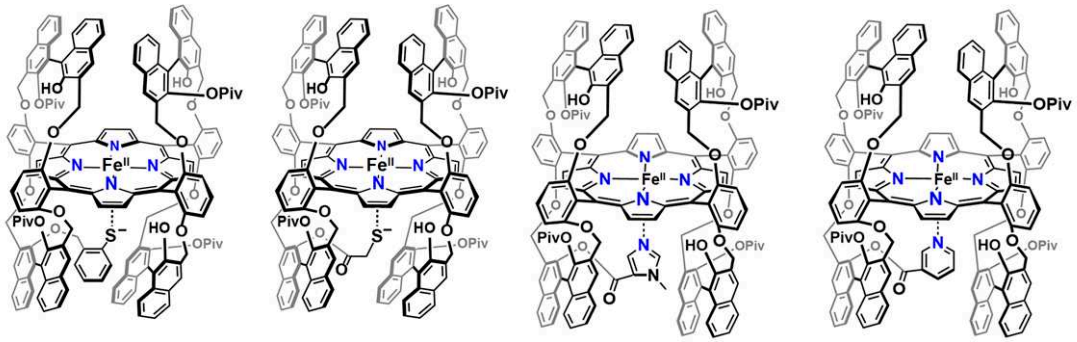

Figure 1.7: Twin coronet Fe porphyrins developed by Naruta et al., that has been used as precursors of ferric superoxo complexes.[52]

In 1999, Karlin et al. prepared and characterized a $Fe^{III}(OO^{\bullet})$ in THF, starting from the $Fe^{II}(F_8TPP)$ porphyrinate (see Figure 1.12 for the molecular structure of the complex). Addition of a Cu complex to this superoxo, led to a Cu-Heme μ-oxo species, an important milestone in the heme-copper chemistry.[53]

In 2020, Fe superoxide chemistry was revisited by Wijeratne and Goldberg research groups. Wijeratne et al. generated and characterized by UV-Vis and Resonance Raman spectroscopy, at 192 K in THF, a series of $Fe^{III}(OO^{\bullet})$ and studied their reactivity with indole substrates (see Chapter 5.1 for detailed discussion).[54]

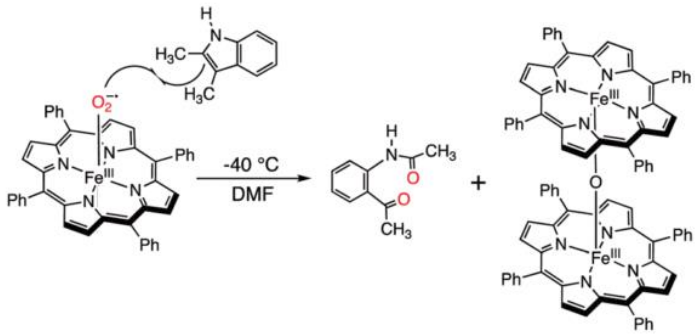

Figure 1.8: System developed by Goldberg et al. for dioxygenation of 2,3-dimethylindole. [55]

A more illustrative example is the work of Goldberg et al., where $Fe^{III}(TPP)(OO^{\bullet})$ is generated after reaction of Fe^{II} with O_2 in d^7-DMF at 232 K.[55] The reaction was followed by NMR and UV-Vis. The superoxo reacts in 1:1 stoichiometry with 2,3-dimethylindole, to give the open-ring di-oxygenated product, and the μ-oxo dimer of the Fe porphyrin (see Figure 1.8).

1.4.2 Ferric peroxo ($Fe^{III}(OO^{-})$) and Ferrous Superoxo ($Fe^{II}(OO^{\bullet})$) species

As discussed in the previous chapter, within biological systems, heme peroxo are typically six coordinated low spin complexes with an end-on bound peroxo moiety, and are rather unstable due to the excess of electronic density on the metal center.

The first report on synthetic $Fe^{III}(OO^{-})$ was the work of Valentine et al., who generated peroxo species of two ferric porphyrinates (FeTPP and FeOEP) by reacting the $Fe^{III}Cl$ with KO_2 in ACN in low temperatures and in DMSO at room temperature (see Figure 1.9). At least two equivalents of KO_2 were required; the first reduces the Fe^{III} to Fe^{II} and the second one reacts with Fe^{II} to give the $Fe^{III}(OO^{-})$.[56-57] UV-Vis, EPR, IR and Resonance Raman spectroscopies led to the conclusion that the peroxo is a high-spin ferric species, with a rhombic symmetry with the oxygen bound in an end-on mode. EXAFS data obtained later by Momenteau, confirmed this assignment.[58]

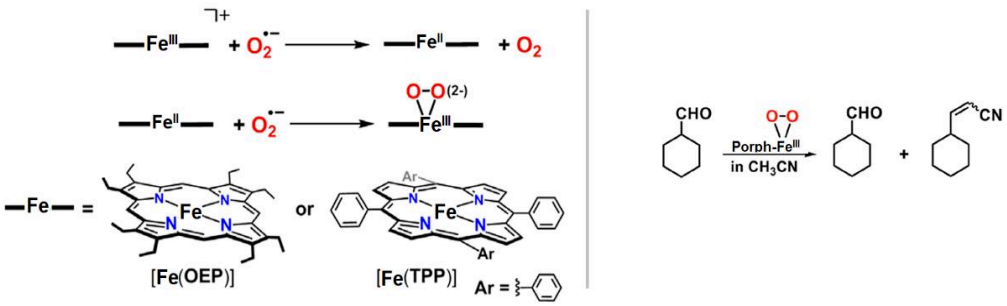

Figure 1.9: (Left) Generation of ferric porphyrinate peroxo species by Valentine[56] (Right) reactivity of ferric peroxo as reported by Watanabe.[59].

Following Valentine's report, James et al. showed that it is possible to generate the $Fe^{III}(OEP)(OO^{-})$ by reducing electrochemically the $Fe^{III}(OO^{\bullet})$ species, or by reacting electrochemically prepared Fe^{I} with O_2 (isoelectronic reaction), nevertheless, the authors of that study were not able to generate the peroxo starting from an Fe^{III}.[60]

Valentine later showed that ferric peroxo species are strong nucleophiles that react with electron deficient olefins. Strong electron withdrawing groups on the porphyrinate could however lead to the attenuation of this reactivity and the significant enhancement of the stability of the species.[61-62] Axial coordination of DMSO to the $Fe^{III}(F_{20}TPP)(OO^{-})$ (see Scheme 1.8 for molecular structure) could lead however to the activation of the nucleophilic character of the species. Watanabe et al. have studied the deformylation reactivity of peroxo species towards cyclohexane-carboxyaldehyde in

ACN leading to both cyclohexanone and nitrilated product (see Figure 1.9).[59] In a related study, Shteinman and Khenkin have shown that $Fe^{III}(TMP)(OO^{-})$ (see Scheme 1.8) reacts with acetic anhydride in cryogenic temperatures to form acyleperoxo species which upon heating lead to the corresponding compound I (formal $Fe^{V}(O)$).[63]

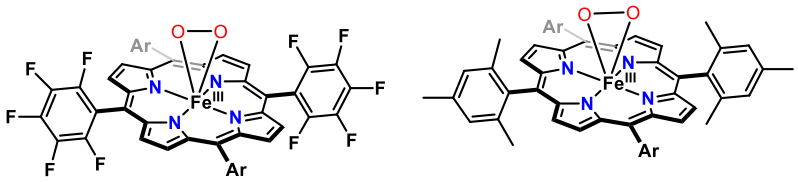

Scheme 1.8: Molecular structure of $Fe^{III}(F_{20}TPP)(OO^{-})$ (left), and $Fe^{III}(TMP)(OO^{-})$, (right).

In a recent study, Naruta et al. described the formation of a ferrous superoxo $Fe^{II}(OO^{\bullet})$ by the γ-ray cryoreduction of the corresponding ferric superoxo $Fe^{III}(OO^{\bullet})$ species, at 77 K, in a 20% ACN in Me-THF mixture. EPR and Resonance Raman spectroscopy confirmed their attributions. [64] Ivanovic-Burmazovic et al. also recently evidenced the formation of a $Fe^{II}(OO^{\bullet})$ adduct supported in a porphyrinate crown ether conjugate that was shown to be in equilibrium with his $Fe^{III}(OO^{-})$ counterpart as shown in Figure 1.10.[65]

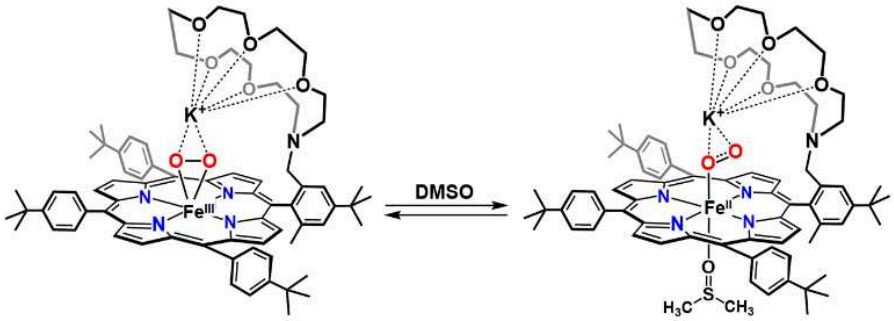

Figure 1.10: Equilibrium between $Fe^{II}(OO^{\bullet})$ and $Fe^{III}(OO^{-})$.supported in a porphyrinate crown ether conjugate as described by Ivanovic-Burmazovic [65]

1.4.3 Ferric hydroperoxo species ($Fe^{III}OOH$)

Tajima et al. in 1989 spectroscopically characterized the first hydroperoxo species, the Fe^{III}(TPP)(OOH). They generated it in DMF at 228 K, by addition of H_2O_2 in the starting ferric chloride, and characterized it using rapid freeze techniques coupled with UV-Vis and EPR spectroscopies.[69] The generation of the species required basic conditions and thus the authors suggested the presence of a hydroxide axial sixth ligand (see Figure 1.11). Later they also described the hydroperoxo species of the OEP and TMP porphyrinates.[66-67]

The intermediacy of a hydroperoxo species have been proposed in a catalase model system developed by Nocera, supported on "hangman" porphyrinates, where addition of H_2O_2 on the starting ferric species resulted in the generation of a high valent Fe^{IV}(O) π radical cation (see Figure 1.11). Importantly the authors were able to prove that intramolecular hydrogen bonding largely effect the reactivity of the system.[68]

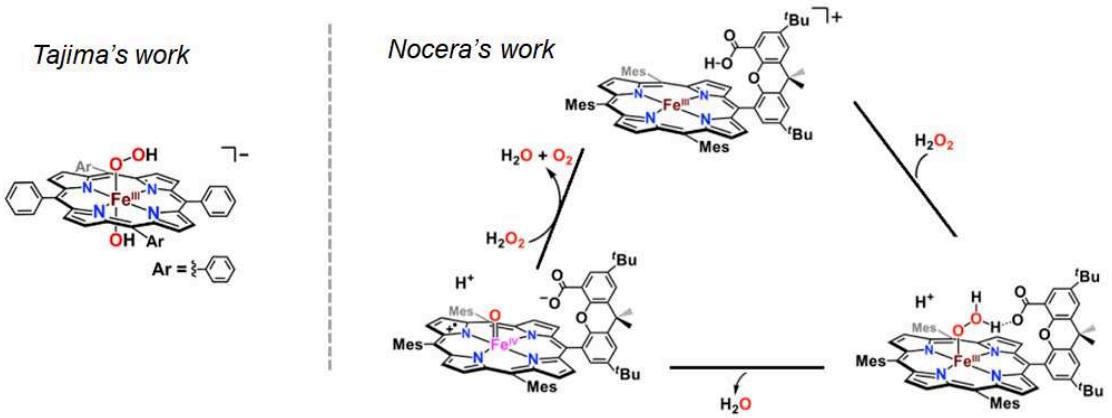

Figure 1.11: Initial reports on hydroperoxo species. (Left) First ever spectroscopically reported hydroperoxo species by Tajima [66](Right) Proposed intermediacy of hydroperoxo Fe in a hangman porphyrin, a catalase model reported by Nocera (see main text). [68]

Fully characterized Fe hydroperoxo species have been described for the first time in the inspiring work by Naruta et al., (see Figure 1.12) where a TMP-derived porphyrinate support with a tethered axial imidazole was used. Three synthetic pathways were proposed. In the first, the initial Fe^{II} species reacts with KO_2 to give the peroxo that is subsequently protonated with methanol, in the second, the reaction of Fe^{II} with KO_2 takes place directly in methanol, and in the third one, Fe^{II} reacts with O_2 to give the superoxo that is subsequently reduced with cobaltocene in presence of methanol (see Figure 1.12). This Fe(OOH) intermediate was characterized by EPR, UV-Vis,

Resonance Raman, and Mossbauer spectroscopies.[69] Later the same group reported two studies with "hangman" porphyrinates.[70] [71] In the first one they demonstrated the first example of end-on low spin ferric peroxo species; which can be quantitatively converted to the corresponding hydroperoxo species by reaction with an excess of methanol in ACN/THF mixtures at 203 K.[70] In the second study, they showed that hydroperoxo species could be generated after reduction of the ferric superoxide, by an intramolecular proton transfer that occurred between the oxygen moiety and the carboxylic group tethered in the hangman porphyrinate.[71]

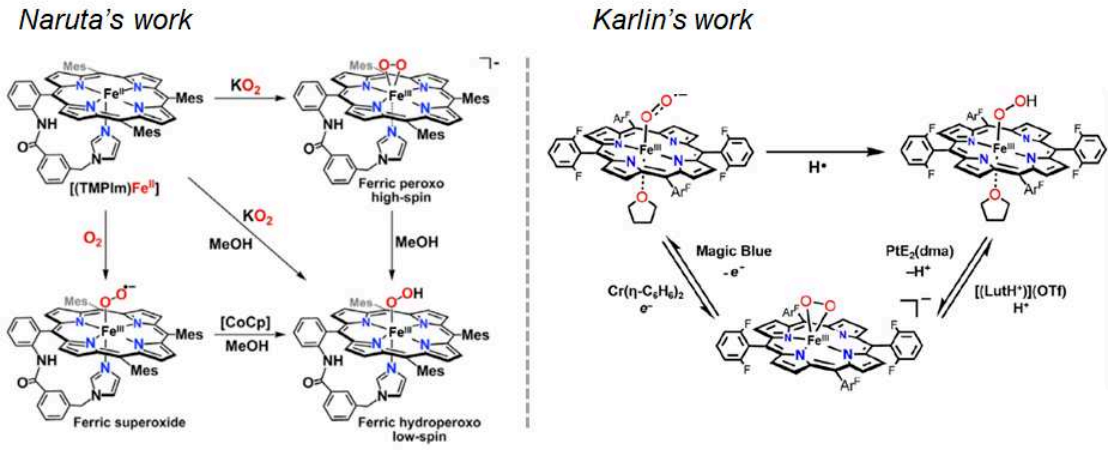

Figure 1.12: (Left) Multiple reaction pathways that result in the first fully characterized hydroperoxo species by Naruta (Right) Reversible reduction of the superoxo and protonation of the peroxo species as reported by Karlin using the Fe(F8TPP) porphyrin(see text).

The Karlin and Wijeratne groups are now enriching the field of iron porphyrin superoxo-peroxo species with their inspiring works. In 2020 Karlin et al. reported on the reversible reduction of the $Fe^{III}(F_8TPP)(OO^{\bullet})$ to $Fe^{III}(F_8TPP)(OO^{-})$, and the reversible protonation of the $Fe^{III}(F_8TPP)(OO^{-})$ to $Fe^{III}(F_8TPP)(OOH)$. The $Fe^{III}(F_8TPP)(OO^{\bullet})$ is generated by reaction between the ferrous porphyrinate and O_2 in THF in 213 K.[72-73] Wijeratne et al. examined the same reaction scheme using a series Fe porphyrins including Fe(TPP) and $Fe^{III}(F_{20}TPP)$.[74]

These works by Naruta, Karlin, and Wijeratne are essential for our work because they provide a throughout insight in to the chemistry and the characterization of superoxo, peroxo, and hydroperoxo Fe porphyrins species, which we aim to generate and characterize by electrochemistry. In particular, the UV-Vis spectra of the chemically

generated species that they report, have served as reference to compare with our own UV-Vis spectroelectrochemistry experiments.

Let us now consider the O-O cleavage in the $Fe^{III}(OOH)$ species. Studies that focus on the electrochemical O_2 reduction reaction by Fe porphyrins, mainly by Mayer et al. [75-76] and Dey et al. [77], focus on the parameters that control the O-O bond cleavage versus the Fe-O bond cleavage. Indeed, this reaction step is crucial for the reaction selectivity (H_2O for O-O bond cleavage, and H_2O_2 for Fe-O bond cleavage). However, this studies do not include spectroscopic characterization of such intermediates.

To the best of our knowledge, detailed studies of the O-O bond cleavage in chemically generated Fe(OOH) species in organic solvents are quite scarce in the literature. However, there is a handful of works reporting of the O-O bond cleavage on alkyl- or acyl-peroxo species, which we are going to discuss in the next paragraph.

1.4.4 On the O-O bond cleavage in $Fe^{III}(OOR)$ species

The chemistry of the O-O cleavage of $Fe^{III}(OOR)$ species, that are usually generated upon reaction of a ferrous or ferric porphyrinate with organic peroxy acids, depend on several parameters such as the nature of the R group, a possible second axial ligand, the metal center, as well as the conditions and the medium.

One of the first reports that looked at this problem, in model systems, was a work by Groves et al. in 1988, where it was demonstrated that addition of m-cpba to a Fe^{III}(TMP)Cl resulted in Compound I in polar solvent, following an O-O bond heterolysis, while in non-polar solvents the addition resulted in the Fe^{III} N-oxide (the oxygen atom is bound to the Fe center and to a nitrogen atom of the porphyrin ring, and the species is isoelectronic to a $Fe^{IV}(O)$).[78] A decade later, in line with this results, the detailed work of Nam et al. showed that the nature of the O-O bond cleavage (heterolytic giving the Compound I and homolytic the Compound II or the Fe^{III} N-oxide) in Fe acylperoxo species in organic solutions, can be modulated by changing the exogenous axial ligand.[79-80]

In 1989, Bruice et al. prepared in water several $Fe^{III}OOR$ complexes of the meso–tetrakis(2,6–dimethyl-3-sulphonato phenyl) porphyrinate (TMPS), with R=alkyl or acyl. The alkyl-peroxo species are produced by reaction of the starting Fe^{III} aquo with an alkyl peroxide (such as $(CH_3)_3COOH$, tert-butyl hydroperoxide, or $(CH_3)_2PhCOOH$, cumene hydroperoxide). The Fe acyl-peroxo are produced by the reaction of the starting

ferric porphyrin with an acyl-peroxide such as m-cpba. The authors found that the the Fe alkyl-peroxo species undego pH-dependent homolytic O-O bond cleavage, while the Fe acyl-peroxo species undergo heterolytic O-O bond cleavage (see Figure 1.13).[81] In a later study, Nam et al. studied a series of Fe porphyrins in DCM/methanol mixtures and draw similar conclusions.[82]

Traylor et al.[83] on the other hand proposed an heterolytic cleavage even for the alkyl-peroxo species in methanol, based on the highly efficient alkene epoxidation demonstrated by the Fe(F_{20}TPP). Traylor[84] further proposed that electron withdrawing substituents on the porphyrin ring favor the heterolysis of the O-O bond.

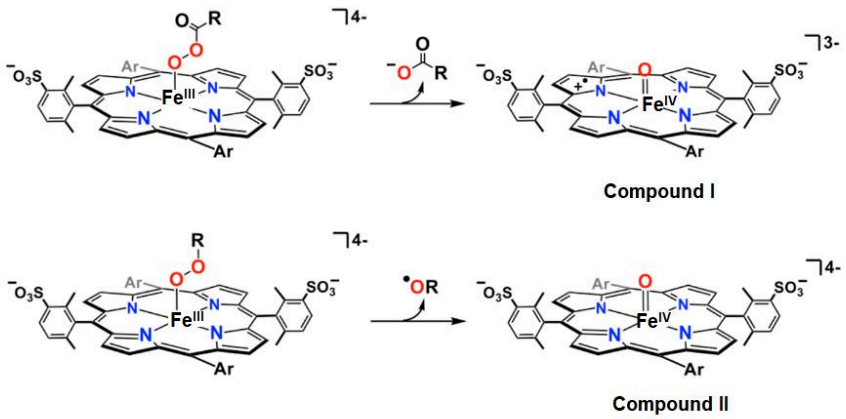

Figure 1.13: Fe^{III}-acylperoxo (top) and Fe^{III} -alkylperoxo (bottom) complexes that lead to heterolytic and homolytic O−O bond cleavage, respectively (in aqueous media), as observed by Bruice and co-workers.[81] The porphyrin ligand is the meso–tetrakis(2,4,6–trimethyl-3-sulphonato phenyl) porphyrinate.

A more recent work by van Eldik et al. shed light to the O-O bond cleavage chemistry in water, using the water-soluble and non-dimer-forming meso–tetrakis(2,4,6–trimethyl-3-sulphonato phenyl) ferric porphyrinate (Fe^{III}(TMPS)) with a variety of oxidants: H_2O_2, PhIO, and m-cpba. Importantly, the authors concluded that in fact, reaction between Fe^{III}(TMPS) and m-cpba would always result in compound I *via* heterolysis, however, in certain pH values, further reduced species could accumulate.[85] More recently, Groves revisited the aqueous chemistry of Fe^{III}(TMPS) reporting on pH-dependence of the equilibria between different high-oxidation state species, generated with m-cpba.[86]

1.4.5 Synthetic models of high valent $Fe^{IV}(O)$ π radical cation(compound I) and $Fe^{IV}(O)$ (compound II) porphyrins.

The Fe-oxo species in biological systems, have mostly been observed as fleeting intermediate due to their strong electrophilicity, with the exception of compound I of peroxidase, the crystal structure of which has been obtained,[87] and of the recent work of Green on Cyt-P450 described above (paragraph 1.3.2).[27]

The first work on high-valent Fe oxo porphyrin species is ascribed to Groves et al., who spectroscopically characterized the $Fe^{IV}(O)$ π radical cation of the Fe(TMP), by reaction between the ferric porphyrinate and the m-cpba, an oxygen atom donor, at 223 K. Based on EPR spectroscopy, they proposed and electronic structure with overall S=3/2, where a porphyrin π radical cation is ferromagnetically coupled with a Fe^{IV} metal center with S=1.[88] Further work demonstrated that generation of high valent species is possible by dimethyldioxirane [89] and ozone.[90] $Fe^{IV}(O)$ is a model of compound II and has been also characterized by Groves et al. in their initial works.[88]

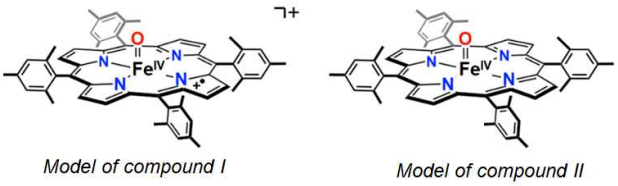

Figure 1.14: High valent species $Fe^{IV}(O)$ π radical cation (left, Compound I) and $Fe^{IV}(O)$ of the FeTMP porphyrin (right, Compound II).

Models of the Cyt-P450 compound I are capable of reacting with many organic substrates. They induce oxo transfer reactions to phosphines and to sulfides, epoxidation of olefines, C-H bond activation in aliphatic and aromatic substrates, and N-,S-, and O-dealkylation reactions.[9, 91]

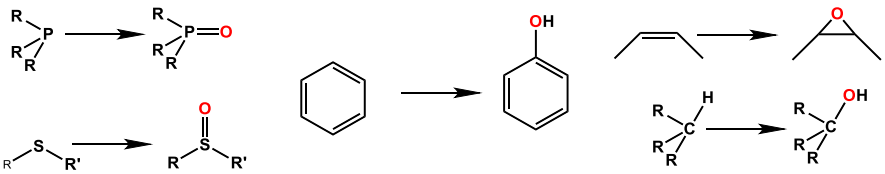

Figure 1.15: Some of the reactions that Compound I type model systems that can promote according to references [9] and 1.

Fe porphyrins with a variety of substituents either on the meso or on the β-pyrrole position, have been used to generate $Fe^{IV}(O)$ π radical cation species. Based on EPR spectroscopy and on theoretical studies (DFT) , two possible π radical cation states have been identified, with orbital of either a_{1u} or a_{2u} symmetry, as HOMO. The homo contains one unpaired electron and the lower energy orbital contains two . Electron withdrawing groups at the meso-position result in lowering of the energy of the HOMO a_{2u} orbital, allowing energy mixing with the a_{1u} molecular orbital, that is fully occupied, *via* vibronic coupling. On the other hand, for the β-pyrrole substituted porphyrinates, the energy of the HOMO a_{1u} decreases along with the energy of the a_{2u} orbital, upon increasing the electron withdrawing character of the substituents (Scheme 1.9).[29]

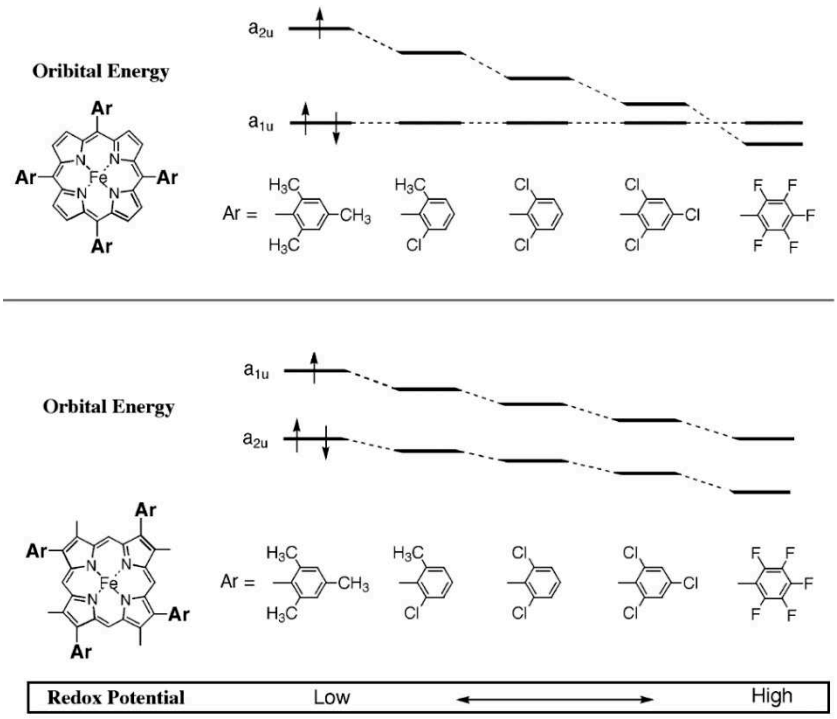

Scheme 1.9: HOMO orbitals for $Fe^{IV}(O)\pi$ radical cation of porphyrins with several different meso (up) or β substituents (down). Adapted from reference [29].

Electron withdrawing substituents in both the meso or β position of the porphyrin ring, increase the reactivity of $Fe^{IV}(O)$ π radical cation complexes, for cyclohexene epoxidation reactions.[92] This finding indicated that the mixing in the ground states (a_{1u} or a_{2u}) that occurs only for the Fe porphyrins with electron-withdrawing meso-substituents, has little effect on the reactivity of the high valent species, since electron-withdrawing β-substituents also lead to higher reactivity. However, this increase of the

reactivity can be linked with the higher $E^0_{Fe^{IV}(o)L^{+\cdot}/Fe^{IV}(O)L}$, as measured in the thorough electrochemical and spectroelectrochemical study of Fujii et al.[26]

Additionally, Fujii et al. reported on the effect of the axial ligand on the reactivity of the Compound I models. When strong electron donor ligands such as imidazole or phenolate are present the rate of the epoxidation reactions of several olefines was substantially increased.

$Fe^{IV}(O)$ π radical cation porphyrinates are able to catalyze the hydroxylation of relatively inert aromatic C-H bond as it is the case for the compound I of Cyt-P450. In a recent example by Groves et al.,[93] evaluated the activity of Compound I model in aqueous solutions. The Fe^{III}(4-TMPyP) (TMPyP = 5,10,15,20-tetrakis(N-methyl-4-pyridinium)-porphyrin) reacts with m-cpba in pH=4 to give the high valent species, that was shown to have a remarkable reactivity towards xanthene.

Regarding now the $Fe^{IV}(O)$ intermediates, they have been reported to be reactive towards triphenyl phosphine and olefins, however, Newcomb et al. raised serious doubts and provided an alternative explanation for these observations.[94] They demonstrated that $Fe^{IV}(O)$ porphyrin intermediates prepared in acetonitrile, showed lower reactivity when they possessed electron withdrawing meso-substituents, a counterintuitive observation based on the previously known chemistry. They proposed and supported experimentally that a disproportionation reaction takes place between $Fe^{IV}(O)$ porphyrin and $Fe^{IV}(O)$ porphyrin π radical cation (Figure 1.1), that favors the $Fe^{IV}(O)$ porphyrin when electron withdrawing meso-substituents (such as the case of $Fe(F_{20}TPP)$) are present. They thus concluded that the only true oxidant is $Fe^{IV}(O)$ porphyrin π radical cation.

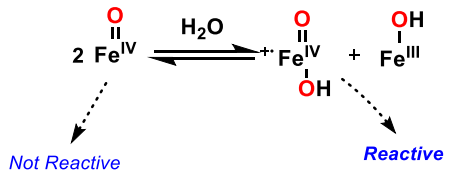

Figure 1.16: Disproportionation reaction that takes place between high valent Fe oxo species in non-dry solvents and in water, as described by Newcomb.[94]

As far as chloroperoxidase models are concerned, during the last decade Fujii et al. have provided important insights in the chemistry of high valent species that play the role or are precursors of chlorinating agents. In their first work on this topic they showed that

the $Fe^{IV}(F_{20}TPP^{\cdot+})(O)$ species generated in low temperature by exposure of the ferric porphyrin to O_3, could react with chloride and *in situ* induce chlorination of substrates such as anisole and cyclohexene in sub-stoichiometric yields.[95] They proposed that Cl^- is oxidized to Cl_2 by $Fe^{IV}(F_{20}TPP^{\cdot+})(O)$, and that Cl_2 was the chlorinating agent. They later showed that $Fe^{IV}(O)$ π radical cation of a series of Fe porphyrins can react with chloride anions (presumably oxidizing them) resulting in the corresponding $Fe^{IV}(O)$ species. However, this was only the case for porphyrins with sufficient electron withdrawing meso-substituents ($E^0_{Fe^{IV}(O)L^{+\cdot}/Fe^{IV}(O)L}$ high enough to oxidize chloride anions).[96]

In another work Fujii et al. prepared and characterized the hypochlorite Fe^{III} species of the $Fe(F_{20}TPP)$, which also was shown to be able to oxidize/chlorinate organic substrates.[97]

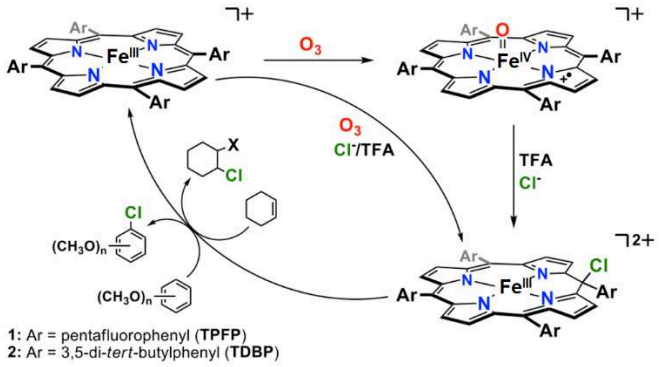

Figure 1.17: Recent work by Fujii et al. where a unique chlorinating agent was characterized, a meso-chloro isoporphyrin, produced by reaction of the ferric porphyrin with ozone gas in presence of chloride and triflic acid.[98]

A new chlorinating agent was observed by addition of chloride to $Fe^{IV}(F_{20}TPP^{\cdot+})(O)$ in presence of trifluoroacetic acid, which based on NMR, EPR, and UV-Vis spectroscopies was formulated as meso-chloroisopophyrin species (see Figure 1.17).[98] Importantly, in this study Fujii et al. proposed a catalytic biphasic system as well, where the catalyst, the substrate, the chloride source and the acid are solubilized in DCM, and the oxidizing agent is H_2O_2 in an aqueous phase (see paragraph 5.3 for more detailed discussion).

High valent Fe-oxo species are in the heart of the Cyt-P450 related studies both in biological and synthetic systems, because it is generally accepted that they are in most

cases the active oxidants. As a result, if we are to reproduce the Cyt-P450 reactivity electrochemically, the understanding of the chemistry of the active oxidants provided in the discussed literature is indispensable. A question that we discuss later in this manuscript is the following: *Is it possible to electrochemically generate Fe-oxo high valent species in a controlled manner and harness their reactivity?*

In the next pages, we will discuss Mn porphyrins as models of the Cyt-P450 that have been studied in parallel with their Fe counterparts. We follow the same order as for the Fe model systems, that is, first we examine the Mn-O_2 adducts, then the O-O bond cleavage, and at the end, the high valent Mn-oxo species that occur after the cleavage of the O-O bond.

1.4.6 Mn-O_2 complexes as models of heme enzymes

Early studies on O_2 activation with Mn porphyrins, were carried out by Basolo et al. in the 70's. The authors demonstrated that Mn^{II}(TPP) porphyrins react with O_2 in toluene, at 210 K, in presence of pyridine, resulting in a $Mn^{II}(TPP)O_2$ adduct after loss of the axially ligated pyridine. [99-100] The adduct exhibits an intermediate spin (S=3/2) and a large zero field-splitting (-2.4 cm^{-1}), and an IR stretching frequency $\nu(O_2)$ between 900 and 990 cm^{-1}, significantly lower than the corresponding Fe and Co compounds (around 1100-1200 cm^{-1}), and thus the authors ascribed it as a formal $Mn^{IV}(OO^{-})$, see Figure 1.18, with a side-on binding mode,[101] an atypical charge distribution at least for the Fe porphyrins.

Valentine et al. examined the reaction between Mn^{III}(TPP)Cl and KO_2 in DMSO. In solutions in coordinating solvents, chloride ion de-coordinates leading to $[Mn^{III}(TPP)]^{+}$ species which reacts with a first equivalent of KO_2 to give Mn^{II}(TPP). The latter reacts with a second equivalent of KO_2 to give the formal $Mn^{II}(TPP)(OO^{\bullet})$ (see Figure 1.18).[102] Crystal structure of both $[Mn^{II}Cl]K$ and $[Mn^{II}(OO^{\bullet})]K$ were later obtained.[103] The formal adduct in the solid state is better formulated as a side on $Mn^{III}(OO^{-})$. However, the authors underline that the data obtained in solution (UV-Vis, NMR) are more in favor of the $Mn^{II}(OO^{\bullet})$ structure. Groves later prepared and characterize the $Mn^{II}(TMP)(OO^{\bullet})$ that exhibited similar characteristics with its TPP analogue.[104] Except these three reports, there are not to date, to the best of our knowledge, other examples of characterization of Mn-O_2 adducts.

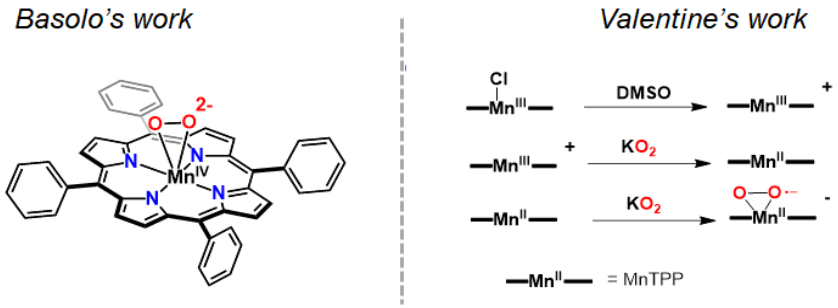

Figure 1.18: (Left) TPP-Mn-O_2 adduct as described by Basolo, generated by reaction of Mn(TPP) with O_2 at low temperatures, in toluene in presence pyridine.[99-100] *(Right) Reaction of Mn(TPP)Cl with 2 equivalents of KO_2 to produce the Mn^{II} superoxo complex, as reported by Valentine.*[102]

As discussed later in the manuscript (Chapter 2), the $Mn^{II}(TPP)(OO^{\bullet})$ adduct can, under certain conditions, react with an electrophile such as benzoic anhydride, and lead to the O-O bond cleavage.

1.4.7 O-O bond scission in $Mn^{III}OOR$, with R= H or acyl group

Organic media: Mn^{III} acyl-peroxo. In an early study, Groves et al. reported on the generation of the first know acylperoxo-Mn^{III} porphyrin by both acylation of the $Mn^{II}(OO^{\bullet})$ or direct addition of m-cpba in the starting solution of $Mn^{III}(TMP)Cl$ in acetonitrile. Warming of an acylperoxomanganic porphyrinate solution from 220 K to 263 K afforded the high valent $Mn^{V}(O)$ complex that results from the O-O bond cleavage (see Figure 1.19), in a similar fashion as for Fe porphyrins.[104]

Aqueous media: Mn^{III} hydroperoxo. The O-O bond cleavage, has also been studied in a $Mn^{III}(OOH)$ species of a water soluble porphyrin, in aqueous solutions. Groves et al., studied the O-O bond cleavage in a Mn hydroperoxo in water, supported by an imidazole meso substituted porphyrin namely TDMImP = 5,10,15,20 tetrakis N,N dimethyl-imidazole porphyrin. They found that the optimum pH range for the reaction of the porphyrin with H_2O_2 that afforded the high valent $Mn^{V}(O)$ species was between 8.5 and 11.5.[105] They suggested that this is due to a push-pull behavior of the O-O bond cleavage. Partial deprotonation of the axial -OH renders it more electron donating and on the other hand the distal oxygen of the hydroperoxo when partially protonated tends to give a water molecule to the solvent, serving as electron withdrawing moiety(see Figure 1.19).[105]

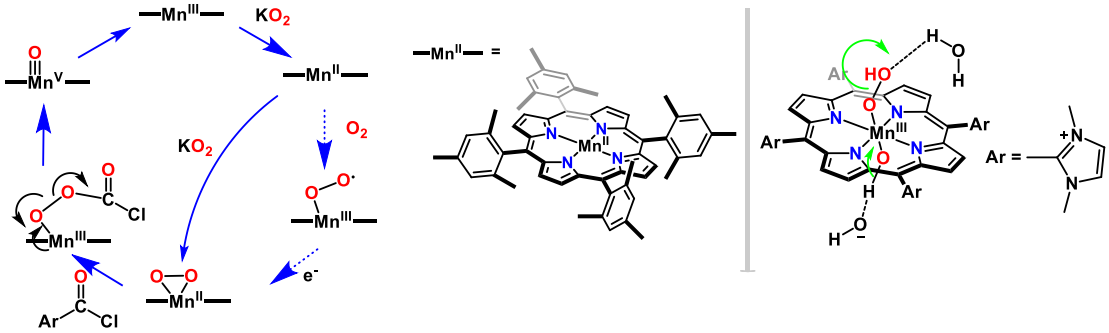

Figure 1.19: O-O bond cleavage in an acyleperoxo Mn^{III} porphyrin in ACN[104] (left) and in an hydroperoxo Mn^{III} porphyrin in water[105] (right) as both described by Groves.

Understanding of the O-O bond cleavage process is crucial because it leads to high valent Mn-oxo species. Such species have been spectroscopically characterized and their reactivity towards substrates evaluated, as we are going to discuss in the next paragraphs.

1.4.8 High valent Mn-oxo porphyrins and their reactivity

High valent oxo Mn^{V} porphyrins have been known for being highly reactive towards C-H bonds.[106] Their characterization however has been challenging due to their high reactivity, in contrast with the corresponding Mn^{IV}(O) species.[107] The first kinetic evaluation was carried out by rapid-mixing stopped-flow techniques on the Mn^{V}(O) that was generated by reaction of mcpba with Mn^{III}TMPyP (TMPyP=5,10,15,20 tetrakis meso N-methyl pyridyl porphyrine).[108] The species was diamagnetic and did not possess the characteristic broad band with λ_{max} higher that 600 nm, suggesting the absence of a π porphyrin radical cation unlike the Fe counterparts.[109]

Important milestones in the Mn^{V}(O) chemistry are firstly the work of Nam et al.,[110] who generated the TF_4TMAP-Mn^{V}(O) (TF_4TMAP = *meso*- tetrakis (2,3,5,6- tetrafluoro-*N*,*N*,*N*-trimethy l-4- aniliniumyl) porphinato dianion) with a triflate as axial ligand, by reaction of Mn^{III} porphyrin with two equivalents of basic hydrogen peroxide in water. Secondly, Naruta et al. synthetized the binuclear Mn^{V}(O) by addition of m-cpba to the manganic porphyrin in presence of tetrabutylammonium hydroxide.[111] A few years later Newcomb reported the generation of several Mn^{V}(O) porphyrinates by laser flash

photolysis of the Mn^{III} perchlorates.[112] In that case the perchlorate anion is the O-atom donor. These three examples are shown in Figure 1.20.

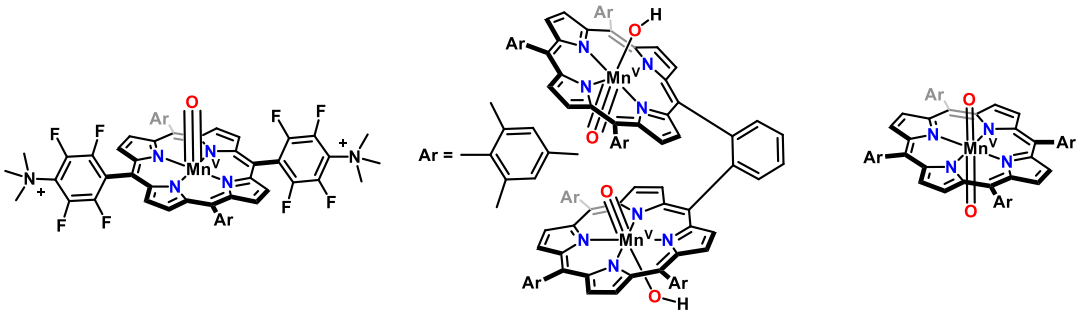

Figure 1.20: From left to right: A water soluble high valent $Mn^{V}(O)$ as described by Nam, a binuclear $Mn^{V}(O)$ as described by Naruta, and the unusual dioxo manganyl species as described by Groves.

More recently Spiro and Groves characterized spectroscopically, by IR and Resonance Raman, the unusual $Mn^{V}(O)_2$ (dioxo manganyl) porphyrinate with several different porphyrin scaffolds (Figure 2.11).[113] Until now, the only first-row transition metal that has been shown to form dioxo high valent species remains manganese.[9] The dioxo species were not very reactive towards oxidizable organic substrates, showing a certain decrease in the electrophilicity, but in lower pH the reactivity was regained suggesting that the species is in equilibrium with the more reactive HO-Mn^{V}≡O counterpart.

Regarding now the reactivity of the high valent manganese species towards substrates, a detailed mechanistic study by Groves et al. recently examined the mechanism of C-O formation during the C-H activation by Mn porphyrins, and conducted some parallel studies with Fe Porphyrins.[114] The reactions with substrates were carried out in organic solvents, with Mn^{III} porphyrin as catalyst and m-cpba or PhIO as oxidants. Firstly, they found that for norcarane oxidation by Mn porphyrins, anionic axial ligands such as F^- or OH^-, led to rearranged products while nitrogenous axial bases led to non-rearranged products (see Figure 1.21). The authors propose that ligands such as F^- or OH^- would diminish the reduction potential of the $Mn^{IV}(OH)$, disfavoring the rebound step, and leading to rearranged products.

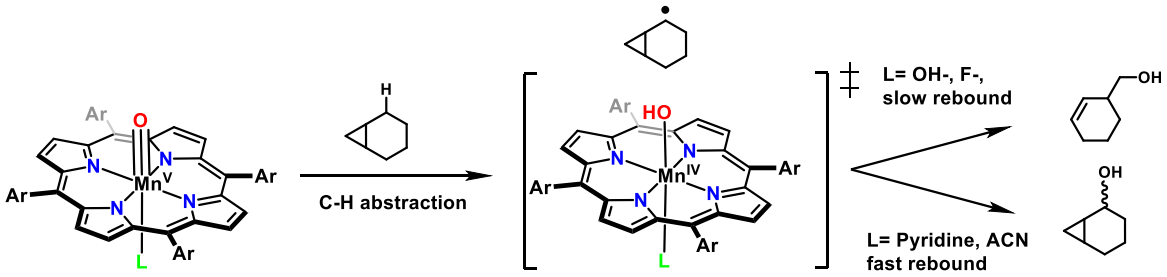

Figure 1.21: Slow vs Fast rebound mechanism in the C-H oxidation with rebound mechanism by Mn Porphyrins as reported by Groves.[114]

Fe and Mn porphyrins have then been compared in the hydroxylation reaction of deuterated ethylbenzene. The stereochemical inversion was found to be sensitive to the metal center. In particular, the retention of configuration was only 8−20% for $Mn^{V}(O)(Cl)$, while $Fe^{IV}(O)(Cl)$ π radical cation showed 80−90% retention. Significantly, $Fe^{IV}(O)(F)$ π radical cation afforded only 60−70% retention, showing that axial ligands such as F^{-} that diminish the reduction potential of the high valent species, lead to a decrease of the stereochemical retention in the product. It was also observed that electron-withdrawing substituents (that have higher reduction potentials) on both Fe-oxo and Mn-oxo porphyrins, lead to less stereochemical inversion at the benzylic hydroxylation site.

Taken into consideration all these observations, Groves et al. confirm the general idea that oxygen rebound step is faster for stronger oxidants and more able to compete with radical cage escape.

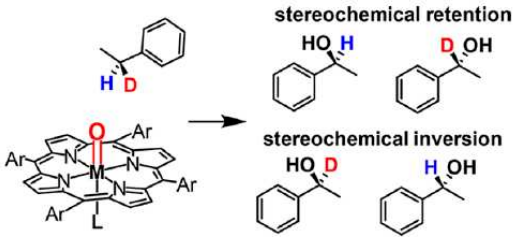

Figure 1.22: Stereochemical retention vs stereochemical inversion in the hydroxylation reaction of deuterated ethylbenzene by Metal-porphyrin-oxo species, Metal=Fe or Mn. From reference [9].

Mn porphyrins have also been studied as catalyst for the C-H bond halogenation reactions. In the first report of Groves et al. in 1980 on the oxidation reactions by $Mn^{V}(O)$, halogenation products had been observed, and the chlorine atom source was

the chloride anions present as counterion/axial ligand.[106] During the last decade, Groves et al. conducted detailed studies on the catalysis of the C-H bond chlorination (and in general halogenation) of elaborate substrates by Mn porphyrins (see Figure 1.23).[115] Amongst others, Mn(TPP) and Mn(F_{20}TPP) have been used as catalysts. Mn(TPP) was first used in a biphasic system, where the catalyst and the substrate were diluted in a DCM phase, and the oxidant was an aqueous phase of sodium hypochlorite solution, and TBACl was added as phase transfer catalyst. Simple substrates such as toluene were chlorinated with yields (based on the oxidant used) ranging from 30% to 70%. More challenging substrates such as trans-decalin were also chlorinated with good regioselectivities.[116] Very recently, and one phase system was used; Mn(F_{20}TPP) and the substrate were dissolved in deuterated ACN, and the TBAOCl was added directly in the solution.[117] This system showed good selectivity with even more challenging substrates and overall higher reactions yields.

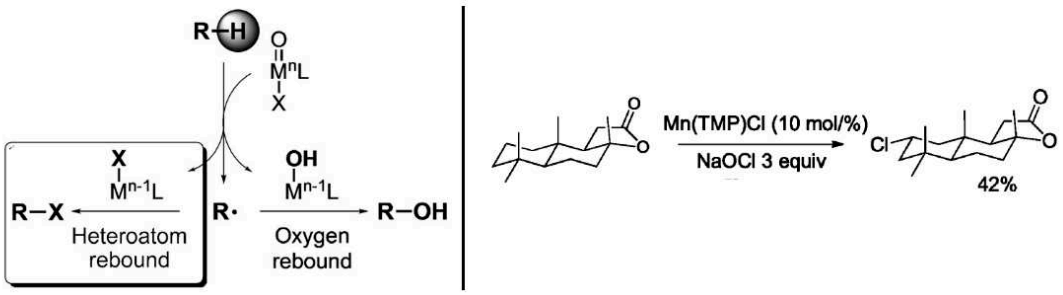

Figure 1.23: (Left) Concept of heteroatom rebound that leads to the chlorinated rather than oxygenated substrate. (Right) C2-selective chlorination of sclareolide with the isolated yield of the reaction. From reference [115].

We believe that these works by Groves, as well as the works by Fujii on halogenation reaction by Fe porphyrins, are important milestones because they explore a reactivity that is not only interesting in itself and with respect to the biological systems, but also relevant to the modern challenges of the chemical industry.[6]

1.5 Electrochemical O_2 reductive activation by Fe and Mn porphyrins

We hope that we have demonstrated in the introduction of the present manuscript, that Fe and Mn porphyrins as models of Cyt-P450 type metalloenzymes have a rich chemistry, that have been examined by the thorough works of Groves, Valentine, Naruta, and some others. However, all these works utilize reducing agents to provide the necessary electrons to the metal center for activating oxygen, or oxidizing agents to generate the oxidizing active species.

In the present work, we propose an alternative approach based on electrochemical reductive activation of O_2 for generating and characterizing intermediate species, and harnessing their potential reactivities. Our tools include cyclic voltammetry, UV-Vis spectroelectrochemistry, Scanning Electrochemical Microscopy, and preparative scale electrolysis. We also propose a set-up for Resonance Raman spectroelectrochemistry. Previous work at LEM includes the PhD thesis of Dr. Célia Achaibou, which focused on developing several SECM modes for studying O_2 activation.

Example of aerobic oxidations of substrates catalyzed by Mn of Fe porphyrins, under electrochemical conditions, are extremely scarce in the literature.[118-119] In a pioneering work, back in the 80's, Murray reported on the electrochemical aerobic oxygenation of olefins catalyzed by MnTPPCl in organic solvents, in presence of anhydride that induced the catalysis.[120] Based on the cyclic voltammetry data the authors proposed a mechanistic reaction scheme, central role to which had the oxidizing $Mn^{V}(O)$.[121]

More recently, Dey et al.,[122] inspired by the work of Collman et al.,[123] have been reporting on a Cyt P450 model system that consists of Fe porphyrins immobilized on gold electrodes using self-assembled monolayers (SAM).[124] The Dey group use Surface Enhanced Resonance Raman Spectroscopy to characterize intermediate Fe porphyrin species attached on imidazole or sulfide terminal groups of the SAMs on gold electrodes.[125] In their reaction system, immobilized Fe porphyrins catalyze C-H oxidation of simple organic molecules in air or O_2 saturated aqueous solutions. The TON reported for substrate oxidation are quite remarkable (up to 20,000).[125-126]

It is important to underline here the remarkable work of Mayer et al. on the homogeneous electrochemical four electron/four proton reduction of O_2 by Fe porphyrins.[127-129] These works provide a very useful insight on several mechanistic

aspects of electrochemical O_2 reduction, and focus on the Cyt c Oxidase mimic for fuel cell applications. Similar work of Nocera, Costentin et al. focused on ORR catalyzed by Mn porphyrins. Our objective is different: we aim to carrying out electro-catalytic oxygenations and halogenation of organic substrates by harnessing the oxidizing power of Fe or Mn oxygen intermediates that are produce during electrochemical O_2 activation. *Our major challenge is to achieve the fine tuning of the electrochemical reactions that will allow us to generated the intermediates with the desired reactivity, in a controlled manner.*

Chapter 2

One electron reduced M^{III} porphyrins (M = Fe or Mn) react with O_2 or $O_2^{\bullet-}$

Fe(or Mn)-porphyrin-O_2 intermediates can be chemically generated by reaction of the ferrous (Fe^{II}) or ferric (Fe^{III}) state porphyrins with $O_2^{\bullet-}$ donors (such as KO_2, see chapter Chapter 1).[56, 102] Following previous work in the Laboratoire d'Electrochimie Moléculaire on non-heme complexes,[130-132] in 2016 it has been demonstrated by Anxolabéhère-Mallart, Fave et al. that the $Fe^{III}(F_{20}TPP)(OO^{-})$ (peroxo) species can be formed by electrochemical O_2 activation in DMF solutions.[133] In this chapter we revisit these results, which have served as a basis for our work, and the we extend our methodology to study O_2 activation by the Fe^{III}(TPP)Cl and Mn^{III}(TPP)Cl complexes.

2.1 Previous results.

The $Fe^{III}(F_{20}TPP)Cl$ porphyrin has been chosen as a starting platform for that first study in LEM,[133] due to its perfluorated meso-substituents. These substituents lead to a 280 mV positive shift of the Fe^{III}/Fe^{II} redox potential ($E^0_{Fe^{III}/Fe^{II}}$) compared to the non-perfluorated analogue Fe^{III}(TPP)Cl, thus resulting in a smaller thermodynamic cost for achieving the Fe^{II} state that reacts with O_2. Furthermore, electro-withdrawing meso-substituents disfavors the formation of μ-oxo dimers in O_2 containing solutions.[134]

DMF has been chosen as solvent because of the high solubility of metal porphyrins to this solvent.[135] Additionally, air saturated DMF solutions display a reversible $O_2/O_2^{\bullet-}$ wave at -0.85 V vs SCE, as shown in (Figure 2.1, red trace).[136]

CV of a 1 mM solution of $Fe^{III}(F_{20}TPP)Cl$ in DMF under argon displays three typical and well-defined waves corresponding to the successive Fe^{III}/Fe^{II}, Fe^{II}/Fe^{I}, and Fe^{I}/Fe^{0} reduction processes occurring at +0.02, −0.80, and −1.315 V vs SCE, respectively (Figure 2.1, black trace).

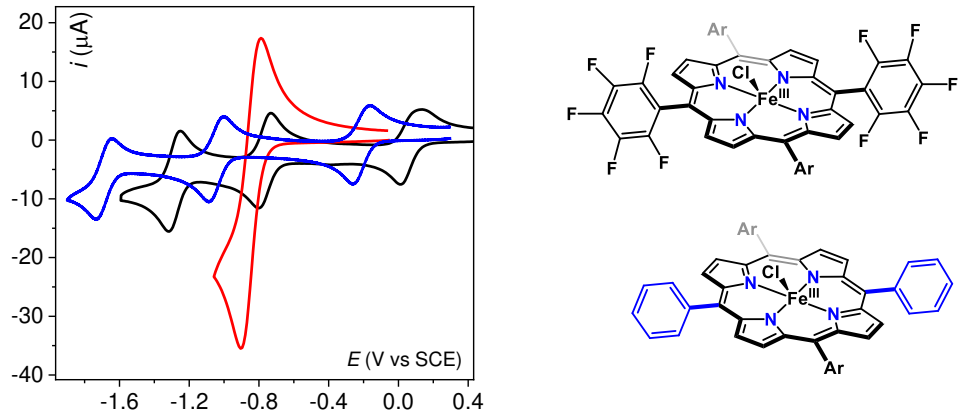

Figure 2.1:(Left) CV of an Ar saturated DMF solution of 1 mM $Fe^{III}(F_{20}TPP)Cl$ (black trace), and CV of a DMF solution of 1 mM of $Fe^{III}(TPP)Cl$ in the same conditions (blue trace). CV of 1 mM solution of O_2 (air saturated, red trace). All solutions contained 0.1 M $TBAPF_6$, and CVs were recorded at a glassy carbon (GC) disk electrode (with an area of 0.071 cm^2), at 0.1 V s^{-1} and T = 293 K. (Right) molecular structures of $Fe^{III}(F_{20}TPP)Cl$ and $Fe^{III}(TPP)Cl$.

We observe that in presence of O_2 the forward Fe^{III}/Fe^{II} reduction peak is not affected (Figure 2.2, red and black traces). However, a new one electron reduction wave appears at -0.5 V vs SCE, and the intensity of the Fe^{II}/Fe^{III} reoxidation peak on the reverse scan decreases (Figure 2.2, red traces).

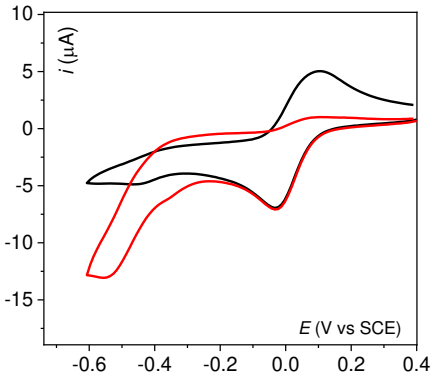

$$E \quad Fe^{III}Cl + e^- \rightleftharpoons Fe^{II} + Cl^- \qquad (2.1)$$

$$C \quad Fe^{II} + O_2 \overset{K_{O_2}}{\rightleftharpoons} Fe^{III}OO^{\bullet} \qquad (2.2)$$

$$E \quad Fe^{III}OO^{\bullet} + e^- \rightarrow Fe^{III}OO^- \qquad (2.3)$$

Figure 2.2: (Left) CV in DMF with 0.1 M $TBAPF_6$ of 1 mM solution of $Fe^{III}(F_{20}TPP)Cl$ under Ar (black), under O_2 (1 mM, air saturated) (Red). CVs recorded at a GC disk electrode (0.07 cm^2), at 0.1 V s^{-1} and T = 293 K. (Right)Proposed reaction mechanism.

The reduction wave at -0.5 V is attributed to the reduction of the $Fe^{III}(F_{20}TPP)(OO^{\bullet})$ (superoxo) adduct to the $Fe^{III}(F_{20}TPP)(OO^{-})$ (peroxo). The whole process is summarized in the ECE reaction scheme of Figure 2.2.

The formation of the Fe superoxo adduct $Fe^{III}(F_{20}TPP)(OO^{\bullet})$, will be discussed in detail in paragraph 2.3, and the coordination phenomena that involve chloride in the Fe^{II} state in paragraph 3.3 (also in reference [135]).

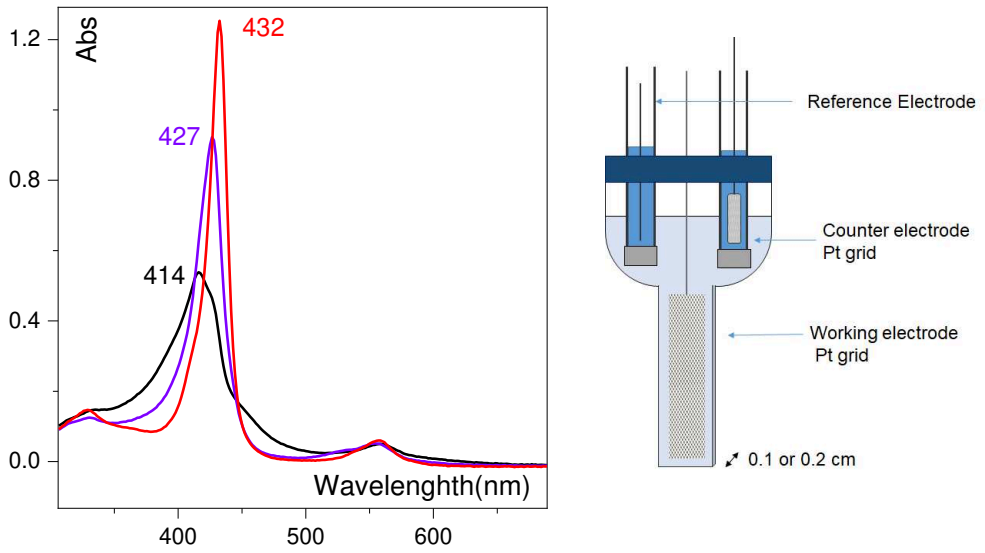

Figure 2.3: (Left) UV-vis spectra recorded in the spectroelectrochemical experiment: 0.05 mM solution of $Fe^{III}(F_{20}TPP)Cl$ in DMF with 0.2 M $TBAPF_6$, (black line), resulting spectra upon applying reductive potential: at -0.25 V vs. SCE, under Ar, T = 293 K to give Fe^{II} (violert line), and after air saturation ($[O_2]$ = 1mM) at -0.60 V vs. SCE, T = 243 K to give $Fe^{III}(OO^{-})$ (red line). Optical path 0.1 cm. (Right) Spectroelectrochemical cell, with platinum grids as working and counter electrode.

The formation of the peroxo adduct $Fe^{III}(F_{20}TPP)(OO^{-})$ was confirmed by EPR spectroscopy and cyclic voltammetry of the in electrochemically generated species and by UV-Vis spectroelectrochemistry at 232 K. The set-up for UV-Vis spectro-electrochemistry experiments and preparative scale controlled-potential electrolysis are described in detail in the experimental part. Briefly, spectroelectrochemistry allows to probe by UV-Vis absorption spectroscopy the reaction layer containing a working electrode at which a certain potential is applied.

Figure 2.3 shows the spectroelectrochemical experiment recorded on a $Fe^{III}(F_{20}TPP)Cl$ solution in DMF. The spectrum of the initial Fe^{III} (Figure 2.3, dotted black trace, λ_{max}=414 nm) evolves to a spectrum with a more intense, red shifted Soret band (black trace), attributed to the $Fe^{II}(F_{20}TPP)$ species. When the same potential is applied in an air saturated solution, a new spectrum is obtained with a Soret band at 432 nm, and a single Q-band at 559 nm. This spectrum fits perfectly previously recorded spectra of

the $Fe^{III}(F_{20}TPP)(OO^{-})$ species that was chemically generated in acetonitrile using KO_2.[62] EPR spectroscopy confirmed our attribution this result.[133]

Furthermore, the CV of an electrolyzed solution at -0.6 V vs SCE in presence of oxygen, at 243 K, reveals an irreversible oxidation peak at + 0.5 V vs SCE. As shown in Figure 2.4. The same oxidation peak is observed in the CV of an Ar saturated solution of $Fe^{III}(F_{20}TPP)Cl$, after addition of 2 equivalents of KO_2, that leads to the formation of the peroxo species $Fe^{III}(OO^{-})$.

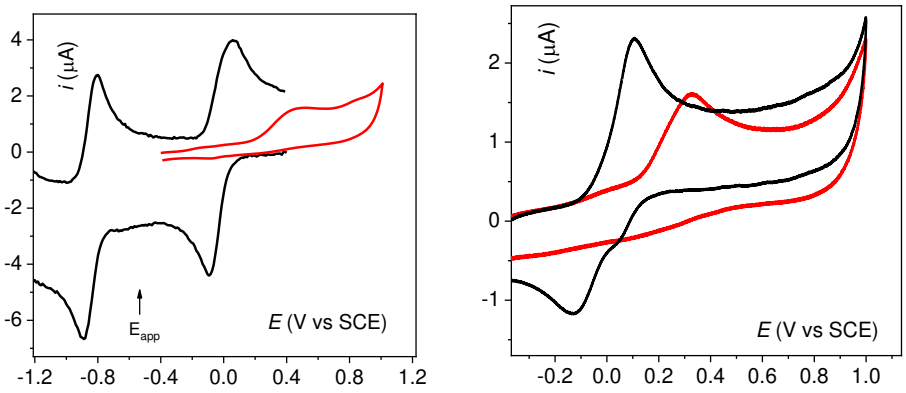

Figure 2.4: (Left) CV of 0.5 mM solution of $Fe^{III}(F_{20}TPP)Cl$ in DMF with 0.2 M $TBAPF_6$, at GC electrode (0.07 cm^2) and 0.1 V s^{-1}: under Ar, T = 293 K (black trace), after bulk electrolysis at E_{app} = -0.60 V vs. SCE, under O_2 (air saturated, 1mM), T = 243 K (red line). (Right) CV in DMF with 0.2 M $TBAPF_6$ of 1 mM of $Fe^{II}(F_{20}TPP)$ at 0.1 V s^{-1} at a GC disk electrode (0.07 cm^2), T = 243 K under Ar (black trace), after addition of 2 eq of KO_2 (red trace).

These results showed that the formation of the $Fe^{III}(F_{20}TPP)(OO^{-})$ can be monitored by low temperature UV-Vis spectroelectrochemistry and CV. In the following paragraphs we show that the same approach can be applied for generating and characterizing the $Fe^{III}(OO^{\bullet})$ species for both the $Fe(F_{20}TPP)$ and Fe(TPP) porphyrins. For the experiments described below, we used a modified set-up for UV-Vis spectroelectrochemistry that includes a carbon paper electrode as working instead of the previous used platinum grid (see paragraph 7.1.3 of annex 1).

2.2 Characterization of the $Fe^{III}(OO^{\bullet})$ and $Fe^{III}(OO^{-})$species of the Fe^{III}(TPP)Cl

The peroxo species of the Fe(TPP) and the Fe(F_{20}TPP) are well known in the literature since the 90's, and have been characterized by various techniques.[61] They are generated by addition of KO_2 in Fe porphyrin solutions in aprotic solvents. In more recent studies, superoxo of the Fe(TPP) is generated by reaction of dioxygen with Fe^{II}(TPP) at low temperatures.[54, 74, 76, 137] The superoxo of the Fe(F_{20}TPP) has also been prepared and characterized following the same methodology by Wijeratne et al.[54, 74] Seeking to generate and characterize these species by spectroelectrochemistry, we estimated that Fe(TPP) is more convenient to start our study because: (i) it has a $E^0_{Fe^{III}/Fe^{II}}$ of -0.18 V vs SCE, that is 130 mV lower than the $E^0_{Fe^{III}/Fe^{II}}$ of Fe(F_{20}TPP), and thus a higher binding constant between O_2 and Fe^{II}, i.e. K_{O_2},[128] that leads to more favorable thermodynamics for the formation of the $Fe^{III}(OO^{\bullet})$ adduct (reactions scheme of Figure 2.2 (ii) since the superoxo adducts are electrophiles, electron-withdrawing substituents of the Fe(F_{20}TPP) destabilize the complex, in contrast with the electron donating phenyl groups of the Fe(TPP).

Figure 2.5 shows representative cyclic voltammograms of a 0.5 mM solution of Fe^{III}(TPP)Cl (in extra dry DMF), under Ar atmosphere (black trace) and under O_2 atmosphere (red trace) where [O_2] = 4 mM (Fe/O_2 ratio close to 1/8[a]) at 233 K. Under Ar, we observe a quasi-reversible Fe^{III}/Fe^{II} wave. As expected, the wave has a relatively high peak separation compared to the experiment at room temperature shown in Figure 2.2 (220 mV vs 100 mV). Under O_2 atmosphere, a new reduction wave appears at -0.65 V vs SCE, and the intensity of the Fe^{II}/Fe^{III} oxidation peak in the reverse scan decreases significantly. Similar behavior has been observed in the case of Fe(F_{20}TPP) (see Figure 2.1).

For the spectroelectrochemical experiments, we use a lower porphyrin concentration (0.15 mM) in order to have a clear image of the Q-band and in the same time do not completely loose the information from the Soret band due to saturation. However, we keep the same Fe/O_2 ratio by performing the experiments in air saturated solutions

[a] Lower Fe/O_2 ratio favors the formation of Fe-O_2 adducts at the expense of an accumulation of reduced (Fe^{II}) species.

([O_2] = 1 mM, Fe/O_2 ratio close to 1/8). When a potential of -0.5 V vs SCE is applied, under argon atmosphere, the Soret band of the initial $Fe^{III}Cl$ shifts at 427 nm and three new Q-bands appear at 532, 562 and 606 nm. This spectrum corresponds to the $Fe^{II}(TPP)$.[76] In presence of oxygen, the resulting spectrum at -0.5 V (Figure 2.5, green trace) displays a Soret band at 416 (suggesting an Fe^{III} intermediate), and Q-bands at 545 nm and 588 nm. These spectral characteristics are identical to those reported by Mayer[76] and Goldberg[137] and attributed to the superoxo $Fe^{III}(TPP)(OO^{\bullet})$ species in DMF solutions at 232 K. We have obtained a similar spectral signature using an alternative set-up at the Université de Bretagne Occidentale, at the Laboratory CEMCA, in the context of a collaboration between LEM and Dr. Nicolas Le Poul. The set-up and the results are detailed in the paragraph 7.2 of Annex 1.

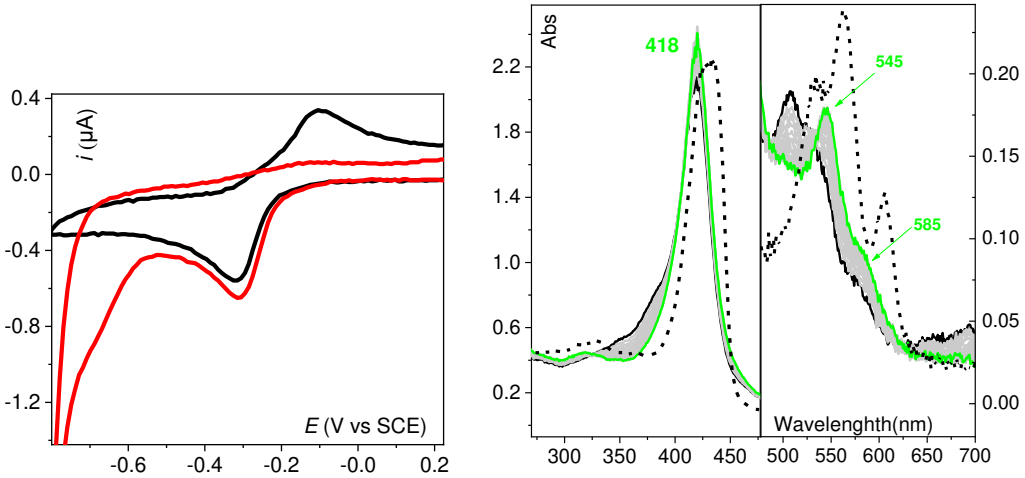

Figure 2.5: (Left) CV in DMF with 0.2 M $TBAPF_6$ of 0.5 mM solution of $Fe^{III}(TPP)Cl$ under Ar (black trace), under O_2 (4 mM) (red trace) at T = 233 K and 0.1 V s^{-1} at a GC disk (0.02 cm^2). (Right) UV-vis spectra recorded in spectroelectrochemical experiment: 0.15 mM DMF solution of $Fe^{III}(TPP)Cl$ with 0.2 M $TBAPF_6$, (black trace) and resulting spectrum upon applying -0.5 V for 10 min: under Ar (black dotted trace), in air saturated solution ([O_2]=1 mM) for 10 min (green trace), and intermediate spectra (grey traces).

Once the superoxo species accumulated, a more negative potential was applied, at -0.65 V. The Soret band of the recorded spectra after applying -0.65 V for another 10 min, shifted to higher wavelengths, at 432 nm, while two new Q bands appear at 565 and 608 nm (Figure 2.6) displaying clear isosbestic points. These data match the previously reported spectrum of the $Fe^{III}(TPP)(OO^{-})$.[56] The fact that the $Fe^{III}(TPP)(OO^{\bullet})$ species is reduced to $Fe^{III}(TPP)(OO^{-})$ with clear isosbestic points confirms that the second reduction wave at -0.65 V corresponds to the

$Fe^{III}(TPP)(OO^{\bullet})/Fe^{III}(F_{20}TPP)(OO^{-})$ reduction. Table 2.1 summarizes the λ_{max} values of the UV-Vis spectral signatures of the Fe(TPP) species characterized.

Table 2.1 Spectral signature of the different Fe-Oxygen porphyrin intermediates

Species	Solvent	λ_{max}(Soret) (nm)	λ_{max}(Q-bands) (nm)
$[Fe^{III}(F_{20}TPP)Cl]^{0}$	DMF	416	502, 576, 627
$[Fe^{II}(F_{20}TPP)]^{0}$	DMF	427	555
$Fe^{III}(F_{20}TPP)(OO^{\bullet})X$ [a]	DMF	412	540
$[Fe^{III}(F_{20}TPP)(OO^{-})]^{-}$	DMF	432	558
$[Fe^{III}(F_{20}TPP)Cl]^{0}$	DCM	352, 412	503, 567, 634
$Fe^{II}(F_{20}TPP)X$	DCM	440	560
$Fe^{III}(F_{20}TPP)(OO^{\bullet})X$	DCM	412	567
$[Fe^{III}(TPP)Cl]^{0}$	DMF	415	508, 529, 654, 694
$[Fe^{II}(TPP)]^{0}$	DMF	427	532, 563, 605
$[Fe^{III}(TPP)(OO^{\bullet})]^{0}$	DMF	418	544, 587
$[Fe^{III}(TPP)(OO^{-})]^{-}$	DMF	435	565, 606

[a]X represents possible axial ligand that could be a DMF molecule in DMF solutions, or a chloride in DCM solutions

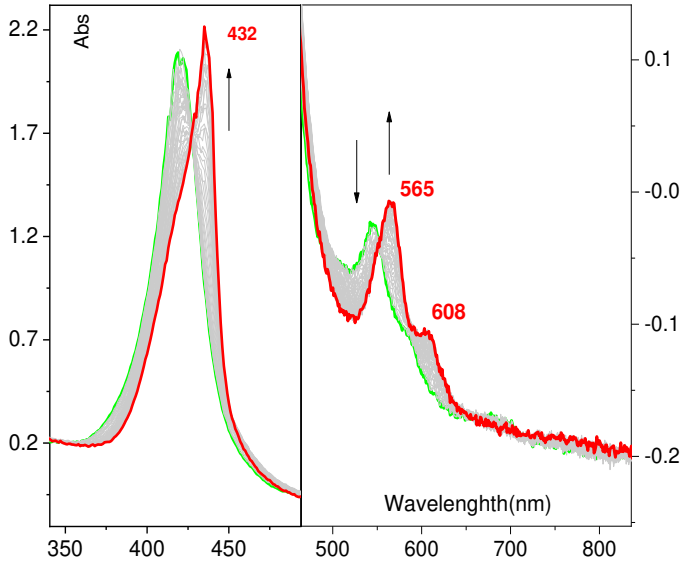

Figure 2.6: UV-Vis spectra recorded in the course of the spectroelectrochemical experiment: 0.15 mM solution of $Fe^{III}(TPP)Cl$ in DMF with 0.2 M $TBAPF_6$, after having applied a potential of -0.5 V vs SCE for 10 min in an air saturated solution (green trace) and spectral evolution upon applying -0.65 V vs SCE, final spectrum (red trace), and intermediate spectra (grey traces).

In conclusion, using our UV-Vis spectroelectrochemistry system we were able to probe the electrochemical formation of the $Fe^{III}(TPP)(OO^{\bullet})$ and its reduction to the corresponding peroxo complex, $Fe^{III}(TPP)(OO^{-})$.

2.3 Characterization of the $Fe^{III}(OO^{\bullet})$·species of the $Fe(F_{20}TPP)$

Accumulation of the adduct formed between $Fe^{II}(F_{20}TPP)$ and O_2, the $Fe^{III}(F_{20}TPP)(OO^{\bullet})$, has been proven to be an experimentally challenging task because of (i) the low binding constant between $Fe^{II}(F_{20}TPP)$ and O_2, and (ii) its instability that can lead to reaction with residual protons, and subsequent formation of μ-oxo or hydroxo species.

In the present paragraph, we first present the experiments we performed in DMF, following our previous work. We also present experiments performed in DCM, that has quite different properties from DMF, giving access to additional mechanistic information.

2.3.1 Studies in DMF

Figure 2.7 shows CVs of 0.5 mM solution of $Fe^{III}(F_{20}TPP)Cl$ in extra dry DMF, under Ar atmosphere (black trace) and under O_2 atmosphere where $[O_2]$ = 4 mM (red trace) at 233 K. Under Ar, we observe a quasi-reversible Fe^{III}/Fe^{II} wave. As in the case of Fe(TPP), the wave has a higher peak separation compared to the experiment in room temperature shown in Figure 2.1 (320 mV vs 140 mV). Under O_2 atmosphere, we observe the $Fe^{III}(F_{20}TPP)(OO^{\bullet})$ /$Fe^{III}(F_{20}TPP)(OO^{-})$ wave at -0.55 V vs SCE, as it is the case in the room temperature experiment (see Figure 2.1). For the spectro-electrochemistry experiment, we use an air saturated ($[O_2]$ = 1 mM) DMF solution with 0.15 mM of porphyrin (Fe/O_2 ratio close to 1/8), keeping similar experimental conditions as for the experiments with Fe(TPP).

When a potential of -0.3 V vs SCE is applied, under Ar atmosphere, after 10 min, a spectrum with Soret band at 427 nm and a single Q-band at 555 nm appear. This spectrum corresponds to the $Fe^{II}(F_{20}TPP)$ (see Figure 2.7).[76] In presence of oxygen, at -0.3 V for 10 min, new spectral changes are induced (Figure 2.7, green trace). The change in the Soret band is minor, and in the Q-region, the bands of the $Fe^{III}Cl$ diminish in favor of a new band at 540 nm. Linear subtraction of the two spectra (initial $Fe^{III}Cl$,

black trace, and after applying -0.3 V for 10 min in presence of O_2, green trace, Figure 2.7) renders these changes more visible, and show that the generated species has a Soret band at 412 nm and a single Q-band at 540 nm. These spectral characteristics match the ones of the $Fe^{III}(F_{20}TPP)(THF)(OO^{\bullet})$ that has been chemically prepared by Wijeratne and Mondal in mixtures of THF and DCM.[54] Based on these information, we attribute the changes in the spectrum to a partial formation of the $Fe^{III}(F_{20}TPP)(OO^{\bullet})$ species. In our conditions, DMF could occupy the axial position. DMF coordinates by its oxygen atom, as it is the case for THF.

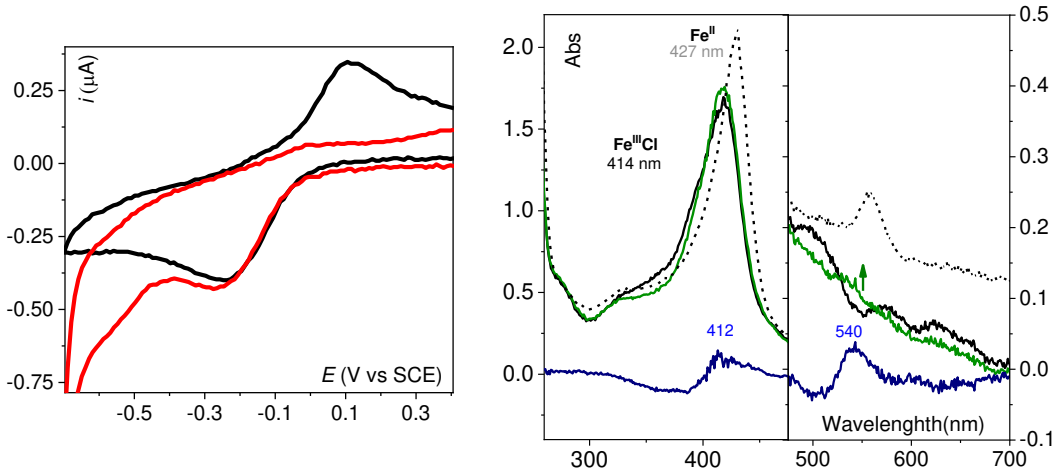

Figure 2.7: (Left) CV in DMF with 0.2 M $TBAPF_6$ of 0.5 mM solution of $[Fe^{III}(F_{20}TPP)Cl]$ under Ar (black), under O_2 (4 mM) (red), scan rate is 0.1 V s^{-1} at a GC electrode (0.02 cm^2), T = 233 K. Under argon at T=293K (black line). (Right) UV-vis spectra recorded in the course of the spectroelectrochemical experiment: 0.15 mM solution of $Fe^{III}(F_{20}TPP)Cl$ in DMF with 0.2 M $TBAPF_6$, (black line) and spectral evolution upon applying -0.3 V for 10 min in air saturated solution (green trace). Liner subtraction of the black and green spectra (navy blue line). Spectrum obtained under Ar after applying -0.3 V vs SCE is shown for comparison (black dotted trace).

2.3.2 Studies in DCM

Spectroelectrochemistry experiments were also performed in DCM. DCM is a non-coordinating solvent in contrast with DMF, possibly modifying the reaction mechanism between Fe and O_2. Furthermore, solubility of O_2 in DCM is quite higher (2.8 mM for an air saturated solution vs 1 mM in DMF)[138] that will favor the reaction between Fe^{II} and O_2 with no need of changing the porphyrin concentration.

Figure 2.9 displays the cyclic voltammograms recorded in DCM solutions of the $Fe^{III}(F_{20}TPP)Cl$ under Ar (black trace) and in presence of O_2 (red trace), as well as the spectra recorded during the spectroelectrochemical experiment. In the CVs, we observe a quasi-reversible Fe^{III}/Fe^{II} wave under Ar, but under O_2, we observe that Fe^{III}/Fe^{II} wave becomes irreversible and the current intensity slightly increases.

We observe two important differences between the CVs in DCM and DMF: i) under Ar, a more negative $E^{p,c}_{Fe^{III}/Fe^{II}}$ [b]in DCM ii) the absence of a clear second reduction wave at -0.5 V vs SCE under O_2 in DCM.

[b] $E^{p,c}_{Fe^{III}/Fe^{II}}$ here refers to the reduction peak potential of the Fe^{III} to Fe^{II}

These differences are better illustrated in the CVs recorded in room temperature (Figure 2.8). At this stage, we hypothesize that these differences are due to chloride coordination, since it is known that DMF can occupy one or both axial positions of the Fe center, while DCM cannot.[135]

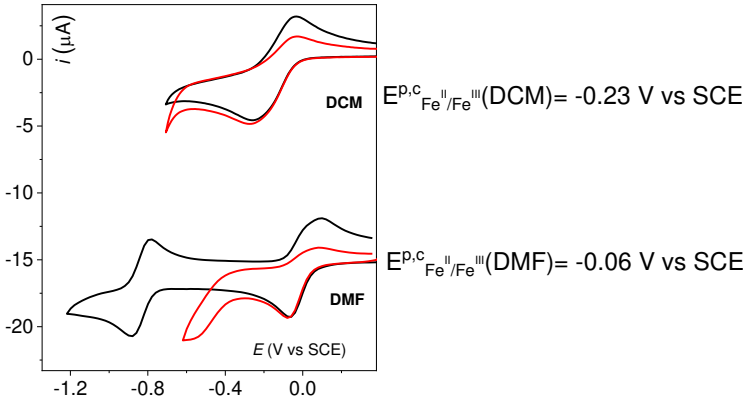

Figure 2.8: CVs of $Fe^{III}(F_{20}TPP)Cl$ in organic solution of 0.1 M $TBAPF_6$ at 0.1 V s^{-1} at a GC electrode (0.07 cm^2), T = 293 K; Under Ar (black trace) and air saturated (red trace), all in 0.5 mM porphyrin solutions. Up: CVs in DCM. Down: CVs in DMF.

In the spectroelectrochemistry experiment, at -0.4 V vs SCE, under Ar a new spectrum appears with a red shifted Soret band at 440 nm, and a single Q-band at 560 nm. We attribute these features to a $Fe^{II}(F_{20}TPP)$ (purple trace, Figure 2.9). The 13 nm difference of the Soret band λ_{max} of the Fe^{II} in DMF and DCM (427 nm vs 440 nm) is most likely due to the axial coordination of chloride that is dissociated from Fe^{II} in DMF,[135] but in DCM it may not be the case since the solvent is not coordinating. [c]

Under O_2, while applying the same potential, -0.4 V vs SCE, a new spectrum is observed, with (i) a broad Soret-band at 411 nm, (ii) a single Q-band at 567 nm. The Soret band of the new spectrum obtained in DCM, is (i) less intense than the one of the Fe^{II} spectrum but as intense as the one of the initial $Fe^{III}Cl$ spectrum, and (ii) its λ_{max} is also very close to the λ_{max} of the Soret band of the $Fe^{III}Cl$, suggesting that the new spectrum corresponds to a ferric (Fe^{III}) species. The single Q-band of the spectrum is slightly blue shifted compared to the Q-band of the Fe^{II} spectrum (567 nm vs 560 nm).

[c] The electrogenerated $Fe^{II}(F_{20}TPP)$ in ACN in presence of 10 equivalents of TBACl also displays a Soret band at 440 nm, supporting our attribution (data not shown).

We note, that a slightly blue shifted Q-band compared to the Fe^{II}, and a red shifted and less intense Soret band, compared to the Fe^{II}, has been previously attributed by Karlin et al, to the $Fe^{III}(F_8TPP)(OO^{\bullet})$ generated by reaction of Fe^{II} with O_2 in THF.[53] We therefore propose that the spectrum obtained in DCM, at -0.4 V in presence of O_2, corresponds to a $Fe^{III}(F_{20}TPP)(OO^{\bullet})$. In Table 2.1 the UV-Vis signatures of the different intermediate species of the present study are summarized for the $Fe^{III}(F_{20}TPP)Cl$ in DCM and DMF.

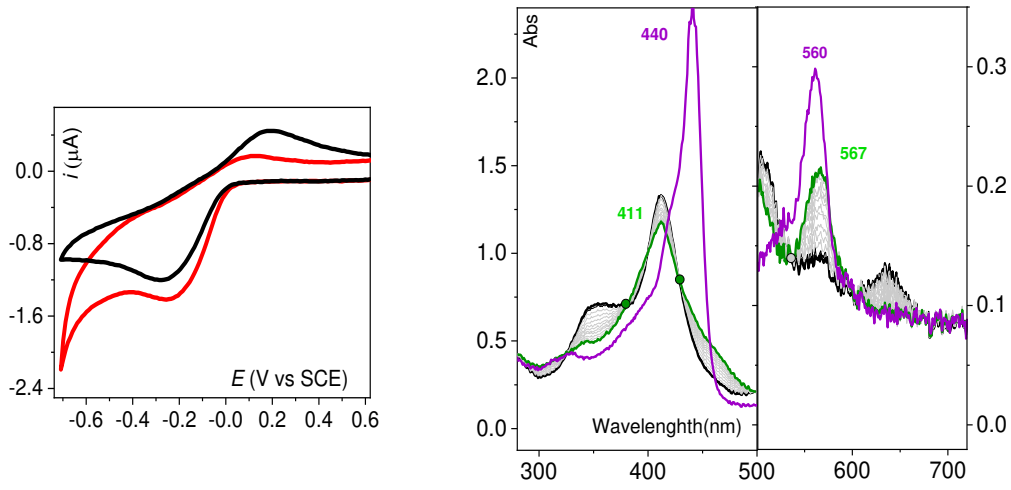

Figure 2.9: (Left) CV in DCM with 0.2 M $TBAPF_6$ of 0.5 mM solution of $Fe^{III}(F_{20}TPP)Cl$ under Ar (black trace), under O_2 (11 mM), (red trace). Scan rate is 0.1 V s^{-1} at a GC electrode (0.02 cm^2) at T = 233 K. (Right) UV-vis spectra recorded in the spectroelectrochemical experiment: 0.15 mM solution of $Fe^{III}(F_{20}TPP)Cl$ in DCM with 0.2 M of $TBAPF_6$, (black line) and resulting spectra upon applying -0.4 V for 10 min in Ar saturated solutions (purple trace), and spectral evolution in air saturated solution (green trace, final spectrum and grey traces intermediate spectra).

Based on the nature of the solvent, we propose that the differences of the spectrum that we attribute to the $Fe^{III}(F_{20}TPP)(OO^{\bullet})$ in DMF and in DCM (mainly the position of the Q-band, 540 nm vs 567 nm respectively), arise from axial coordination. In DCM the axial position could be occupied by chloride while in DMF chloride is dissociated. Chloride coordination in the electrogenerated $Fe^{III}(F_{20}TPP)(OO^{\bullet})$ species in DCM, can also explain the absence of $Fe^{III}(F_{20}TPP)(OO^{\bullet})/Fe^{III}(F_{20}TPP)(OO^{-})$ reduction wave: a $[Fe^{III}(F_{20}TPP)(OO^{\bullet})(Cl)]^{-}$ would be a negatively charged species, in contrast with the neutral $Fe^{III}(F_{20}TPP)(OO^{\bullet})$, it would thus probably be reduced at more negative

potentials than the $Fe^{III}(F_{20}TPP)(OO^{\bullet})$ (reduced at -0.5 V vs SCE), and thus would overlap with the $O_2/O_2^{\bullet-}$ reduction wave.

Other spectroelectrochemical techniques, such as Resonance Raman Spectro-electrochemistry, could complete the characterization of the $Fe^{III}(F_{20}TPP)(OO^{\bullet})(Cl)$ obtained in DCM.

In conclusion, we were able to use UV-Vis spectroelectrochemistry to characterize Fe-Oxygen species for two Fe porphyrins. In the case of Fe(TPP) we were able to electrochemically generate the superoxo and peroxo species for the first time, by controlling the applied potential. At -0.3 V vs SCE we generate the superoxo, and at -0.6 we reduce the superoxo to peroxo. In the case of $Fe(F_{20}TPP)$ we discussed how different solvents (DMF and DCM) influence the generation of the superoxo species. Being able to control the generation of intermediates by changing the applied potential, the coordination sphere of the catalyst, or the catalyst itself, is of outmost importance for our reactivity studies that we present in Chapter Chapter 5.

In the next subchapter we will extend our approach to a simple Mn porphyrin, the Mn(TPP).

2.4 Reaction of Mn(TPP) with O_2 and $O_2^{\bullet-}$ in DMF and DCM

Mn porphyrins and in particular Mn(TPP) are known for being able to activate O_2 both chemically[100, 102, 104, 139] and electrochemically.[120-121, 140] However, the best of our knowledge manganese-porphyrin oxygen intermediate species have not been generated and characterized by spectroelectrochemistry until now.[119] These species are not reactive themselves but they can lead to the generation of high valent Mn-oxo species that are reactive towards substrates.[104]

Figure 2.10 shows CVs of $Mn^{III}(TPP)Cl$, under Ar (black trace) and O_2 (air saturated, red trace) in a DCM solution. Under argon atmosphere, the one electron Mn^{III}/Mn^{II} reduction is quasi-reversible with $E^0_{Mn^{III}/Mn^{II}}$ = -0.35 V vs SCE. In presence of O_2, the cathodic current increases and an additional new oxidation peak is present on the reverse scan at $E_2^{p,a}$ = -0.16 V vs SCE. These observations strongly suggest a chemical reaction between Mn^{II} O_2 species as previously proposed by Murray et al. [120-121]

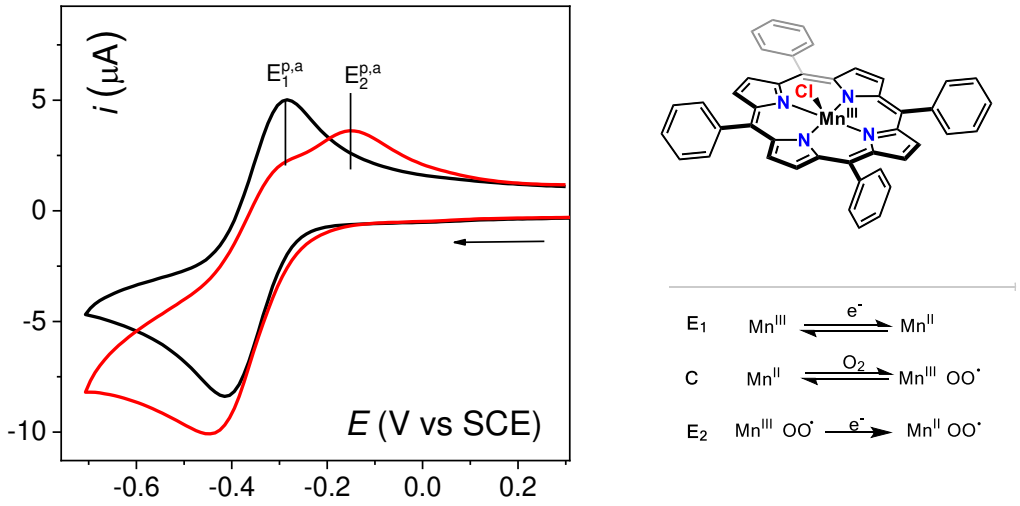

Figure 2.10: (Left) CVs of 0.5 mM Mn^{III}TPPCl in a 0.1 M $TBAPF_6$ DCM solution at a GC electrode, at 293 K; under Ar (black trace), under O_2 (air saturated, red trace).(Right) Molecular structure of Mn^{III}(TPP)Cl and proposed reaction scheme.

In those works, Murray et al. proposed that O_2 reacts with Mn^{II}(TPP) generated at the electrode. The resulting adduct "$Mn^{II}O_2$", quickly undergoes a one electron reduction, following an ECE-type mechanism as displayed in Figure 2.10. This interpretation is consistent with the increase of the current of the Mn^{III}/Mn^{II} reduction wave in presence of O_2 which shows that indeed more than one electron per Mn(TPP) molecule is provided by the electrode surface. They proposed that the new species formed [Mn^{III} + O_2 + $2e^-$] is oxidized at a more positive potential than the Mn^{II}(TP) (E_2^a = -0.16 V vs E_1^a = -0.29 V vs SCE). However, to the best of our knowledge, there has been no spectroscopic evidence to support the formation of a $Mn^{II}O_2$ type adduct in order to confirm the above interpretation. UV-Vis spectroelectrochemistry is the ideal technique to investigate this system. The results of spectroelectrochemical experiments that we conducted are presented in the following paragraphs.

The experiments were performed either at room (293 K) or at low temperature (253 K) using the set-up previously described. The spectrum of Mn^{III} in DCM shows a Soret band centered at 471 nm (Figure 2.11). Under Ar atmosphere, when reducing the DCM solution of Mn^{III}(TPP)Cl at -0.45 V vs SCE (Figure 2.11, black trace), at 253 K, a new Soret band appears at 444 nm, while the Mn^{III} band at 471 nm attenuates, as shown in Figure 2.11, left (purple trace). Under O_2 atmosphere (Figure 2.11, right), when reducing the initial solution of Mn^{III} at -0.45 V vs SCE, at 293 K, a new Soret band appears at 447 nm, as shown in Figure 2.11 (red trace). The full conversion of the

species that is testified by the absence of absorbance band at 471 nm, is achieved at low temperature (red dotted line). The spectral signature of the accumulated species under O_2 (broad peak 397 nm, Soret 447 nm and Q bands of 530, 572 and 612 nm) is the same as the one reported by Valentine et al. for samples prepared by adding two equivalents of KO_2 to Mn^{III}(TPP) solution in DMSO (398 nm wide, Soret 446 nm, and Q bands at 530 nm, 572 and 614 nm).[102] This spectrum has been attributed to a $Mn^{II}(OO^{\bullet})$ species. As postulated by the authors, the first equivalent of KO_2 reduces Mn^{III}(TPP) to Mn^{II}(TPP), and the second reacts with Mn^{II}(TPP) to give the Mn^{II}(TPP)($OO^{\bullet}$). By addition of two equivalents of KO_2 in a Mn(TMP) solution in ACN, a similar UV-Vis spectrum was also obtained, that has been attributed to the Mn^{II}(TMP)($OO^{\bullet}$).[104] Based on these data we attribute the spectral signature obtained at -0.45 V vs SCE in air saturated DCM solution of Mn^{III}(TPP)Cl, to the Mn^{II}(TMP)($OO^{\bullet}$) species [$Mn^{III} + O_2 + 2e^-$] (Figure 2.10).

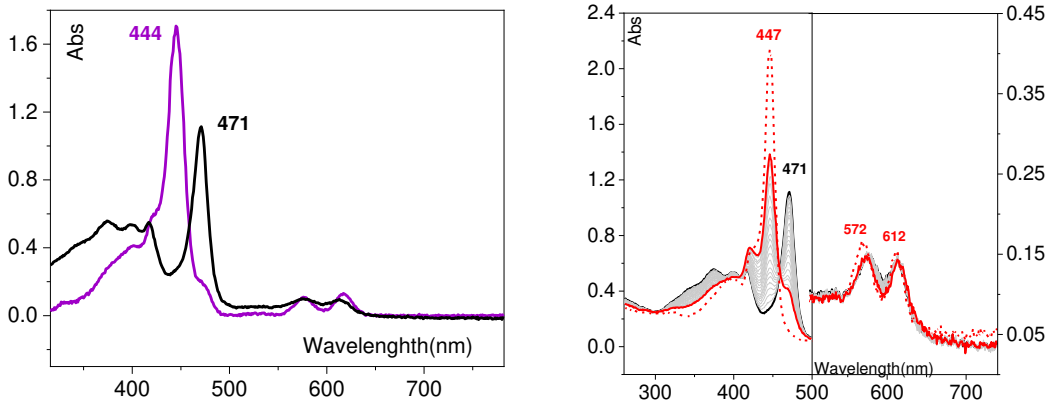

Figure 2.11: (Left) UV-Vis spectrum of 0.1 mM Mn^{III}(TPP)Cl, at 293 K, in 0.2 M $TBAPF_6$/DCM. Mn^{III} spectrum under Ar at 293 K for comparison (black trace), spectrum obtained upon applying after E_{app} = -0.45 V vs SCE for 10 min under Ar (purple trace) at 253 K and (Optical Path 0.2 cm, normalized intensities). (Right) UV-Vis spectrum of 0.1 mM Mn^{III}(TPP)Cl, at 293 K, in 0.2 M $TBAPF_6$/DCM under air before applying potential (black trace) and after E_{app} = -0.45 V vs SCE, (one spectrum per 20 s, grey traces, with final spectrum red trace). Spectrum obtained after 10 min at 232 K is shown (red dotted trace).

We note that accumulation of a $Mn^{III}(OO^{\bullet})$ ([$Mn^{III} + O_2 + 1e^-$], (Figure 2.10) in our spectroelectrochemical experiment can be excluded, since that adduct has already been characterized in toluene and its UV-Vis spectrum displays characteristics of a manganic (Mn^{III}) species, different from the spectrum that we recorded.[100]

As far as the electron distribution of our electrogenerated $Mn^{II}(TMP)(OO^{\bullet})$ is concerned, we suggest that it is indeed better described as a $Mn^{II}(OO^{\bullet})$ (instead of $Mn^{III}(OO^{-})$, manganic peroxo), based on its UV-Vis signature, that is closer to a Mn^{II} species (sharp and intense Soret band around 445 nm, Figure 2.11) than to a Mn^{III} species. This attribution is in accordance with the work of Goff et al. who conducted deuterium NMR spectroscopy of the corresponding chemically prepared adduct.[141]

This species has also been characterized in solid state. The crystal structure of $[Mn^{III} + O_2 + 2e^{-}]K$ has been obtained by Valentine et al.[103] Even if $[Mn^{III} + O_2 + 2e^{-}]K$ species is better formulated as a side-on $Mn^{III}(OO^{-})$ due to the length of the O-O bond, the authors conclude that the electronic density on the Mn center falls between Mn^{II} and Mn^{III}. We note however, that important changes in the metal center can occur between the solid state and in solution and we should not rely only on them to draw our conclusions.

As we showed in paragraph 2.3, the role of the solvent can be central in the electrochemical reaction of a metal porphyrin with O_2. Let us now discuss the electrochemistry of Mn(TPP)Cl in DMF, that is a coordinating solvent. Let us first note that Mn^{III}(TPP)Cl in known to be fully dissociated to $[Mn^{III}(TPP)(DMF)]^{+}$ and Cl^{-} in solvents such as DMF (and DMSO).[102] CVs of the Mn^{III}(TPP)Cl recorded in a DMF solution under Ar (Figure 2.12) displays an important positive shift of the E^0 (where $E^0 = \frac{E^p_{anodic}+E^p_{cathodic}}{2}$) for the Mn^{III}/Mn^{II} wave compared to those recorded in DCM (E^0_{DMF} = -0.18 V vs E^0_{DCM}= -0.35 V). This observation corroborates the presence of $[Mn^{III}(TPP)(DMF)]^{+}$ species in DMF solutions of Mn(TPP)Cl.[102] Moreover, the difference between the UV-Vis spectra of the Mn(TPP) recorded in DMF and in DCM is indicative of a change in the coordination sphere of the metal (see Table 2.2).

Interestingly, the Mn^{III}/Mn^{II} wave is identical under Ar and O_2 atmosphere in DMF, in contrast to our observations in DCM (Figure 2.12). If more negative potentials are scanned in air saturated DMF solutions, a shoulder at the foot of the $O_2/ O_2^{\bullet-}$ wave is observed (Figure 2.12) suggesting a chemical reaction between Mn^{II} and $O_2^{\bullet-}$.[132] Additionally, two anodic peaks are observed in the reverse scan, at -0.08 and at -0.78 V vs SCE. The latter corresponds to oxidation of $O_2^{\bullet-}$ generated at the electrode, while the former appears at a potential close to the one observed for the oxidation of $Mn^{II}(OO^{\bullet})$ in DCM, and could be ascribed to oxidation of a $Mn^{II}(OO^{\bullet})$ intermediate.

The intensity of this wave indicates a two electron oxidation, that is in accordance to an oxidation of the $Mn^{II}(OO^{\bullet})$ to Mn^{III} and O_2, as one would expect.

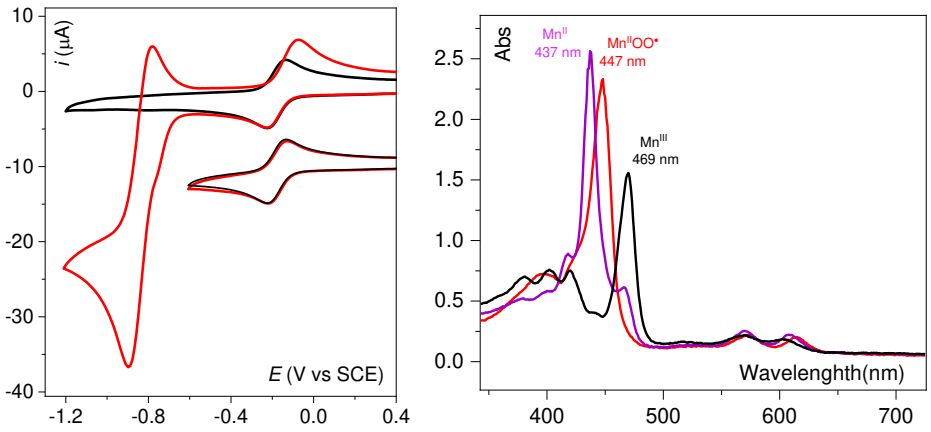

Figure 2.12: (Left) CVs of 0.5 mM Mn^{III}(TPP)Cl, at 293 K, in 0.1 M $TBAPF_6$/DMF under Ar (black traces) and O_2 (red traces)at a GC electrode, at 293 K. (Right) UV-vis spectrum of 0.1 mM Mn^{III}(TPP)Cl, at 253 K, in 0.2 M $TBAPF_6$/DMF under air before applying potential (black trace) and after E_{app} = -0.45 V vs SCE, for 10 min (purple trace) and after E_{app} = -1.1 V vs SCE, for 10 min (red trace).

Spectroelectrochemistry has been use to follow the processes taking place in DMF. If we apply a potential of -0.45 V vs SCE in an Ar saturated Mn^{III} solution (Figure 2.12), the obtained spectrum has a single Soret band at 437 nm and Q-bands at 569 nm and 609 nm. The same spectrum is obtained when we apply a potential of -0.45 V vs SCE in an air saturated Mn^{III} solution. The spectral signature is attributed to the Mn^{II} species in accordance with the literature.[18] This observation suggests that Mn^{II} does not react with O_2 in solution, in accordance with the CV experiment.

When a potential of -1.1 V vs SCE is applied under O_2 atmosphere, we obtain a spectroscopic signature with a Soret band at 447 nm and q-bands at 570 nm and 612 nm, that is identical to the one obtained in DCM and attributed to the $Mn^{II}(OO^{\bullet})$adduct (Figure 2.12). The above observations strongly suggest that two different pathways lead to the formation of the $Mn^{II}(OO^{\bullet})$ in the two different solvents solvent. In DCM, electrogenerated Mn^{II} binds to O_2, and the intermediate formed is reduced at the same potential to give the $Mn^{II}(OO^{\bullet})$, while in DMF the latter results from the reaction of Mn^{II} with the electrogenerated $O_2^{\bullet-}$ at -1.1 V vs SCE (Scheme 2.1).

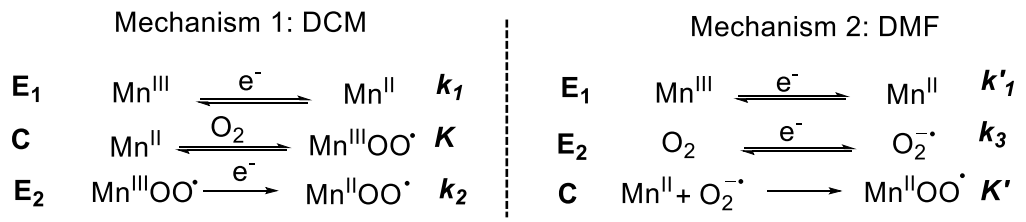

Scheme 2.1 Proposed mechanisms for the formation of the Mn^{II} superoxo adduct in the two different solvents under study.

To explain these observations, we propose that DMF can bind to the Mn^{III} and Mn^{II} ion, limiting the coordination of the O_2 in the Mn^{II} center. On the other hand, $O_2^{\bullet-}$ is a strong Lewis base and can easily replace DMF in the coordination sphere. In the non-coordinating DCM, competition for the coordination of dioxygen does not occur and as a result O_2 can easily bind to the Mn^{II} center, resulting in a formation of an unstable intermediate that is reduced to $Mn^{II}(OO^{\bullet})$.

Table 2.2 Potential values and spectroscopic characteristics of the electrogenerated species.

	DCM	**DMF**
$E^0_{Mn^{II}/Mn^{III}}$	-0.347 (ΔE^p=130 mV)	-0.178(ΔE^p=90 mV)
	λ_{max} in nm	**λ_{max} in nm**
Mn^{III}	471, 575 and 612	466, 566 and 601
Mn^{II}	444, 576 and 616	437, 569 and 609
[Mn^{III} / Ar / E_{app} = -0.45]	444, 576 and 616	437, 569 and 609
[Mn^{III} / O_2 / E_{app} = -0.45]	447, 570 and 612	437, 569 and 609
|Mn^{III} / O_2 / E_{app} = -1.1]	----	447, 570 and 612

2.5 Conclusion

In Chapter 2 we use cyclic voltammetry and UV-Vis spectroelectrochemistry to study the reaction of electrogenerated Fe^{II} and Mn^{II} poprhyrins towards O_2 in solutions of DMF and DCM. The Fe analogues (Fe(TPP) and Fe(F_{20}TPP)) react in the Fe^{II} state with O_2 resulting in $Fe^{III}(OO^{\bullet})$. The latter can be one electron reduced to $Fe^{III}(OO^{-})$. The Mn analogue (Mn(TPP)) in DCM reacts in the Mn^{II} state with O_2 resulting in an intermediate Mn^{II}-O_2 that is one electron reduced in the same potential resulting in a $Mn^{II}(OO^{\bullet})$, while in DMF Mn^{II} reacts with $O_2^{\bullet-}$, that is generated -1.1 V vs SCE on the electrode surface, resulting in the same $Mn^{II}(OO^{\bullet})$. We thus show how

electrochemistry can circumvent the need for chemical reducing agents and offers better control on the potential of the injected electrons. In the next chapter we focus on the reactivity of the $Fe^{III}(OO^{\bullet})$ and $Fe^{III}(OO^{-})$ in presence of protons.

Chapter 3

Electrochemical activation of O_2 by $Fe(F_{20}TPP)Cl$ in presence of Protons.

In the present chapter we examine the electrochemical reductive activation of O_2 catalyzed by the Fe(F_{20}TPP)Cl in DMF solutions, promoted by Brønsted-Lowry Acids. The complete $4e^-/4H^+$ electrochemical reduction of O_2 to H_2O (ORR) catalyzed by Fe porphyrins occurs through the activation of O_2 and breaking of the O-O bond. The Mayer group has contributed a number of important articles on this subject, that focused on the kinetics of the ORR catalyzed by a series of Fe porphyrins using cyclic voltammetry and spectrochemistry experiments.[76, 128] On the other hand, our approach relies on controlling the production of key postulated catalytic intermediates, that are probed *in situ* or *operando* by UV-Vis spectroelectrochemistry. This approach aims at broadening our understanding of the O_2 reductive activation mechanism. We choose as catalyst the Fe(F_{20}TPP), that is less reactive than the Fe(TPP), facilitating the isolation of intermediates and the identification of different mechanistic pathways.

3.1 Two possible pathways. PET vs EPT

Figure 3.1 shows CVs obtained for the Fe(F_{20}TPP) under Ar and O_2 and in the presence of acid. Under an argon atmosphere, CVs display three reversible monoelectronic waves which correspond to the successive Fe^{III}/Fe^{II}, Fe^{II}/Fe^{I}, and Fe^{I}/Fe^{0} redox processes (Figure 3.1, black trace). Upon O_2 saturation, a new monoelectronic wave appears at -0.60 V vs SCE (Figure 3.1, red trace) attributed to the reduction of $Fe^{III}(OO^{\bullet})$ to $Fe^{III}(OO^{-})$ complex (Scheme 3.1), as already discussed. The intense peak at −0.85 V vs SCE in the red trace corresponds to the direct reduction of the excess O_2 in the diffusion layer (O_2 not bound to the Fe ion). Figure 3.1 also shows the CV of the same solution after addition of a strong acid ($HClO_4$). Upon addition of $HClO_4$, the current intensity at -0.60 V sharply increases, indicating a catalytic process.[142] This catalytic process is attributed to O_2 catalytic reduction triggered by the protonation of the $Fe^{III}(OO^{-})$ intermediate (EPT pathway, Scheme 3.1)

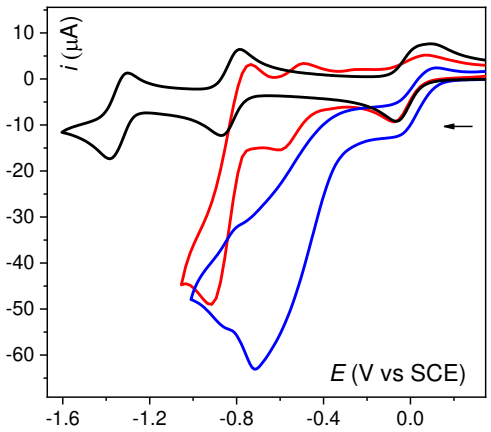

Figure 3.1: CVs at GC disk electrode (area 0.07 cm^2) of 1 mM solution of $Fe^{III}(F_{20}TPP)Cl$ in DMF with $TBAPF_6$ (0.1 M), v = 0.1 V s^{-1}, T = 293 K; under Ar (black trace), under O_2 (air saturated, 1 mM) (red trace) and under O_2 with 10 mM $HClO_4$ (blue trace).

In addition to the catalytic current at -0.60 V, an increase of the current at the Fe^{III}/Fe^{II} wave is observed at +0.02 V vs SCE along with a slight anodic shift of peak potential. However, the $Fe^{III}(OO^{-})$ intermediate is not yet generated at such an anodic potential, suggesting that the present catalytic process involves the protonation of the superoxo $Fe^{III}(OO^{\bullet})$ species leading to an $Fe^{III}(OO^{\bullet}H^{+})$ intermediate (PET pathway, Scheme 3.1). We will now discuss and analyze in detail these two different catalytic pathways that occur at two different potentials.

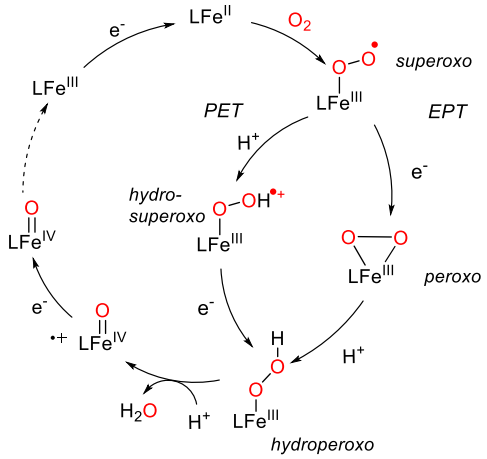

Scheme 3.1: Proposed catalytic cycle of O_2 reductive activation by $Fe^{III}(F_{20}TPP)Cl$. Total charges of intermediates and axial ligands are omitted for clarity.

3.2 Cyclic voltammetry and *operando* UV-Vis spectro-electrochemistry at high overpotential: EPT pathway.

3.2.1 Cyclic Voltammetry

Let us now take a closer look at the catalytic process taking place at -0.6 V vs SCE in the above mentioned reaction pathways. To better describe this catalytic process, the direct reduction of O_2 in presence of protons occurring at the glassy carbon electrode [143] has to be taken into consideration.

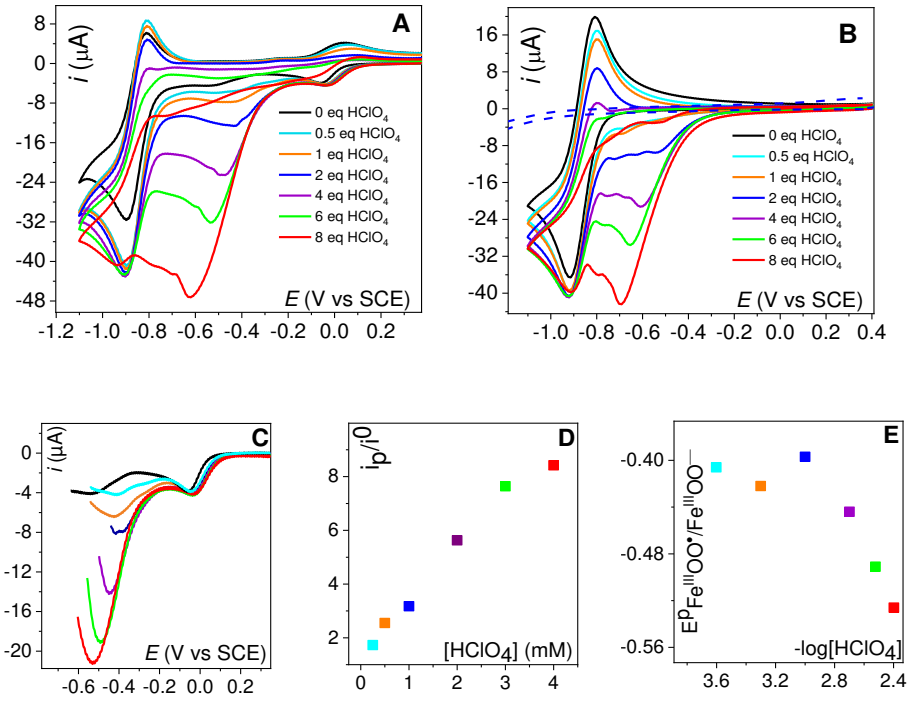

Figure 3.2 A: CV of $Fe^{III}(F_{20}TPP)Cl$ (0.5 mM) in DMF with $TBAPF_6$ (0.1 M) at 0.1 V s^{-1} and 293 K at a GC electrode (0.07 cm^2), under O_2 (air saturated, 1 mM) (black line) and in the presence of increasing concentration of $HClO_4$ (0.025 mM/light blue, 0.5 mM/orange, 1mM/blue, 2 mM/violet, 3 mM/green and 4 mM/red). B: Same conditions as A in absence of porphyrin. C: A after subtraction of B. D: Variation of the i_p/i^0 , where i^0 is the current in absence of substrate, and E: variation of the $E^p_{Fe^{III}OO^{\bullet}/Fe^{III}OO^-}$ with increasing concentrations of acid. Color code is identical in for A, B, C, D and E.

To do so, we recorded CVs of air saturated DMF solutions, in the absence of porphyrin, and with various concentrations of $HClO_4$ (Figure 3.2 B) and then subtracted from the

traces shown in Figure 3.2 A (in presence of the porphyrin) resulting in Figure 3.2 C. Figure 3.2 D and E shows the dependence of the peak potential of the $Fe^{III}(OO^{\bullet})$ /$Fe^{III}(OO^{-})$ couple ($E^{p}_{Fe^{III}OO^{\bullet}/Fe^{III}OO^{-}}$) and of the normalized peak current (i_p/i^0) with the concentration of acid. With less than 2 equivalents of $HClO_4$ the peak potential of the $Fe^{III}(OO^{\bullet})/Fe^{III}(OO^{-})$ couple, initially centered at −0.60 V, slightly shifts to a less negative potential indicative of an electron transfer followed by a fast chemical reaction, in that case a proton transfer (EC process). Upon an increase in the acid concentration (more than two eq), the i_p/i^0 increases indicating a catalytic process, and the peak potential slightly shifts toward more negative values. The negative potential shift that occurs in higher acid concentration is atypical for catalytic processes,[142] and probably indicates the presence of secondary phenomena such as slow diffusion of O_2 in the diffusion layer.[144]

Overall, we propose that, in a Cyt-P450-like behavior,[145] the protonation of the $Fe^{III}(OO^{-})$ peroxo intermediate leads to the catalytic O−O bond cleavage (Scheme 3.1, EPT pathway). [d] Full kinetic analysis of this catalytic process is beyond the scope of the present study.

3.2.2 Spectroelectrochemistry

As reported in Chapter Chapter 2, thin layer UV-Vis spectroelectrochemistry can provide useful information about intermediates that are formed in the reaction layer surrounding the electrode surface. We may now present the results that were obtained by performing low temperature, thin layer UV-Vis spectroelectrochemistry, *operando*, i.e., in presence of protons that induce the catalysis of O_2 reduction, by the $Fe^{III}(F_{20}TPP)Cl$ at -0.6 V vs SCE.

---

[d] We note that in the case of chemically prepared $Fe^{III}(OO^{-})$ of the $Fe(F_8TPP)$, in the studies of Karlin et al [73] H_2O_2 has been detected upon protonation of the species, implying that the Fe-O bond braking occurs in that case. However, these studies have been carried out in Me-THF that is significantly less polar than DMF and ACN, solvents known to play a pivotal role in the protonation modes of peroxo and superoxo Fe porphyrin species and may promote the O-O bond cleavage.72. Kim, H.; Rogler, P. J.; Sharma, S. K.; Schaefer, A. W.; Solomon, E. I.; Karlin, K. D., Heme-Fe(III) Superoxide, Peroxide and Hydroperoxide Thermodynamic Relationships: Fe(III)-O_2(*-) Complex H-Atom Abstraction Reactivity. *J Am Chem Soc* **2020,** *142* (6), 3104-3116, 128. Pegis, M. L.; McKeown, B. A.; Kumar, N.; Lang, K.; Wasylenko, D. J.; Zhang, X. P.; Raugei, S.; Mayer, J. M., Homogenous Electrocatalytic Oxygen Reduction Rates Correlate with Reaction Overpotential in Acidic Organic Solutions. *ACS Cent Sci* **2016,** *2* (11), 850-856.

Upon reduction of an air saturated solution of $Fe^{III}(F_{20}TPP)Cl$ at - 0.60 V vs. SCE, in presence of one equivalent of $HClO_4$, a characteristic Q band appears at 547 nm with a shoulder at 570 nm, with total conversion obtained after 5 min (Figure 3.3, red trace). These spectral features are characteristic of a high valent $Fe^{IV}(O)$ species (Soret band: 414 nm, Q-bands: 547 and 570 nm). Indeed, the UV-Vis absorption spectrum of this electrochemically generated species matches well the spectrum of the chemically prepared species by addition of an excess of m-cpba to an $Fe^{III}(F_{20}TPP)Cl$ solution, and is also in perfect accordance with data previously published. [94-95, 97]

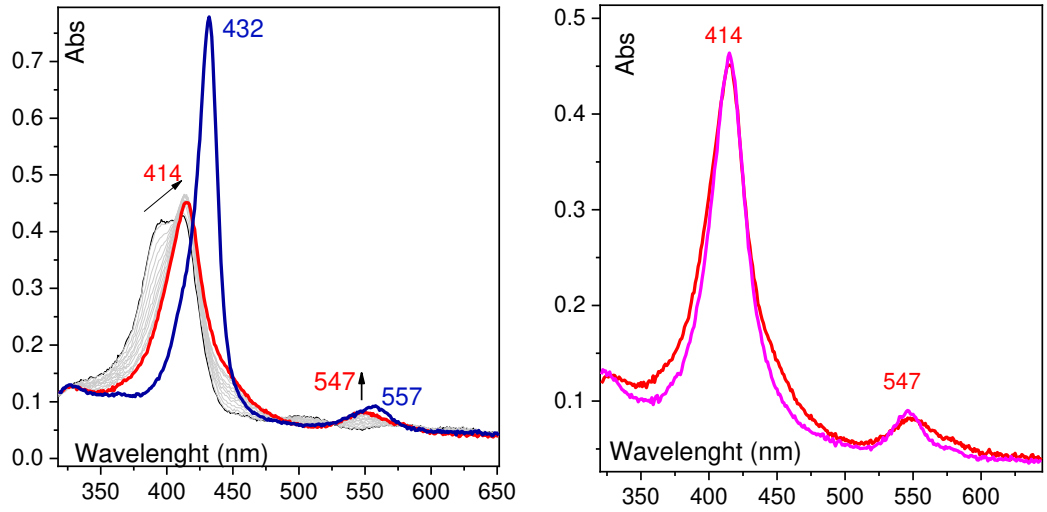

Figure 3.3: (Left) UV-Vis spectra of $Fe^{III}(F_{20}TPP)Cl$ (0.05 mM) in DMF with $TBAPF_6$ (0.2 M), under O_2 (air saturated) with $HClO_4$ (0.05 mM), at T= 258 K, (black trace); with E_{app} = -0.60 V vs. SCE after 5 min electrolysis (red trace) and after 20 min electrolysis (navy blue trace).(Right) Comparison of $Fe^{IV}(O)$ species obtained chemically in an Ar saturated DMF solution of 0.05 mM $Fe^{III}(F_{20}TPP)Cl$ with excess of mcpba at 253 K (magenta trace) compared to red spectrum of the left part of the figure (normalized intensities).

We propose that in the present case, the $Fe^{III}(OO^{-})$ reacts efficiently with the protons of the strong acid, leading to the O-O cleavage. The resulting $Fe^{IV}(O)$ π radical cation, reacts either with the solvent or is further reduced to $Fe^{IV}(O)$ (Scheme 3.2), either on the electrode surface or by homogeneous electron transfer with reduced Fe species in solution. We propose that the heterolytic cleavage of the O-O bond takes place, rather than the homolytic one that could result directly to a $Fe^{IV}(O)$, based on previous studies where it was shown that heterolytic cleavage prevails in $Fe^{III}(OOH)$ of porphyrins containing electron-withdrawing substituents.[82]

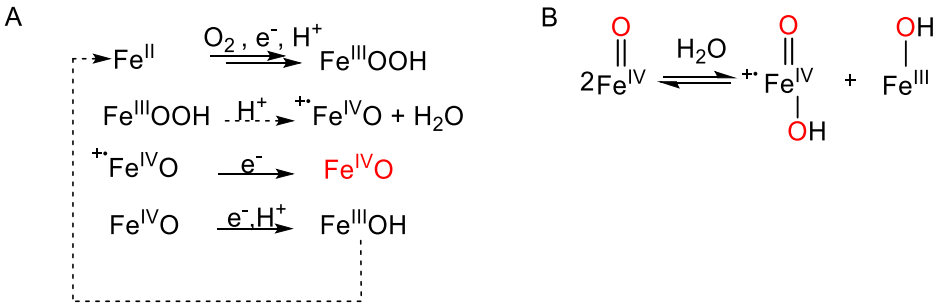

Scheme 3.2 A: reactions taking place in the catalytic cycle involving the $Fe^{IV}(O)$ species. B: Disproportionation reaction of $Fe^{IV}(O)$.

One possible explanation of the fact that $Fe^{IV}(O)$ accumulates in reductive conditions is the involvement of the disproportionation reaction that takes place between $Fe^{III}OH$ and $Fe^{IV}(O)$ π radical cation (Scheme 3.2 B). This reaction is known to favor $Fe^{IV}(O)$ formation in organic media.[94] Under catalytic conditions, the $Fe^{III}OH$ that is generated after the reduction of $Fe^{IV}(O)$, reacts with the $Fe^{IV}(O)$ π radical cation to give back $Fe^{IV}(O)$, thus creating a "kinetic trap" for this latter. In addition, the electro-withdrawing substituents of the porphyrin ring shift the equilibrium towards the left side of the reaction ($Fe^{IV}(O)$ formation), according to the study of Newcomb et al.[94]

As displayed in Figure 3.4 (blue trace), while maintaining reductive potential, -0.60 V vs. SCE, after about 20 minutes, the $Fe^{IV}(O)$ signature is replaced by the characteristic spectrum of the $Fe^{III}(OO^{-})$ species (Soret band at 432 nm and Q band at 557 nm).[133] This transformation takes place because of the consumption of protons inside the probed optical part of the spectroelectrochemical cell, before the diffusion of protons from the bulk solution can compensate it, thus stopping the catalytic process.

Moreover, the $Fe^{III}(OO^{-})$ at open circuit potential, is transformed back to $Fe^{IV}O$ as shown in Figure 3.4, because protons of the bulk solution diffuse to the electrode surface. This observation further supports our propositions that the $Fe^{IV}O$ observed under our conditions originates from the O-O bond cleavage.

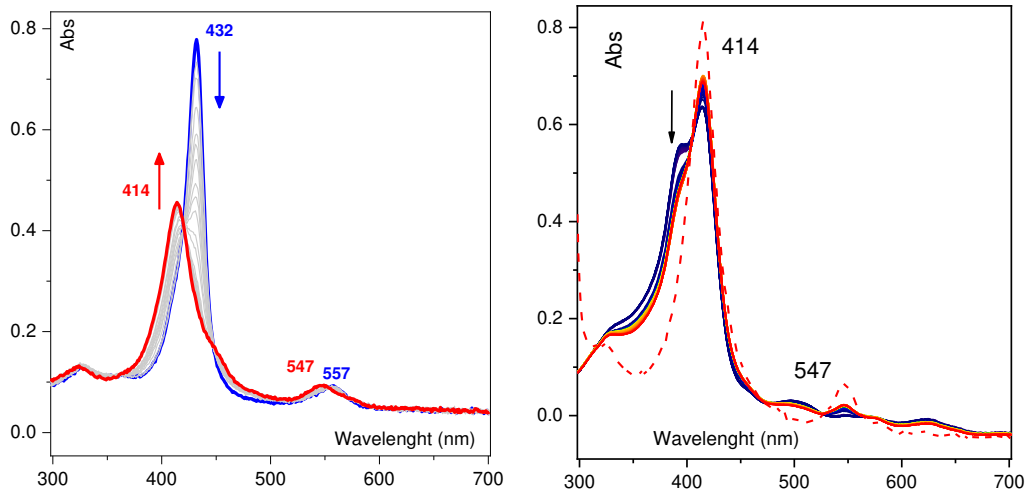

Figure 3.4 (Left) Evolution of UV-Vis spectrum of $Fe^{III}(OO^{-})$, electrochemically generated from O_2 (air saturated) solution of 0.05 mM of $Fe^{III}F_{20}TPPCl$ in DMF with $TBAPF_6$ (0.2M), T= 258 K at -0.60 V vs SCE, in presence of 0.05 mM of $HClO_4$ (navy blue trace) and its evolution with time (red trace obtained after 10 min).(Right) UV-Vis spectral evolution after addition of 10 eq of H_2O_2 from a freshly prepared solution of H_2O_2/Urea in H_2O/DMF 1:1 in a 0.1 mM solution of $FeF_{20}TPPCl$ in presence of 1 mM of $HClO_4$ at 253 K. The final spectrum (red trace) is obtained after 10 min. For comparison, UV-vis spectrum of chemically $Fe^{IV}(O)$ generated with mcpba is added (red dotted trace).

Possible involvement of H_2O_2 generated by the direct O_2 reduction on the carbon electrode in the generation of the $Fe^{IV}(O)$ species can be ruled out by the following control experiment (see Figure 3.4). In that experiment, in an Ar saturated DMF solution of the $Fe(F_{20}TPP)Cl$ at 253 K, 10 equivalents of H_2O_2 are added in the presence of $HClO_4$ and UV-Vis spectra were recorded. The characteristic Q bands of $Fe^{IV}(O)$ (547 nm with a shoulder at 570 nm) appears but the complete conversion is not observed. The Q bands of the starting $Fe^{III}Cl$ (500, 565 and 620 nm) remain clearly present even when the 547 reaches its maximum value (after ~ 10 min, Figure 3.4 right). The $Fe^{IV}(O)$ species has been previously observed by Dey et al. using Surface enhanced Resonance Raman spectroscopy under electrocatalytic conditions, in the case of Fe porphyrins immobilized onto gold electrodes, but only in small amounts in mixture of species.[122, 125] To the best of our knowledge, the present observation of accumulated high valent species in reductive conditions has never been reported before. [146]

3.3 Cyclic voltammetry and *operando* UV-Vis spectro-electrochemistry at low overpotential: PET pathway.

3.3.1 Cyclic Voltammetry

We shall now study the catalytic activity observed at +0.02 V vs SCE, Figure 3.5 A shows the evolution of the Fe^{III}/Fe^{II} wave and of the $E_{cat}^{p/2}$ [e] upon increasing the amount of $HClO_4$ (up to 20 mM).

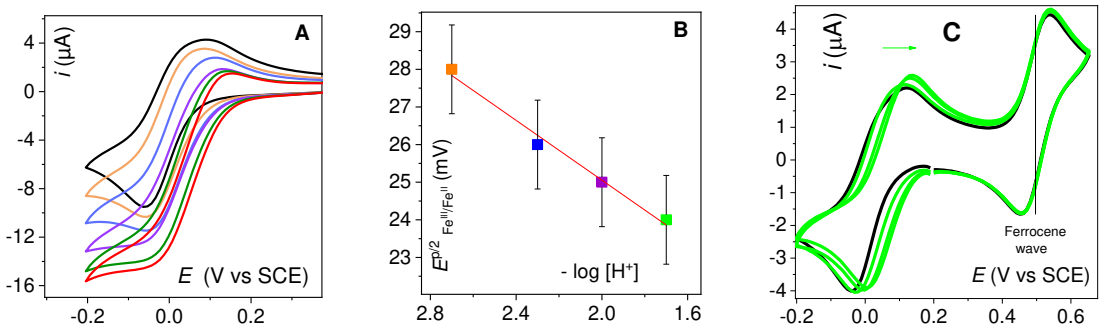

Figure 3.5: A: CV of $Fe^{III}(F_{20}TPP)Cl$ (1 mM) in DMF with $TBAPF_6$ (0.1 M), v = 0.1 V s^{-1}, T = 293 K, at a glassy carbon electrode (0.07 cm^2) under O_2 (air saturated) in the presence of increasing concentration of $HClO_4$ (1 mM/orange, 2 mM/blue, 5 mM/violet, 10 mM/green and 20 mM/red). B: Variation of the half-wave potential of the Fe^{III}/Fe^{II} couple with increasing concentrations of acid. Color code is identical in A and B. C: $Fe^{III}(F_{20}TPP)Cl$ (1 mM) with ferrocene (added as internal reference) under argon (black solid trace), with increasing concentration of $HClO_4$ (green solid trace): 0, 0.5, 5, 10 mM.

In an Ar saturated solution in the absence of $HClO_4$ (Figure 3.5 A, black trace), the CV exhibits a reduction wave in the forward scan corresponding to the reduction of Fe^{III} with the reoxidation wave in the reverse scan being composite. It involves two overlapping waves. *i.e.* the oxidation of the $Fe^{II}(F_{20}TPP)Cl^-$ and of the $Fe^{II}(F_{20}TPP)DMF^0$ species. This behavior is rather typical for Fe chloride porphyrins[135] in solvents such as DMF, that are coordinating, and can be analyzed using a square scheme (Figure 3.6). The predominance of every species has been confirmed by recording CVs after addition of either $AgClO_4$ that abstracts the chloride leading to the $Fe^{III}(F_{20}TPP)(DMF)_x^+$ (x= 1 or 2) or 10 equivalents of TBACl that leads

[e] $E_{cat}^{p/2}$ is the potential at which the current is equal the half of the catalytic peak (or plateau) current.

to the predominance of $Fe^{III}(F_{20}TPP)Cl^0$. Addition of $HClO_4$ in an Ar saturated solution of $Fe^{III}(F_{20}TPP)Cl$ (Figure 3.5 C) leads to a positive shift of the $E^p_{Fe^{III}/Fe^{II}}$ suggesting that in presence of acid the $Fe^{III}(F_{20}TPP)(DMF)_x^+$ form is favored at the expense of the $Fe^{III}(F_{20}TPP)Cl^0$ one. The reasons for this observation are not yet clear and need further investigation.

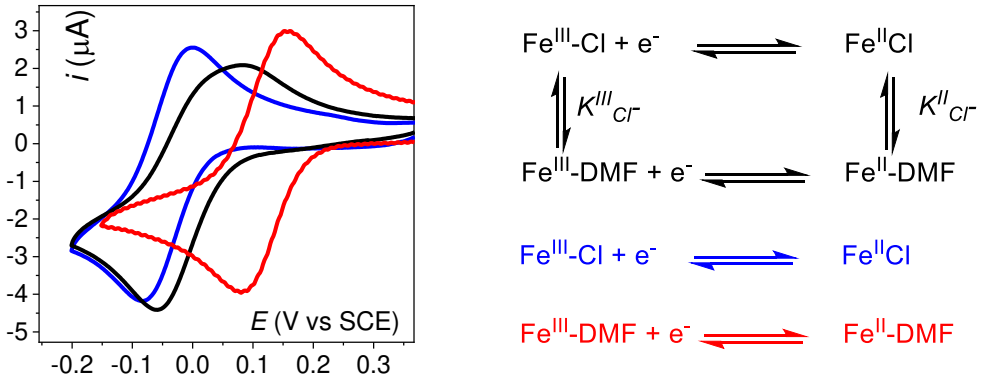

Figure 3.6: (Left) Cyclic voltammetry at glassy carbon disk electrode (0.07 cm²) of 0.5 mM solution of $Fe^{III}F_{20}TPPCl$ with $TBAPF_6$ (0.1 M) under argon (black solid trace), with 5 mM TBACl (blue solid trace), with 0.5 mM $AgClO_4$ (red solid trace) at v = 0.1 Vs^{-1}, T = 293 K. (Right) Schematic representation of the square scheme (see main text).

By addition of $HClO_4$ in air saturated DMF solution of $Fe^{III}(F_{20}TPP)Cl$ (Figure 3.5 A), an increase of the cathodic current occurs with a concomitant decrease of the anodic component until the wave becomes irreversible and plateau shaped. We note that addition of acid to a porphyrin solution in the absence of O_2 does not lead to any current variation. These observations lead to the conclusion that a catalytic process that involves both O_2 and protons is triggered at the Fe^{III}/Fe^{II} wave.

In this process, the $Fe^{III}(OO^{\bullet})$ generated after the reduction of Fe^{III} to Fe^{II}, is protonated in the presence of $HClO_4$ to give the hydro-superoxo $Fe^{III}(OO^{\bullet}H^+)$ intermediate that is subsequently reduced to the $Fe^{III}OOH$ (hydroperoxo) (see Scheme 3.1). This PET pathway leads to the O-O bond breaking at fairly low overpotential. This pathway has also been postulated in a recent study of Mayer et al.[76] based on spectrochemical experiments that aimed at analyzing the kinetics of the O_2 reduction by $Fe^{II}(TPP)$. Moreover, at +0.02 V, the EPT pathway (Scheme 3.1) is not thermodynamically accessible because the $Fe^{III}(OO^{-})$ species cannot be formed. [133] The PET pathway is

leading to smaller catalytic current but occurs at less cathodic potential than EPT one and is thus energetically more favored.

As shown in Figure 3.7 (green trace), addition of a weaker acid than $HClO_4$, the perfluoro-*tert*-butanol, (with a pK_A of 11.8 in DMF[147]) does not have any effect on the Fe^{III}/Fe^{II} wave while catalytic current is observed at the peroxo wave at -0.5 V, confirming that the superoxo $Fe^{III}(OO^{\bullet})$ is less basic than $Fe^{III}(OO^{-})$.

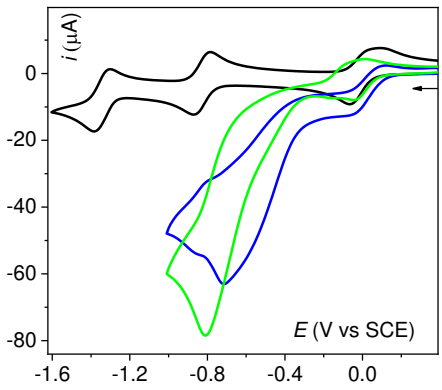

Figure 3.7: Cyclic voltammetry at glassy carbon disk electrode (d=0.3cm) of 1 mM of $Fe^{III}F_{20}TPPCl$ in 0.1M $TBAPF_6$, DMF at 100mV s^{-1} at room temperature under argon (black), under air after addition of ten equivalents of $C(CF_3)_3OH$ (green), after addition of ten equivalents of $HClO_4$ (blue).

We also note that a Fe-O bond breaking pathway (peroxide shunt) is also possible, leading to the formation of H_2O_2. Nevertheless, it has been shown by Mayer that production of H_2O_2 is rather unfavorable in the case of Fe porphyrins in organic solvents and it does not significantly interfere in mechanistic analyses.[128]

3.3.2 Spectroelectrochemistry

In the following paragraphs we present the results that were obtained by performing low temperature, thin layer UV-Vis *operando* spectroelectrochemistry at the Fe^{III}/Fe^{II} wave.

Upon reducing an air saturated solution of the porphyrin at - 0.20 V vs. SCE in the presence of one equivalent[f] of acid ($HClO_4$), the spectrum corresponding to the initial $Fe^{III}Cl$ (Soret band, λ = 414 nm and Q-bands, λ = 500, 558 and 610 nm) evolves to a

[f] We chose to start with a stoichiometric amount of acid because the less substrate the slower the catalysis, favorizing the stability of intermediate species

new one with a red shifted Soret band (λ = 420 nm) and two Q-bands at 530 and 550 nm respectively (Figure 3.8 Left, blue trace). [g] This spectrum is identical to the one obtained by applying the same potential in an Ar saturated DMF solution of a chemically prepared $Fe^{III}OH$ (by addition of LiOH, Figure 3.8 right). We thus attribute it to a $Fe^{II}(OH)^-$ species.

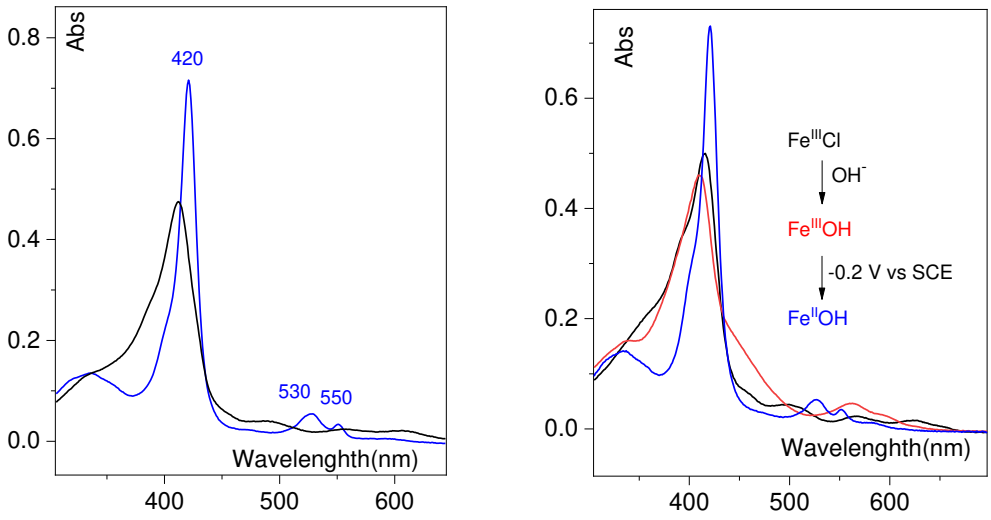

Figure 3.8: (Left) UV-Vis spectra of $Fe^{III}(F_{20}TPP)Cl$ (0.05 mM) in DMF with $TBAPF_6$ (0.2 M), T= 258 K, under O_2 (air saturated) with $HClO_4$ 0.05 mM at open circuit (black trace) and at E_{app}= -0.20 V vs. SCE after 5 min (blue trace). (Right) UV-Vis spectra of $Fe^{III}F_{20}TPPCl$ (0.05 mM) in DMF under Ar at 253 K (black dashed trace), with 10 eq of LiOH (red trace) and then with E_{app} = -0.2 V vs SCE for 10 min (blue trace).

Given that partial reduction of O_2 to H_2O_2 is a minor pathway in organic media,[12] we propose that the $Fe^{II}(OH)^-$ formation originates from the O-O bond cleavage (see Scheme 3.3) and not from a possible H_2O_2 disproportionation reaction.

We note here that hydroxo species of the porphyrin under study have been previously generated chemically and characterized by UV-Vis spectroscopy in acetonitrile solutions by van Eldik et al.[148] In that study, the authors described the species that resulted from the addition of 10 eq of TBAOH in a $Fe^{III}Cl$ ACN solution, as a $Fe^{III}(OH)_2^-$ (ferric di-hydroxo).The latter is isoelectronic and has a similar UV-Vis spectrum with our $Fe^{II}(OH)^-$.

[g] Control experiment performed under argon in presence of acid gave a spectrum identical to the spectrum of the well-known Fe^{II} (λmax= 427, 555 nm)

After addition of 10 equivalents of $HClO_4$ to the electrogenerated $Fe^{II}(OH)$ while maintaining the same electrode potential without mixing the thin layer, the $Fe^{II}(OH)$ spectrum evolves to new one with features at 410 (Soret band), 490, 555 and 605 nm (Figure 3.9 left, orange trace) with several clean isosbestic points.

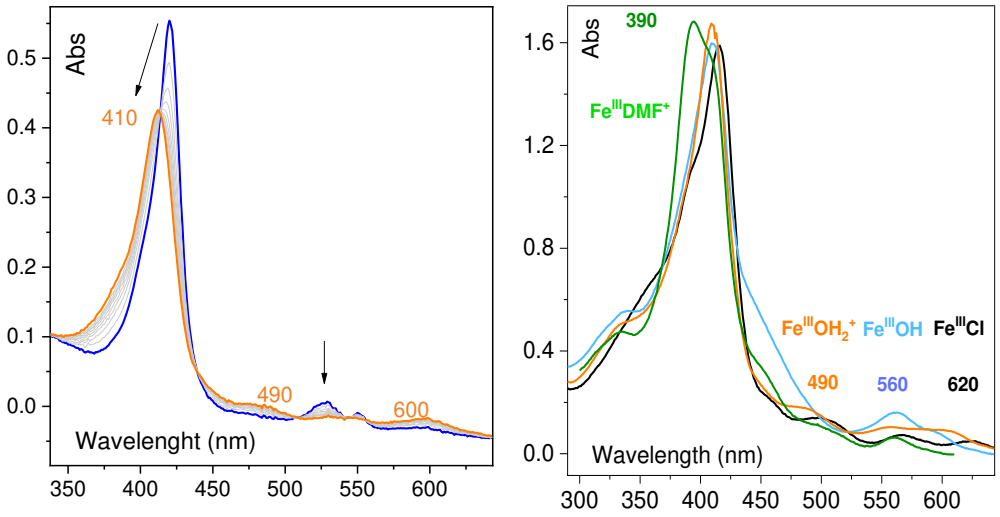

Figure 3.9: (Left) Spectral evolution of the electrogenerated $Fe^{II}(OH)$ of $Fe^{III}(F_{20}TPP)Cl$ (0.05 mM) solution (blue trace) upon addition of $HClO_4$ 0.5 mM while at-0.20 V vs SCE after 5 min (orange trace).(Right) UV-Vis spectra (normalized intensities) of Fe^{III}-X species of the $Fe(F_{20}TPP)$ in DMF with 0.1 M of $TBAPF_6$ at 293K. $Fe^{III}Cl$ (black trace), $Fe^{III}OH$ (light blue trace) generated upon addition of 1 eq of $AgClO_4$ and 1 eq of LiOH in a $Fe^{III}Cl$ solution, $Fe^{III}(DMF)^+$ (green trace) obtained by addition of 1 eq of $AgClO_4$ in a $Fe^{III}Cl$ solution, and $Fe^{III}(OH_2)^+$ (orange trace) obtained by neutralization of $Fe^{III}(OH)$ with 4 eq of $HClO_4$

This spectrum is identical to the distinct UV-Vis spectrum obtained after neutralization with excess $HClO_4$ of a of chemically prepared $Fe^{III}(OH)$ solution in DMF and it is thus attributed to a $Fe^{III}(OH_2)^+$ (ferric aquo) species (Figure 3.9 right, orange trace). Figure 3.9 Right displays the UV-Vis spectra of Fe^{III}-X, where X are different axial ligands, that we generated chemically in order to make this attribution. The spectrum of the solution resulting from addition of $AgClO_4$, that induces abstraction of chloride, to a $Fe^{III}(F_{20}TPP)Cl$ solution followed by and addition of OH^-, fits well the literature data for the $Fe^{III}(OH)$ species.[97, 148]

Table 3.1: UV-Vis spectra and Fe^{II}/Fe^{III} reduction potential of chemically prepared intermediates of $Fe(F_{20}TPP)Cl$ in DMF.

Upon addition of 1 eq of $HClO_4$ to the $Fe^{III}OH$ solution, a new distinct spectrum is obtained (orange trace, Figure 3.9 B), and is attributed to a $Fe^{III}(OH_2)$.[h]

The corresponding CVs of the various Fe^{III}-X species are presented in Figure 3.10. The $Fe^{III}(OH)$ and $Fe^{III}(OH_2)^+$ species display more negative Fe^{III}/Fe^{II} reduction peak potentials than the $Fe^{III}Cl$ (Table 3.1), fact that we attribute to the different axial coordination effects in these complexes.

Species	Soret band λ_{max} (nm)	Q-bands λ_{max} (nm)	$E^{p}_{Fe^{II}/Fe^{III}}$ (V vs SCE)
$Fe^{III}Cl$	414	500, 565, 620	-0.05
$Fe^{III}(DMF)^+$	392	450(sh), 500, 560	+0.08
$Fe^{III}(OH)$	410	450, 563, 592 (sh)	-0.14
$Fe^{III}(OH_2)^+$	408	490, 555, 605	-0.11

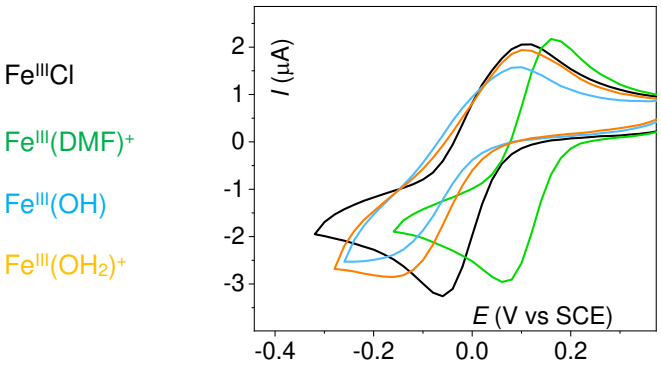

Figure 3.10: CVs of Fe^{III}-X species of the $Fe(F_{20}TPP)$ in DMF with 0.1 M of $TBAPF_6$ at 293K. $Fe^{III}Cl$ (black trace), $Fe^{III}OH$ (light blue trace) generated upon addition of 1 eq of $AgClO_4$ and 1 eq of LiOH in a $Fe^{III}Cl$ solution, $Fe^{III}(DMF)^+$ (green trace) obtained by addition of 1 eq of $AgClO_4$ in a $Fe^{III}Cl$ solution, and $Fe^{III}(OH_2)^+$ (orange trace) obtained by addition neutralization of $Fe^{III}(OH)$ with 4 eq of $HClO_4$. Inset: CVs of the various ferric species at 0.5 mM of the starting $Fe^{III}(F_{20}TPP)Cl$ in DMF with 0.1 M of $TBAPF_6$ at 293 K

[h]The species has a formal charge of +1, but the hydrogen atoms of the water molecule can form hydrogen bonds with DMF partially neutralizing the charge, and we cannot exclude the presence of the weakly coordinating ClO_4^- in the coordination sphere, that could also neutralize the positive charge

The fact that $Fe^{III}(OH_2)^+$ is accumulated in presence of an excess of acid and O_2, shows that it is the steady state intermediate in the probed thin layer of the spectro-electrochemical cell under those conditions. This is reminiscent of the Cyt-P450 resting state (see paragraph 1.3.2), and is in accordance with the fact that $Fe^{III}(OH_2)^+$ has a lower reduction potential than the initial $Fe^{III}Cl$ (see Figure 3.9). Once the protons in the probed thin layer are consumed, the $Fe^{II}(OH)^-$ signature appears again.

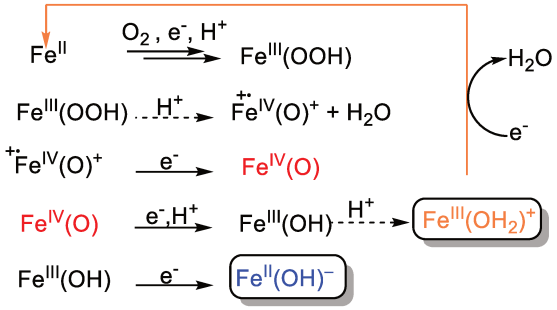

Scheme 3.3: reactions taking place in the catalytic cycle involving the various catalytic intermediate species. In stoichiometric amount of protons, the $Fe^{II}(OH)^-$ is accumulated, while with an excess of acid the $Fe^{III}(OH_2)^+$ is accumulated as steady-state intermediate.

3.3.3 Tracking the $Fe^{III}(OOH)$ intermediate

In order to obtain a more accurate image of the Q-bands of intermediate species, we repeated the spectroelectrochemical experiment of Figure 3.9 with 10 times higher concentration of the starting $Fe(F_{20}TPP)Cl$. Since the experiment was carried out in air saturated solution, the Fe/O_2 ratio increases from 1/20 to 1/2. When applying a potential of -0.2 V vs SCE, in an air saturated solution in presence of one equivalent of acid, we obtain a spectral signature with two broad Q-bands at 530 nm and 553 nm. These features match the spectral characteristic of the $Fe^{III}(F_{20}TPP)(OOH)$ (hydroperoxo) species that was chemically prepared in THF, reported in 2021 by Wijeratne et al.[74] This observation further corroborates our proposition, that in air saturated solution of $Fe(F_{20}TPP)Cl$ in presence of acid, at -0.2 V vs SCE, a PET pathway leads to $Fe^{III}(OOH)$ species (Scheme 3.1).

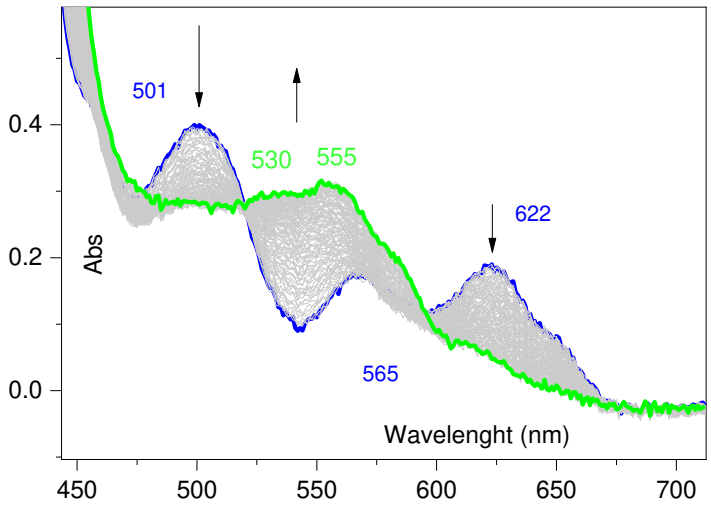

Figure 3.11: UV-Vis spectra of $Fe^{III}(F_{20}TPP)Cl$ (0.5 mM) in DMF with $TBAPF_6$ (0.2 M), T= 258 K, under O_2 (air saturated) with $HClO_4$ (0.5 mM) at open circuit potential (blue trace) and at -0.20 V vs. SCE after 5 min (green trace). Grey traces are intermediate spectra.

Importantly, in the previous study in LEM, electrochemical formation of the $Fe^{III}(F_{20}TPP)(OOH)$ has also been evidenced by EPR spectroscopy after addition of a weak Bronsted-Lowry acid in a solution of electrochemically prepared peroxo in presence of 1-methylimidazole.[133] These observations supports that the two pathways, PET and EPT, eventually pass throughout the same hydroperoxo intermediate.

Discussion

An important question arises following the experimental observations in spectro-electrochemistry. Why do we accumulate different Fe porphyrin species by changing Fe/O_2 ratio at -0.2 V vs SCE? With low Fe/O_2 ratio (1/20) upon applying -0.2 V, we accumulate a $Fe^{II}(OH)$ that occurs presumably after the O-O bond cleavage. However, with higher Fe/O_2 ratio (1/2) upon applying -0.2 V we accumulate a $Fe^{III}(OOH)$, a species that occurs right before the O-O bond cleavage step.

Let us first consider the Fe/O_2 ratio. With high concentration of O_2 compared to the Fe (low Fe/O_2 ratio) the O_2 consumption is less likely to be limiting for the electrochemical reaction. Fe/O_2 ratio may thus alter the steady-state of the catalytic reaction, resulting in detection of different intermediate. A second parameter that we have to take into consideration is that, even if in both experiments, we add one equivalent of acid, in the case of low porphyrin concentration, one equivalent of acid

corresponds to 0.05 mM, and in that case the analytical error is higher due to practical reasons. Acid concentration is crucial and would also alter the reaction kinetics.[127]

In order to clear this point, more spectroelectrochemical experiments with varying Fe/O_2 concentrations need to be performed.

As a general comment we want to note that spectroelectrochemistry does not allow the determination of the rate determining step of the catalytic process unequivocally because many parameters can interfere to the probed species, such as the heterogeneous electron transfer and the geometry of the cell that influences the proton and O_2 diffusion from the bulk solution.

3.4 Conclusion

The present study provides new experimental proof and thermodynamic arguments for the accessibility of the PET pathway. Figure 3.12 summarizes the two different pathways that lead to the formation of $Fe^{III}(OOH)$ species and to the subsequent O−O bond cleavage. The PET process occurs at a low overpotential (green path), while the EPT occurs at a higher overpotential (blue path).

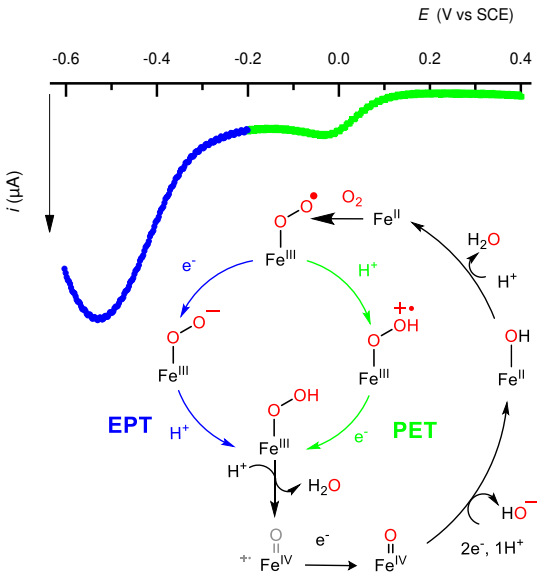

Figure 3.12: CV of $Fe(F_{20}TPP)Cl$ (1 mM) in DMF with $TBAPF_6$ (0.1 M) at a GC electrode under O_2 (air saturated) in the presence of 10 mM $HClO_4$ (after subtraction of the current due to the direct reduction of O_2) and parallel catalytic pathways occurring at −0.10 V vs SCE (green) and at −0.60 V vs SCE (blue), respectively.

Upon changing the applied potential and the porphyrin concentration we were able to characterize *operando*, the following species $Fe^{II}(OH)$ and $Fe^{III}(OH_2)$ at low

overpotential and low porphyrin concentration, $Fe^{III}(OOH)$ at low overpotential and higher porphyrin concentration, and $Fe^{IV}(O)$ at high overpotential and low porphyrin concentration. The work presented in this chapter, (except the paragraph 3.3.3) has been published in *Inorganic Chemistry*.[146]

The next Chapter is devoted to Scanning Electrochemical Microscopy studies that bring new insights and quantitative information in O_2 activation by Fe porphyrins.

Chapter 4

Probing Fe^{III} peroxo porphyrin intermediates in reaction layer during electrochemical reductive activation of O_2 using Scanning Electrochemical Microscopy

Scanning electrochemical microscopy (SECM) has been utilized for studying Oxygen Iron Porphyrin intermediates in homogeneous conditions, for the first time in a collaborative work between LEM (E. Anxolabéhère-Mallart, C. Fave) and ITODYS (J.-M. Noël, F. Kanoufi). In the present chapter we show how we can have access to reduction and oxidation potentials of several Fe oxygen intermediate species using the dynamic Substrate-Generator/Tip Collector SECM mode, and how this data can be combined with simulations to afford structure reactivity relationships for a series of three Fe porphyrins with different meso-substituents. Initial work on the subject and exploration of other SECM modes, have been analyzed in Dr. Célia Achaibou's thesis manuscript.[149]

4.1 The SECM for studying complex homogeneous redox systems

The SCEM is an electrochemical scanning probe technique that have been developed some 32 years ago by Bard et al. [150] In the four electrode configuration, which requires the use of a bipotentiostat, the scanning electrochemical microscope includes (i) an electrochemical cell with a reference, a counter and two working electrodes, usually a substrate electrode, and an ultramicroelectrode (UME), called tip, and (ii) a motorized system that allows the accurate positioning of the ultramicroelectrode near the surface of the substrate working electrode.[151].

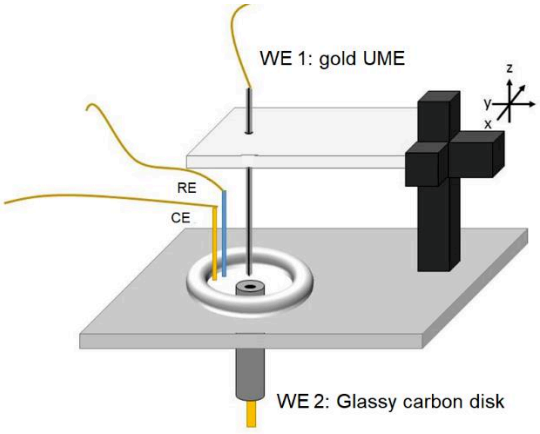

Figure 4.1: Graphical representation of the SECM set-up used in the present study.

In the literature, there has been no precise definition of an UME, but it is generally accepted that the electrode's surface falls in the same order of magnitude as its diffusion layer. Ultramicroelectrodes usually have a radius between 1 and 25 µM. Many

applications of this kind of electrodes rest on this property, that renders it rather easy to reach a steady state current, and others on the fact that small electrodes have lower ohmic drops.[151]

In a solution where a redox couple O/R present (R is oxidized to O), and the tip is far enough from the substrate (which can be polarized or not), the recorded cyclic voltammogram displays a sigmoidal curve form (Figure 4.2) characterized by the half wave potential $E^{1/2}$ and the plateau current which is proportional to the bulk concentration of R, C_R^* and the diffusion coefficient of the species R, D_R as follows:

$$i_\infty = 4nFD_R C_R^* a \qquad (4.1)$$

Where F is the faradaic constant, n the number of electrons and a the radius of the electrode. The ∞ indicator, means that the current in measured at infinite distance from the surface of the substrate electrode.

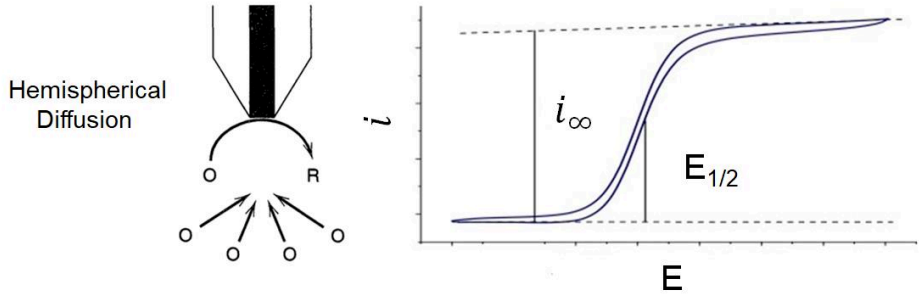

Figure 4.2: (Left) diffusion of the redox active species on the UME inside the bulk solution. (Righ) Sigmoidal CV obtained on the Tip showing the steady state current obtained after the redox wave, and the half-wave potential.

SECM measurements can be performed using different operational modes such as Feedback Mode, Generation-Collection Mode, and Redox Competition Mode. We will first describe the Feedback mode, which is the most common one, and then the Generation-Collection Mode, and in particular the Substrate Generation Tip Collection type, which we have been mostly using in the present work.

In the Feedback Mode, when the tip approaches the surface of the substrate within a few L, where $L = d/a$, (d = distance between tip and substrate, a is the tip's radius) while applying a potential at the plateau current region of the reduction of O to R, the following observations are made. The diffusion of the species O, to the tip is blocked, leading to a decrease of the current, while in the same time, if the substrate is an

electrode that regenerates O, it can lead to a larger flux of O that results in an increase of the current. If the substrate is an insulating surface the first effect prevails. Figure 4.3 shows the approach curves, which represents the current of the tip as function of the distance between the tip and the substrate, in two characteristic cases.

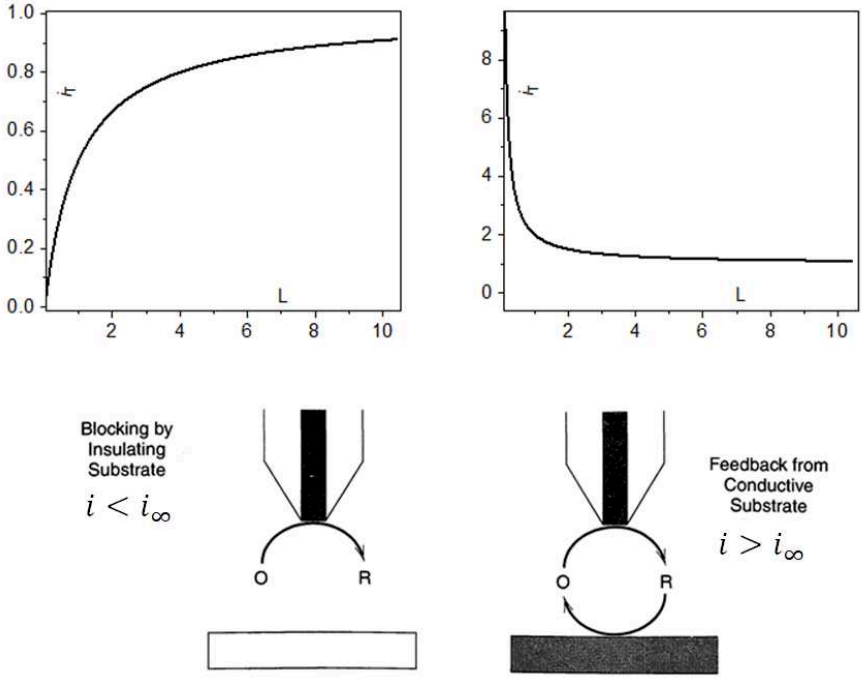

Figure 4.3:(Left) Approach curve for a system where the substrate is an insulating surface, where blocking of the substrate diffusion takes place. Right: Approach curve a system where the substrate is a conducting surface that regenerates the O species.

Let us now examine the Substrate Generator – Tip Collector mode (SG/TC) mode that we have used to study O_2 activation by Fe porphyrins. In this mode, the tip is positioned in a fixed distance from substrate electrode and the electrochemical reaction of the redox species is probed in the layer between the two electrodes. The electrochemical reaction, for example the reduction of O to R, takes place at the substrate electrode now called generator. The second electrode, the tip, collect the generated species, in this case thanks to its oxidation on the electrode. [152]

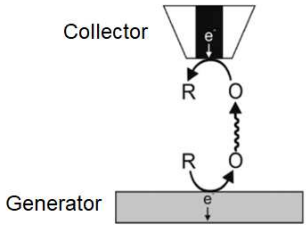

Figure 4.4: Graphical representation of the substrate electrode generator, tip collector SEC mode.

The generation-collection mode can be particularly useful for *probing the reactivity of intermediate species directly in the diffusion layer* where they are generated, by calculating for example the distance d traveled by the intermediate as a function of its lifetime τ and its diffusion coefficient D according to equation below: [153]

$$d = \sqrt{D * \tau} \qquad (4.1)$$

Thus, this mode can in principle provide quantitative information for a redox active species under study.[154-157] Indeed, this experimental technique is close, from a conceptual point of view, to the rotating ring disc electrode (RRDE). However, the SECM offers a better spatio-temporal resolution because the generator-collector distance can reach the order of a micrometer (with ultramicroelectrodes) rendering the diffusion between the two electrodes very fast even in the absence of convection. Additionally, the generator-collector distance in SECM can vary while the disc-ring distance is fixed.

4.2 Study of O_2 activation by Fe(F_{20}TPP)Cl using SECM. Previous results.

In recent studies, scanning electrochemical microscopy has already been described as an elegant approach to probe unstable intermediates.[154, 158] For O_2 activation by Fe porphyrins, however, another generation-collection technique, the RRDE is much more commonly used, in order to quantify the final products of the ORR (H_2O_2 vs H_2O).[127, 159-161] SECM has been previously used to study metal porphyrins deposited on electrode surface,[162] and as far as O_2 activation is concerned, it was again used to evaluate the product selectivity.[163-164] Herein we propose an alternative approach where

Fe-O porphyrin intermediates are directly probed *in situ*, inside the electrode diffusion layer.

Figure 4.5 A shows a graphical representation of the experimental set-up used for O_2 activation by the $Fe^{III}(F_{20}TPP)Cl$, where the two working electrodes are shown: the substrate generator (G) where the intermediates are generated and the tip collector (C) where the intermediates are oxidized. Figure 4.5 B displays representative CVs at the G, for the reduction of $Fe^{III}(F_{20}TPP)Cl$ obtained under Ar (black trace) and under O_2 (red trace). As previously described under Ar, the two reversible successive waves are characterized by their redox potentials, $E^0_{Fe^{III}/Fe^{II}} = -0.08\,V$ and $E^0_{Fe^{II}/Fe^{I}} = -0.9$ V, while in presence of O_2, a new reduction occurs that corresponds to the one electron reduction of $Fe^{III}(OO^{\bullet})$ to $Fe^{III}(OO^{-})$ with $E^p_{Fe^{III}OO^{\bullet}/Fe^{III}OO^{-}} \approx -0.6$ V. [133]

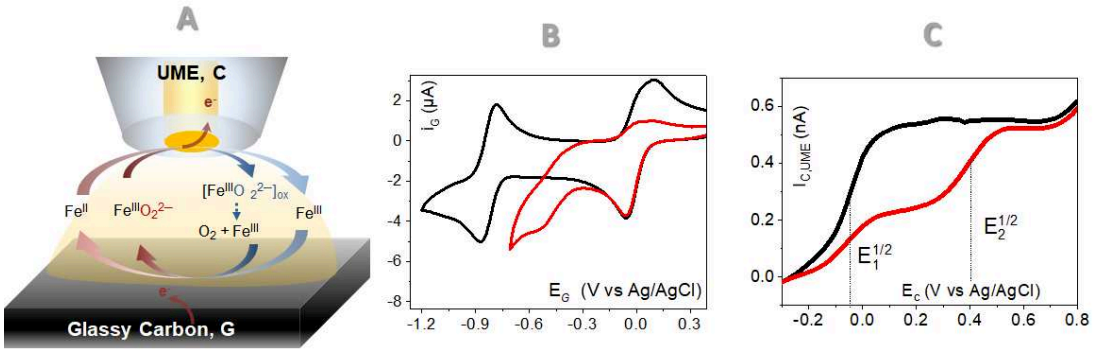

Figure 4.5: A: Graphical representation of the setup used for a typical SECM experiment in the SG/TC mode for O_2 activation by Fe porphyrins. B: CVs recorded at GC disk electrode (G, with diameter of 3 mm) at 100 mV/s and C: LSVs recorded at a gold UME (C, with diameter of 25 mm) at v=20 mVs^{-1}, in SG/TC mode, held at d=8±2 mm from G, that is polarized at E_G= -0.7 V vs. Ag/AgCl, in DMF with 0.1 M $TBAPF_6$ and 0.5 mM $Fe(F_{20}TPP)Cl$ under Ar (black trace) and with 1 mM O_2 (red trace, air saturated).

In the SECM experiment, using the the SG/TC mode, the potential on the G is hold at $E_G = -0.7\,V$, while recording a linear sweep voltammogram (LSV) on the UME in positive potentials. Under argon atmosphere, we observe a single oxidation wave at $E^{1/2}_{1,C} \approx -0.05\,V$, (Figure 4.5 C) corresponding to the Fe^{II}/Fe^{III} reoxidation, confirming the collection of the electrogenerated Fe^{II} on the UME. When O_2 is introduced (air saturation of the solution), a new oxidation wave appears along with the smaller intensity Fe^{III}/Fe^{II}, at $E^{1/2}_{2,C} \approx 0.4\,V$, that corresponds to the oxidation of $Fe^{III}(OO)$ (see

Figure 2.4 of Chapter 2 and reference [133]). The fact that this oxidation occurs at + 0.4 V, while the $Fe^{III}(OO^{\bullet})/Fe^{III}(OO^{-})$ reduction at – 0.6 V, suggests that the species is not reoxidized to $Fe^{III}(OO^{\bullet})$. Such reversible redox process between Fe peroxo and Fe superoxo species has been only observed in low temperatures (210 K) is THF. [72] Importantly, the sum of the two oxidation currents under O_2, that correspond to the oxidative collection of the Fe^{II} at $E_{1,C}^{1/2} \approx -0.05\ V$, $I_{Fe^{II}}$, and of the $Fe^{III}(OO)$ at $E_{2,C}^{1/2} \approx 0.4\ V$, $I_{Fe^{III}OO^{-}}$, matches the current of the oxidative collection of Fe^{II} under Ar. This conservation of the faradaic balance, confirms that the oxidation of the $Fe^{III}(OO^{-})$ should involve one electron, as it is the case for the reoxidation of Fe^{II}. Additionally, the smaller amount of Fe^{II} collected under O_2 agrees, from a qualitative point of view, with the loss of reversibility on the CV recorded on the G.

At this stage, we hypothesize that oxidation of $Fe^{III}(OO^{-})$ leads to $[Fe^{III}(OO^{-})]_{ox}$ that *via* a chemical reaction leads back to Fe^{III} (see Scheme 4.1).

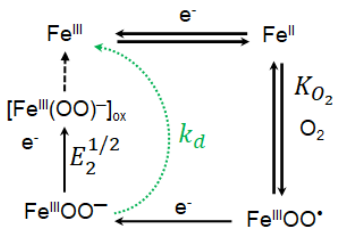

Scheme 4.1 Simplified reaction scheme used for the simulations.

Simulations were performed to evaluate the relevance of these SECM experiments, using COMSOL® Multiphysics. The simple reaction scheme shown in Scheme 4.1 was used (see paragraph 7.1.5 for further information). The potential of the reductive formation of $Fe^{III}(OO^{-})$ and its oxidation are taken under consideration, along with two chemical reactions, association between O_2 and Fe^{II} characterized by the equilibrium constant K_{O_2}, and the chemical instability of the $Fe^{III}(OO^{-})$ the constant k_d. We later show by spectroelectrochemistry (see paragraph 4.4) that this constant is a pseudo first order one. The influence of these two constants on the simulated LSV is shown in Figure 4.6 A-D.

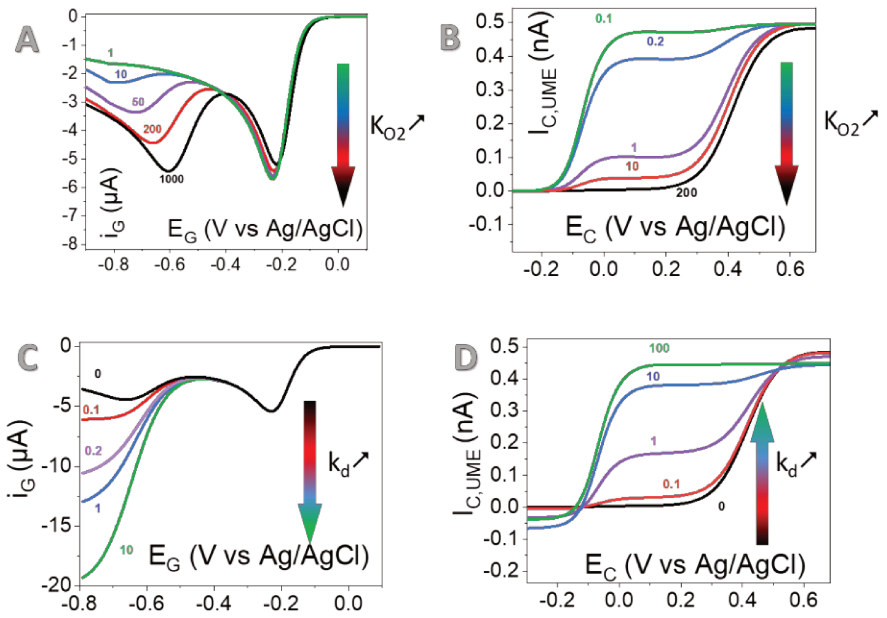

Figure 4.6: Influence of K_{O_2} and kd on the simulated LSV curves at G (A,C) and at C in the SG/TC mode, d=8 mm, (B, D). A,B: kd=0 s^{-1} and A) K_{O_2} =1–1000 M^{-1} and B) K_{O_2} = 0.1–200 M^{-1} from top to bottom. C,D) K_{O_2} =200M^{-1} and D) k_d=0–100 s^{-1} from top to bottom and E) k_d=0–10 s^{-1} from bottom to top.

Regarding K_{O_2}, at the G electrode (substrate generator) we observe that an increase of the constant leads to (i) an enhancement of the $Fe^{III}(OO^{\bullet})/Fe^{III}(OO^{-})$ reduction current up to an one electron process and (ii) to less negative $E^{p}_{Fe^{III}OO^{\bullet}/Fe^{III}OO^{-}}$ while in C electrode (tip collector), the $I_{Fe^{III}OO^{-}}$ increases at the expense of $I_{Fe^{II}}$. A high K_{O_2} (200 M^{-1}) leads to a complete attenuation of the $I_{Fe^{II}}$ at the C electrode, while even with a very low K_{O_2} (0.1 M^{-1}) the $Fe^{III}(OO^{-})$ is detected. On the other hand, a high k_d (10 s^{-1}) leads to catalysis-like current at the G electrode, because high instability of the species in our model leads to regeneration of Fe^{III}. At the C electrode, higher k_d (100 s^{-1}) attenuates completely the $I_{Fe^{III}OO^{-}}$ because the species does not have a lifetime high enough to reach the UME surface. The opposite trend between K_{O_2} and k_d allows determining only one couple of K_{O_2} and k_d for which the simulation can fit the LSV at G and the C response. The best fits of the LSVs on the substrate generator and on the tip collector for DMF solutions of $Fe(F_{20}TPP)Cl$ give a $K_{O_2} = 25 \pm 10\ M^{-1}$, and a $k_d = 1 \pm 0.3\ s^{-1}$.

Previously, Lexa et al. measured the K_{O_2} directly at the Fe^{II} state of sterically hindered porphyrins using UV-Vis spectroscopy.[165] They measured values between $3.6 \cdot 10^1$ M^{-1} and $4.6 \cdot 10^6$ M^{-1} depending on the Fe^{II} porphyrin. More recently, Mayer et al. estimated the K_{O_2} of a series of Fe porphyrins using DFT calculations,[129] and the obtained values lie between the same orders of magnitude as the ones calculates by Lexa et al.

In the present work, it is the first time that a K_{O_2} value is estimated combining experimental electrochemical data and simulations. Even if the K_{O_2} value for the Fe(F_{20}TPP)Cl has not been previously estimated, the value that we report here is between the limits of previously reported values for other Fe porphyrins *kd* to the best of our knowledge has not been used by previous studies. In paragraph 4.4, we evaluate it by UV-Vis spectroelectrochemistry.

In the following paragraphs, we will apply the same approach to two more Fe porphyrins, in order to compare the K_{O_2} and k_d values with those calculated for Fe(F_{20}TPP)Cl and ultimately draw relationships between the values of the constants and structural characteristics of the porphyrin.

4.3 SECM study of O_2 activation by three Fe porphyrins

Let us now extend our study and include Fe^{III}(TPP)Cl and Fe^{III}(T-(2-COOH)PP)Cl in SECM. The molecular structures of all three porphyrins used in the SECM study are shown in Figure 4.7. The LSVs recorded in air saturated DMF solutions at the G electrode, and at the C electrode during the SECM experiment are shown in Figure 4.7.

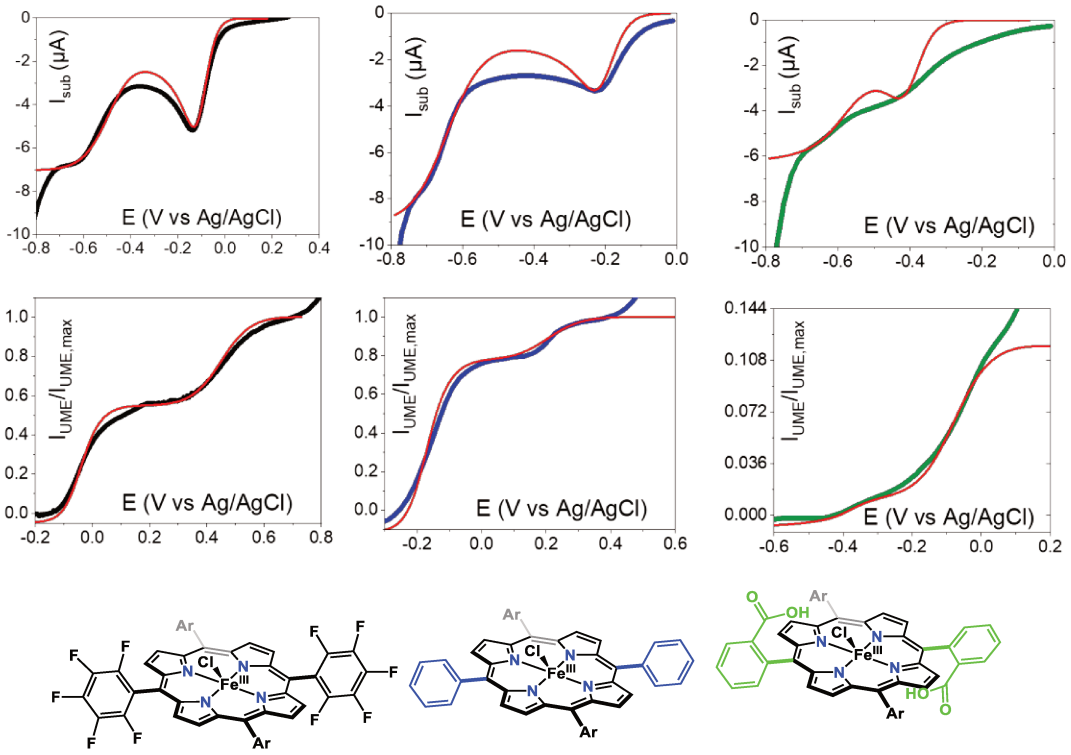

Figure 4.7: Experimental LSVs recorder at the G (generator electrode, top graphs) at 50 mV·s^{-1}, and LSVs obtained at C (collector microelectrode) at 50 mV·s^{-1} in SG/TC mode (bottom graphs) placed at d=8 ± 2 mm from G, while holdings the G at -0.7 V vs Ag/AgCl, in air saturated solutions of DMF, with 0.1 M TBAPF$_6$, and 0.5 mM of porphyrin from left to right Fe(F_{20}TPP)Cl, Fe^{III}(TPP)Cl and Fe^{III}(T-(2-COOH)PP)Cl. Red traces correspond to simulated curves. Molecular structures of the three Fe porphyrins are also shown.

Black, blue and green traces correspond to Fe(F_{20}TPP)Cl, Fe^{III}(TPP)Cl and Fe^{III}(T-(2-COOH)PP)Cl respectively, while red traces correspond to the simulated curves that fit the best the experimental curves. We observe a satisfactory match between the experiment and simulations, except for the LSV of the Fe^{III}(T-(2-COOH)PP)Cl on the

substrate electrode. In that case, the discrepancy between experiment and simulation may arise from the nature of the porphyrin's meso substituents.

The constants values estimated by simulations for the three Fe porphyrins are show in Table 4.1 and commented below.

- First of all, different $E^0_{Fe^{III}/Fe^{II}}$ are measured for each Fe porphyrin. As already discussed in paragraph 2.2, Fe(F_{20}TPP)Cl has less negative $E^0_{Fe^{III}/Fe^{II}}$ than Fe^{III}(TPP)Cl un (-0.05 vs -0.18 V). This is due to the electron withdrawing meso substituents of Fe(F_{20}TPP)Cl which stabilize the Fe^{II}, as reported in the literature.[128] Moreover, Fe^{III}(T-(2-COOH)PP)Cl has a lower $E^0_{Fe^{III}/Fe^{II}}$ than Fe(TPP)Cl (-0.37 vs -0.18 V), meaning that the meso-substituents of the former are electron donating. The already reported donating effect of the COOH substituents[128] can be explained by intraligand hydrogen bonding effects, that can lead to lower apparent pK_a of the COOH group resulting in a +I effect.
- We then observe that the K_{O_2}increases as the potential value decreases. As we already discussed in Chapter Chapter 2 this is presumably due to a higher electron density on the Fe^{II} (reflected in the lower $E^0_{Fe^{III}/Fe^{II}}$). We will further discuss this trend in paragraph 4.5.
- The k_d values do not seem to follow a specific trend, the values being 1 s^{-1}, 5 s^{-1}, and 0.3 s^{-1} for Fe(F_{20}TPP)Cl, Fe^{III}(TPP)Cl and Fe^{III}(T-(2-COOH)PP)Cl respectively. We will discuss in detail this observation in paragraph 4.5.

Table 4.1 Values of the $K_{O_2}$and k_d constants used for the simulations of Figure 4.7

Catalyst	$E^0_{Fe^{III}/Fe^{II}}$ **(V vs Ag/AgCl)**	K_{O_2} **(M^{-1})**	k_d**(s^{-1})**
Fe^{III}(F_{20}TPP)Cl	-0.05±0.03	25±10	1±0.3
Fe^{III}(TPP)Cl	-0.18±0.01	100±40	5±1
Fe^{III}(T-(2-COOH)PP)Cl	-0.37±0.02	500±100	0.3±0.1

In order to be able to build structure-reactivity relationships based on the calculated constants, we need a quantitative measure of the porphyrins' reactivity. As such, we have chosen the TOF (Turn over frequency) for the catalysis of the four electron four proton O_2 reduction to H_2O (ORR) in acidic media. Even though our studies do not

focus on the catalysis of ORR, the ORR TOF is relatively simple to estimate and the reaction quite well-studied.[128]

In order to calculate the ORR TOF of our three porphyrins we have used Foot-of-the-wave (FOTW) analysis, that is an analytical method based on cyclic voltammetry developed by Savéant et al. in the past decade.[144] FOTW analysis of cyclic voltametric catalytic responses allows the determination of parameters such as the TOF regardless of the side-phenomena that interfere at high current densities, preventing the expected catalytic current plateau from being reached.

In presence of O_2 and a proton source in organic media, the Fe^{II} porphyrins catalyze ORR. FOTW analysis links the catalytic rate constant, with the current and potential of the cyclic voltametric response using the following equation:

$$\frac{I_G}{I_{G,p}^0} = \frac{2.24\sqrt{\left(\frac{RT}{Fv}\right)k_{obs}}}{1 + exp\left[\left(\frac{F}{RT}\right)\left(E_G - E_{G,pq}^0\right)\right]} \qquad (4.3)$$

where $I_{G,p}^0$ is the current of the Fe^{III}/Fe^{II} reduction wave under argon in presence of protons (the G indicator corresponds to the glassy carbon disk electrode, same as the SECM substrate electrode), v is the scan rate, and $E_{G,pq}^0$ is the $E_{Fe^{III}/Fe^{II}}^0$ under argon in the same solution as the one where the catalysis response is observed but in absence of O_2 (p and q are the non-reduced and reduced form of the catalyst, here Fe^{III} and Fe^{II} respectively). Plotting $\frac{I_G}{I_{G,p}^0}$ over $\frac{1}{1+exp\left[\left(\frac{F}{RT}\right)\left(E_G-E_{G,pq}^0\right)\right]}$ for the different values of potential, E_G, of the glassy carbon generator electrode gives rise to a pseudo linear function. The slope can give direct access to k_{obs} of the equation 4.3, that can be analyzed as follows:

$$k_{obs} = n_{cat}{}^{2\sigma} k C_A^0 \qquad (4.4)$$

n_{cat} is the number of electrons involved in a single catalytic cycle (in this case 4), and if we assume that all the electrons originate from the electrode surface, σ =1.The TOF can be deduced from k_{obs} as follows:

$$TOF = kC_A^0 \qquad (4.5)$$

Where C_A^0 is the concentration of the substrate ($[O_2]$ = 4 mM in O_2 saturated DMF solution).[129] We follow herein the definition of the TOF that is proposed by Mayer et al.[128]

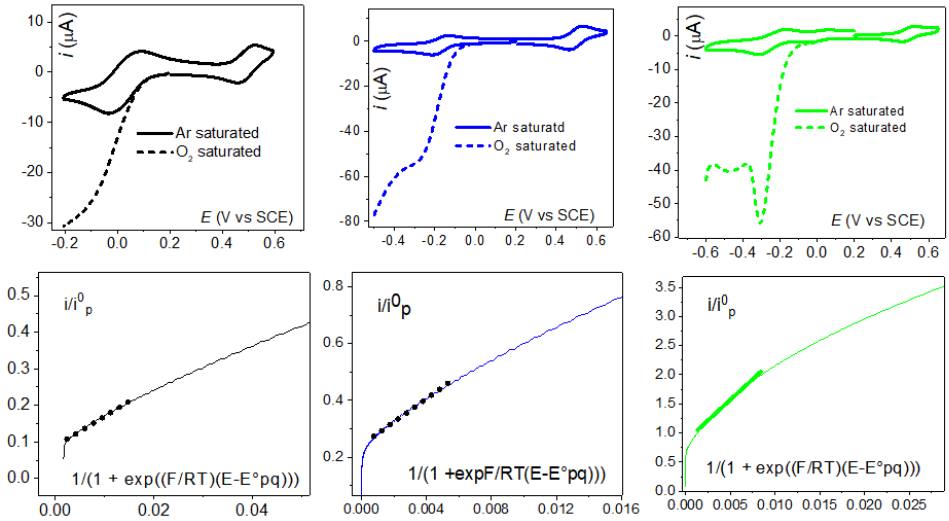

Figure 4.8 Top: CVs of 0.5 mM porphyrin solutions in DMF with 0.1 TBAPF6, with excess (10 eq) of $HClO_4$ and TBACl in presence (dotted trace) and in absence (normal trace) of oxygen. Bottom plot of $\frac{I_G}{I^0_{G,p}}$ *over* $\frac{1}{1+exp\,[(\frac{F}{RT})(E_G-E^0_{G,pq})]}$ *deduced from the corresponding CVs from left to right* $Fe(F_{20}TPP)Cl$, $Fe^{III}(TPP)Cl$ *and* Fe^{III}*(T-(2-COOH)PP)Cl.*

The ORR TOF values that we calculated were 12 s^{-1}, 350 s^{-1}, and 3300 s^{-1} for $Fe(F_{20}TPP)Cl$, $Fe^{III}(TPP)Cl$ and Fe^{III}(T-(2-COOH)PP)Cl respectively. We observe first of all, that the three porphyrins have TOF values of different order of magnitude, showing that the meso-substituents have an important effect on the catalysis. Furthermore, TOF varies linearly with the $E^0_{Fe^{III}/Fe^{II}}$. More negative $E^0_{Fe^{III}/Fe^{II}}$ leads to higher catalytic activity. In paragraph 4.5, we will show how the TOF can be used as a measure of the activity of these catalysts allowing us to draw structure-reactivity relationships. We note here that Mayer et al. have calculated using FOTW TONs of 27 s^{-1} and 2000 s^{-1} for $Fe^{III}(TPP)Cl$ and Fe^{III}(T-(2-COOH)PP)Cl respectively, values that are quite different from ours. However, FOTW analysis is a very sensitive method and comparison of the obtained TOF values is straightforward only between a series of experiments that are performed in exactly the same experimental conditions (proton source, electrode surface, porphyrin counter anion/axial ligand).

4.4 Studying the stability of the $Fe^{III}(OO^{-})$ by UV-Vis Spectroelectrochemistry

4.4.1 Evaluation of k_d

In order to obtain a further insight in the stability of the peroxo species of the Fe(F_{20}TPP)Cl and Fe^{III}(TPP)Cl, UV-Vis spectroelectrochemistry was implemented. At this stage we have not yet performed spectroelectrochemical experiments with the Fe^{III}(T-(2-COOH)PP)Cl porphyrin. The UV-Vis signature of the corresponding peroxo intermediate has not been reported so far for this porphyrin, and a complete study would necessitate additional spectroscopic characterization.

Starting with the Fe(F_{20}TPP)Cl porphyrin, the peroxo species $Fe^{III}(OO^{-})$ can be electrogenerated at 253 K, by applying a potential of -0.6 V in air saturated DMF solutions of the porphyrin.[133] The UV-Vis spectrum of the peroxo has a characteristic sharp Soret band at 432 nm, that can be used as probe for the concentration of the peroxo form. As shown in Figure 4.9, after the generation of the species, in open circuit (i.e. no applied potential), the peroxo dissociates within one and a half hour at 253 K. The plot of the natural logarithm of the absorbance at 432 nm versus time (in seconds) is shown in Figure 4.9.

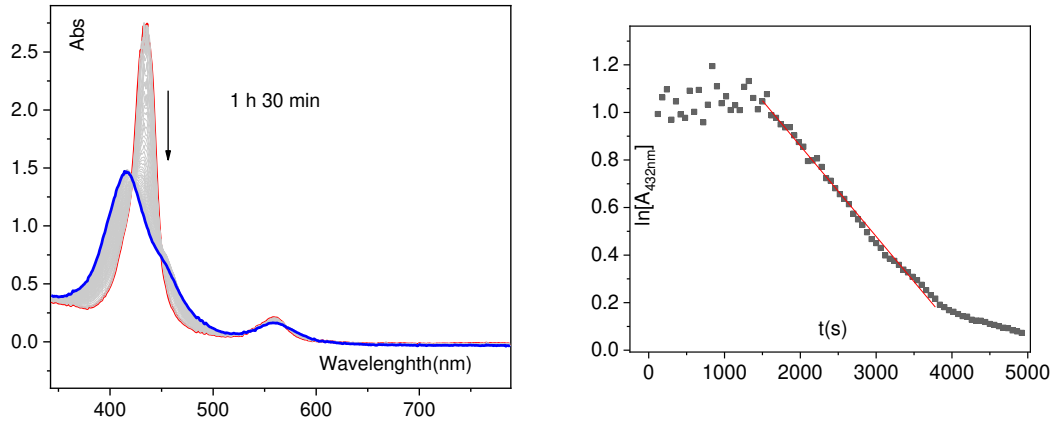

Figure 4.9: (Left) UV-Vis Spectral evolution of an electrochemically generated $Fe^{III}(F_{20}TPP)(OO—)$, with a concentration of 0.2 mM in air saturated DMF solution with 0.2 M $TBAPF_6$ in spectroelectrochemical cell in open circuit potential at 253 K. At this concentration the Soret band of the peroxo species is initially saturated (red trace). Blue trace shows the resulting Fe^{III}. (Right) Time evolution of the absorbance at 434 (peroxo Soret band) nm with time.

The rate law for (pseudo)-first order reactions is expressed by the following equation[166]:

$$\frac{d[A]}{dt} = -k_d'[A] \qquad (4.6)$$

Where [A] is the concentration of the reactant, in this case A is the $Fe^{III}(F_{20}TPP)(OO^{-})$, and k_d' is its dissociation constant. The integration of the equation 4.6 gives:

$$ln\left(\frac{[A]}{[A_0]}\right) = -k_d't \qquad (4.7)$$

As a result, from the plot of $ln[A]$ vs t we can calculate the dissociation constant constant k_d'. First of all, the linearity of the $ln[A]$ vs t plot[i] with $R^2 > 0.99$ confirms the pseudo-first order character of the dissociation constant. The value for the k_d'. that we calculate is $3.8 \cdot 10^{-4} \pm 0.1 \cdot 10^{-4}$ s^{-1} at 253K.

With the same porphyrin, the $Fe(F_{20}TPP)Cl$, a value of 1±-0.3 s^{-1} at 293 K is estimated from simulations of the SECM experiment. The difference of the estimated values between the SECM and the UV-Vis experiment in mainly attributed to the difference of temperature between the two. Unfortunately, the instability of the peroxo species did not allow us to perform spectroelectrochemical experiments at room temperature (293 K) and directly compare the obtained value with the one calculated by SECM.

Performing the spectroelectrochemical experiment at various low temperatures (for example between 210 K and 263 K) could allow us to acces the k_d' in room temperature as follows. We consider the Arrhenius equation:

$$ln(k_d') = lnB - \frac{E_a}{RT} \qquad (4.8)$$

where B is the preexpodential factor, E_a is the activation energy of the reaction, T is the temperature and R the gas constant. Plotting $ln(k_d')$ over $\frac{1}{T}$ may give us access, by extrapolation, to values of the constant in higher temperatures. However, such a study was not considered a priority at the course of the present work.

Let us now examine the species that occurs after dissociation of the $Fe^{III}(F_{20}TPP)(OO^{-})$. As shown in Figure 4.10, after the electrochemical generation of the $Fe^{III}(F_{20}TPP)(OO^{-})$, the intensity its Soret band at 432 nm diminishes with time. Complete attenuation of the peak at 432 nm (that corresponds to the complete dissociation of the peroxo complex) results in a new spectrum (Figure 4.9 left, blue trace). This spectrum has a Soret band at 416 nm and one sole Q-band at 558. As shown in Figure 4.10, this spectrum (green trace) is very close to a chemically prepared

[i] Until 1500 s the Soret bans remains saturated, so we take into account the points after 1500s.

$Fe^{III}OH$ (Figure 4.10, red trace). From the experimental data at hand, it is not yet clear why exactly a OH^- occupies the axial position after the dissociation of the peroxo species. However, we shall note that this observation is not unprecedented, since Karlin et al. have previously spectroscopically observed a $Fe^{III}OH$ after thermal decomposition of their chemically prepared $Fe^{III}(F_8TPP)(OO^-)$ in THF.[167] Importantly, electrolysis at -0.6 V of the resulting solution after decomposition of the peroxo, leads again to the formation of the peroxo. This observation corroborates our hypothesis, that this resulting species from the decomposition of $Fe^{III}(OO^-)$ enters back to the reaction cycle (see Scheme 4.1).

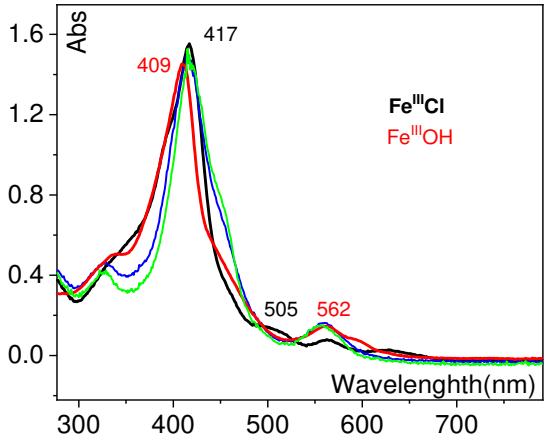

Figure 4.10: Spectra of a 0.2 mM $Fe^{III}(F_{20}TPP)Cl$ at 253 K in an air saturated DMF solution with 0.2 M $TBAPF_6$ in the spectroelectrochemical cell before (black trace) and after electrochemical generation of the peroxo by applying -0.6 V vs SCE for 10 min, and subsequent decomposition in open circuit (blue trace). Second electrolysis of that solution at -0.6 V vs SCE and subsequent decomposition in open circuit leads to the green trace spectrum. A chemically prepared $Fe^{III}OH$ is also shown in the figure for comparison (red trace).

Spectroelectrochemistry experiments has also been performed for the Fe(TPP) analogue (Figure 4.11). The value that we calculate is $2.48 \cdot 10^{-4} \pm 0.06 \cdot 10^{-4}$ s^{-1} at 233 K. Due to the lower stability of the Fe(TPP) peroxo analogue compared to the Fe(F_{20}TPP) one (see Chapter Chapter 2), lower temperature was required for a successful experiment (233 K vs 253 K), and thus we cannot compare the obtained k_d' for the two complexes. However, once again the pseudo-first order character of the dissociation of the peroxo species is confirmed.

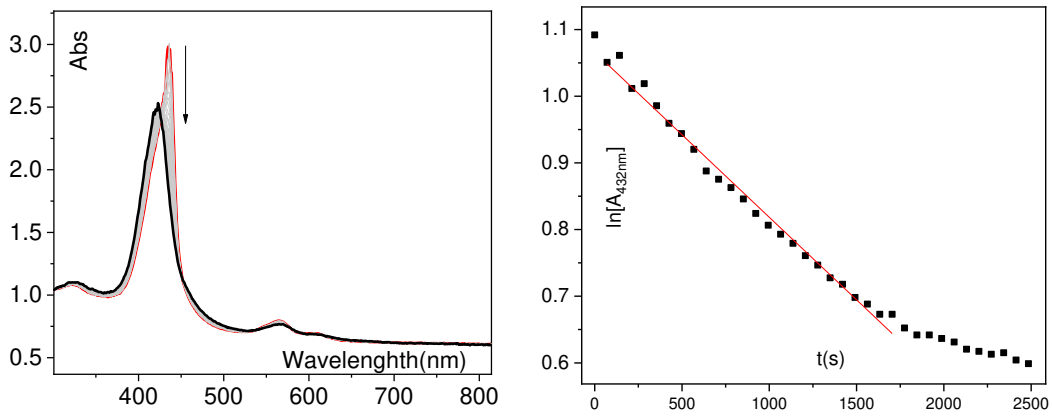

Figure 4.11: Left: UV-Vis Spectral evolution of an electrochemically generated $Fe^{III}(TPP)(OO^{-})$, with a concentration of 0.2 mM in air saturated DMF solution with 0.2 M $TBAPF_6$ in spectroelectrochemical cell in open circuit potential at 253 K. Black trace shows the resulting Fe^{III}. Right Time evolution of the absorbance at 434 (peroxo Soret band) nm with time.

4.4.2 *In situ* oxidation of the electrogenerated $Fe^{III}(F_{20}TPP)(OO^{-})$

As shown already discussed, the CV of an electrogenerated $Fe^{III}(F_{20}TPP)(OO^{-})$ in DMF, show an irreversible one electron oxidation peak at +0.5 V vs Ag/AgCl. This oxidation process was used to detect the peroxo at the C electrode, in the SECM experiments. We are now interested in evaluating the fate of the species while applying a potential of +0.6 V vs Ag/AgCl, in the context of the present spectroelectrochemical study,

As show in Figure 4.12, when a potential of +0.6 V is applied in the solution of the electrogenerated peroxo species, its Soret band quickly attenuates, and the resulting spectrum displays a Soret band at 417 nm, a shoulder at 450 nm, and a Q-band at 562. The spectrum is identical to the spectrum obtained in open circuit.

The oxidative potential resulted in acceleration of the peroxo dissociation rate of the species ($k'_{d,ox}$ = $7.2 \cdot 10^{-4} \pm 0.2 \cdot 10^{-4}$ s^{-1}) compared to the open circuit experiment (k'_d = $3.8 \cdot 10^{-4} \pm 0.1 \cdot 10^{-4}$ s^{-1}), but resulted in the same UV-Vis spectrum. These observations suggest that the spontaneous dissociation and the oxidation-triggered dissociation pathways share common chemical steps.

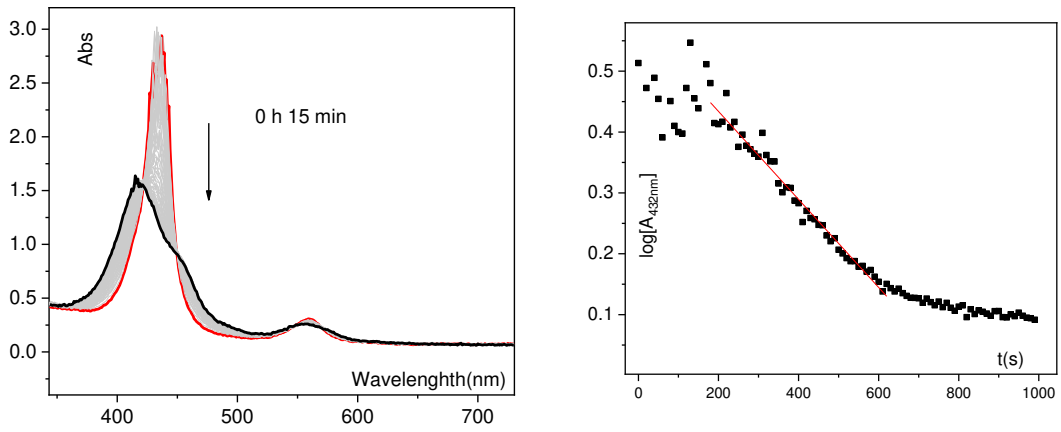

Figure 4.12: (Left) UV-Vis Spectral evolution of an electrochemically generated $Fe^{III}(F_{20}TPP)(OO^{-})$, with a concentration of 0.2 mM in air saturated DMF solution with 0.2 M $TBAPF_6$ in spectroelectrochemical cell while applying + 0.5 V vs SCE at 253 K. At this concentration the Soret band of the peroxo species is initially saturated. Black trace shows the resulting Fe^{III}. (Right) Evolution of the absorbance at 434 (peroxo Soret band) nm with time.

In conclusion, by UV-Vis spectroelectrochemistry we have experimentally shown that the dissociation of the $Fe^{III}(F_{20}TPP)(OO^{-})$ and the $Fe^{III}(TPP)(OO^{-})$ complexes follow a pseudo-first order reaction, as we had hypothesized when building our simulation model.

4.5 Discussion – Structure reactivity relationships

In the previous paragraphs we showed how we calculated for three different porphyrins, the K_{O_2} (the binding constant between Fe^{II} and O_2), the k_d (the dissociation constant of the $Fe^{III}(OO^{-})$) from the SECM experiments and simulations, and the TOF for ORR using the FOTW analysis. In the present paragraph we examine how we can combine our findings to build structure-reactivity relationships. Table 4.2 shows all the potentials measured in the SECM experiments, the constants K_{O_2} and k_d calculated by fitting the LSV on the G and on the C electrodes with simulations, and the TOF that we calculated based on cyclic voltammetry data.

Table 4.2 Parameters calculated in the SECM study.

Catalyst	$E^0_{Fe^{III}/Fe^{II}}$	$E^p_{Fe^{III}OO^\bullet/Fe^{III}OO^-}$	$E^{1/2}_{Fe^{III}OO^\bullet/Fe^{III}OO_{ox}}$	TOF (s^{-1})	K_{O_2} (M^{-1})	k_d(s^{-1})
$Fe^{III}Fe_{20}$TPPCl	-0.05±0.03	-0.58±0.05	0.39±0.04	12	25±10	1±0.3
Fe^{III}TPPCl	-0.18±0.01	-0.64±0.01	0.18±0.03	250	100±40	5±1
Fe^{III}T(2-COOH)PP)Cl	-0.37±0.02	-0.62±0.02	-0.07±0.03	3300	500±100	0.3±0.1

Redox potentials of catalytic intermediates in V vs Ag/AgCl, TOF for ORR, binding constant (K_{O_2}), and apparent dissociation constant (k_d) of the peroxo species, all at 293 K. The errors on the potentials were estimated from 3-4 different experiments for each porphyrin and the errors on the constant values were estimated by fitting in simulations.

We can exploit the experimentally determined oxidation and reduction potentials of the different intermediates and the values of K_{O_2}, k_d and TOF, in order to gain access to structure–reactivity relationships within the iron porphyrin series. Let us first examine the correlation between the logarithm of K_{O_2}, k_d and TOF with the $E^0_{Fe^{III}/Fe^{II}}$ that is presented in Figure 4.13.

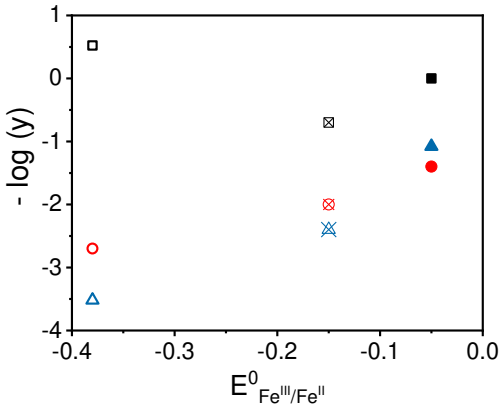

Figure 4.13 log(y), y being k_d (■), K_{O_2} (●) and the TOF (▲) plotted versus $E^0_{Fe^{III}/Fe^{II}}$. Bold signs correspond to the Fe(F_{20}TPP)Cl, crossed signs to the Fe^{III}(TPP)Cl and void signs to the Fe^{III}(T-(2-COOH)PP)Cl

We observe the following.

(i) Log(K_{O_2}) varies linearly with the Fe^{III}/Fe^{II} redox potential and the slope is 60 mV per decade, that agrees with the trend that was previously observed by Mayer et al.[128] In that study however, the values of K_{O_2} were estimated by DFT calculations. *How can we explain this trend?* More electron

donating meso-substituents lead to more negative $E^0_{Fe^{III}/Fe^{II}}$ that reflects higher electron density on the Fe^{II}. This higher electron density leads to higher affinity for O_2, that is represented by the binding constant.

(ii) Log(k_d) is lower for the Fe(F_{20}TPP)Cl than for the Fe^{III}(TPP)Cl. This means that the Fe^{III}(F_{20}TPP)(OO^-) is more stable than the Fe^{III}(TPP)(OO^-). This fact is in accordance with our previous experimental observation, that Fe^{III}(TPP)(OO^-) could be electrochemically generated only in extra dry DMF at temperatures not higher than 233 K. As we have previously discussed the main reason for the higher stability of the Fe^{III}(F_{20}TPP)(OO^-) is that electron withdrawing groups in meso positions, that stabilize the high electron density of the Fe^{III}(OO^-) moiety. Nevertheless, an even lower k_d value is calculated for Fe^{III}(T-(2-COOH)PP)Cl, despite the electron donating character of the meso substituents. A plausible explanation for this observation is that interactions between the the -COOH and the Fe^{III}(OO^-) moieties can stabilize the excess electron density on the latter (see Scheme 4.2).

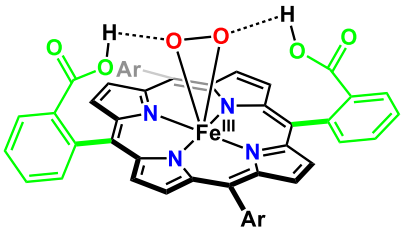

Scheme 4.2 Representation of possible intraligand hydrogen bonding in the Fe^{III}(T-(2-COOH)PP)(OO^-) complex.

(iii) Log(TOF) also varies linearly with $E^0_{Fe^{III}/Fe^{II}}$, and the TOF values for ORR are larger for catalysts with more negative $E^0_{Fe^{III}/Fe^{II}}$. When the catalyst's $E^0_{Fe^{III}/Fe^{II}}$ is more negative, its reduced form (the Fe^{II}, that is the catalytically active species) is more electron rich, making the initial reaction of Fe^{II} with O_2 more favorable, as reflected by the higher K_{O_2}. This leads to an overall higher catalytic activity.

Looking at our experimental results, we make another important observation. $E^p_{Fe^{III}OO^{\bullet}/Fe^{III}OO^-}$ does not depend on the porphyrin ligand as it is the case for

$E^0_{Fe^{III}/Fe^{II}}$ (see Table 4.2). However, one would expect that it should have, if the only process involved in the reduction of the superoxo was an heterogeneous electron transfer. We thus suspected that a possible protonation of the species from residual water in DMF in also involved. Such a process would explain the fact that the species is unstable in room temperature, as already reported in the present manuscript and in the literature (see paragraphs 1.4.1 and 1.4.2).

To further illustrate this point, let us now correlate $E^p_{Fe^{III}OO\bullet/Fe^{III}OO^-}$ (here expressed as $E^0_{app,1}$) and $E^0_{Fe^{III}/Fe^{II}}$. We start from the equation 4.9 (see annex) that takes into consideration the K_{O_2}.

$$E^0_{app,1} = E^0_{Fe^{III}/Fe^{II}} - 0.06pK_{O_2} + C'' \qquad (4.9)$$

With $C'' = 0.06\log[O_2] + \Delta E$, $\Delta E = E^0_{Fe^{III}OO\bullet/Fe^{III}OO^-} - E^0_{Fe^{III}/Fe^{II}}$. If we plot, based on this equation, the $E^0_{Fe^{III}/Fe^{II}}$ over $E^0_{Fe^{III}OO\bullet/Fe^{III}OO^-} - 0.06pK_{O_2}$, we obtain a curve that deviates considerably from unity (see Figure 4.14). We then introduce two corrections:

(i) We replace the $0.06pK_{O_2}$ factor by $0.09pK_{O_2}$ that fits better the slope of the plot of $E^0_{Fe^{III}OO\bullet/Fe^{III}OO^-}$ over pK_{O_2}calculated in the simulated curves, for the Fe(F_{20}TPP) (data not shown).

(ii) We take into consideration the protonation reaction of the peroxo , with a $K_a = \frac{[Fe^{III}OOH]}{[H^+][Fe^{III}OO^-]}$

These two modifications lead to the new equation

$$E^0_{app,2} = E^0_{Fe^{III}/Fe^{II}} - 0.09pK_{O_2} + 0.06\Delta pK_a + B'' \qquad (4.10)$$

With $B'' = 0.06\log[O_2] - 0.06pH + \Delta E$ that is constant between the porphyrin series. In order to achieve a slope near unity, we take $pK_a = 0$ for Fe(F_{20}TPP) and we test different values for the for the ΔpK_a of the other two porphyrins. The values that we estimated were 0.4 and 2.6 for Fe(TPP) and Fe(T(2-COOH)PP) respectively. The ΔpK_a values that we propose are rather reasonable considering the values reported for a series of porphyrins including Fe(TPP)Cl and Fe(F_{20}TPP) by Wijeratne et al. in THF, values

measured spectroscopically from chemically prepares species (ΔpK_a= 1 for Fe(TPP)(OO^{-}) and Fe(F_{20}TPP)(OO^{-})) .[74]

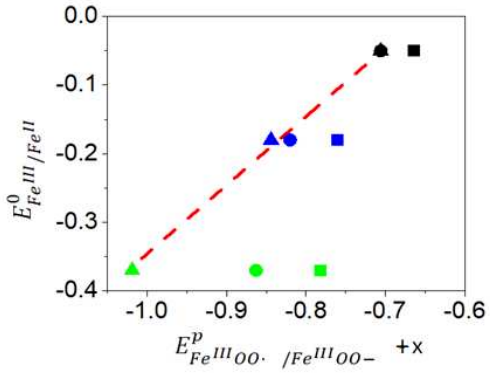

Figure 4.14 Evolution of the $E^0_{Fe^{III}/Fe^{II}}$ with $E^0_{Fe^{III}O_2^{\bullet-}/Fe^{III}O_2^{2-}} - x$ where(■) $x = 0.06pK_{O_2}$, (●)$x = 0.09pK_{O_2}$ or (▲)after pKa correction $x = 0.09pK_{O_2} - 0.06\Delta pK_a$. Red dash trace corresponds to unity slope. Black, blue and green dots correspond to Fe(F_{20}TPP)Cl, Fe^{III}(TPP)Cl and Fe^{III}(T-(2-COOH)PP)Cl respectively

These arguments show that the involvement of a protonation step in the dissociation of the peroxo species is plausible, and could explain the variation of the $E^0_{Fe^{III}OO^{\bullet}\ /Fe^{III}OO^{-}}$ with the porphyrins used in the present study.

How could we now take advantage of the ΔpK_a values that we calculated ? Mayer et al. have previously shown that TOF can be correlated with ΔpK_a and pK_{O_2} using the following equation:

$$log(TOF) = -pK_{O_2} + a\Delta pK_{a(superoxo)} + B'' \qquad (4.11)$$

Where a and B'' are constant within the series. They obtained linear relationships when $a = 0.22$. In that work, $pK_{a(superoxo)}$ and pK_{O_2} values were calculated using DFT, and only a PET pathway was considered (where the $Fe^{III}(OO^{\bullet})$ and not the $Fe^{III}(OO^{-})$ is protonated). We used the same equation and we introduced the experimentally determined K_{O_2} and the estimated $\Delta pK_{a,peroxo}$. We obtained quite satisfactory correlations with the TOF. We also note that in our case ΔpK_a relates to the peroxo species, showing that the EPT can equally be envisaged for the ORR (see Figure 4.15).

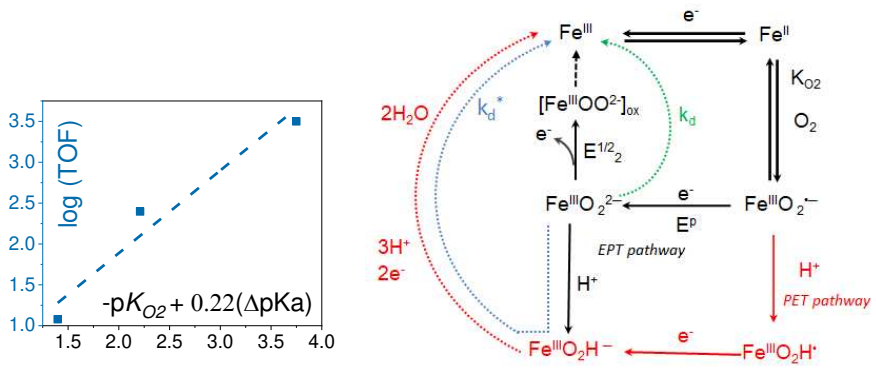

Figure 4.15 Left: Dependence of the TOF on a factor containing both K_{O_2} and pK_a.of the peroxo based on the equation log(TOF) = -pK$_{O2}$ + a $pKa_{Fe^{III}OO^-/Fe^{III}OOH}$ + B" with B" and α constant terms within the series. Right: Reaction scheme displaying different reaction pathways considered.

In conclusion, in this chapter we demonstrate the potentiality of the SECM in SG/TC mode to decipher homogeneous catalytic systems based on the *in situ* probing of reaction intermediates, exemplified by the study of O_2 reduction by Fe porphyrins. We first showed that using the SG/TC mode of the SECM, the $Fe^{III}(F_{20}TPP)(OO^{-})$ species which is generated at the substrate electrode can be probed at the ultramicroelectrode. This methodology is then successfully applied for the porphyrins Fe(TPP) and Fe(T(o-(COOH))PP). We then simulated the LSVs recorded on each electrode and with a simple reaction scheme, and we were thus able to calculate the pK_{O_2} and k_d. We thus show that the SECM tool allows not only to characterize different reaction intermediates in a single experiment, but also, combined with simulations, to determine the kinetic and thermodynamic parameters. The obtained parameters allow drawing structure activity correlations pertinent to address the catalysis of O_2 reduction by such catalysts. The importance of O_2 binding and of the peroxo protonation is highlighted through experimental estimates that correlate to TOF. Parameters used previously in the literature to draw structure-reactivity relationships were only estimated by DFT calculations.

The work presented in this chapter has been published in *Angewandte Chemie.*[168]

Chapter 5

Electrochemical Aerobic oxygenations and halogenations of organic substrates by Fe and Mn porphyrins

The electrochemical approach in the generation and characterization of metal-oxygen porphyrin intermediates in model systems, is in itself scientifically exciting but it also constitutes the first step towards the development of systems that are able to efficiently reproduce the oxygenation or halogenation reactivity of enzymes such as Cyt-P450 or haloperoxidases.

In chapters 2, 3, and 4, we have shown that it is possible to electrochemically generate and characterize various metal-oxygen intermediate species, starting from air-stable Fe^{III} or Mn^{III} porphyrins. In the present chapter, based on our previous findings on O_2 activation, we show that we can achieve electrocatalytic oxidation of organic substrates, in the antipode of the approach that utilizes chemical oxidants that is much more common, as discussed in Chapter Chapter 1. Our approach is very scarce in the literature, to the best of our knowledge only the groups of Murray and Dey have followed similar approaches, and it is the first time that such a methodology is developed at LEM.

In our approach, we start with an air stable M^{III} porphyrin (M=Fe or Mn), which when electrochemically reduced, reacts with O_2. Changing the reaction conditions or the catalyst can allow the generation of various intermediates which have different reactivities (see Scheme 5.1).

- In the case of Fe porphyrins, Fe^{II} reacts with O_2 in absence of acid to generate superoxo species (Chapter Chapter 2). It has previously been demonstrated that such species can act as an electrophiles and oxidize indoles.[54, 137] We herein explore the reactivity of electrochemically generated superoxo species.[j]
- In presence of acid, the Fe^{II}/O_2 systems can lead to the cleavage of the O-O bond that generates Fe-Oxo high valent species as we showed in Chapter Chapter 3. Such species are strong electrophiles able to activate C-H bonds.[9] We also explore electrochemical halogenation reactivity, in presence of acid and chloride, inspired by previous studies showing that chemically generated Fe-oxo species in presence of chloride can lead to halogenation of simple organic substrates.[95, 98]

[j] Corresponding Mn species do not demonstrate such reactivity according to the literature, and have not been considered in reactivity studies in the present work.

- Mn^{II}/O_2 systems are also capable of oxidizing organic substrates in presence of Lewis acids under electrochemical conditions.[120-121] We herein revisit this methodology and explore possible halogenase reactivity in presence of chloride.

In each electrocatalysis experiment, we first record CVs in the desired conditions, and then perform the controlled potential electrolysis in an appropriate set-up (see Annex 1, paragraph 7.1.2). The parameters that vary in our experiments are (i) the metal, Fe or Mn (ii) the ligand, since meso substituents of the porphyrin ring also affect reactivity of the intermediate species (see Scheme 5.1) (iii) the presence and the nature of the acid (strong protic, weak protic, or Lewis acid), and (iv) the solvent, that can be more or less prone to interactions with the reactive intermediates. All the experiments presented here have been performed at room temperature.

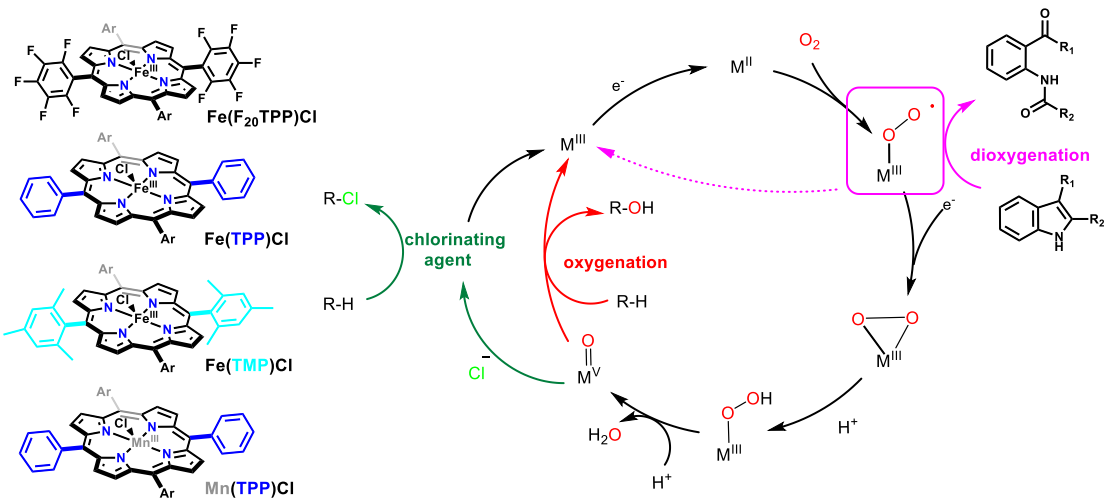

Scheme 5.1: (Left) Porphyrins used as catalyst for the catalytic studies. (Right) Three characteristic reaction pathways considered in the present manuscript.

In the next pages, we will present the results that we have obtained during these studies.

5.1 Dioxygenase-type reactivity of electrogenerated Fe porphyrin superoxide, $Fe^{III}(OO^{\bullet})$

As discussed in the Chapter 1 , recent works of the Goldberg [55] and Wijeratne [54] groups modeled the 2,3 tryptophan dioxygenase. Wijeratne et al. were able to generate the Fe porphyrin superoxo species of different Fe porphyrins, including Fe(TPP) and Fe(F_{20}TPP), at 192 K in mixtures of DCM:THF 9:1. They demonstrated that the superoxo species can react with a series of substituted indoles to produce the corresponding di-oxygenated molecules, as shown in Scheme 5.2, and they make the following observations:

- $Fe^{III}(F_{20}TPP)(OO^{\bullet})$ complex reacted the fastest with the substrate, and could react at 217 K while $Fe^{III}(TPP)(OO^{\bullet})$ needed slightly higher temperatures to react (232 K). The fact that $Fe^{III}(F_{20}TPP)(OO^{\bullet})$, which is more electrophilic than $Fe^{III}(TPP)(OO^{\bullet})$, thanks to the electron withdrawing substituents, is at the same time the most reactive, suggest that the reaction mechanism takes place throughout an electrophilic attack (See Chapter 1.3.3).
- The most electron rich indole substrate, the 2,3-dimethylindole (R_1=R_2=CH_3, Scheme 5.2), reacted the faster with all the Fe superoxo, corroborating the mechanism proposition.
- The highest observed yield was 31% with respect to the catalyst, showing that the reaction is sub-stoichiometric, and after completion of the reaction the porphyrin species present the well-known a μ-oxo dimer $(Porph)Fe^{III}$-O-$Fe^{III}(Porph)$. Presence of 2-methylimidazole in the reaction mixture did not improve the reaction yields. It prevented the formation of the dimer but occupied both axial positions in the metal center after completion of the reaction thus preventing it from being catalytic.

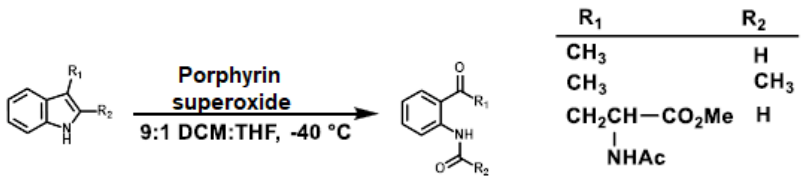

Scheme 5.2: Di-oxygenation of indoles with different substituents, by reaction with Fe porphyrin superoxide, as described by Wijeratne et al.[54]

On the other hand, Goldberg et al. performed the reaction at 232 K in d^7-DMF, using only Fe(TPP) superoxide as reactive species and 2,3-dimethylindole as substrate, with a maximum yield of 61 ± 9% with respect to the complex. In that report, the reaction was sub-stoichiometric as well, because the reaction resulted in the formation of the μ-oxo species dimer that is not reactive and does not participate in the catalytic cycle.[137] Importantly, they have shown that the reaction could also proceed at room temperature suggesting transient formation of the superoxo.[55]

In view of these results, we wanted to reproduce this reactivity using our electrochemical approach, since we have spectroscopically shown that Fe porphyrin superoxo can be electrochemically generated from an Fe^{III} and O_2 at reductive potentials. We chose to start our experiments in DMF, using Fe^{III}(TPP)Cl as catalyst, at room temperature, conditions closer to Goldberg's system that gave better yields. We used the commercially available 2,3-dimethylindole (R_1=R_2=CH_3, Scheme 5.2) as substrate, following both of these previous studies. It has been obtained commercially. The expected product of the dioxygenation reaction, N-2-(methylphenylacetamide), has been synthesized by a simple protocol were $NaIO_4$ was used as oxidant (see paragraph 7.1.1 of Annex 1). The characteristic amide proton of the N-2-(methylphenylacetamide) (11.6 ppm in $CDCl_3$ and 10.7 ppm in DMF/$CDCl_3$) and its peaks in the aromatic region in ^{1}H-NMR are used as probe of its formation. The ^{1}H-NMR spectra of both the substrate and the expected product are shown in Figure 5.1.

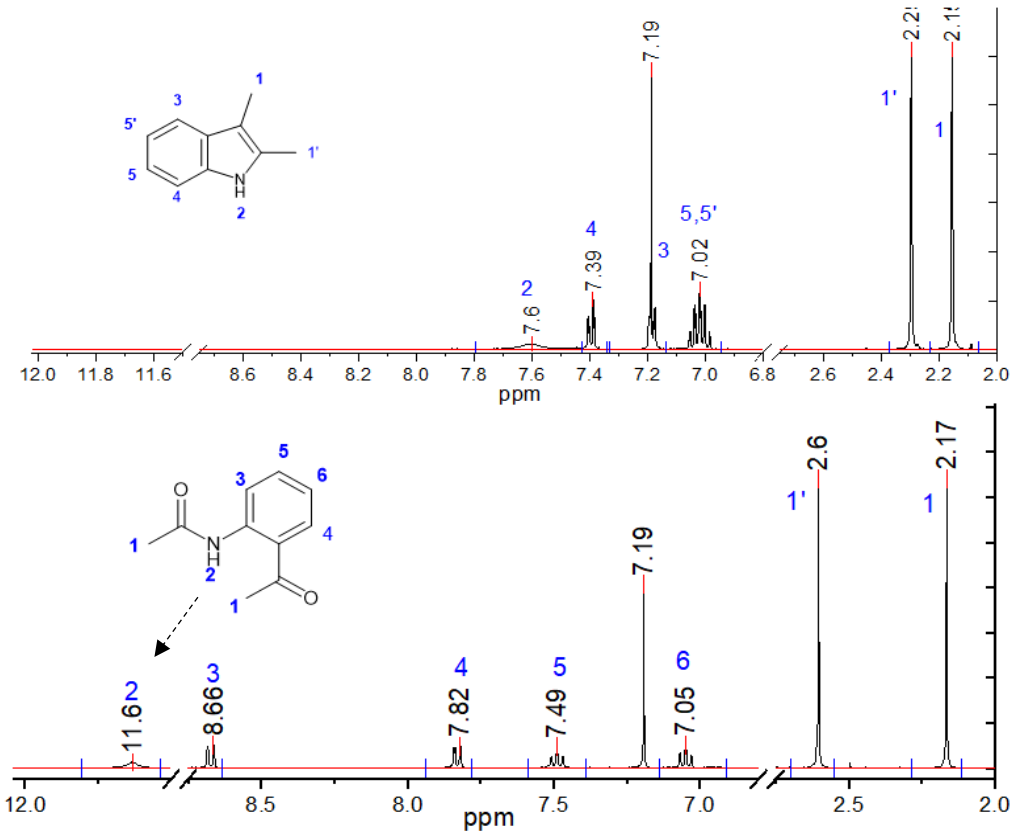

Figure 5.1 ^{1}H-NMR spectra of 2,3-dimethylindole (Up), and the N-2-(methylphenylacetamide) (Down). In the insets are shown the molecular structures of the two complexes. Peak at 7.19 ppm corresponds to the solvent, $CDCl_3$. 1 and 1' numbers correspond to three methyl-protons.

Figure 5.2: A shows CVs of a DMF solution of Fe(TPP)Cl, under Ar (black trace) and under O_2 (red trace), and in presence of 2,3-dimethylindole (blue trace). The Fe^{III}/Fe^{II} in reversible under argon with $E^0_{Fe^{III}/Fe^{II}} = -0.2\ V\ vs\ SCE$. The irreversibility of the wave observed under O_2 is due to the reaction of the electrogenerated Fe^{II} with O_2 to form the $Fe^{III}(OO^{\bullet})$, as we previously explained (See Chapter Chapter 2). Addition of substrate under O_2 induces a small increase of the current. Controlled-potential electrolysis was then performed at -0.2 V vs SCE for 1 h, and the current vs time plot is shown in Figure 5.2 B.

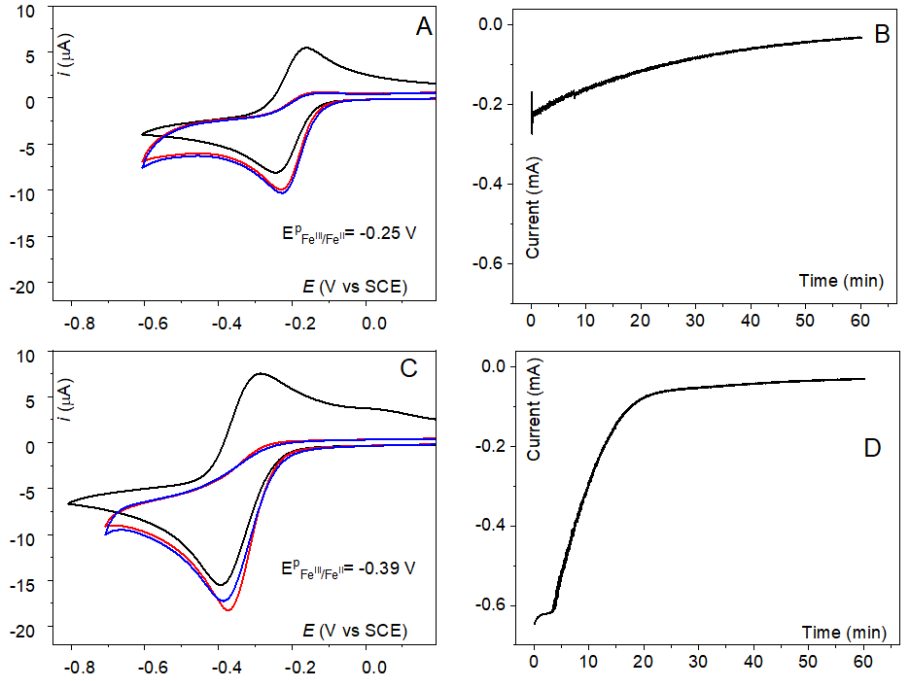

Figure 5.2: A: CV in DMF with 0.1 M $TBAPF_6$ of 1 mM solution of $Fe^{III}(TPP)Cl$ under Ar (black trace), under O_2 (1 mM, air saturated) (red trace) and under O_2 after addition of 20 eq of 2,3-dimethylindole (blue trace). Scan rate is 0.1 V s^{-1} at a GC disk electrode (0.07 cm^2), T = 293 K. B: i vs t plot of the controlled potential electrolysis at -0.2 V vs SCE for 1 h in DMF. C: CVs in DCM otherwise same conditions as in A. D: Electrolysis at -0.4 V vs SCE for 1h in DCM.

NMR analysis of a sample collected before and a sample collected after the controlled-potential electrolysis, revealed no formation of the expected product nor of other aromatic products. The two NMR spectra are quasi identical (see Figure 5.3). Moreover, the UV-Vis spectrum at the end of the electrolysis indicated the formation of the well-known μ-oxo dimer (UV-Vis signature reported in references [76] and [55], λ_{max} at 408, 556, and 585 nm). We hypothesize that the reason for the diminution of the current during the electrolysis (Figure 5.2 B) is the formation of the μ-oxo, that is inert at the applied potential.[169]

In view of this results, we also tried out another Fe porphyrin, the Fe^{III}(TMP)Cl (TMP= tetramesityl- porphyrin) that is more sterically hindered and the formation of the μ-oxo dimer is supposed to be disfavored. However, it was not the case experimentally, and the results did not defer from Fe(TPP).

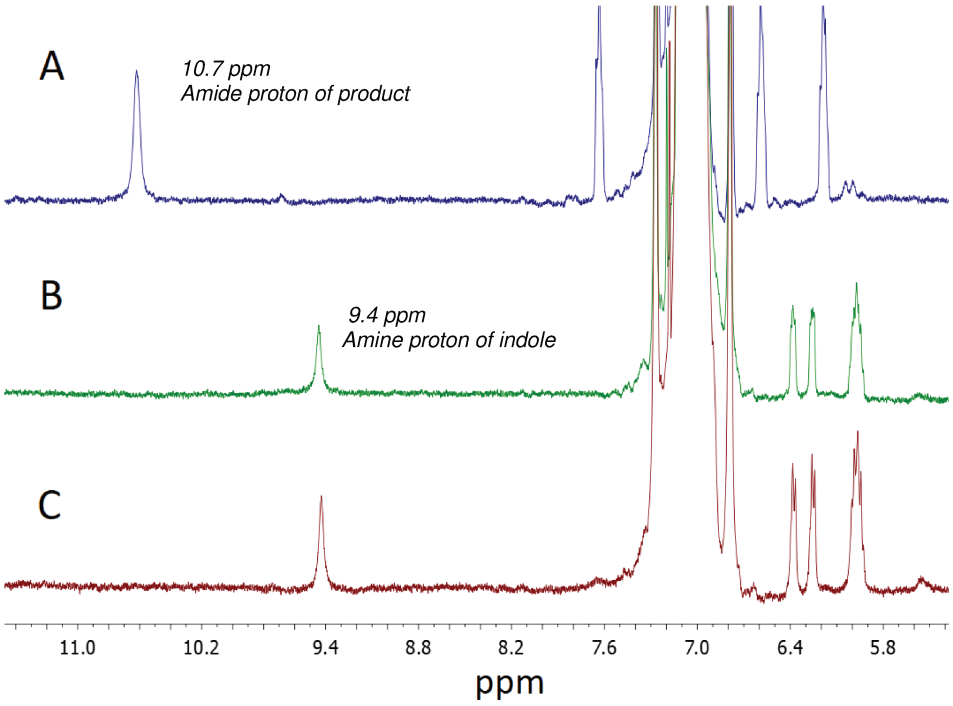

Figure 5.3 A: ^{1}H-NMR spectra of the synthesized N-2-(methylphenylacetamide) in a solution of 4:2 DMF/$CDCl_3$. B: ^{1}H-NMR spectra of air saturated solution of Fe(TPP)Cl with 2,3-dimethylindole in presence of 0.1 M $TBAPF_6$ after electrolysis at -0.2 V vs SCE for 1h. C: Before electrolysis. For C and B 0.2 mL $CDCl_3$ were added in 0.4 mL of sample in DMF.

We then decided to study the impact of the solvent, and thus performed experiments in DCM instead of DMF. DCM is *a priori* a better solvent to perform oxidation reactions, because it is more difficult to oxidize than DMF. In DCM, The Fe^{III}/Fe^{II} wave is quasi reversible under Ar and becomes completely irreversible under O_2 (Figure 5.2 C), as it is the case in DMF, while the addition of 2,3-dimethylimidazole has a little effect on the CV response. The Fe^{III}/Fe^{II} reduction potential is lower in DCM compared to DMF (-0.39 and -0.25 V vs SCE), probably due to coordination phenomena as discussed in paragraph 2.3. Electrolyses in DCM were performed at -0.4 V v s SCE (at the Fe^{III}/Fe^{II} peak) for one hour. NMR analysis of a sample collected before and a sample collected after the controlled-potential electrolysis. The expected product was detected in the post-electrolysis sample. However, the same quantity of product was detected in the sample collected before electrolysis. Furthermore, the μ-oxo dimer was again observed at the end of the electrolysis. Experiments with Fe(TMP)Cl led to similar results.

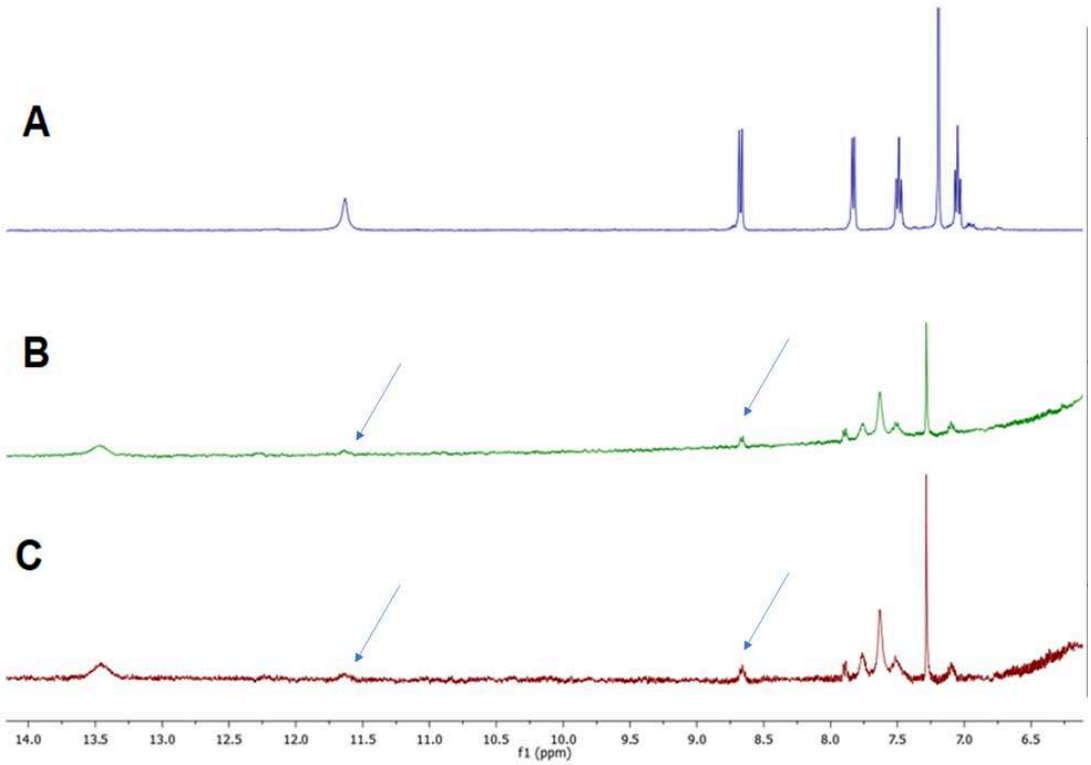

Figure 5.4: A: solution of the synthesized product N-2-(methylphenylacetamide) in 0.1 mL $CDCl_3$ in with 0.5 mL of DCM B: ^{1}H-NMR spectra of air saturated solution of Fe(TPP)Cl with 2,3-dimethylindole in presence of 0.1 M $TBAPF_6$ after1h electrolysis at -0.35 V vs SCE. C: before electrolysis. For C and B 0.1 mL $CDCl_3$ is added in 0.5 mL of sample in DCM.

In order to further examine the reasons for this observation, we performed several blank experiments directly inside NMR tubes using CD_2Cl_2 as solvent. In an air saturated solution of 2,3-dimethylindole and in absence of porphyrin in CD_2Cl_2, the aromatic peaks show clear changes (Figure 5.5 D and E) suggesting that the compound under these conditions is being chemically transformed. Moreover, in the presence of Fe^{III}(TPP)Cl, whether the solution was air or Ar saturated, the N-2-(methylphenylacetamide) was spontaneously formed.

We also suspected that the reaction could proceed photochemically. However, NMR spectrum of a tube with sample kept in the dark, also showed presence of the N-2-(methylphenylacetamide) thus invalidating our hypothesis. These observations show that DCM is not appropriate for this study, at least as far as 2,3-dimethylindole is concerned.

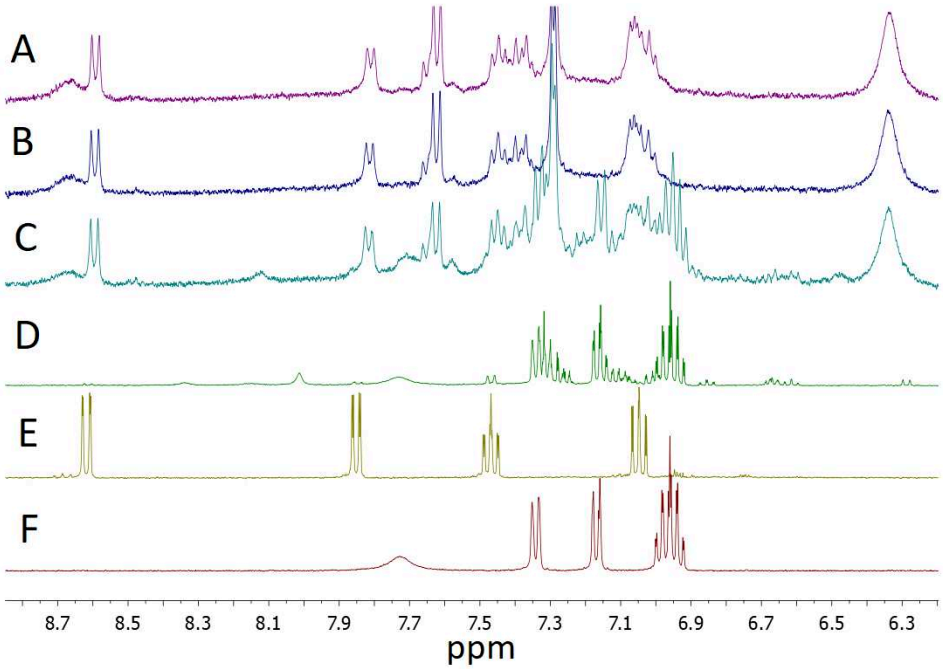

Figure 5.5: Different ^{1}H-NMR spectra recorded in CD_2Cl_2. A: Air saturated solution of 2,3-dimethylindole in presence of Fe(TPP)Cl after 48 h in light. B: Air saturated solution of 2,3-dimethylindole in presence of Fe(TPP)Cl after 48 h in dark. C: Argon saturated solution of 2,3-dimethylindole in presence of Fe(TPP)Cl after 48 h. D: air saturated solution of substrate 2,3-dimethylindole after 48 h. E: Fresh solution of product N-2-(methylphenylacetamide) F: Fresh solution of substrate 2,3-dimethylindole.

Moreover, the $Fe^{III}(F_{20}TPP)Cl$ has been also considered because it is sterically hindered and the corresponding superoxo is reactive in DCM/THF mixtures at 213 K as reported by Wijeratne. However, in our conditions (DMF as solvent, at 293 K) the reaction between Fe^{II} and O_2 in DMF is not thermodynamically favored, as suggested by the low binding constant KO_2 (see Chapter 4), the difficulties in accumulating the species at low temperature (see Chapter 2), and the very slight difference between the CVs under Ar and under O_2 in the Fe^{III}/Fe^{II} level (see Figure 5.6). Thus, we have not performed any electrolysis with the $Fe(F_{20}TPP)$ yet. It is more convenient from an electrochemical point of view, to first find appropriate conditions for the Fe(TPP) complex and then try the $Fe(F_{20}TPP)$.

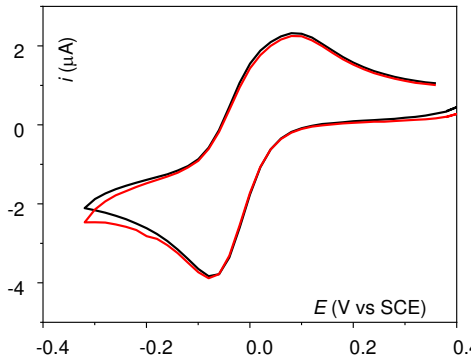

Figure 5.6: 0.5 mM solution of $Fe^{III}(F_{20}TPP)Cl$ in DMF, under Ar (black), and under O_2 (1 mM) (red trace) with 0.1 M $TBAPF_6$. Scan rate is 0.1 V s^{-1} at a GC disk electrode (0.07 cm^2), T = 293 K.

In conclusion, so far, it has not been possible to collect evidence for dioxygenase activity of the Fe superoxide under electrochemical conditions using Fe(TPP) or Fe(TMP). In DMF, no di-oxygenated products of 2,3-dimethylindiole were observed, while in DCM the substrate is oxidized spontaneously, so evaluation of the electrochemical reactivity of these Fe porphyrins was not possible. Importantly, in both cases, formation of the μ-oxo dimer was observed at the end of the electrolysis.

In order to address the problem of the stability of the substrate in DCM, other solvents or solvent mixtures can be tried out, for example DCM/THF mixtures, as in the work of Wijeratne group.[54] In that case, detailed CV studies in this solvent mixture has to be carried out first. Another option would be to use a less reactive substrate such as the 3-methylindole.

In the author's opinion, a major issue that we need to address is the formation of μ-oxo dimer during electrolysis that prevents multiple turnovers. To overcome this issue, we may try firstly to use axial ligands that can impede the dimer formation such as imidazoles and thiols, and secondly Fe porphyrins the structure of which could completely prevent this pathway, such as basket porphyrins.[170] Heterogenization of the Fe porphyrins could also efficiently impede the dimer formation (see paragraph 6.2.1 for further discussion).

5.2 Cyt-P450 type reactivity of Fe porphyrins in presence of Brønsted-Lowry acids

As shown in the Chapter Chapter 3, the Fe superoxo and Fe peroxo species (that are generated after reaction of the Fe porphyrin with O_2 in organic solvents such as DMF), react with protic acids, leading to the breaking of the O-O bond and the generation of high valent species. As discusses in Chapters Chapter 1 and Chapter 3, previous studies have demonstrated that in acidic organic solution at reductive potentials, Fe porphyrins catalyze preferentially the four electrons-four protons reduction of O_2 to H_2O.[129] We hypothesized however, that in the presence of an oxidizable (nucleophilic) organic substrate, this reactivity could be switched from Cyt-c-oxidase type to Cyt-P450 type, as shown in Scheme 5.3.

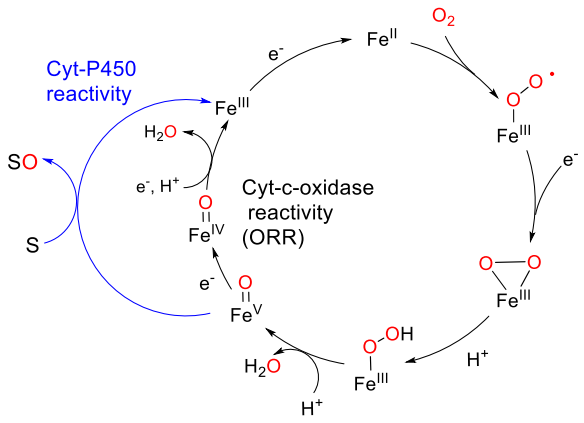

Scheme 5.3 O_2 activation by Fe porphyrins can lead either to ORR or to Oxidation of substrates.

We began our study with Fe(F_{20}TPP)Cl since it was the first porphyrin we used in a Fe/O_2/H^+ system, and because the corresponding Fe-oxo high valent species are powerful oxidants as demonstrated by their high oxidation potential.[26] As an acid we used $HClO_4$, that is a strong and fully dissociated acid in organic solvents.[129] Figure 5.7 (blue trace) shows representative cyclic voltammograms of solutions of the Fe(F_{20}TPP)Cl in three different organic solvents, DMF, ACN and DCM.

In all three solvents used, we observe reversible Fe^{III}/Fe^{II} redox waves with $E^{p}_{Fe^{III}/Fe^{II}}$ of -0.06 V, -0.04 V, and -0.23 V vs SCE, in DMF, ACN and DCM respectively. In presence of O_2 the Fe^{III}/Fe^{II} redox wave changes. In DMF, the apparition of a second

reduction wave occurs after the Fe^{III}/Fe^{II} reduction, and corresponds to the reduction of Fe superoxo to Fe peroxo, as shown in Chapter Chapter 2. In ACN a similar behavior is observed. In DCM no such wave is observed as discussed in paragraph 2.3.2.

Addition of acid, in all three cases, induces the apparition of a catalytic current that is stronger at more reductive potentials. The catalytic current is higher in ACN and DCM compared to DMF, an observation which can be in part attributed to the higher solubility of O_2 in ACN and DCM (2.7 mM of O_2 in DCM, 2 mM in ACN and 1 mM in DMF).[138]

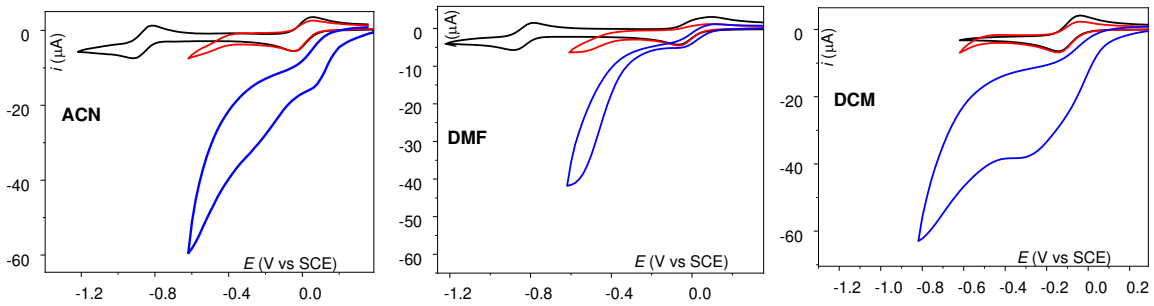

Figure 5.7: CVs at glassy carbon disk electrode (0.07 cm^2) of 0.5 mM solution of $Fe^{III}(F_{20}TPP)Cl$ in DMF with $TBAPF_6$ (0.1 M), v = 0.1 V s^{-1}, T = 298 K; under argon (black trace), under O_2 (air saturated, 1 mM) (red trace) and under O_2 with 10 mM $HClO_4$ (blue trace). A: in DMF, B: in ACN C: in DCM.

We first used styrene for our experiment because it is a typical substrate that is used for oxygenation reactions,[126] with most common products styrene oxide and benzaldehyde (Scheme 5.4). We analyze the electrolyzed samples as describes in Annex 1 (paragraphs 7.1.2 and 7.1.6)

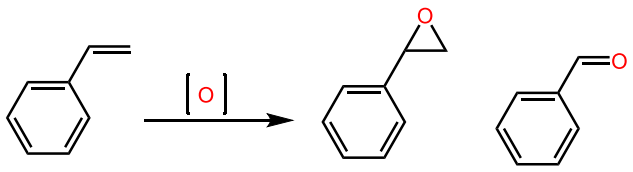

Scheme 5.4 Styrene, and two possible oxygenation products, styrene epoxide and benzaldehyde.

After addition of the acid in the air saturated porphyrin solutions, 20 equivalents of styrene were added to the solution and electrolysis were performed. For every electrolysis three samples were collected, one before electrolysis, on after 20 min of electrolysis at -0.05 V vs SCE (Fe^{III}/Fe^{II} wave) and one after electrolysis at -0.5 V vs SCE (Fe superoxo/Fe peroxo wave).

Unfortunately, GC/MS analysis of the post electrolysis samples in ACN and DCM, showed that oxidation products did not occurs. In DMF, the styrene epoxide was detected in small amounts in the sample before and after electrolysis, suggesting that it was not formed electrochemically. We did not however perform quantitative analysis to confirm this result. The results of the three electrolyses corresponding to Figure 5.7 are presented in Table 5.1 (entries 1-3).

In view of these results, we performed experiments using different substrates namely cyclooctene and cyclohexene in DMF in the same conditions as for styrene oxide. Unfortunately, with those substrates, no oxidation product was observed by GC/MS.

We then changed the proton source and we increased the time of the electrolysis in order to eventually accumulate more oxygenation product. We used perfluoro-tert-butanol ($(CF_3)_3COH$) which is a weaker protic acid than $HClO_4$, and cyclooctene as substrate, but no oxidation product was observed either in DCM. Using the [Fe(F_{20}TPP) /O_2 /$(CF_3)_3COH$/cyclooctene] system, we also performed electrolysis in presence of 1-methylimidazole that can axially coordinate to the metal center and has previously been implemented in chemically driven systems for oxidations with Fe porphyrins.[171] However, no improvement was observed. We then tried benzoic anhydride as a Lewis acid instead of using a proton source in the [Fe(F_{20}TPP)/O_2/cyclooctene system], but no oxidation products were observed either.

The use of Fe(TPP) instead of Fe(F_{20}TPP) in the [catalyst/ O_2/cyclooctene/benzoic anhydride] system did not improve the catalysis either. Table 5.1 gathers all the experimental conditions that were tested and which did not lead formation of products that could be detected by GC/MS. Longer times of electrolysis did not seem to have any effect either.

The data reported Table 5.1, although not including all the possible combination of parameters, suggest that Fe porphyrins might not be appropriate catalyst for implementing this type of reactivity.

Table 5.1 Electrolysis conditions with Fe porphyrin for substrate oxygenation

Entry	Solvent	Catalyst	Acid	Susbtrate	E(V) vs SCE	Time	Comments
1	**DMF**	**Fe(TPPF$_{20}$)Cl**	$HClO_4$ 10 eq.	**Styrene 20 eq**	-0.05 -0.5	30 min 30 min	--
2	**ACN**	**Fe(TPPF$_{20}$)Cl**	$HClO_4$ 10 eq	**Styrene 20 eq**	-0.05 -0.5	30 min 30 min	--
3	**DCM**	**Fe(TPPF$_{20}$)Cl**	$HClO_4$ 10 eq	**Styrene 20 eq**	-0.05 -0.5	30 min 30 min	--
4	**DMF**	**Fe(TPPF$_{20}$)Cl**	$HClO_4$ 10 eq.	**Cyclooctene 20 eq**	-0.05 -0.5	30 min 30 min	--
5	**DCM**	**Fe(TPPF$_{20}$)Cl**	$(CF_3)_3COH$ 100 eq.	**Cyclooctene 20 eq**	-0.5	4 h	--
6	**DCM**	**Fe(TPPF$_{20}$)Cl**	$(CF_3)_3COH$ 100 eq.	**Cyclooctene 20 eq**	-0.5	4 h	+ 10 eq of 1-MeIm
7	**DCM**	**Fe(TPPF$_{20}$)Cl**	Benzoic anhydride 100 eq.	**Cyclooctene 20 eq**	-0.5	4 h	--
8	**DCM**	**Fe(TPP)Cl**	Benzoic anhydride 100 eq.	**Cyclooctene 20 eq**	-0.5	4 h	--
9	**DCM**	**Fe(TPP)Cl**	Benzoic anhydride 100 eq.	**Cyclooctene 20 eq**	-0.5	4 h	+ 10 eq of 1-MeIm

The starting solution was 5 mL of solvent with 0.1 $TBAPF_6$, 0.5 mM of porphyrin. SCE was used as reference electrode, platinum as counter and glassy carbon as working (1.6 cm^2 surface). All experiments were performed in RT in a constant flux of air.

Although no oxidation products have been detected by GC/MS, catalytic currents have been observed, that are absent when one of the system's component is missing (O_2, protons, or catalyst). Based on previous literature reports and our discussion in Chapter Chapter 2,[129] we propose that the current that passes during the electrolysis is due to the ORR.

A plausible explanation for the fact that no oxygenation reactivity has been observed with the Fe porphyrins, would be that the kinetics of the ORR are too fast, and that the four electron-four proton reduction of O_2 to H_2O is favored in all cases: indeed Mayer et al. have shown that Fe porphyrins catalyze the ORR in air saturated organic solutions even in presence of weaker acids than $HClO_4$.[128,75]

Possible alternatives that will be tried out in the near future include:

- The use of a very reactive substrate that would react fast with the high valent species of the catalytic cycle, such as phosphines.
- The use of metal cations as Lewis acids instead of protons. In a recent example by Que et al.,[172] a non-heme Fe^{III} peroxo complex reacts with Sc^{3+} leading to the formation of a $Fe^{IV}(O)$ (see paragraph 6.2.2)

In the following paragraph 5.3 we examine potential halogenase-type reactivity of Fe porphyrins.

5.3 Halogenase-type reactivity of Fe porphyrins

As discussed in the introduction, several example of haloperoxidases have been developed during the last decade, using Fe and Mn porphyrins. In particular, Fujii et al. have demonstrated that reaction of a chemically prepared $Fe^{IV}(O)$ π radical cation at 190 K with substrates such as anisole and cyclohexene, in presence of chloride anions, led to chlorination of these substrates with moderate yields (around 10% with respect to the porphyrin, that is TON=0.1).[95] They later generated and characterized Fe^{III} porphyrin hypochlorite by addition of TBAClO in a $Fe^{III}OH$, that was also reactive towards oxidation and chlorination of simple substrates.[97] Importantly, based on the observation of a Fe^{III} meso-chloro-isoporphyrin as the active chlorination agent under certain conditions (see paragraph 1.4.5), they developed a catalytic system where an aqueous solution of hydrogen peroxide is vigorously stirred with a mixture of $Fe^{III}(F_{20}TPP)Cl$, triflic acid, chloride, and 1,3,5-trimethoxybenzene as substrate in DCM at room temperature, with a TON= 85.[98]

In view of these results, we wanted to examine whether chlorination reaction catalyzed by Fe porphyrins could be carried out in our electrochemical conditions. We have chosen as first substrate thymol, (2-isopropyl-5-methylphenol), inspired by a recent study where it has been chlorinated by an enzymatic system.[173]

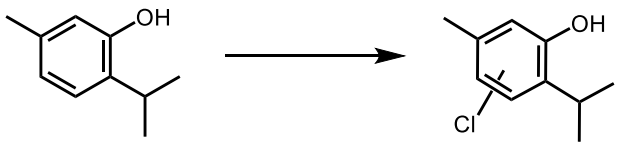

Scheme 5.5 Thymol and its chlorinated product.

Figure 5.8 displays representative CVs of $Fe(F_{20}TPP)Cl$ in air saturated ACN. Under Ar a quasi-reversible Fe^{III}/Fe^{II} wave is observed. As already discussed, under O_2 the Fe^{II}/Fe^{III} reoxidation wave slightly decreases due to the reaction of Fe^{II} with O_2. In presence of O_2 and DMFHTfO a catalytic current is observed. DMFHTfO is a strong acid and fully dissociated in DMF, like $HClO_4$.[129] It is highly hygroscopic crystalline

solid but if properly conserved contains no water, in contrast with $HClO_4$ that is received as a 70% solution in water.

Addition of an excess of TBACl to an air saturated solution of Fe(F_{20}TPP)Cl containing protons, leads to an increase of the catalytic current, while the $E_{cat}^{p/2}$ of the catalytic peak shifts to more negative potentials. We hypothesize that the cause for these changes, is the coordination of the chloride in the axial position, based on the change of the Fe^{III}/Fe^{II} reduction potential induced by the presence of chloride (see Chapter Chapter 3).

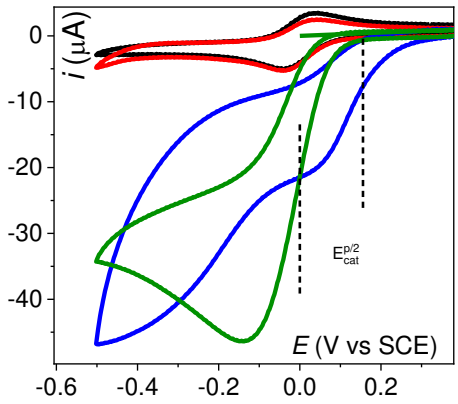

Figure 5.8 CVs of 0.5 mM of Fe(F_{20}TPP)Cl in ACN with $TBAPF_6$, under Ar (black trace), and in air saturated solution (red trace), with 5 mM of DMFHTfO added (blue trace), and with both 5 mM of DMFHTfO and 5 mM of TBACl (green trace), at a 0.07 cm^2 GC electrode at 100 mV s^{-1}.

Preparative electrolyses were then performed in presence of thymol in air saturated solutions of Fe(F_{20}TPP)Cl in organic solvents in presence of an acid and chloride by applying a potential near the Fe^{III}/Fe^{II} wave (usually at -50 mV vs SCE), typically for 1 h. Samples were collected before and after electrolysis and analyzed by GC/MS. Interestingly, in several experiments chlorothymol was observed. Its concentration in the samples was calculated using calibration curves (see Annex 1, paragraph 7.1.6) where n-octanol was used as internal standard.

Various conditions have been tried out in order to improve the yield, some of which are displayed in Table 5.2. The best yield was obtained in an electrolysis performed in ACN, in presence of 10 eq TBACl as chloride source and DMFHTfO as proton source. We have observed that the reaction yield was clearly improved in ACN compared to DMF, probably due to the fact that DMF is more prone to oxidation itself, and can thus be oxidized at the expense of the substrate. Excess of chloride did not improve the yield.

On the other hand, the acid seems also to affect the yield significantly, although both $HClO_4$ and DMFHTfO are strong acids and completely dissociated in ACN and DMF, while it seems rather improbable that the water content of the $HClO_4$ is responsible for the observed difference. Unfortunately, tests with other substrates namely trimethoxy-benzene, toluene, cyclohexene, cyclooctene and anisole were not fruitful.

Table 5.2 Chlorination of thymol.

Entry	Solvent	Acid	Chloride Source	Conversion to chlorothymol after 0h30
1	DMF	$HClO_4$ 10 eq.	TBACl 10 eq.	Detected, less than 0,1 %
2	AcN	DMFHTfO 10 eq	TBACl 10 eq.	0,8%
3	AcN	$HClO_4$ 10 eq.	TBACl 10 eq.	0,4%
4	AcN	DMFHTfO 10 eq	TBACl 50 eq.	Not detected
5	AcN	DMFHTfO 50 eq	TBACl 50 eq.	*Detected, less than 0,1 %

The starting solution was 5 mL of solvent with 0.1 $TBAPF_6$, 0.5 mM of $Fe(F_{20}TPP)Cl$. The applied potential for all the electrolyses was -0.05V. SCE was used as reference, platinum as counter and glassy carbon as working (1.6 cm^2 surface). All experiments were performed in RT. Concentration of thymol was 10 mM.

The maximum TON, where TON=mole of product/mol of catalyst, obtained was 0.16, close to what Fujii et al. reported for the chemically driven reaction for similar substrates in his first report,[95] but are far from the TON=85 that he obtained in his catalytic system.[98]

Fe(TMP)Cl was also used as catalyst in the same reaction conditions as entry 2 of Table 5.2. However, chlorothymol was not observed. The absence of product with this catalyst can be rationalized as follows. Fujii has previously proposed that during halogenation reactions promoted by Fe-oxo species, chloride is oxidized by these species and results in the chlorinating agent of the reaction. Reaction between chloride and $Fe^{IV}(O)\pi$ radical cation necessitates that the latter's $Fe^{IV}(O)$/ $Fe^{IV}(O)\pi$ radical cation reduction potential is high enough. It is not the case for Fe(TMP)Cl but it is the case for Fe porphyrins with electron withdrawing groups, such as $Fe(F_{20}TPP)Cl$.[96]

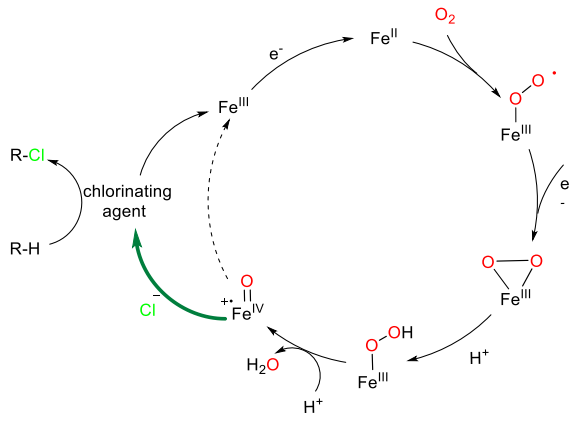

Scheme 5.6: A simple mechanistic pathway proposed for the chlorination induced be O_2 reductive activation by Fe porphyrins. Bold green arrow corresponds to the reaction of the high valent species with Cl^-.

Electrochemical chlorination of thymol with a Fe(F_{20}TPP)Cl is to the best of our knowledge reported in this manuscript for the first time. The main drawbacks of the is [Fe(F_{20}TPP)Cl /O_2/H^+/Cl^-] electro-catalytic system, that need to be overcome is that reaction was not catalytic (TON = 0.16) and a series of substrates were not reactive.

At this point we considered changing the metal of our catalyst, and examined a manganese porphyrin, as we detail in the next paragraph.

5.4 Cyt-P450 type and halogenase-type reactivities of a Manganese porphyrin

We will now discuss the reactivity studies with Mn(TPP) as the catalyst. This complex has been previously been implemented for electrochemical oxidation studies by Murray,[120] and for chemically driven halogenation studies by Groves.[116]

Figure 5.9 C, displays the cyclic voltammogram of a DCM solution of Mn(TPP) under Ar (black dotted trace), under O_2 (air saturated, red trace). As shown in paragraph 2.4, under Ar the a reversible Mn^{II}/Mn^{III} redox wave is present, while in presence of oxygen the wave loses its reversibility because $Mn^{II}(OO^{\bullet})$ species is generated throughout an ECE mechanism.

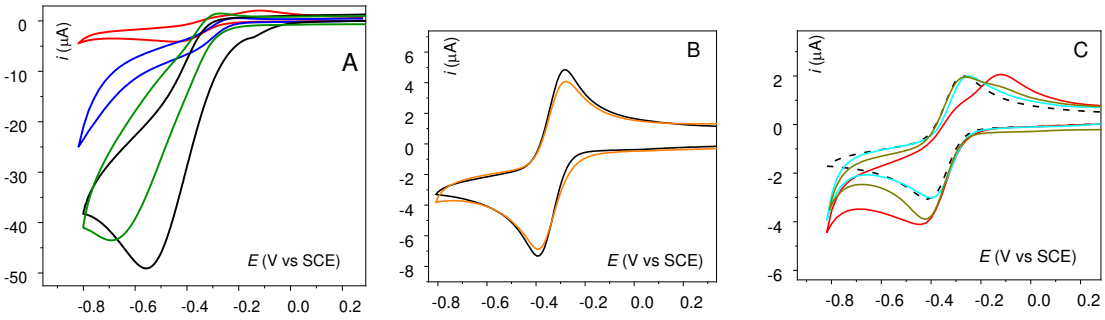

Figure 5.9: A: CVs of DCM solution of 0.5 mM Mn(TPP)Cl with 0.1 M $TBAPF_6$ on a GC electrode with 440 mM benzoic anhydride, (black trace) and with addition of 20 mM 1-MeIm (blue trace) or with 5 mM TBACl (green trace). CV of air saturated solution without benzoic anhydride is given for comparison (red trace). B: Under Ar without (black trace) and with 440 mM of anhydride (orange trace). C: Under Ar (dotted trace), under O_2 (blue trace), under O_2 after addition of 20 mM of 1-MeIm (red trace) or 5 mM of TBACl (green trace). All CVs were recorded at 293 K.

Figure 5.9 C also shows the CVs of air saturated DCM solution of Mn(TPP)Cl in presence of 1-methylimidazole (cyan trace), or in presence of chloride (dark yellow trace). In both cases we observe a decrease of the current intensity after addition of the axial ligand compared to the air saturated solution without axial ligand, and a partial recovery of the reversibility of the wave. We propose that this observation is due to the occupation of the axial position by the exogeneous ligands, that competes with O_2 binding, therefore impeding the ECE mechanism. *Why these axial ligands?* 1-methylimidazole is an axial base often considered in such systems (metal porphyrins oxidation reactions) because of its similarity with histidine proximal site in certain O_2 activating enzymes,[9] while chloride is often the chlorine atom source in chlorination reactions.[98]

Figure 5.9 A shows CVs of Mn(TPP)Cl in presence of benzoic anhydride. The addition of benzoic anhydride in air saturated solution causes an increase of the current, suggesting a catalytic activity that occurs at the onset of the Mn^{III}/Mn^{II} redox wave. At this stage we hypothesize that benzoic anhydride can react with the $Mn^{II}(OO^{\bullet})$ and triggers the catalytic cycle of the Scheme 5.7. This reaction presumably leads to the transient generation of a Mn^{III}-acyleperoxo intermediate, the O-O bond of which is cleaved to give a high valent $Mn^{V}(O)$. The latter can either react with a nucleophile or get reduced on the electrode surface, resulting in both cases to the regeneration of the Mn^{III} species (see Scheme 5.7) and thus to a catalytic current response. To corroborate

this proposition, Figure 5.9 B shows CVs under argon in presence and absence of benzoic anhydride, that show that Mn^{II} does not react with the anhydride.

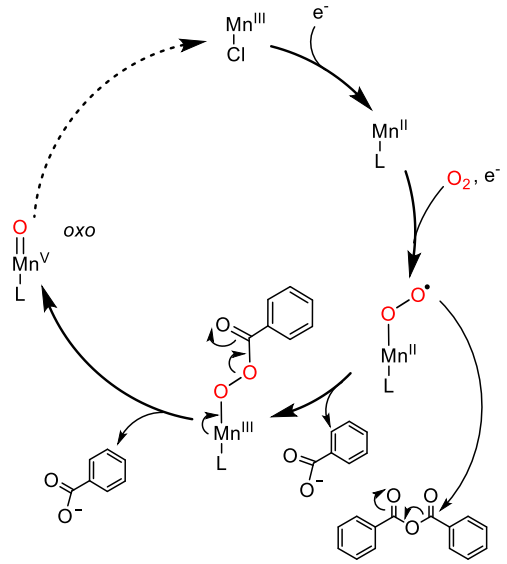

Scheme 5.7: Catalytic cycle for O_2 activation by Mn porphyrins in presence of anhydride.

Figure 5.9 A also shows that addition of an exogenous ligand, 1-methylimidazole or chloride, modifies the catalytic response in air saturated Mn(TPP)Cl solutions in presence of anhydride. Both axial ligands induce a decrease of the catalytic current, presumably due to the competition with O_2 for the axial positions of the metal center.

Given that catalytic currents have been observed, and since the catalysis takes place presumable *via* an O-O bond cleavage and a transient generation of high valent O species, we performed electrolyses in presence of cyclooctene. Preparative scale electrolysis was first performed in air saturated DCM solution of Mn(TPP) at 293 K with an E_{app} = -0.45 V vs SCE, in presence of benzoic anhydride (440 mM), and 1-methylimidazole (20 mM), with cyclooctene as substrate (10 mM). We performed the first essays in presence of 1-methylimidazole because it axially coordinate to the metal center and has previously been implemented in chemically driven systems for oxidations with Fe porphyrins.[171]

The 4 hours electrolysis (entry 1, Table 5.2), lead to the formation of cyclooctene oxide that has been detected by GC/MS with a TON of *ca.* 7.3. The product was quantified by a calibration curved in which anisole was used as the internal standard. This result corroborates the report of Murray et al. who worked under similar conditions.[120] They

obtained a TON=11 working in O_2 and not air saturated DCM solutions, and in presence of 100 mM of substrate.

The faradaic yield (or faradaic efficiency, F.E.) is given by the fraction of the number of electrons used for the oxidation of cyclooctene epoxide (2 electrons per molecule if the $Mn^{V}(O)$ is the oxidant, see Scheme 5.7) over the total charge passed, calculated by integrating the current versus time plot. The faradaic yield of the reaction in this case was 81%. We note here that electrolysis in DMF did not give any products as expected by the fact that Mn^{II} in DMF does not even bind to O_2 as shown in chapter 2.4, while in ACN the TON was quite lower (*ca.* 2) compared to DCM. [k]

Table 5.3 Electrochemical Chlorination – Oxidation of cyclooctene by Mn(TPP)

Entry	Solvent	1-MeIm	TBACl	cyclooctene-oxide	chlorocyclooctene
0	DCM			traces	Not detected
1	DCM	20 mM	-	TON=7.3 F.E.= 81%	Not detected
2	DCM	20 mM	5 mM	TON=7.1	Not detected
3	DCM	-	5 mM	traces	TON=4.8 F.E.=53%
4	DCM	-	40 mM	traces	TON=1.6
5	CAN	20 mM	-	TON=2	Not detected

Preparative scale electrolyses were performed at 293 K under O_2. Conditions: 0.5 mM Mn(TPP)Cl, 10 mM cyclooctene and 440 mM benzoic anhydride with 0.1 M $TBAPF_6$, at E_{app} = -0.45 V vs SCE for 4h. TON = mole of product / mole of catalyst

Inspired by the recent work by Groves et al. reporting on substrate halogenation catalyzed by Mn(TPP) using NaOCl as oxidant,[116] we examined the electrochemical chlorination of cyclooctene. Addition of chloride in the CVs of air saturated DCM solution of Mn(TPP), in presence of benzoic anhydride, showed a small decrease of the catalytic current, and a shift of the potential as expected (see Figure 5.9). We performed electrolysis in presence of 10 equivalents of TBACl instead of 1-methylimidazole. In the resulting solution, after 4 h electrolysis, we detected chlorocyclooctene with a TON of *ca.* 4.8, and a faradaic yield of 53% (Table 5.2 entry 3). Since the product was not commercially available, we used the same calibration curve as for cyclooctene oxide. Table 5.2 shows the results of electrolysis under different conditions. Higher concentration of TBACl did not lead to higher yields, on the contrary the TON was 1.6 in that case (Table 5.2 entry 4). A possible explanation is the competition for the axial

[k] Cyclic voltammetry in ACN closely resembles the characteristics of the DCM experiments.

position of Mn between O_2 and chloride that favors chloride with higher concentrations of TBACl. Importantly we note here, that when imidazole is present, oxygenation of olefin occurs and no chlorination even if chloride anions are present as well, in accordance with previous observations in chemically driven systems.[116]

We note here, that bromination of cyclooctene have also been tried out in presence of bromide anions, but have not been fruitful yet.

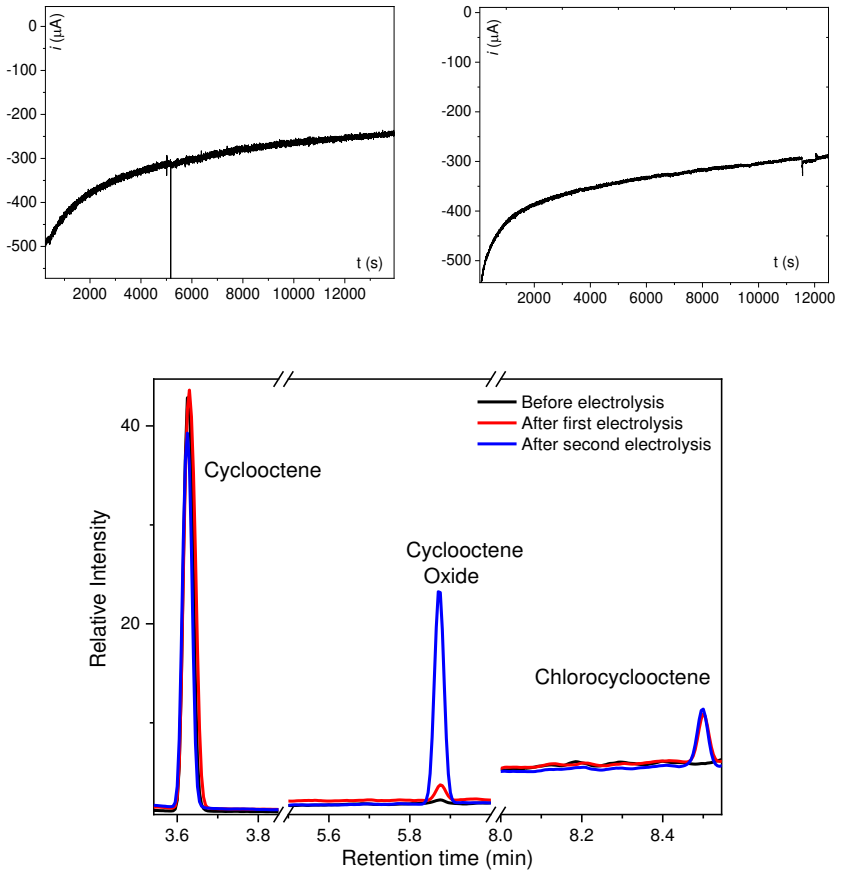

Figure 5.10: (Top) i(μA) vs t(s) plot of electrolysis at 293 K of an air saturated DCM solution with 0.5 mM of :Mn(TPP)Cl, 0.1 M TBAPF$_6$ and 0.44 M of anhydride (Top Left): with 40 mM of 1-MeIm (faradaic efficiency for cyclooctene oxide 81%). (Top, right) with 5 mM of TBACl with E_{app} = -0.45 V for 4 hours (faradaic efficiency for cyclooctene chloride 53%). (Bottom) Preparative scale at. E_{app} = -0.45 V for 4 hours. Chromatograms before electrolysis: black trace, after: red trace and after second electrolysis of the same solution for 12 hours after addition of 20 mM of 1-MeIm: blue trace.

In Figure 5.10 we show a representative chromatogram, and current vs time plots of two characteristic experiments. The causes for the decrease of the current during the electrolysis has not been investigated in detail but the catalyst was intact (UV-Vis) and there was not any detectable species on the electrode after rinsing the electrode at the end of the electrolysis by copious amounts of solvent.

We have thus shown that oxidative transformation of cyclooctene is possible under electrocatalytic conditions at the Mn^{III}/Mn^{II} wave in DCM in presence of benzoic anhydride: when an excess of chloride is added the reaction is directed towards chlorination of the substrate, whereas cyclooctene-oxide is selectively formed when 1-

MeIm is used. We have now in hands a simple way to direct the reaction pathway from oxygenation to halogenation by simple swapping of the exogenous ligand. We also note here that the obtained TONs are around one order of magnitude lower than the ones reported by Groves for chlorination reactions for his system, where the oxidant is NaOCl.

To rationalize the fact that by changing the exogenous axial ligand from 1-methylimidazole to chloride, we can switch the reactivity of Mn(TPP) from oxygenation to halogenation of cyclooctene we propose a forked mechanistic pathway. This pathway diverges after the O-O bond cleavage that takes place in the Mn^{III}-acylperoxo intermediate. 1-methylimidazole ligand presumably promotes the oxo transfer between the $Mn^{V}(O)$ that occurs and the olefin, in the presence of excess chloride instead, the selectivity of the reaction changes towards halogenation of the substrate. A usually proposed but never spectroscopically observed intermediate that can play the role of the chlorinating agent is the Mn^{III}-OCl (manganic hypochlorite).[116-117] The modulation of the Mn(TPP)Cl reactivity in electrochemical conditions, by changing the exogeneous ligand is an original concept proposed in this manuscript and has been published in *Chemical Communications*, along with the spectroscopic characterization of the electrochemically generated $Mn^{II}(OO^{\bullet})$.

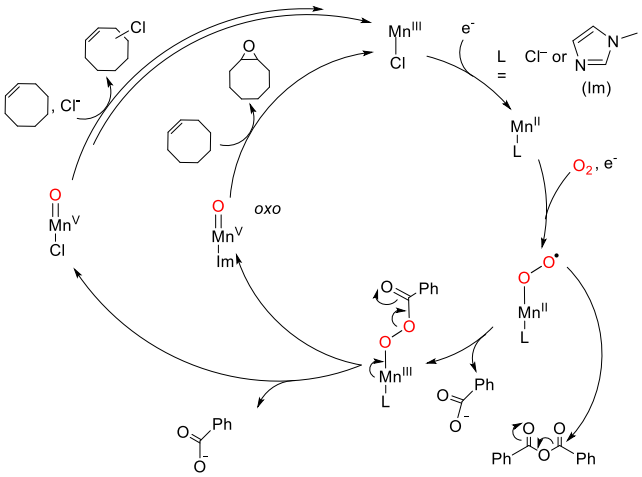

Scheme 5.8: Activation of O_2 catalyzed by Mn(TPP)Cl in DCM, in the presence of benzoic anhydride, and 1-MeIm or Cl^- leading to oxygenation or chlorination of cyclooctene, respectively

We then wanted to generalize our approach by testing systems with different acid and/or substrate. First, we showed that styrene can also be epoxidized at -0.6 V vs SCE using

otherwise the same conditions as for cyclooctene , with a TON of 14.3, and a F.E. of 62%. In presence of chloride instead of 1-methylimidazole, at the end of the electrolysis no chlorinated product was observed, and epoxidized product was generated in lower yield (see Table 5.4, entries 2 and 3).

Secondly, we demonstrate that we can catalytically oxidize cyclooctene at -0.45 V vs SCE in presence of a protic acid, instead of anhydride, namely perfluoro-tert-butanol, and otherwise the same conditions. The TON was equal to 3, two times less that with benzoic anhydride, and the F.E. equal to 80% similar to the F.E. obtained with benzoic anhydride (see Table 5.4, entries 1 and 4). Additionally, when the electrolysis was performed at -0.6 V vs SCE, we obtained a TON of 7.5, but a decreased F.E. of 36% (see Table 5.4, entries 4 and 5). The lower faradaic efficiency obtained when a more negative potential was applied suggest that other reactions could also take place, such as the direct reduction of O_2 at the electrode promoted by the H^+ of the acid.

Furthermore, chlorocyclooctene was observed in presence perfluoro-tert-butanol, and of chloride instead of 1-methylimidazole (see Table 5.4, entry 6), but in smaller quantities compared to the experiment with benzoic anhydride.

Styrene was also epoxidized with perfluoro-tert-butanol instead of benzoic anhydride, in presence of 1-methylimidazole. Interestingly when chloride was used as the exogenous ligand, benzaldehyde was observed as oxidation product of styrene, at the expense of styrene oxide (benzaldehyde/styrene epoxide ration was equal to 1/3, see Table 5.4, entry 8). This result will be further investigated, in the pursuit of a protocol that will allow the selective oxidation of styrene to benzaldehyde.

Table 5.4: Oxidation reactions of styrene and cyclooctene by Mn(TPP)Cl

Entry	Substrate	Solvent	Ligand	Acid	Epoxide	Second product	Potential
1	Cyclooctene	DCM	20 mM 1-MeIm	440 mM benzoic anhydride-	TON=7.3	---	-0.45 V
2	Styrene	DCM	20 mM 1-MeIm	-440 mM benzoic anhydride-	TON=14.3		-0.6 V
3	Styrene	DCM	5 mM TBACl	-440 mM benzoic anhydride-	TON=2.1		-0.6 V
4	Cyclooctene	DCM	20 mM 1-MeIm	50 mM perfluoro-tert-butanol	TON =3	---	-0.45 V
5	Cyclooctene	DCM	20 mM 1-MeIm	50 mM perfluoro-tert-butanol	TON =7.53	---	-0.6 V
6	Cyclooctene	DCM	5 mM TBACl	50 mM perfluoro-tert-butanol	Detected	Chlorocyclooctene Detected---	-0.6 V
7	Styrene	DCM	20 mM 1-MeIm	50 mM perfluoro-tert-butanol	TON =7.9	---	-0.6 V
8	Styrene	DCM	5 mM of TBACl	50 mM perfluoro-tert-butanol	TON =6	TON= 1.8 Benzaldehyde	-0.6 V

Preparative scale electrolyses were performed at 293 K under O_2. Conditions: 0.5 mM Mn(TPP)Cl, 10 mM substrate with 0.1 M $TBAPF_6$ for 4h.

It is quite interesting that a protic acid can promote the reductive activation of O_2 catalyzed by Mn(TPP), because it suggests the involvement of Mn^{III} hydroperoxo instead of a Mn^{III} acylperoxo, the former leading to a reactive high valent $Mn^{V}(O)$ in close resemblance to the Fe porphyrin pathway. In this case, protons play the role of the Lewis acid instead of C_6H_5-C^{+}=O. In addition, to the best of our knowledge, such reactivity in presence of a protic acid for Mn porphyrin or non-porphyrin complex has not previously been reported. In Scheme 5.9 we summarize the reactions that we have evidenced in the present paragraph.

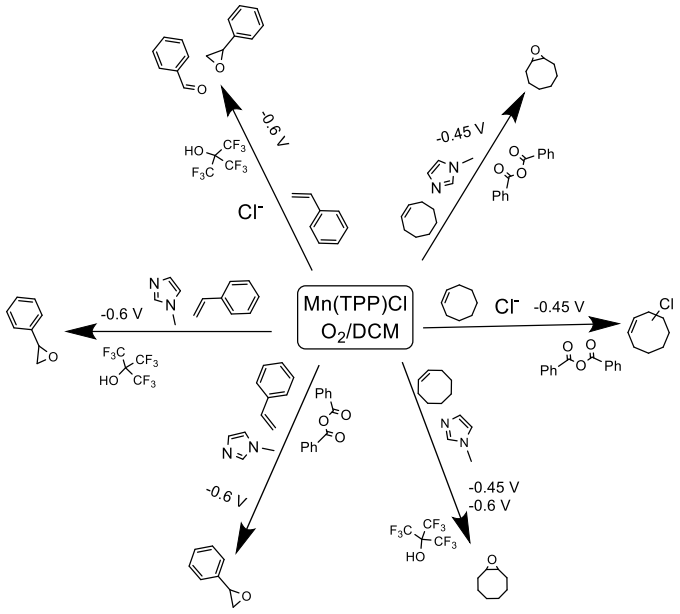

Scheme 5.9: Electrochemical reactions catalyzed by Mn(TPP)Cl.

5.5 Conclusion

In the present chapter we first explored the electrochemical reactivity of Fe porphyrins in air saturated solutions in absence of acid, at potentials where the $Fe^{III}(OO^{\bullet})$ species is generated, species which has been previously shown to be reactive towards indoles. We then studied potential electrochemical reactivity of Fe porphyrins in air saturated solutions, in presence of acid where high valent Fe-oxo species are transiently generated. However, in both of these cases, the results were not fruitful.

We then looked at the reactivity of Mn(TPP) with promising results, which have been the following: (i) Mn(TPP) catalyzes the electrocatalytic oxygenation or halogenation of cyclooctene in presence of benzoic anhydride, depending on the exogenous ligand: 1-methylimidazole promotes epoxidation while chloride promotes chlorination. (ii) Styrene was also oxidized to styrene oxide in presence of imidazole. (iii) Cyclooctene and styrene epoxides are also observed when benzoic anhydride is replaced by perfluoro-tert-butanol. (iv) In the presence of tert-butanol and chloride ions, the styrene is oxidized to epoxide and benzaldehyde in a ratio of 3:1. Moreover, thymol chlorination is also observed with $Fe(F_{20}TPP)Cl$ as catalyst in relatively low yields (TON=0.16).

The TONs obtained for the reactions catalyzed by Mn (TPP) are near 10, while in the literature for the reactions using chemical oxidants the TON is around TON = 100. However, in our approach we use oxygen from the air as oxidant and the necessary

electrons for the activation come from the electrode surface. There is for sure, plenty of modifications that can be tried out in order to increases the obtained yields or to explore new reactivities. In the next chapter (paragraph 6.2) the author proposes some ideas to do so.

Chapter 6

Perspectives

In the previous chapter, we were able to show that our electrochemical approach combining CV, SECM, UV-Vis SEC, and preparative scale electrolysis can shed light to O_2 activation by Fe and Mn porphyrins. Furthermore, we demonstrated that Mn(TPP) can catalyze the electrochemical aerobic epoxidation/chlorination reactions. We showed that characterization of intermediates offers an advantageous insight into the reaction mechanism that is indispensable for the understanding and optimization of the corresponding electrocatalytic species system for performing electrocatalytic reaction. Thus, two main directions are envisaged for the continuation of the present work. The first concerns the further development of the spectroelectrochemical approach. To this goal we have been working on making an operational cell, and conducted some preliminary experiments that we describe below. The second direction focus on the reactivity studies. We herein discuss the optimization of the electrocatalytic system that we developed with the Mn(TPP), the heterogenization of this system on electrode surfaces using carbon materials such as nanotubes, and some alternative reactivity pathways worth exploring.

6.1 Resonance Raman spectroelectrochemistry

Metalloporphyrin systems are well suited for Resonance Raman investigations due to their Soret bands that have a very high molar attenuation coefficient, up to 10^6 $L{\cdot}mol^{-1}{\cdot}cm^{-1}$, that is resonant with several symmetric ligand vibrations. The energy of these vibrations in some cases reflect the oxidation and spin states of the metals chelated by these ligands. In particular, the combination of the ν_4 (~1,330–1,375 cm^{-1}) and the ν_2 (~1,540– 1,575 cm^{-1}) ligand vibrations are widely used to diagnose the ground-state electronic structure of iron porphyrin complexes and enzyme active sites.[113, 174-175]

Our initial motivation to perform Resonance Raman experiments was to further characterize the $Fe^{IV}(O)$ that we observed during electrocatalytic O_2 reduction at -0.6 V vs SCE with the $Fe^{III}(F_{20}TPP)Cl$ (see paragraph 3.2). To determine whether this was *a priori* possible or not, we attempted to characterize the chemically prepared species by Resonance Raman Spectroscopy. The experiment has been carried out in an acetonitrile solution of the $Fe^{III}(F_{20}TPP)Cl$. In the solution of the initial $Fe^{III}Cl$ (black trace, Figure 6.1) the two marker bands were clearly observed in the Resonance Raman spectrum at 1336 and 1562 cm^{-1}. Then, excess of m-cpba has been added in the solution at room temperature. Several new features were then observed: importantly, the width of the

marker bands increases and they are slightly shifted to higher wavelengths. After linear subtraction of the two spectra, we can more clearly distinguish two new marker bands at 1377 and 1582 cm^{-1}, that are close to values previously reported on chemically prepared $Fe^{IV}(O)$ species of porphyrins with similar structures.[176] Additionally, a new peak appears at 830 cm^{-1}. We propose that this peak corresponds to the stretching of the Fe=O bond, based on the work of Kitagawa et al., who have reported a Fe=O stretching at 843 cm^{-1} for the $Fe^{IV}(TMP)(O)$ in toluene.[176] With this preliminary experiment, we were able to obtain the Resonance Raman signature of the $Fe^{IV}(F_{20}TPP)(O)$, which we can use to compare with future electrochemical experiments aiming to characterize this species *in situ* or *operando*.

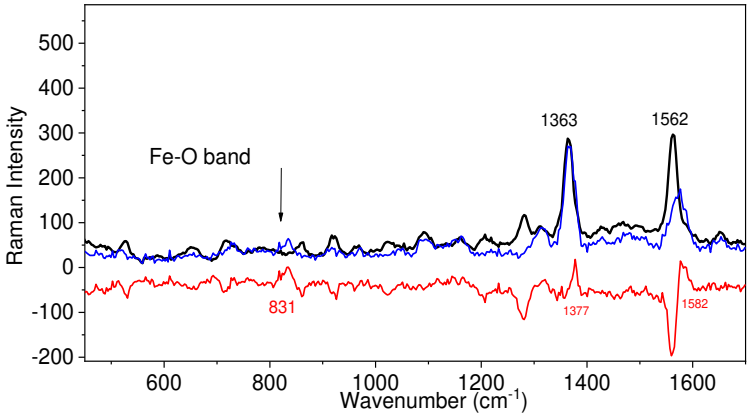

Figure 6.1: Resonance Raman spectrum of an acetonitrile solution of 0.1 M $TBAPF_6$ with 0.5 mM of 0.5 mM $Fe(F_{20}TPP)Cl$ (black trace). After addition of an excess of mcpba in the solution (red trace). Linear subtraction of the two spectra (red trace). Excitation radiation at 406 nm.

For spectroelectrochemical experiments an appropriate cell has been developed similar to the one used in UV-Vis spectroelectrochemistry (see Annex 1, paragraph 7.1.4 for details). It is made from quartz and contains four electrodes, a platinum counter electrode protected in a glass frit, an activated carbon reference, a thin glassy carbon disc electrode for recording CVs and a carbon paper electrode in the probed layer.

In a first spectroelectrochemical experiment, we start with an ACN solution of the $Fe^{III}(F_{20}TPP)Cl$. Figure 6.1 shows the RR (Resonance Raman) spectrum recorded on the initial $Fe^{III}Cl$ (black trace) solution, in the spectroelectrochemical cell. The two marker bands were clearly observed at 1362 and 1562 cm^{-1}. A potential of -0.3 V vs SCE has then been applied ot the solution under Ar. In the course of the experiment,

both marker bands shift slightly to lower wavelengths and become wider. Linear subtraction of the initial $Fe^{III}Cl$ spectrum from the spectrum obtained after applying -0.3 V for 2,5 min, leads to a spectra where two new marker band appear at 1342 and 1542 cm^{-1}. We proposed that these two new marker bands correspond to the electrogenerated Fe^{II} species. We observe a shift of 20 cm^{-1} towards lower wavelengths going from Fe^{III} and Fe^{II} species, which is in accordance with the report of Spiro et al. for Fe(TPP) solutions in DCM.[177]

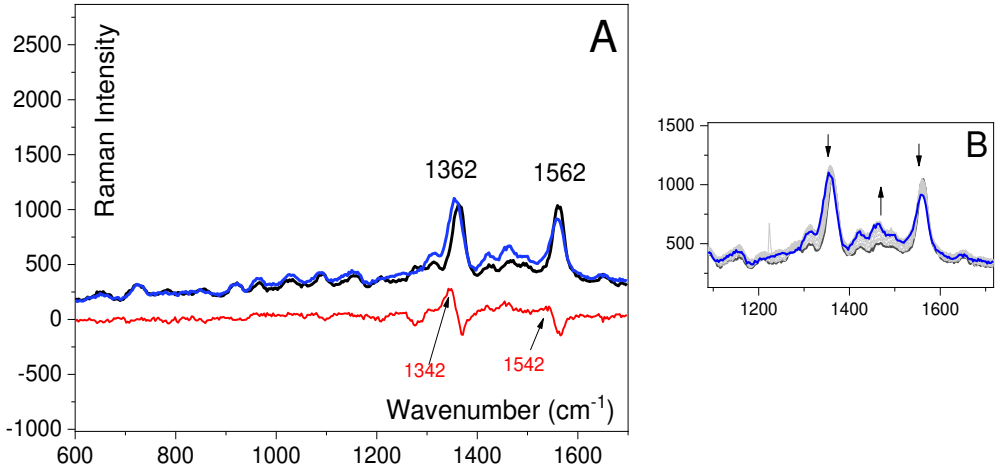

Figure 6.2: A: Resonance Raman spectrum of an acetonitrile solution of 0.1 M $TBAPF_6$ of 0.5 mM Fe(F_{20}TPP)Cl before (black), and after (blue trace) the application of -0.3 V vs SCE under Ar. Red trace represents the different of the before and after spectra. Excitation at 406 nm. B: Marker band region of the spectra recorded during the electrolysis (blue and black traces are identical with (A)).

The next steps that we will pursue after this characterization of the electrogenerated Fe^{II} are the following. First, we will *in situ* characterize the $Fe^{III}(OO^{\bullet})$ and , $Fe^{III}(OO^{-})$ of the Fe(F_{20}TPP) and Fe(TPP) in the appropriate conditions, as we already did by UV-Vis spectroelectrochemistry. Second, we will perform *operando* Resonance Raman spectroelectrochemistry experiments as the ones described in paragraph 3.2.2 aiming at obtaining the Resonance Raman spectrum of the electrochemically generated $Fe^{IV}(O)$. We may underline that to undoubtedly attribute bands to Fe-O or O-O bond, experiments with $^{18}O_2$ are needed.

We are convinced that Resonance Raman Spectroelectrochemistry can be of great interest. Indeed, it a very useful tool to characterize intermediate species generated

electrochemically, using information obtained by parallel UV-Vis experiments and literature reports.[113, 122, 125, 177] We may note that Resonance Raman Spectroelectrochemistry can also be used to characterize porphyrin complexes immobilized on electrode surfaces, provided that the loading allows a satisfactory signal to noise ratio.

Many efforts in the REACTE group of LEM are now directed towards the development of spectroelectrochemical techniques. Dr. Claudio Cometto, a previous PhD student, has successfully used IR spectroelectrochemistry for the characterization of intermediate species in the catalytic cycle of CO_2 reduction by a Co quaterpyridine.[178] Daniela Mendoza-Franzese, current PhD student at LEM, has been developing X-ray absorption spectroelectrochemistry for the characterization of intermediate species produced during CO_2 activation by Fe poprhyrins in the context of a collaborative work between LEM and Dr. Benedikt Lassalle-Kaiser from Synchrotron-Soleil. This collaborative effort could be in the near future applied to O_2 activation.

6.2 Electrocatalytic substrate oxidations-halogenations

Scheme 6.1 gathers the main reactivities that we described in the previous chapter.

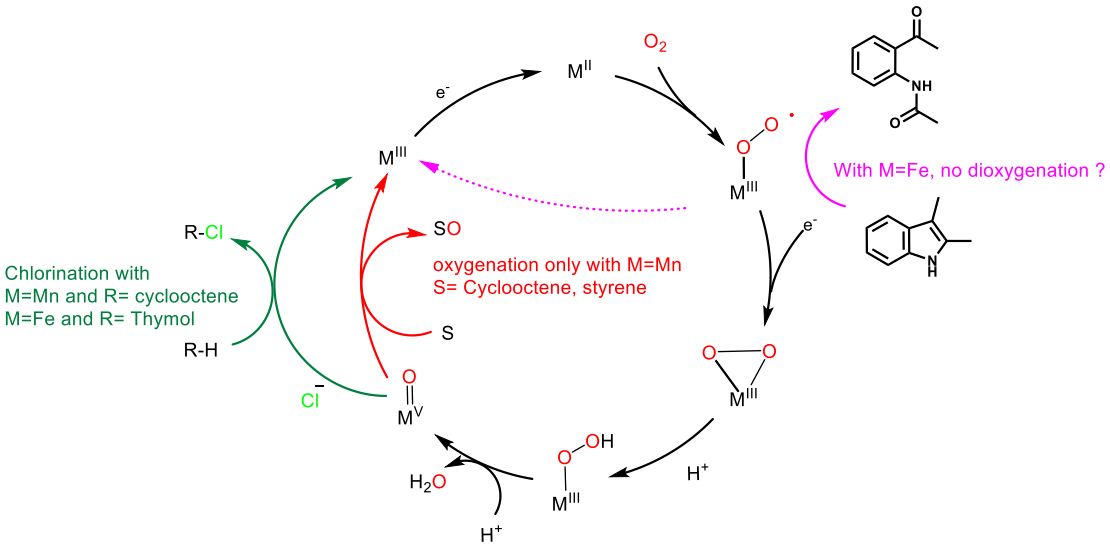

Scheme 6.1 Reactivity pathways discusses in Chapter 5

In the present paragraph we will discuss certain aspects of the reactivity studies that we have described in Chapter Chapter 5. Based on the information that we deduced from our experimental results, and on bibliographic data, we will first propose some solutions

to specific problems that we have encountered, and we then examine certain modifications of our electrocatalytic system that could lead to its optimization or open new reactivity routes.

6.2.1 Dioxygenation reactions of Fe superoxo

As we have shown in paragraph 5.1, we have not observed any dioxygenase activity of the Fe superoxide under electrochemical conditions. In DMF, we did not detect any di-oxygenated products of 2,3-dimethylindole, while in pure DCM the substrate that we have chosen can get oxidized spontaneously. The first alternative that we may try, would be the use of a less reactive substrate such as the 3-methylindole, that can probably allow the evaluation of the reaction in DCM, where 2,3-dimethyl indole is not sufficiently stable. Secondly, working in DCM/THF mixtures is an alternative worth trying, since reactivity has been observed in such mixtures, in the work of Wijeratne et al.[54] who prepared the reactive superoxo species chemically.

A major limitation of this reactivity, is the difficulty to achieve a catalytic reaction, because the formation of a μ-oxo dimer is highly likely after the first turnover as discussed in paragraph 5.1, and highlighted in the works of Wijeratne[54] and Goldberg.[55]. To overcome this problem, a first option would be the use axial ligands such as 1-methylimidazole that can impede the dimer formation. A second option is the use of sterically hindered porphyrins which could completely prevent the dimer formation, such as basket porphyrins.[170] In that case the first turnover can lead to the formation of a $Fe^{III}OH$ that can potentially reenter the catalytic cycle, as discussed in paragraph in 4.4.

Heterogenization of the Fe porphyrins on electrode surfaces could also efficiently impede any dimer formation and lead to a electrocatalytic reaction of several TON. An interesting option for performin the heterogenization reaction would be the modification of a carbon material such as carbon nanotubes with imidazole moieties that will axially bind to the Fe center (see Scheme 6.2). A protocol is described in the literature for such modification of carbon nanotubes,[179] providing a good starting point to develop this approach.

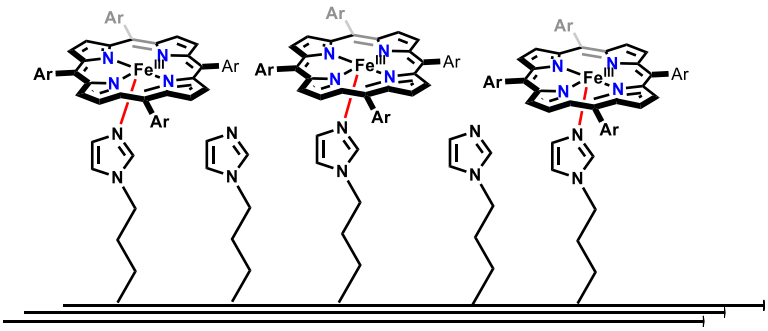

Scheme 6.2 Representation of Fe porphyrins immobilized on imidazole modified electrode surface.

6.2.2 Electrocatalytic Cyt-P450 -type reactivity of Fe porphyrins. Fe/O_2/Acid systems.

As discussed in paragraph 5.2, no Cyt-P450 type reactivity has been observed with Fe porphyrin, despite varying a series of electrolysis parameters. Importantly, three different organic solvents have been tried out, DMC, ACN and DCM, and acids of different strength (weak or strong) and type (protic acids or anhydrides), and all of these acids seem to favor the ORR instead of substrate oxidation. However, the Fe metal center needs a partner in order to activate the bound O_2 and cleave that O-O bond. An interesting alternative would be the use of redox-inactive metal cations that would act as Lewis's acids.

In 2013, Que et al. reported that Sc^{3+} was able to react with a Fe peroxo adduct of a non heme Fe complex, and lead to the cleavage of the O-O bond (see Scheme 6.3).[172] The authors spectroscopically observed a high valent Fe^{IV}(O)species.

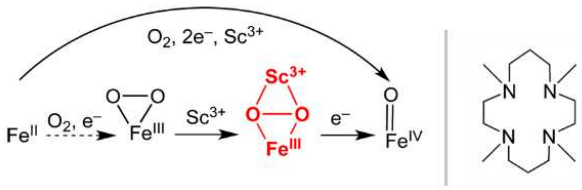

Scheme 6.3 Right: Fe peroxo reacts with Sc^{3+} cations as described by Que et al. [172] Left: Ligand of the Fe complex

Inspired by this work, we performed cyclic voltammetry experiments with Fe(TPP) and Fe(F_{20}TPP) in DMF, in presence of Sc(TfO)$_3$. In Figure 6.3 (right), representative CVs of a 0.5 mM solution of Fe^{III}(TPP)Cl are displayed , under Ar atmosphere (blue trace) and under O_2 atmosphere (red trace). Under Ar, we observe a quasi-reversible

Fe^{III}/Fe^{II} wave. Under O_2 atmosphere, the reduction wave becomes irreversible due to the reaction of the electrogenerated Fe^{II} with O_2 to give Fe superoxo as discussed in paragraph 2.2. Addition of 1 eq of Sc^{3+} leads to a small increase of the current and a slight shift of the potential to more positive values. This observation suggests that the electrogenerated Fe superoxo reacts with Sc^{3+}.

In the experiment with $Fe(F_{20}TPP)$ we observe, as we already discussed, the one electron reduction wave appears at -0.5 V vs SCE corresponds to the reduction of the $Fe^{III}(F_{20}TPP)(OO^{\bullet})$ (superoxo) adduct to the $Fe^{III}(F_{20}TPP)(OO^{-})$ (peroxo). Addition of 1 eq of Sc^{3+} leads to an increase of the current at -0.5 V indication that the electrogenerated $Fe^{III}(F_{20}TPP)(OO^{-})$ maybe react with Sc^{3+}. Based on these observation we can envisage preparative scale electrolysis in presence of Sc^{3+} and a substrate, to determine whether substrates can be oxygenated. In that case we note that reaction between Fe-oxygen adduct and Sc^{3+} would lead to cleavage of the O-O bond and subsequent Fe-Oxo species generation.

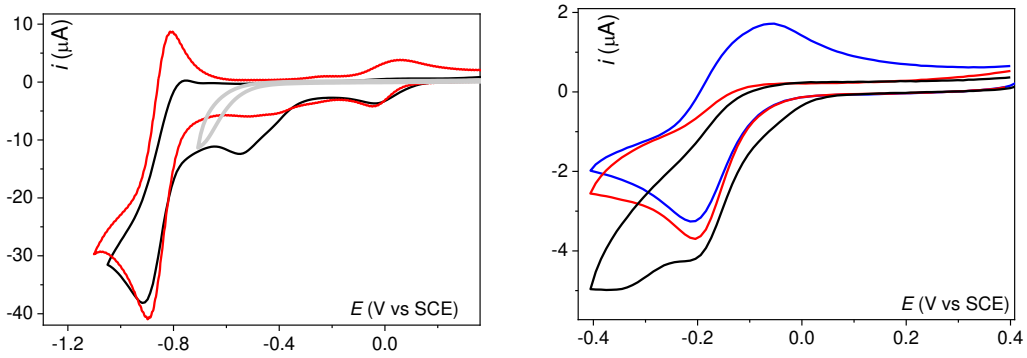

Figure 6.3: (Left) CV in DMF with 0.1 M $TBAPF_6$ of 0.5 mM solution of $Fe^{III}(F_{20}TPP)Cl$ under O_2 (1 mM, air saturated) (red trace), after addition of 1 eq of $Sc(TfO)_3$ (black trace), and 0.5 mM of $Sc(TfO)_3$ under O_2 without porphyrin (grey line). (Right) CV in DMF with 0.1 M $TBAPF_6$ of 0.5 mM solution of $Fe^{III}(TPP)Cl$ under Ar(blue trace), air saturated (red trace), and air saturated after addition of 1 eq of $Sc(TfO)_3$ (black trace). Scan rate is 0.1 V s^{-1} at a GC disk electrode (0.07 cm^2), T = 293 K.

We note here that another scope of this chemistry that has not yet been explored, is the electrochemical reactivity of water-soluble porphyrins in water towards organic substrates. This constitutes a large undertaking, such as a full PhD thesis project.

6.2.3 Mn(TPP) for substrate oxidation and halogenation

As we discussed in paragraph 5.3, Mn(TPP) in presence of benzoic anhydride catalyzes the electrocatalytic oxygenation of cyclooctene and styrene in presence of 1-methylimidazole and the halogenation of cyclooctene in presence of chloride. Importantly, in presence of perfluoto-tert-butanol (instead of anhydride) and chloride as the exogenous ligand, styrene was oxidized to its epoxide and to benzaldehyde in 3: 1 ratio. The latter results need to be further investigated, if we are to determine a protocol that will allow selective oxidation of styrene to benzaldehyde.

A possible pathway of benzaldehyde formation would be the opening of the epoxide, and the subsequent cleavage of the C-C bond in the 1,2 diol molecule. In order to examine this possibility, we purchased the 1-phenyl-1,2-ethanediol, and we will perform electrolyses starting from it as substrate to see if benzaldehyde is formed. If it is the case we will look for conditions that favor the epoxide opening in order to be able to form benzaldehyde selectively.

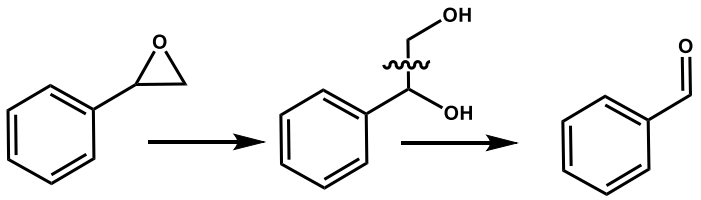

Scheme 6.4 A possible pathway of oxidative formation of benzaldehyde from styrene.

We can further vary several parameters to our electrolyses in order to try to increase the yield of our reactions, but if we are to develop a system that is to be used for practical applications, we will need anyway to consider the heterogenization of our catalyst.[180]

Immobilization of molecular catalysts on electrode surfaces is a very well-studied subject in the REACTE group at LEM since several years, mainly for CO_2 reduction in aqueous conditions. [181] Attachment of the electro-catalyst on the electrode surface offers several advantages, such as faster electron transfer to the metal center leading to an overall faster catalysis, and the possibility to work in aqueous conditions even with the catalysts that are not water soluble.

In close collaboration with Jérémy de Freitas, during his M2 internship in LEM, we have worked on the immobilization of Mn(TPP) onto glassy carbon electrodes. We first examined the non-covalent immobilization, that is carried out by dropcasting of the electrode surface with an ink, containing the catalyst, a carbon material and Nafion.[182] The ink was prepared in water, with a MWCNT:Mn(TPP)Cl ratio of 10:1

(MWCNT=multi-walled carbon nanotubes). Once prepared and agitated, 10 μL of the ink was deposited onto a 3mm in diameter glassy carbon disk electrode, and the deposit was dried in a 110°C oven.

Once the ink was deposited onto the electrode surface, it was studied in a classical set-up for CVs in an aqueous solution at pH=8.

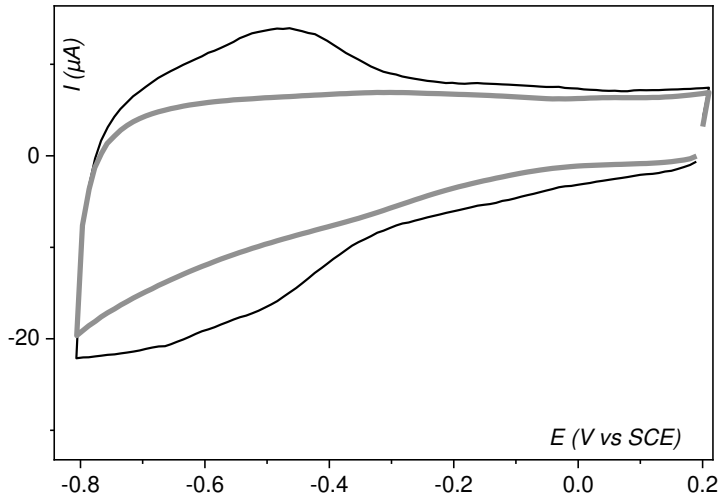

Figure 6.4: CV of deposited Mn(TPP)Cl/MWCNT into a glassy carbon electrode, in a water solution of $KHCO_3$ 0.1M (pH = 8) at ambient temperature, at v=100mV/s under Ar. CVs with Mn(TPP)Cl adsorbed to the MWCNT(black trave), and in short CV of MWCNT without Mn(TPP)Cl (grey trace).

Figure 6.4 shows CVs under Ar of the modifies electrode, reveal reduction and oxidation features at -0.6 V vs SCE (black trace). Since the features are absent if the porphyrin is absent (dotted line), they could be attributed to the Mn^{II}/Mn^{III} redox couple. This is a first step towards building a heterogeneous system for electrocatalytic oxidation of substrates in water.

Regarding organic solvents, we have experimentally observed that our modified electrodes when immersed in organic solvents, Mn(TPP) leaks in the solution. Thus, functionalization of nanotubes will be required, for example with imidazole moieties that will covalently bind to the metal center. There are various examples in the literatures that include such modifications that we can modify and use for our system.[179,183]

General Conclusion

The activation of dioxygen is at the center of current economic challenges, as oxygenation and halogenation reactions play a major role in the chemical industry. These current oxidation processes often use harmful chemical oxidants, or dioxygen under drastic temperature and pressure conditions in the presence of noble metal catalysts. This is due to the kinetic stability of oxygen. As we described in **Chapter 1,** the metalloenzymes of the Cytochromes P450 superfamily are capable of surpassing the kinetic barrier under mild conditions, and carry out oxidation reactions efficiently and selectively in living cells, through the so-called reductive activation of dioxygen, which takes advantage of the potent oxidizing power of this molecule. This process begins with the coordination of dioxygen with iron at the active site, through a succession of reduction and protonation steps leading to the breaking of the oxygen-oxygen bond and the formation of a high valent $Fe^{V}(O)$ species, a highly reactive species capable of oxidizing an organic substrate. For several decades the Fe and Mn porphyrins have been widely studied as models of the active site of these enzymes. Corresponding literature focuses on the chemically driven formation of various metal-oxygen intermediate species, their spectroscopic characterization and reactivity studies. The alternative approach that we are proposing in the present manuscript, includes a combination of CV, Scanning Electrochemical Microscopy, and UV-Vis Spectroelectrochemistry for the preparation and characterization of intermediate species, and preparative scale electrolysis for the evaluation of the reactivity of those intermediates.

Based on previous work conducted at the Laboratory of Molecular Electrochemistry (LEM), we start our approach in **Chapter 2** by studying the electrochemical activation of O_2 by electrogenerated Mn^{II} and Fe^{II} porphyrins. We demonstrate using cyclic voltammetry and UV-Vis spectroelectrochemistry that two iron analogues (Fe(TPP) and Fe(F_{20}TPP)) react in the Fe^{II} state with O_2 to give a superoxo species $Fe^{III}(OO^{\bullet})$ that can be one-electron reduced to give a peroxo, $Fe^{III}(OO^{-})$. The generated species exhibit the same spectral characteristics as the chemically prepared species previously reported. The Mn analogue (Mn(TPP)) in DCM reacts in the Mn^{II} state with O_2 and gives Mn^{II}-O_2 which is immediately reduced at the same potential to give a $Mn^{II}(OO^{\bullet})$while Mn^{II} in DMF only reacts with $O_2^{\bullet-}$ (generated on the electrode surface) to give that species.

We showed that our electrochemical approach can bypass the need for chemical reducing agents and provides better control of the injected electrons.

We then examined the electrochemical reductive activation of O_2 catalyzed by the Fe(F_{20}TPP)Cl in DMF solutions, in presence of Brønsted-Lowry Acids, using cyclic voltammetry and spectroelectrochemistry. We choose the Fe(F_{20}TPP) as catalyst, that is less reactive than its non perfluorated analogue, the Fe(TPP), facilitating the isolation of intermediates and the identification of different mechanistic pathways. In **Chapter 3** we have provided new experimental evidence for two mechanistic pathways that lead to the formation of Fe^{III}(OOH) species and to the subsequent O−O bond cleavage. The PET (proton electron transfer) process occurs at a low overpotential, while the EPT (electron-proton transfer) occurs at a higher overpotential. Upon changing the applied potential and the porphyrin concentration we identified *operando*, using spectroelectrochemistry, the following species: Fe^{II}(OH) and $Fe^{III}(OH_2)$ at low overpotential and low porphyrin concentration, Fe^{III}(OOH) at low overpotential and higher porphyrin concentration, and Fe^{IV}(O) at high overpotential and low porphyrin concentration.

Scanning Electrochemical Microscopy is a technique which consists of using a 4-electrode set-up that includes an ultramicroelectrode (UME) used as a probe, that is positioned in a determined distance from a conductive surface (substrate) to study the electrochemical processes that take place in the diffusion layer. For our study we used the "generator substrate-collecting probe" (SG / TC) mode. In **Chapter 4** we showed that the Fe^{III}(F_{20}TPP)(OO^{-}). species which is generated at the generator substrate electrode at -0.6 V vs SCE, can be probed at the ultramicroelectrode thanks to its mono-electronic oxidation wave at +0.5 V vs SCE. This methodology is then successfully applied for the porphyrins Fe(TPP) and Fe(T(o-(COOH))PP). We then simulated the LSVs recorded on each electrode. We used a simple reaction scheme, where two parameters vary, (i) the binding constant between O_2 and Fe^{II}, K_{O_2} and (ii) the peroxo dissociation constant k_d. The SECM tool allows not only to characterize different reaction intermediates in a single experiment, but also, combined with simulations, to determine the kinetic and thermodynamic parameters associated with the ORR reaction that allow drawing structure-reactivity relationships. .

The electrochemical approach in the generation and characterization of metal-oxygen porphyrin intermediates, is the first step towards the development of systems that are

able to efficiently reproduce the oxygenation or halogenation reactivity. In **Chapter 5**, was devoted to the reactivity test. For the experiments, we start with an air stable M^{III} porphyrin (M=Fe or Mn), which when electrochemically reduced to M^{II}, reacts with O_2, inducing different reactivities depending on the conditions (presence of acid or chloride, and choice of catalyst). Our study showed that porphyrin Mn(TPP) catalyzes the electrocatalytic oxygenation or halogenation of cyclooctene in the presence of benzoic anhydride, depending on the exogenous ligand: 1-methylimidazole promotes epoxidation (TON=8) while chloride promotes chlorination (TON=5) . Styrene could also be oxidized to epoxy-styrene under the same conditions. By using perfluoro-tert-butanol, a protic acid, instead of benzoic anhydride, we have demonstrated that cyclooctene as well as styrene can be epoxidized. Benzaldehyde has also been observed as an oxidation product of styrene in small amounts. By changing the experimental parameters, we were able to promote its production: in the presence of chloride, styrene is oxidized to epoxide and benzaldehyde with a 3: 1 ratio. We also demonstrated that the electrochemical chlorination of thymol was possible using the $Fe(F_{20}TPP)Cl$ complex, with a low yield.

As described in Chapter 6, our current efforts and future work focus on two directions: (i) to complete spectroelectrochemical characterization of intermediate species using various spectroscopies such as Resonance Raman or XAS, and (ii) to improve the catalytic reactivity of our electrocatalytic system in homogeneous and heterogeneous conditions. Using a cell that we developed in LEM, we have already been able to characterize by Resonance Raman the chemically generated $Fe^{IV}(F_{20}TPP)(O)$ and to probe the electrochemical transformation of Fe^{III} into Fe^{II}. In parallel, we are conducting catalyst heterogenization studies with inexpensive materials, such as carbon nanotubes, at electrode surfaces.

Chapter 7

Annex 1: experimental part, additional experiments, additional calculations

7.1 Experimental details

7.1.1 General

In all the experiments, three gasses were used. Argon, O_2 or compressed air. The air was dried by passing it through a glass tube filled with $CaCl_2$, the O_2 and Ar obtained commercially were sufficiently dry (provided by Air Liquide). All reagents and solvents were obtained commercially (Acros Organics and Sigma Aldrich). [Fe(F_{20}^{III}TPP)Cl], [Fe^{III}(TPP)Cl], [Fe^{III}(TMP)Cl] and [Mn^{III}(TPP)Cl] (HPCL grade, ≥ 95%) were purchased from PorLab, [Fe^{III}(T-(2-COOH)PP)Cl], tetrabutylammonium hexafluorophosphate ($TBAPF_6$, supporting electrolyte), tetrabutylammonium chloride (TBACl), cyclooctene oxide, anisole, 1-Methylimidazole, benzoic anhydride, perfluoro-tert-butanol, thymol, chlorothymol, were purchased from Sigma-Aldrich and used as received. N,N-Dimethylformamide (DMF, over molecular shieves, 99.9%) and Acetonitrile (over molecular shieves, 99.8%) was obtained from Acros Organics. DCM was distilled over CaH_2 and purified by alumina before every experiment. Extra dry DMF was obtained by transferring the commercial anhydrous DMF into a flask, inside the glove box, with freshly activated molecular sheaves (3 Å,Sigma Aldrich), at 250°C under vacuum for 48 h. Cyclooctene was purified on alumina column before experiments. Its purity was checked by GC/MS.

N-2-(methylphenylacetamide) has been prepared by a modified literature procedure:[184] in a stirring solution of $NaIO_4$ (0.5676g, 0.00265 mol) 10 mL of H_2O, a solution of 2,3-dimethylindole in 10 mL of methanol (0.1725g, 0.00119 mmol) is added dropwise in 5 minutes. The dispersion is stirred overnight for the reaction to be completed. The product is obtained after extraction with DMC and solvent evaporation.

The ^{1}H-NMR analyses described in the manuscript were caried out in a Bruker Avance 400 MHz spectrometer was used.

7.1.2 Cyclic voltammetry and preparative scale electrolysis

For all the experiments, a Metrohm AUTOLAB was used, and the interface software was NOVA 2.1. A well-known set-up has been used for cyclic voltammetry experiments, shown in Figure 7.1. The counter electrode was a platinum or gold wire, the reference electrode was a KCl saturated calomel electrode (SCE, purchased from

Biologic) in a glass frit that both protects the electrode and prevents KCl leaks inside the cell.

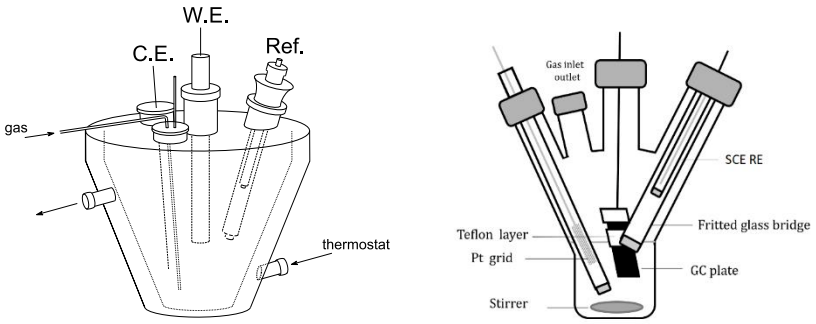

Figure 7.1 (Left) Cyclic voltammetry cell (Right) Preparative scale electrolysis cell.

When needed, the cell was maintained at low temperatures using a Julabo cryostat. The working electrode was a glassy carbon disk (Biologic, 3 or 1.6 mm diameter) carefully polished before each voltammogram with a 1 µm diamond paste, and washed with ethanol and acetone. The experiments were performed under Ar, or O_2. Dry O_2 atmosphere was achieved by purging the solution with compressed air (or O_2) throughout a glass tube filled with $CaCl_2$. Temperature regulation, when needed, was ensured by a Julabo circulation cryostat.

For controlled potential electrolysis, experiments were carried out in a slightly modified cell (Figure 7.1) made by the Glass Blower of the chemistry department, using a glassy carbon plate as working electrode of a surface of 1.6 cm^2, and a SCE reference electrode in a glass frit, closely positioned one from the other. The Pt grid counter electrode was separated from the cathodic compartment with a glass frit. During the electrolysis there was a continuous flow of dry air or Ar. Post-electrolysis samples were injected directly in the GC/MS without separation or dilution.

7.1.3 Thin layer UV-Vis spectroelectrochemistry

All the experiments were performed in a Cary-60 (Agilent Technologies) spectrophotometer. This technique allows the *in situ* UV-Vis characterization of intermediate species that are produced in the diffusion layer of an electrode. To do so, it is necessary to use a special cell, to which can be integrated three electrodes of the classical CV set-up, and that can be in the same time mounted in the spectrophotometer. The first set-up used in LEM, has been developed by Lexa et al.,[135,

[185] (see Figure 2.3) and a modified version of it, has been used for the present study. The electrochemical cell, is mounted in a transparent Dewar-type support inside the spectrophotometer. The former consists of a 0.2 cm quartz UV-Vis-NIR cell surmounted by a glass compartment. The Dewar was cooled, when needed, by a Julabo circulation cryostat.

In the original set-up, a platinum grid protected in a glass frit has been used as the counter electrode, reference electrode was a $Ag/AgNO_3^{ACN}$ one, also in a glass frit, and the working electrode was a platinum grid. In the new version used in the present study, the working electrode has been replaced by a Toray carbon paper electrode (Alfa Aesar, TGP-H-60) with holes allowing the light to pass through, connected with golden thread. This carbon material has a behavior much closer to the GC electrode than platinum, so the CV analysis can be directly correlated with the results in the spectroelectrochemical experiment. Then the reference electrode has been replaced by an activated carbon pseudoreference electrode[186] that is very stable for several hours, avoiding in the same time Ag^+ leaks in the solution that can be detrimental for electrochemistry experiments. Finally, a GC electrode (of 1.6 mm diameter, Biologic) has been integrated in the set-up, allowing the recording of CVs inside the cell.

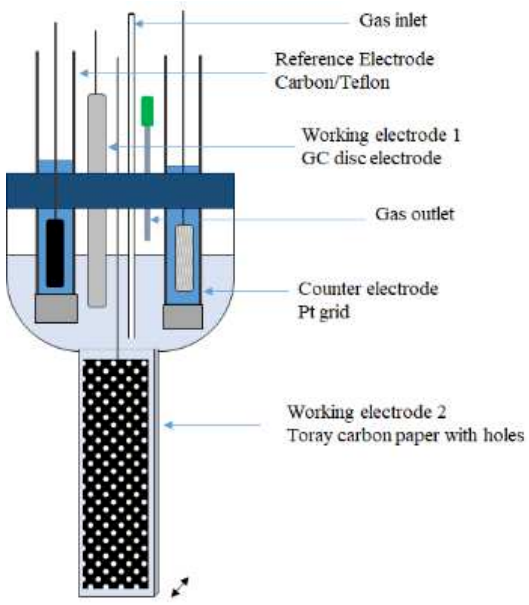

Figure 7.2: Schematic representation of modified cell used in the present study in UV-Vis spectroelectrochemistry.

Figure 7.3 shows how this spectroelectrochemical set up is constructed from its parts and Figure 7.4 the special Dewar that is mounted inside the spectrophotometer.

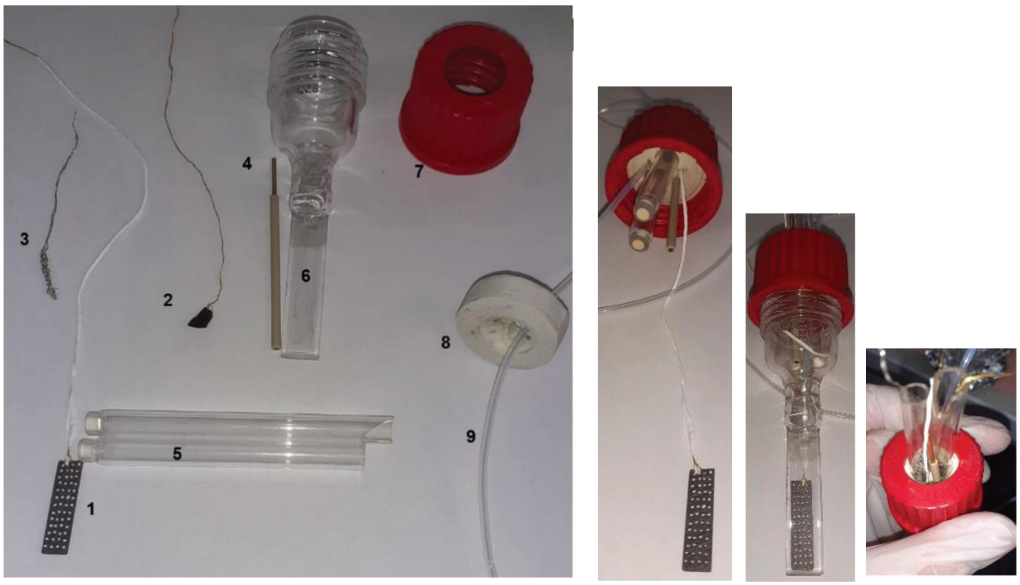

Figure 7.3: A: Parts that consist the spectroelectrochemical cell. 1: Carbon paper electrode connected to gold cloth covered with Teflon tape to avoid contact with the solution. 2: Reference carbon/Teflon electrode connected with gold cloth. 3: Platinum counter electrode. 4. Commercial Glassy Carbon electrode (of 1.6 mm diameter, Biologic). 5: Glass frites. 6: Spectroelectrochemical cell (quartz, 0.1 mm optical path). 7: Plastic nut screw. 8: Septum part with holes 9: Teflon tube. B: Electrodes, frites, and nut screw on the septum. C: Final view of the cell D: Final view of the cell from the top.

In order to pass the working electrode throughout the septum while keeping it air tight, a small piece of Teflon tube is used that is easily passed through with the aid of a needle, the electrode is passed thought the tube, and then the tube is carefully removed leaving a tight hole in the septum. Then, the two frites and the second working electrode are put in the septum as demonstrated in figure Figure 7.3 B. The septum is then put in the nut screw, and the plastic nut screw is screwed assuring the air-tightened of the system. The counter and reference electrodes are finally inserted in the bridges.

Figure 7.4: Dewar mounted in the spectrophotometer.

7.1.4 Resonance Raman Spectroelectrochemistry

For spectroelectrochemical experiment a special cell had to be developed. We elaborated the cell based on the cell that is used for UV-Vis spectroelectrochemistry, and the cell was made by the glass blower of the chemistry department. a new cell has been made by the glass blower. The cell has two compartments, a thin one that contains a carbon paper electrode and is probed and a bigger one that contained that bulk solution and three electrodes, a GC disk electrode, a platinum grid as counter and an activated carbon electrode as reference.

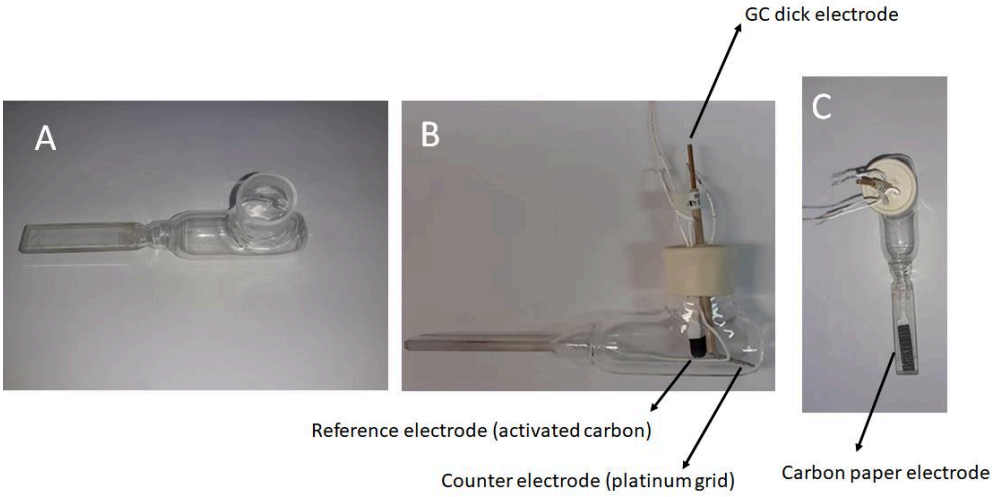

Figure 7.5: Developing a cell for Resonance Raman spectroelectrochemistry. A: Quartz cell used. Cell containing a septum and the electrodes, B: side view. C: top view.

The experiments were performed in the ITODYS laboratory, with the help of Dr. Stéphanie Lau. The apparatus used was a Horiba/Jobin Yvon LabRam HR instrument equipped with a laser emitting at 406 nm.

7.1.5 Scanning Electrochemical microscopy

The SCEM experiments were performed under controlled atmosphere in a glove bag. The cell consisted of a Teflon support and a glass bell with two holes, one for constant bubbling of the solution and the other for the ultramicroelectrode. For performing the different electrochemical measurements, a bipotentiostat was used (CHI, #760 C) and the ultramicroelectrode was positioned and moved using a micromotor controlled by a small controller. The system was guided using an interface called LabView that was implemented by the TERS team. The previously used set-up used by the team, was modified for the study of Fe porphyrins in solution by Jean-Marc Noël and Célia Achaibou.

The gold ultramicroelectrodes were made in the laboratory from borosilicate capillaries (Shutter Instruments) with an external diameter of 1.0 mm and an internal of 0.5 mm, in which a gold cloth (dimeter of 25 µm, Goodfellow Cambridge Ltd, 99.99%) was introduced. The capillaries are then stretched and sealed by a laser stretcher (Shutter Instruments, model # P-2000). Subsequently, the electrical contacts are made by introducing carbon powder and stainless steel wires into the capillaries. The UMEs are then polished on polishing discs of different roughness

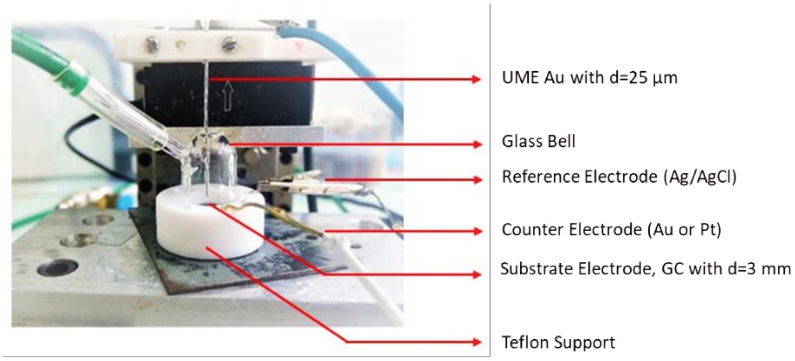

Figure 7.6: Set-up used for Scanning Electrochemical Microscopy Experiments.

Approach curves have been recorded in the positive feedback mode (see Chapter 4.1) in order to place the collection UME close to the generator glassy carbon electrode. While applying a potential at the UME, it is moved vertically to the G, until the former touches physically the surface of the latter, giving a plateau current. Then, the TIP is

retracted to 8 µm with a velocity of 1 µm.s^{-1} from that point using the positioning system. The estimation of the distance error is carried out by comparing the plot of the normalized current $I_{C,norm} = I_C / I_{C,inf}$ over the normalized distance. $L = d/a$ (with I_C is the current on the C and $I_{C,inf}$ is the current on the C at infinite distance from the G, d is the distance and a is the dimeter of the electrode) with theoretical curves obtained by methods already described in the literature (see reference [168] and refs therein).

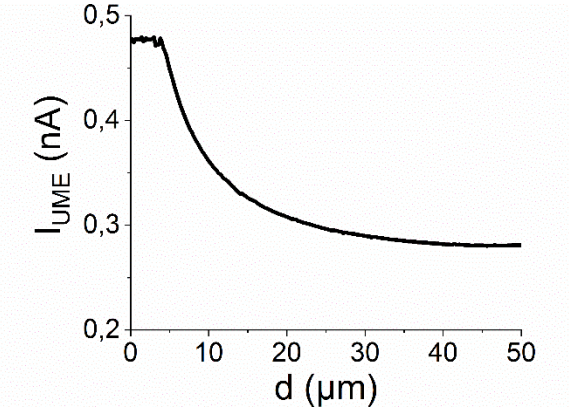

Figure 7.7: Approach curved obtained in a SECM set-up with a velocity of 1 µm s^{-1}, in a DMF solution with 0.1 M TBAPF6 and 0.25 mM of $Fe^{III}(F_{20}TPP)Cl$ under argon. A potential of -0.4 V vs Ag/AgCl is holded in the UME resulting in reduction of Fe^{III} to Fe^{II} while in the generator substrate a potential of -0.5 V vs Ag/AgCl is applied resulting in oxidation of Fe^{II} to Fe^{III}.

The simulations of the electrochemical responses from the SECM experiment have been performed by Frédéric Kanoufi and Jean-Marc Noël. The COMSOL Multiphysics software was used, and a 2D axisymmetric mode was used. Regarding the geometry of the UME, it had a radius of a = 12.5µm and it was surrounded by a cylindrical insulating body with a radius of $rg = 4a$. The UME was positioned at different distances d from a generator electrode (G). The concentration of the different species involved, were evaluated by solving their time-dependent diffusion equations. Additionally, the electrochemical conversion of the various species is taken into account through a classic Butler-Volmer rate law for the diffusive flux of each species at both electrodes. Importantly, the LSV of the UME that were simulated for the the species that are generated at the generator are obtained by taking into consideration the applied potential on the generator while the tip potential is scanned. Further details are available in reference [168].

7.1.6 Calibration curves for GC/MS

For the chlorination of thymol, the analyses have been performed using a GCMS of "Thermo-Electron" (Column 5% Phenyl-dimethyl Polysiloxane, analysis in EI), and for the calibration curve n-octanol was used. For the cyclooctene and styrene stydies, a Shimadzu GCMS has been used (column type Rtx- WAX, analysis in EI), and anisole was used as internal standard for the calibration curve.

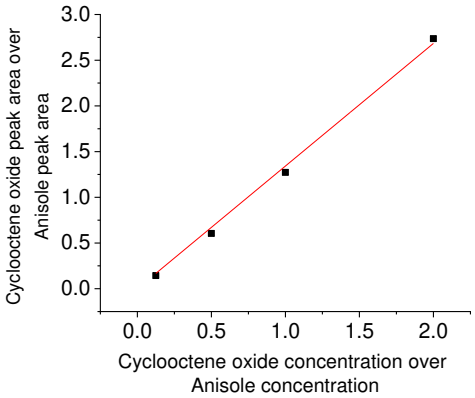

Figure 7.8: Calibration curve for cyclooctene oxide. The internal standard used was anisole. The concentration of the latter was 2 mM on every sample. The concentrations of cyclooctene were: 0.25 mM, 1 mM, 2 mM and 4 mM.

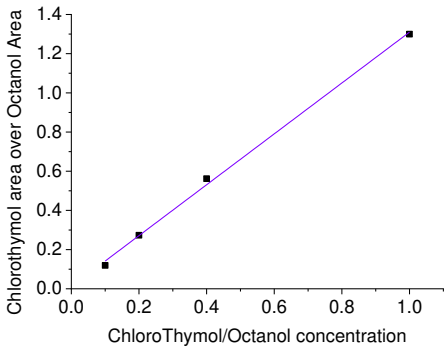

Figure 7.9: Calibration curve of chlorothymol using n-octanol as internal standard. The concentration of the latter was 1 mM on every sample. The concentrations of cyclooctene were: 0.05 mM, 0.1 mM, 0.2 mM and 1 mM.

7.2 Alternative set-up for low temperature UV-Vis spectroelectrochemistry

An alternative set-up for performing UV-Vis spectroelectrochemistry in low temperatures, have been successfully used in Université de Bretagne Oxidentale, in the Laboratory CEMCA (Chimie, électrochimie moléculaires et chimie analytique), under the guidance of Dr. Nicolas Le Poul. The author's stay in Brest has been financially supported by the FrenchBic (French Bioinorganic Chemistry Association).

In that set-up an optical fiber is positioned in close proximity of a GC disk electrode and probes the UV-Vis spectrum of the species present in the diffusion layer. The set-up is shown in Figure 7.10. The set-up has previously been used successfully.[187]

The spectra were obtained by using a Varian Cary 50 spectrophotometer. It was equipped with a Hellma low-temperature immersion probe. The temperature was controlled with a Lauda RK8 KS cryostat.

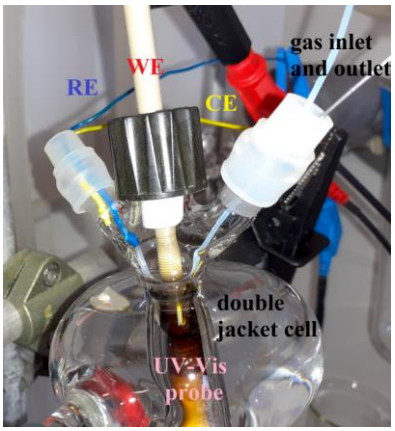

Figure 7.10: Alternative set-up for UV-Vis low temperature spectroelectrochemistry. Platinum wires were used both as pseudoreference and counter electrode, glassy carbon disk as working electrode, a Teflon tube was used as gas inlet and a needle as gas outlet. The UV-Vis probe was positioned from the bottom of the cell with the aid of a net screw. Double-jacket served in keeping the solution in low temperature.

In a Fe(TPP)Cl solution in DMF, at 233 K, CVs were performed at the GC electrode and at the same time UV-Vis absorption spectra were recorded using this optical probe. Under Ar, a spectrum corresponding to Fe^{II} was obtained while under O_2 the bands corresponding to the Fe^{III} superoxo appeared, as it was the case in the classical UV-Vis spectroelectrochemistry set-up (paragraph 2.2). The advantage however of the alternative set-up is that is much easier to handle, and that the spectra are directly correlated to the obtained CV in a classical GC electrode.

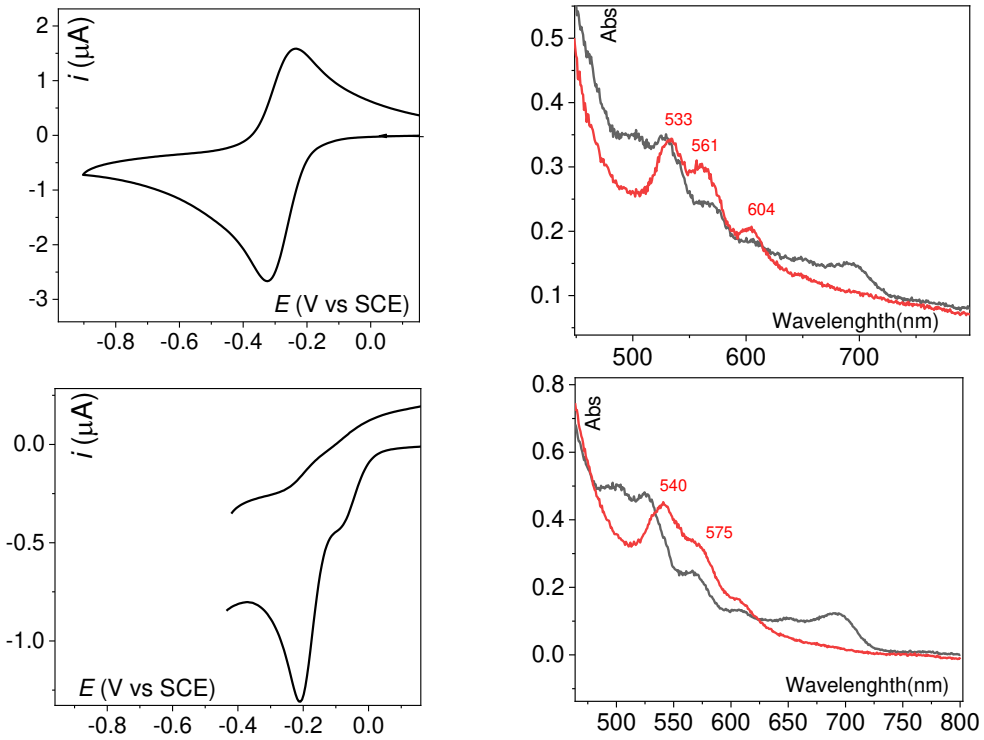

Figure 7.11: CV recorded on a 3 mm GC electrode of a 1 mM Fe(TPP)Cl in DMF solution with 0.1 M TBAPF6, at 233 K, at 0.01 V/s (up left) UV-Vis spectra recorded before(black trace) and after (red trace) the forward scan of the CV under Ar (up right). CV recorder in air saturated solution (down, left) and UV-Vis spectra (down, left) recorded before the CV(black trace) and after 153 s at -0.4 V after the forward scan of the CV (red trace).

7.3 Approximations used for the equation 4.9

The dependence of $E^0_{Fe^{III}/Fe^{II}}$ on various parameters relevant to the SECM experiment have been estimated using a simple mathematic model developed by Jean-Marc Noël and Frédéric Kanoufi as follows.

We take into consideration the following equations. Letter E corresponds to an electrochemical and letter C to chemical reactions

E$_1$: $Fe^{III} + e^- \rightleftharpoons Fe^{II}$ $\quad E^0_{Fe^{III}/Fe^{II}}$

C$_1$: $Fe^{II} + O_2 \rightleftharpoons Fe^{III}OO^{\bullet}$ $\quad K_{O_2}$

E$_2$: $Fe^{III}OO^{\bullet} + e^- \rightarrow Fe^{III}OO^-$ $\quad E_{Fe^{III}OO^{\bullet}/Fe^{III}OO^-}$

C$_2$: $Fe^{III}OO^- + H^+ \longrightarrow Fe^{III}OOH$ $\quad K_a$

If, in a first approximation, we do not consider in the calculations the reaction C$_2$, we can consider the following application of the Nernst's law for E$_2$:

$$E^{p}_{Fe^{III}OO^{-}/Fe^{III}OO^{-}} = E^{0}_{Fe^{III}OO^{\bullet}/Fe^{III}OO^{-}} + \frac{RT}{F} ln(\frac{Fe^{III}OO^{\bullet}}{Fe^{III}OO^{-}})$$

With $K_{O_2} = \frac{[Fe^{III}OO^{\bullet}]}{[O_2][Fe^{II}]}$ and considering that $K_{O_2} \times [O_2] < 1$, it leads to the following equations:

$$E^{0}_{app,1} = E^{p}_{Fe^{III}OO^{\bullet}/Fe^{III}OO^{-}} = E^{0}_{Fe^{III}OO^{\bullet}/Fe^{III}OO^{-}} - 0.06pK_{O_2} + 0.06\log[O_2]$$

We then hypothesize that the trend that is observed for the $E^{0}_{Fe^{III}/Fe^{II}}$,that is decrease with increase of the electron donating ability of the meso-substituents, should be also followed in the $E^{0}_{Fe^{III}OO^{\bullet}/Fe^{III}OO^{-}}$. In that case the $\Delta E = E^{0}_{Fe^{III}OO^{\bullet}/Fe^{III}OO^{-}} - E^{0}_{Fe^{III}/Fe^{II}}$ should remain constant within the series leading to the equation

$$E^{0}_{app,1} = E^{0}_{Fe^{III}/Fe^{II}} - 0.06pK_{O_2} + C''$$

With $C'' = 0.06\log[O_2] + \Delta E$. This equation has then been used as explained in the main text.

Annex 2: Résumé substantiel en français

Mots-cléfs : Porphyrine, électrocatalyse, oxygène, oxydation, spectroélectrochimie

Introduction Générale

Le dioxygène a été découvert en 1774 par le chimiste anglais Joseph Priestley et le nom « oxygène » a été donné par Antoine De Lavoisier en 1778. Le mot oxygène signifie « ce qui génère de l'acide » et vient des mots grecs ὀξὺ (oksý, acide) et γεννῶ (gennô, générer, donner naissance), et trouve son origine dans la fausse, comme cela a été prouvé plus tard, conclusion que tous les acides contenaient un atome d'oxygène.

Le dioxygène constitue environ 21 % en volume de l'atmosphère terrestre actuelle, tandis qu'une quantité importante de dioxygène est dissoute dans les eaux de surface. Il y a environ 2,4 milliards d'années, la "Grande oxydation" a eu lieu , liée à l'activité des cyanobactéries photosynthétiques, qui a augmenté les niveaux de dioxygène dans l'atmosphère de plus de 4 ordres de grandeur (le 1/10 des niveaux actuels). Cet événement a changé le cours de la vie sur terre. Dans une atmosphère aérobie, les composés contenant du carbone et de l'hydrogène, présents dans tous les êtres vivants, sont thermodynamiquement instables à l'oxydation en dioxyde de carbone et eau. Cependant, l'oxydation directe des composés organiques par l'oxygène est cinétiquement lente : nous vivons dans un monde métastable et coexistons avec l'oxygène dans un piège cinétique.

Le dioxygène joue un rôle central dans la vie terrestre. En effet, des nombreuses enzymes sont directement liées à cette molécule. L'un de plus anciennes enzymes connues est le photosystème II, système très performent, qui oxyde l'eau en dioxygène par photocatalyse et est indispensable à la photosynthèse. D'autres enzymes telles que les catalases, qui catalysent la dismutation du H_2O_2, et les superoxyde dismutases, qui catalysent la dismutation du $O_2^{\bullet -}$, sont capables de protéger les cellules vivantes contre les ERO (espèces réduites du dioxygène). Il existe également des enzymes, tel que le Cyt-P450 (Cytochrome P450), capables de catalyser l'activation partielle et contrôlée de l'oxygène qui conduit à l'oxydation de substrats organiques. Ces enzymes sont toutes des métalloprotéines qui contiennent un ion métallique (Fe, Mn, ou Cu) dans leur site actif. Les systèmes hémiques qui contiennent un ion Fe et un ligand porphyrinique constituent une sous-catégorie de ces métalloprotéines. Les travaux présentés dans ce manuscrit sont inspirés de l'activité catalytique de ces systèmes hémiques, et plus particulièrement du Cyt-P450.

Dans une approche bio-inspirée, nous utilisons des catalyseurs moléculaires, des porphyrines de Fe ou de Mn, qui ont des structures similaires au site actif du Cyt-P450. Nous cherchons à reproduire la remarquable réactivité du Cyt-P450, réactivité d'oxydation des substrats organiques par activation réductrice du dioxygène. Les électrons nécessaires pour cette activation sont fournis, dans notre approche, par voie électrochimique, reproduisant l'activité du NADPH, cofacteur qui transfère les électrons dans les systèmes naturels. De plus, l'utilisation des méthodes électrochimiques (voltamétrie cyclique, électrolyse préparative) couplées à des méthodes spectroscopiques (UV-Vis, Raman) permettent de sonder les intermédiaires réactionnels mis en jeu dans les réactions catalytiques.

Le présent manuscrit de thèse est organisé selon six chapitres et une annexe incluant une partie expérimentale et une partie détaillant certain calcules présentés dans le texte principal. Le chapitre 1 constitue une introduction bibliographique sur les systèmes naturels et bioinspirés capables d'activer O_2. Le chapitre 2 décrit notre approche électrochimique et la préparation et caractérisation des adduits de type M-O_2 (M= Fe, Mn). Le chapitre 3 décrit l'activation réductrice de O_2, par la porphyrine Fe(F_{20}TPP) dans le DMF, en présence de protons et détaille différents chemins catalytiques. Dans le chapitre 4, une étude détaillée à l'aide de la microscopie électronique à balayage (SECM), permit de mesurer des paramètres cruciaux impliqués dans l'activation électrochimique de O_2, par des porphyrines de Fe et d'établir des relations structure-réactivité pour une série des porphyrines. Le chapitre V ressemble les résultats de réactivité électrocatalytique d'oxygénation de d'halogénation obtenus pour une série des porphyrines de Fe et de Mn. Enfin le chapitre 6 présente les perspectives envisagées pour la suite de ce travail de thèse, en particulier sur le développement d'un montage pour la spectroélectrochimie Raman en résonance, et la possible hétérogénéisation du système électrocatalytique et. Ce manuscrit est complété par une introduction générale et une conclusion générale, ainsi qu'une bibliographie à la fin du document.

Chapitre 1 : Introduction

Le dioxygène est un oxydant puissant d'un point de vue thermodynamique, mais il est cinétiquement inerte grâce à son caractère diradicalaire : il réagit préférentiellement avec un autre radical (pour que le spin soit conservé) ou forme un produit qui possède un état fondamental triplet, un processus rare.[3] Ainsi, les voies principales de réactivité

du dioxygène impliquent des radicaux (par exemple, des métaux de transition avec des électrons non appariés) ou nécessitent une excitation vers l'oxygène singulet, son premier état excité.

Les réactions d'oxydation sont des procédés utilisés dans l'industrie des polymères pour produire de grandes quantités d'intermédiaires réactionnels et des monomères. [6] Les oxydants actuellement utilisés dans les procédés industriels incluent HNO_3, H_2SO_4 et SO_3/H_2SO_4 (oléum), Cl_2, MnO_2, CrO_3, $KMnO_4$. Ces composés sont toxiques et leur production énergivore et souvent onéreuse. L'utilisation de l'oxygène atmosphérique comme agent oxydant constitue une alternative souhaitée, car cet oxydant est abondant et accessible. Néanmoins, à ce jour, son utilisation nécessite l'utilisation des températures et de pressions très élevées, et des procédés onéreux et élaborés. Il convient donc de développer des processus catalytiques plus respectueux des contraintes environnementales et énergétiques désormais incontournables. [188]

Dans ce contexte, les métalloenzymes constituent une grande source d'inspiration dans ce contexte, car elles présentent de nombreux avantages par rapport aux procédés industriels :

- elles fonctionnent dans des conditions douces (physiologiques)
- elles font intervenir les oxydants les plus verts que l'on connaisse, c'est-à-dire O_2 ou H_2O_2,
- le seul produit secondaire est le H_2O
- elles utilisent des métaux non nobles et abondantsdans leurs sites actifs, comme le Fe, le Mn, ou le Cu

Dans les systèmes biologiques, des divers métalloenzymes effectuent une réduction partielle ou complète du dioxygène. Dans leur site actif, elles contiennent des ions de métaux de transition tels que le Fe ou le Cu. Les résidus d'acides aminés du site actif jouent un rôle central dans plusieurs étapes du processus. Les métalloenzymes qui catalysent la réduction du dioxygène peuvent être classées en quatre catégories générales (i)Oxydases et monooxygénases de Cu[1] (ii) Oxygénases non-hémiques contenant du Fe[8] (iii) Oxydases hémiques contenant du Cu[1] (iii) Enzymes hémiques.[1, 9-11]

Dans cette thèse, nous nous concentrons sur les enzymes hémiques qui catalysent des oxydations de substrats organiques. Le Cyt-P450 catalyse l'oxydation des liaisons C-H des substrat tel que le camphre (pour le Cyt-$P450_{cam}$). Au cours de la réaction, l'espèce

oxydante Fe^{IV}=O π radical cation, issue de la cassure de la liaison O-O de l'intermédiaire Fe(OOH), réagit avec le substrat, résultant en l'insertion de l'atome d'oxygène dans la liaison C-H. Le ligand axial du fer dans le site actif est un résidu cystéine (voir Figure 88). Les haloperoxidases, une autre enzyme hémique, sont capables d'oxyder (halogéner) des substrats, en présence d'halogénures, mais elles utilisent le H_2O_2 comme source d'oxygène ; elles ont beaucoup de caractéristiques structurales et mécanistiques en commun avec les Cyt-P450. Les dioxygenenases, quant à elles, sont capables d'oxyder des liaisons C-C dans des substrats de type indole, et d'insérer deux atomes d'oxygène; l'espèce active dans ce cas est un Fe^{III} superoxo ($Fe^{III}(OO^{\bullet})$.[39]

Au cours des 60 dernières années, les efforts de nombreux chercheurs en chimie bio-inorganique, se sont concentrés sur la modélisation des sites actifs de plusieurs enzymes hémiques et la caractérisation spectroscopique d'intermédiaires réactionnels, non seulement pour améliorer la compréhension du fonctionnement de ces enzymes hémiques, mais aussi parce que les systèmes modèles présentent des réactivités intéressantes vis-à-vis des substrats.[1, 9]

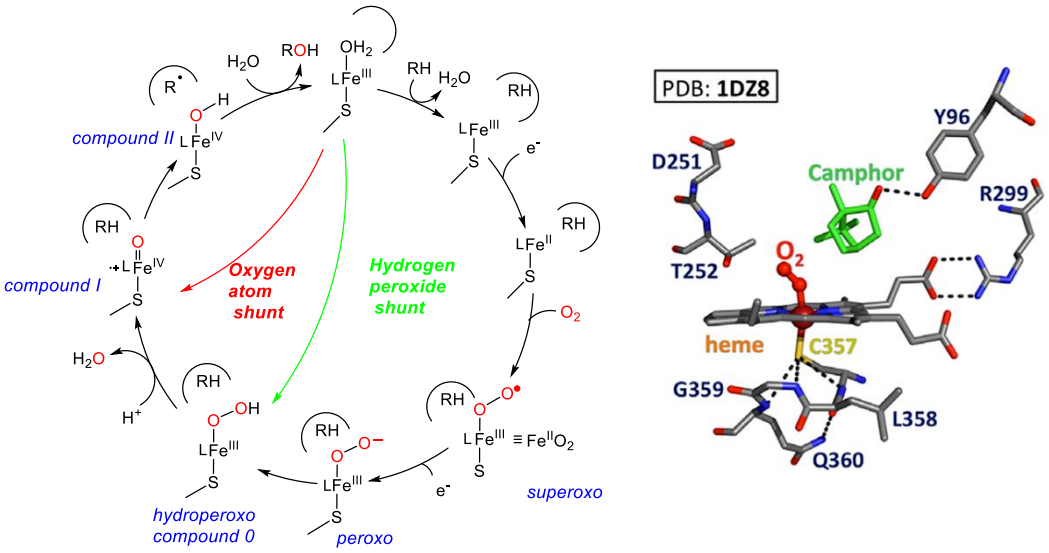

Figure 88 (Gauche) Cycle catalytique proposé pour les enzymes Cyt P450. Toutes les espèces intermédiaires citées ont été observées dans littérature par spectroscopie, mais la structure cristalline des intermédiaires, y compris les Cmpd I et II peroxo et hydroperoxo, n'est pas encore disponible. (Droite) Vue rapprochée du oxy-Cyt P450 mettant en évidence le substrat camphre, le centre hémique hexacoordinné et les interactions critiques de liaison H impliquant le résidu cystéine.

Les porphyrines de Fe et de Mn, en tant que modèles de métalloenzymes de type Cyt-P450, ont une chimie très riche Les travaux classiques des années quatre-vingts de Groves[88, 189] et de Mansuy[171, 190] ont introduit l'étude des espèces de haute valence de Fe ($Fe^{IV}(O)$ et $Fe^{IV}(O)$ π radical cation) préparées en utilisant des donneurs d'oxo comme le H_2O_2 et l'acide métachoroperbezoique (mcpba). Les groupes de Valentine[56-57, 61-62] et Naruta[52, 69-70] sont ensuite concentrés à la préparation et la caractérisation des espèces de type peroxo, superoxo, et hydroperoxo (voir Figure 88). La chimie de ces espèces intermédiaires est récemment revisitée dans les travaux de Karlin.[72, 191] Très récemment aussi, Groves[116-117] et Fujii[95, 97-98] ont étudié la réactivité d'halogénation en présence d'halogénures des espèces de haute valence de Mn et de Fe respectivement. Cependant, tous ces travaux utilisent des agents réducteurs pour fournir les électrons nécessaires au centre métallique pour activer l'oxygène, ou des agents oxydants pour générer les espèces de haute valence

Les exemples d'oxydations aérobies de substrats catalysées par des porphyrines de fer ou de manganèse, par activation électrochimique de O_2, sont extrêmement rares dans la littérature.[118-119] Dans les années 80's, Murray a décrit l'oxygénation aérobie électrochimique des oléfines, catalysée par la porphyrine MnTPPCl dans des solvants organiques, en présence d'anhydride benzoïque.[120] Les auteurs, sur la base des données de voltamétrie cyclique, ont proposé un schéma de mécanisme réactionnel, dont l'espèce oxydant est le complexe Mn^{V}=O.[121]

Plus récemment, Dey et al.,[122] inspirés par les travaux de Collman et al.,[123] ont introduit un système modèle du Cyt-P450 qui se compose de porphyrines de fer immobilisées sur des électrodes d'or à l'aide de SAM (self-assembled monolayer).[124] Le groupe de Dey utilise la spectroscopie Raman à résonance pour caractériser les espèces intermédiaires de porphyrine de Fe attachées sur des groupes terminaux d'imidazole ou de sulfure des SAM sur des électrodes d'or.[125] Dans leur système réactionnel, les porphyrines de Fe immobilisées catalysent l'oxydation des liaisons C-H de molécules organiques simples dans des solutions aqueuses en présence de dioxygène. Les TON obtenus pour ces réactions d'oxydation sont très élevés (à l'ordre de 10.000). [126] Cependant, ces systèmes présentent certains inconvénients tels qu'une stabilité relativement faible et des difficultés de caractérisation complète des espèces à la surface.[125-126]

Dans le présent travail, inspirés par tous ces travaux, nous proposons une approche électrochimique pour générer et caractériser les espèces intermédiaires, et exploiter

leurs potentielles réactivités. Les catalyseurs que nous avons utilisés sont de simples porphyrines de Fe and de Mn, qui sont commerciales. Leurs structures moléculaires sont représentées dans le Schéma 1.

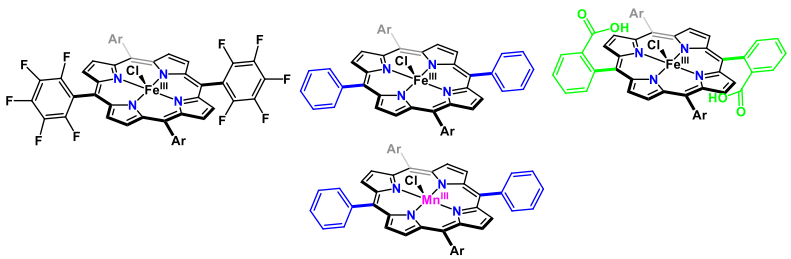

Schéma 1 : Structures moléculaires des porphyrines étudiées dans cette thèse. De gauche à droite : [Fe^{III}(TPP)Cl], [Fe^{III}(F_{20}TPP)Cl] et [Fe^{III}(T----(2-COOH)PP)Cl], et en bas [Mn^{III}TPPCl].

Chapitre 2: Activation électrochimique de O_2 par des porphyrines de Fe ou de Mn

Les intermédiaires de type porphyrine-Fe (ou Mn) -oxygène peuvent être générés par réaction entre les porphyrines M^{II} ou M^{III} et le $O_2^{\bullet-}$ (en utilisant par exemple le KO_2@18-Crown-6).[56, 102] En 2016, Anxolabéhère-Mallart, Fave et al. ont montré que l' espèce $Fe^{III}(OO^{-})$ (peroxo) de la Fe(F_{20}TPP) peut être formée par activation électrochimique du dioxygène dans des solutions aérobies de DMF.[133] Dans ce chapitre, nous revenons sur ces résultats, qui ont servi de base à nos travaux, et nous étudions des nouveaux aspects de cette chimie, en utilisant d'autres porphyrines. Nous démontrons à l'aide de la voltamétrie cyclique et de la spectroélectrochimie UV-Vis que deux analogues de fer (Fe(TPP)Cl et Fe(F_{20}TPP)Cl) réagissent à l'état Fe^{II} avec O_2 pour donner une espèce superoxo $Fe^{III}(OO^{\bullet})$. Ce dernier peut être réduit à un électron pour donner un peroxo ($Fe^{III}(OO^{-})$). Les espèces préparées électrochimiquement ont les mêmes signatures spectrales que les espèces préparées chimiquement rapporté antérieurement dans la littérature.[54, 56, 76] L'analogue Mn(TPP) dans le dichlorométhane (DCM) réagit à l'état Mn^{II} avec O_2 et donne un $Mn^{II}O_2$ qui est réduit immédiatement à la surface de l'électrode au potentiel de formation du Mn^{II}, à -0.4 V vs SCE, pour donner l'espèce $Mn^{II}(OO^{\bullet})$. De façon remarquable, on observe que dans le DMF le complexe Mn^{II}(TPP) ne réagit pas avec O_2, mais il peut réagir avec $O_2^{\bullet-}$ pour donner le $Mn^{II}(OO^{\bullet})$. Le $O_2^{\bullet-}$ est généré à la surface de l'électrode après réduction à un électron de O_2 à -1,1 V vs SCE. Les deux chemins mécanistiques sont montrés sur le Schéma 2. On montre

ainsi dans ce chapitre que l'utilisation de l'électrochimie pour l'activation réductrice de O_2 permet de mieux contrôler la génération d'espèces réactives grâce au contrôle fin du potentiel appliqué à l'électrode.

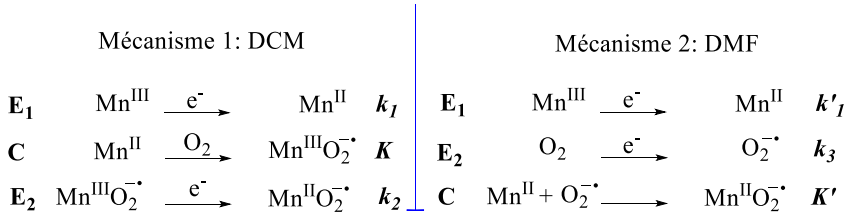

Schéma 2 Mécanismes proposés pour la formation de l'adduit Mn^{II} superoxo dans les deux différents solvants de notre étude.

Chapitre 3 : Activation électrochimique de O_2 par la Fe(F_{20}TPP)Cl en présence de protons.

Ce domaine est très bien étudié par Mayer et al.[129] qui ont montré que la réaction conduit à la cassure de la O-O, plutôt que la liaison Fe-O, et à la production de deux molécules d'eau par molécule de dioxygène (ORR, Oxygen Reduction Reaction). Notre étude par spectroélectrochimie apporte de nouveaux arguments à la discussion sur le mécanisme. En étudiant la catalyse de l'ORR par la porphyrine Fe(F_{20}TPP)Cl, nous avons fait les observations décrites ci-après.

À - 0.6 V vs SCE, l'espèce Fe^{II}(F_{20}TPP) générée à la surface de l'électrode réagit avec O_2 pour former le superoxo, Fe^{III}($OO^{\bullet}$), qui est réduit à un électron pour donner le peroxo, Fe^{III}(OO^{-}). En présence d'un acide fort ($HClO_4$), on observe une augmentation de courant en voltamétrie cyclique. Ce courant est attribué à la protonation de l'espèce peroxo, qui conduit à la cassure de la liaison O-O et à la régénération du Fe^{III}, c'est-à-dire à la catalyse de la réduction de O_2 *via* une voie EPT (Figure 13).

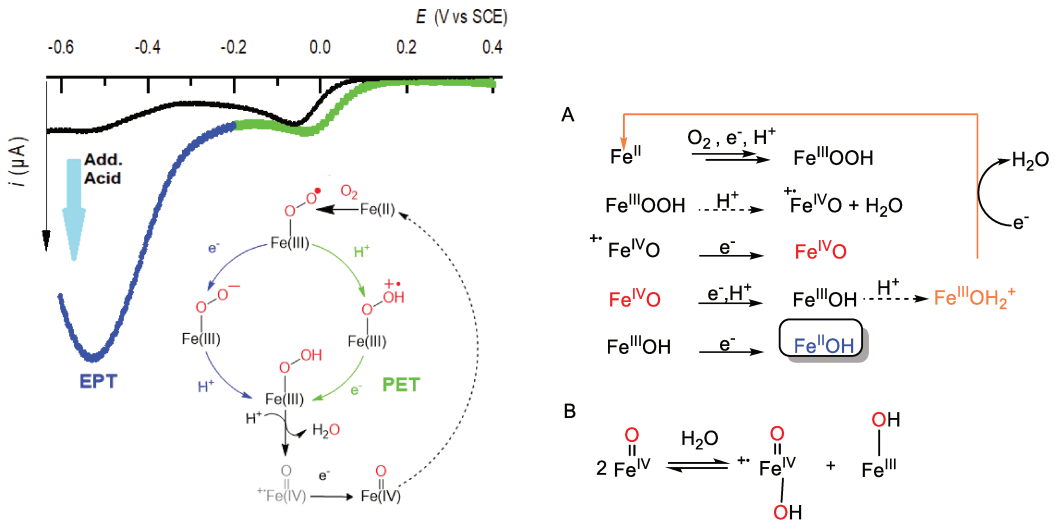

Figure 13 (Gauche) Deux chemins réactionnels pour la catalyse de la réduction de O_2 par la porphyrine Fe(F_{20}TPP)Cl. (Droite) A, intermédiaires réactionnels après la cassure de la liaison O-O B, réaction de dismutation du $Fe^{IV}(O)$.

À des potentiels moins négatifs, à -0.2 V vs SCE, le $Fe^{III}(OO^{\bullet})$ ne peut pas être réduit, mais en présence de $HClO_4$ nous observons quand même un courant catalytique bien que de plus faible intensité que celui observé à -0.6 V vs SCE. Dans ce cas, le $Fe^{III}(OO^{\bullet})$ est d'abord protonée, puis réduit à un électron en hydroperoxo (chemin réactionnel PET, Figure 13). On met ainsi en évidence deux chemins réactionnels conduisant à la cassure de la liaison O-O

Nous avons ensuite observé par spectroélectrochimie UV-Vis, qu'à -0.2 V vs SCE nous pouvons accumuler une espèce $Fe^{II}OH$ issue de la cassure de la liaison O-O à travers le chemin PET (Schéma méchanistique A, Figure 13). À des potentiels plus négatifs, l'espèce $Fe^{IV}(O)$ est accumulée. Ce $Fe^{IV}(O)$résulte de la réduction du $Fe^{IV}(O)$ π radical cation, issu de la cassure de la liaison O-O de l'espèce $Fe^{III}(OOH)$. L'accumulation de l'espèce $Fe^{IV}(O)$ à des potentiels réducteurs, est promue par la réaction de dismutation entre le $Fe^{V}(O)(OH_2)$ et le $Fe^{III}(OH)$ (deux intermédiaires réactionnels) pour donner du $Fe^{IV}(O)$, réaction favorisée par les groupements électroattracteurs C_6F_5 de la porphyrine (Figure 13 B). [94] Les travaux de ce chapitre ont donné lieu à une publication dans le journal *Inorganic Chemistry*. [146]

Chapitre 4 : Utilisation de la microscopie électronique à balayage (SECM) pour sonder les intermédiaires réactionnels Fe^{III} peroxo. Mise en évidence de relations structure-réactivité.

La microscopie électrochimique à balayage (Scanning Electrochemical Microscopy) est une technique de microscopie à sonde locale développée à la fin des années 1980 par l'équipe de Bard.[150] Cette technique consiste à utiliser un montage à 4 électrodes dont une ultramicroélectrode (UME) utilisée comme sonde, approchée d'une surface conductrice (substrat) pour étudier les processus électrochimiques qui ont lieu dans la couche de diffusion.

Pour notre étude nous avons utilisé le mode « substrat générateur-sonde collectrice » (SG/TC).

Dans ce mode, une électrode - sonde collectrice, se trouve à une distance fixe par rapport à une électrode - substrat conducteur et la réactivité d'une espèce redox est sondée dans le gap entre les deux électrodes. Plus précisément, une réaction électrochimique, par exemple la réduction du Fe^{III} en Fe^{II}, a lieu à une électrode classique à carbone vitreux qui est substrat générateur en appliquant un potentiel réducteur. À la seconde électrode, ici une ultramicroélectrode d'or, un LSV est enregistré, et la vague de réoxydation du Fe^{II} généré au substrat générateur est observée. Ainsi, une espèce générée au substrat générateur peut être alors collectée à l'électrode sonde.

De cette façon, nous avons pu démontrer que l'espèce $Fe^{III}(F_{20}TPP)(OO^{-})$ généré à l'électrode substrat à -0.6 V vs SCE, peut être sondée à la ultramicroélectrode grâce à sa vague d'oxydation mono-électronique à +0.5 V vs SCE (Figure 14). Cette méthodologie est ensuite appliquée avec succès pour les porphyrines Fe^{III}(TPP)Cl et Fe^{III}(T-(2-COOH)PP)Cl (Schéma 1). Les LSV enregistrés au substrat et a l'ultramicroélectrode sont ensuite simulés en utilisant Comsol Multiphysics, à l'aide d'un schéma mécanistique simple (Figure 14, droite) en faisant varier deux paramètres, la constante d'association K_{O2} du Fe^{II} avec O_2 at la constante de dissociation k_d de l'espèces $Fe^{III}(OO^{-})$. Les valeurs k_d ont également été estimées par spectroélectrochimie UV-Vis.

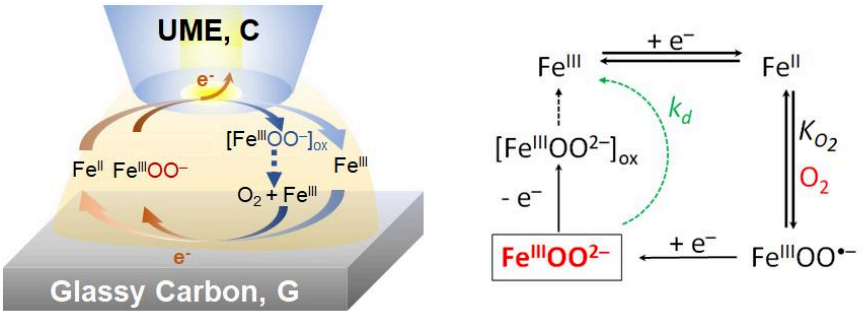

Figure 14 (Gauche)représentation d'une expérience SECM pour la détection de l'espèce peroxo. (Droite) Schéma réactionnel utilisé pour les simulations.

En utilisant les données obtenues, nous pouvons calculer une valeur de K_{O2} et une valeur de ΔpKa pour chacune des trois porphyrines. La constante Ka correspond au couple $Fe^{III}(OO^{-})$/ $Fe^{III}(OOH)$, et pour notre approximation ΔpKa=0 pour l'espèce $Fe^{III}(F_{20}TPP)(OO^{-})$. Nous avons aussi calculé le TOF de chaque porphyrine pour la ORR au milieu organique en présence d'acide. Une analyse détaillée permet de relier les valeurs de TOF avec les valeurs de ΔpKa et K_{O2}. On met ainsi en évidence une relation structure/réactivité, proche à celle publiée par Mayer sur la base de calculs DFT pour la détérminations des valeurs de ΔpKa et K_{O2}.[128]

Les porphyrines comportant des groupements électrodonneurs comme meso-substituants ont des potentiels $E^{0}_{Fe^{III}/Fe^{II}}$ plus négatifs, des K_{O2} et des ΔpKa plus élevées. Leur activité catalytique pour l'ORR (TOF) est également élevée. Nous avons donc pu mettre en évidence à la base des données experimentales, des relations structure-réactivité établies par Mayer de façon théorique.

En conclusion, l'outil SECM permet non seulement de caractériser de différents intermédiaires réactionnels dans une seule expérience, mais aussi, avec l'appui de simulations, de déterminer les paramètres cinétiques et thermodynamiques associées à la réaction ORR. Les travaux de ce chapitre ont donné lieu à une publication dans le journal *Angewandte Chemie*. [168]

Chapitre 5 : Oxygénations et halogénations aérobies de substrats organiques par des porphyrines de fer et de manganèse au cours de l'activation réductrice électrochimique du dioxygène.

L'approche électrochimique pour la génération et la caractérisation d' intermédiaires oxygène-métalloporphyrines des systèmes modèles, est en soi scientifiquement intéressante mais elle constitue également la première étape vers le développement de systèmes capables de reproduire efficacement la réactivité d'oxygénation ou d'halogénation d'enzymes telles que le Cyt-P450. Dans le chapitre 5, sur la base de nos résultats précédents sur le comportement électrochimique des métalloporphyrines vis-à-vis de l'activation de O_2, nous proposons une approche alternative ambitieuse pour réaliser l'oxydation catalytique de substrats organiques, aux antipodes des procédés usuels nécessitant l'utilisation d'oxydants chimiques.

Dans notre approche, nous commençons avec une porphyrine M^{III} (M=Fe, Mn) stable dans l'air, qui après réduction électrochimique à l'état M^{II} réagit avec O_2 de l'air, générant des intermédiaires métalloporphyrines-oxygène. La modification des conditions réactionnelles ou l'utilisation des différents catalyseurs, peut permettre la génération de plusieurs intermédiaires différents qui ont des réactivités différentes :

- Dans le cas des porphyrines de Fe, l'ion Fe^{II} réagit avec O_2 en absence d'acide pour générer des espèces superoxo $Fe^{III}(OO^{\bullet})$. Il a déjà été démontré que de telles espèces peuvent agir comme électrophiles et oxyder les indoles.[54, 137] Nous explorons ici la réactivité des espèces superoxo générées électrochimiquement.
- En présence d'acide, les systèmes Fe^{II}/O_2 peuvent conduire à la cassure de la liaison O-O qui génère des espèces à haute valence Fe-oxo comme nous l'avons montré au chapitre 3. Ces espèces sont des électrophiles puissants capables d'activer les liaisons C-H. [9] Nous explorons également la réactivité d'halogénation électrochimique, en présence d'acide et d'ion chlorure, inspirée par des études antérieures montrant que les espèces Fe-oxo générées chimiquement en présence de chlorure peuvent conduire à l'halogénation de substrats organiques simples.[95, 98]
- Les systèmes Mn^{II}/O_2 sont également capables d'oxyder des substrats organiques en présence d'acides de Lewis dans des conditions électrochimiques. [120-121] Nous revisitons ici cette méthodologie et explorons une éventuelle réactivité d'halogénase en présence de chlorure.

Dans chaque expérience d'électrocatalyse, nous enregistrons d'abord des CV dans les conditions souhaitées, puis effectuons l'électrolyse à potentiel contrôlé dans une configuration appropriée. Les paramètres qui varient dans nos expériences sont (i) le

métal, Fe ou Mn peut avoir des réactivités différentes (ii) le ligand, puisque les substituants méso du cycle porphyrinique affectent également la réactivité des espèces intermédiaires (iii) la présence et la nature de l'acide (protique fort, protique faible ou acide de Lewis), et (iv) le solvant, qui dans certains cas réagit avec les intermédiaires réactionnels.

Les résultats principaux de nos expériences sont les suivants :

1. L'utilisation de la porphyrine Mn(TPP)Cl et d'anhydride benzoïque comme acide de Lewis, conduit à l'oxydation catalytique du cyclooctène. De façon remarquable, le produit d'oxydation et l'époxyde en présence du ligand exogène 1-méthylimidazole, et l'espèce monochloré en présence d'ion chlorure (et absence de 1-méthylimidazole).
2. Dans les mêmes conditions, le styrène est époxydé mais aucun produit de chloration est observé.
3. Le cyclooctène et le styrène sont également époxydé lorsque l'anhydride benzoïque est remplacé par le perfluoro-tert-butanol, un acide protique.
4. En présence de perfluoro-tert-butanol et d'ions chlorure, le benzaldéhyde est oxydé en époxy et en benzaldéhyde, en ration 3:1.
5. Nous avons également démontré la chloration du thymol en utilisant le catalyseur Fe(F_{20}TPP)Cl.

Les TONs que nous avons obtenus pour les réactions catalysées par la Mn(TPP) sont de l'ordre de grandeur de 10, soit un ordre de grandeur plus faible que ceux de la littérature pour des réactions qui utilisent des oxydants chimiques sont de de l'ordre de grandeur de 100.[98, 116-117] En effet, nos résultats sont prometteurs car notre approche utilise l'oxygène de l'air comme oxydant et de l'énergie électrique pour l'activer. Certes il y a encore des améliorations possibles dans notre système pour augmenter les TON. Nous espérons que nos résultats, qui ont été publiés dans le journal *Chemical Communications* [192] contribueront au domaine de l'oxydation aérobie électrochimique des substrats et inspireront d'autres travaux.

Chapitre 6 : Perspectives.

Nos efforts maintenant visent à deux directions. D'un part nous sommes en train de développer un set-up expérimentale pour effectuer des expériences de spectroélectrochimie Raman à résonance. Nous avons déjà pu caractériser le

$Fe^{IV}(F_{20}TPP)(O)$ généré chimiquement dans notre cellule, et aussi qu'il est possible de sonder la transformation électrochimique du Fe^{III} en Fe^{II}. D'autres méthodes de spectroélectrochimie sont développées en parallèle dans le laboratoire, comme par exemple la spectroélectrochimie XAS et IR. D'autre part, nous conduisons des études en hétérogénéisation des catalyseurs avec des matériaux peut couteux, comme les nanotubes des carbones, à des surfaces des électrodes.

Conclusion

Dans les chapitres précédents, nous avons pu montrer que notre approche électrochimique combinant CV, SECM, SEC UV-Vis et électrolyse préparative peut éclairer l'activation de l'O_2 par les porphyrines de Fe et de Mn, et que la Mn(TPP) peut catalyser l'époxydation aérobie électrochimique du cyclooctène et du styrène, ainsi que la chloration du premier. La caractérisation des intermédiaires offre un aperçu avantageux du mécanisme de réaction qui est indispensable pour la compréhension et l'optimisation du système pour réaliser les réaction électrocatalytiques.

References

1. Adam, S. M.; Wijeratne, G. B.; Rogler, P. J.; Diaz, D. E.; Quist, D. A.; Liu, J. J.; Karlin, K. D., Synthetic Fe/Cu Complexes: Toward Understanding Heme-Copper Oxidase Structure and Function. *Chem Rev* **2018,** *118* (22), 10840-11022.

2. Κατάκης, Δ.; Μεθενίτης, Κ.; Μητσοπούλου, Χ.; Πνευματικάκης, Γ., *Ανόργανη Χημεία Β', Τα στοιχεία*. Εκδόσεις Παπαζήση ΑΕΒΕ: Αθήνα, 2002.

3. Schroder, D.; Schwarz, H., *Essays in Contemporary Chemistry: From Molecular Structure towards Biology*. Wiley/VCH: Weinheim, 2001.

4. Conry, R. R., Dioxygen & Related Ligands Based in part on the article Dioxygen & Related Ligands by Rebecca R. Conry & Kenneth D. Karlin which appeared in the Encyclopedia of Inorganic Chemistry, First Edition. In *Encyclopedia of Inorganic and Bioinorganic Chemistry*, John Wiley & Sons: 2011.

5. Warner, J. C.; Cannon, A. S.; Dye, K. M., Green chemistry. *Environmental Impact Assessment Review* **2004,** *24* (7), 775-799.

6. Cavani, F.; Teles, J. H., Sustainability in catalytic oxidation: an alternative approach or a structural evolution? *ChemSusChem* **2009,** *2* (6), 508-34.

7. Teles, J. H.; Hermans, I.; Franz, G.; Sheldon, R. A., Oxidation from Ullmann's Encycolpedia of Industrial Chemistry Wiley-VCH Verlag GmbH & Co KGaA: 2015.

8. Costas, M.; Mehn, M. P.; Jensen, M. P.; Que, L., Dioxygen Activation at Mononuclear Nonheme Iron Active Sites: Enzymes, Models, and Intermediates. *Chem Rev* **2004,** *104* (2), 939-986.

9. Huang, X.; Groves, J. T., Oxygen Activation and Radical Transformations in Heme Proteins and Metalloporphyrins. *Chem Rev* **2018,** *118* (5), 2491-2553.

10. Denisov, I. G.; Makris, T. M.; Sligar, S. G.; Schlichting, I., Structure and Chemistry of Cytochrome P450. *Chem Rev* **2005,** *105* (6), 2253-2278.

11. Ortiz de Montellano, P. R., Hydrocarbon Hydroxylation by Cytochrome P450 Enzymes. *Chem Rev* **2010,** *110* (2), 932-948.

12. Collman, J. P.; Boulatov, R.; Sunderland, C. J.; Fu, L., Functional Analogues of Cytochrome c Oxidase, Myoglobin, and Hemoglobin. *Chem Rev* **2004,** *104* (2), 561-588.

13. Bren, K. L.; Eisenberg, R.; Gray, H. B., Discovery of the magnetic behavior of hemoglobin: A beginning of bioinorganic chemistry. **2015,** *112* (43), 13123-13127.

14. Pauling, L.; Coryell, C. D., The Magnetic Properties and Structure of Hemoglobin, Oxyhemoglobin and Carbonmonoxyhemoglobin. **1936,** *22* (4), 210-216.

15. Weiss, J. J., Nature of the Iron–Oxygen Bond in Oxyhæmoglobin. *Nature* **1964,** *202* (4927), 83-84.

16. McClure, D. S., Electronic Structure of Transition-Metal Complex Ions. *Radiation Research Supplement* **1960,** *2*, 218-242.

17. Goddard, W. A.; Olafson, B. D., Ozone Model for Bonding of an O_2 to Heme in Oxyhemoglobin. **1975,** *72* (6), 2335-2339.

18. Wilson, S. A.; Green, E.; Mathews, I. I.; Benfatto, M.; Hodgson, K. O.; Hedman, B.; Sarangi, R., X-ray absorption spectroscopic investigation of the electronic structure differences in solution and crystalline oxyhemoglobin. **2013,** *110* (41), 16333-16338.

19. Sono, M.; Roach, M. P.; Coulter, E. D.; Dawson, J. H., Heme-Containing Oxygenases. *Chem Rev* **1996,** *96* (7), 2841-2888.

20. Mansuy, D., The great diversity of reactions catalyzed by cytochromes P4501This aricle was invited by Guest Editors Dr John J. Stegeman and Dr David R. Livingstone to be part of a special issue of CBP on cytochrome P450 (Comp. Biochem. Physiol. 121 C, pages 1–412, 1998).1. *Comparative Biochemistry and Physiology Part C: Pharmacology, Toxicology and Endocrinology* **1998,** *121* (1), 5-14.

21. Poulos, T. L.; Finzel, B. C.; Howard, A. J., High-resolution crystal structure of cytochrome P450cam. *J Mol Biol* **1987,** *195* (3), 687-700.

22. Poulos, T. L., Heme Enzyme Structure and Function. *Chem Rev* **2014,** *114* (7), 3919-3962.

23. Wong, L.-L.; Bell, S. G., Iron: Heme Proteins, Mono- & Dioxygenases Based in part on the article Iron: Heme Proteins, Mono- & Dioxygenases by Masanori Sono & John H. Dawson which appeared in the Encyclopedia of Inorganic Chemistry, First Edition. In *Encyclopedia of Inorganic Chemistry*, 2005.

24. Raag, R.; Poulos, T. L., The structural basis for substrate-induced changes in redox potential and spin equilibrium in cytochrome P-450CAM. *Biochemistry* **1989,** *28* (2), 917-922.

25. Davydov, R.; Ledbetter-Rogers, A.; Martásek, P.; Larukhin, M.; Sono, M.; Dawson, J. H.; Masters, B. S. S.; Hoffman, B. M., EPR and ENDOR Characterization of Intermediates in the Cryoreduced Oxy-Nitric Oxide Synthase Heme Domain with Bound l-Arginine or NG-Hydroxyarginine. *Biochemistry* **2002,** *41* (33), 10375-10381.

26. Takahashi, A.; Kurahashi, T.; Fujii, H., Redox potentials of oxoiron(IV) porphyrin pi-cation radical complexes: participation of electron transfer process in oxygenation reactions. *Inorg Chem* **2011,** *50* (15), 6922-8.

27. Rittle, J.; Green, M. T., Cytochrome P450 Compound I: Capture, Characterization, and C-H Bond Activation Kinetics. **2010,** *330* (6006), 933-937.

28. Rittle, J.; Younker, J. M.; Green, M. T., Cytochrome P450: The Active Oxidant and Its Spectrum. *Inorg Chem* **2010,** *49* (8), 3610-3617.

29. Fujii, H., Electronic structure and reactivity of high-valent oxo iron

porphyrins. *Coord Chem Rev* **2001**.

30. Huang, X.; Groves, J. T., Beyond ferryl-mediated hydroxylation: 40 years of the rebound mechanism and C–H activation. *JBIC Journal of Biological Inorganic Chemistry* **2017,** *22* (2), 185-207.

31. Groves, J. T.; McClusky, G. A.; White, R. E.; Coon, M. J., Aliphatic hydroxylation by highly purified liver microsomal cytochrome P-450. Evidence for a carbon radical intermediate. *Biochem Biophys Res Commun* **1978,** *81* (1), 154-160.

32. Lombardi, A.; Nastri, F.; Pavone, V., Peptide-Based Heme−Protein Models. *Chem Rev* **2001,** *101* (10), 3165-3190.

33. Hayaishi, O.; Katagiri, M.; Rothberg, S., Mechanisme of the pyrocatechase reaction. *J Am Chem Soc* **1955,** *77* (20), 5450-5451.

34. Mason, H. S.; Fowlks, W. L.; Peterson, E., Oxygen transfer and electron transport by the phenolase complex1. *J Am Chem Soc* **1955,** *77* (10), 2914-2915.

35. Wilks, A., Heme Oxygenase. In *xPharm: The Comprehensive Pharmacology Reference*, Enna, S. J.; Bylund, D. B., Eds. Elsevier: New York, 2007; pp 1-8.

36. Davydov, R. M.; Yoshida, T.; Ikeda-Saito, M.; Hoffman, B. M., Hydroperoxy-Heme Oxygenase Generated by Cryoreduction Catalyzes the Formation of α-meso-Hydroxyheme as Detected by EPR and ENDOR. *J Am Chem Soc* **1999,** *121* (45), 10656-10657.

37. Hayaishi, O.; Rothberg, S.; Mehler, A. H.; Saito, Y., Studies on oxygenases: enzymatic formation of kynurenine from tryptophan. *J Biol Chem* **1957,** *229* (2), 889-896.

38. Hirata, F.; Hayaishi, O.; Tokuyama, T.; Senoh, S., In Vitro and in Vivo Formation of Two New Metabolites of Melatonin. *J Biol Chem* **1974,** *249* (4), 1311-1313.

39. Efimov, I.; Basran, J.; Thackray, S. J.; Handa, S.; Mowat, C. G.; Raven, E. L., Structure and reaction mechanism in the heme dioxygenases. *Biochemistry* **2011,** *50* (14), 2717-2724.

40. Lewis-Ballester, A.; Batabyal, D.; Egawa, T.; Lu, C.; Lin, Y.; Marti, M. A.; Capece, L.; Estrin, D. A.; Yeh, S.-R., Evidence for a ferryl intermediate in a heme-based dioxygenase. **2009,** *106* (41), 17371-17376.

41. Poulos, T. L., Heme Enzymes. In *Reviews in Cell Biology and Molecular Medicine*, 2006.

42. Valentine, J. S.; Sheridan, R. P.; Allen, L. C.; Kahn, P. C., Coupling between oxidation state and hydrogen bond conformation in heme proteins. **1979,** *76* (3), 1009-1013.

43. Schonbaum, G. R.; Lo, S., Interaction of Peroxidases with Aromatic Peracids and Alkyl Peroxides: Product Analysis. *J Biol Chem* **1972,** *247* (10), 3353-3360.

44. Fujii, H., Chapter 9 Model Complexes of Heme Peroxidases. In *Heme Peroxidases*, The Royal Society of Chemistry: 2016; pp 181-217.

45. Momenteau, M.; Reed, C. A., Synthetic Heme-Dioxygen Complexes. *Chem Rev* **1994,** *94* (3), 659-698.

46. Collman, J. P.; Gagne, R. R.; Reed, C. A.; Robinson, W. T.; Rodley, G. A., Structure of an Iron(II) Dioxygen Complex; A Model for Oxygen Carrying Hemeproteins. **1974,** *71* (4), 1326-1329.

47. Collman, J. P.; Gagne, R. R.; Halbert, T. R.; Marchon, J. C.; Reed, C. A., Reversible oxygen adduct formation in ferrous complexes derived from a picket fence porphyrin. Model for oxymyoglobin. *J Am Chem Soc* **1973,** *95* (23), 7868-7870.

48. Pauling, L., Nature of the Iron–Oxygen Bond in Oxyhæmoglobin. *Nature* **1964,** *203* (4941), 182-183.

49. Li, J.; Noll, B. C.; Oliver, A. G.; Schulz, C. E.; Scheidt, W. R., Correlated ligand dynamics in oxyiron picket fence porphyrins: structural and Mossbauer investigations. *J Am Chem Soc* **2013,** *135* (41), 15627-41.

50. Wilson, S. A.; Kroll, T.; Decreau, R. A.; Hocking, R. K.; Lundberg, M.; Hedman, B.; Hodgson, K. O.; Solomon, E. I., Iron L-Edge X-ray Absorption Spectroscopy of Oxy-Picket Fence Porphyrin: Experimental Insight into Fe–O2 Bonding. *J Am Chem Soc* **2013,** *135* (3), 1124-1136.

51. Tani, F.; Matsu-ura, M.; Nakayama, S.; Ichimura, M.; Nakamura, N.; Naruta, Y., Synthesis and Characterization of Alkanethiolate-Coordinated Iron Porphyrins and Their Dioxygen Adducts as Models for the Active Center of Cytochrome P450: Direct Evidence for Hydrogen Bonding to Bound Dioxygen. *J Am Chem Soc* **2001,** *123* (6), 1133-1142.

52. Tani, F.; Matsu-ura, M.; Ariyama, K.; Setoyama, T.; Shimada, T.; Kobayashi, S.; Hayashi, T.; Matsuo, T.; Hisaeda, Y.; Naruta, Y., Iron Twin-Coronet Porphyrins as Models of Myoglobin and Hemoglobin: Amphibious Electrostatic Effects of Overhanging Hydroxyl Groups for Successful CO/O_2 Discrimination. **2003,** *9* (4), 862-870.

53. Kopf, M.-A.; Neuhold, Y.-M.; Zuberbühler, A. D.; Karlin, K. D., Oxo- and Hydroxo-Bridged Heme-Copper Assemblies Formed from Acid−Base or Metal−Dioxygen Chemistry. *Inorg Chem* **1999,** *38* (13), 3093-3102.

54. Mondal, P.; Wijeratne, G. B., Modeling Tryptophan/Indoleamine 2,3-Dioxygenase with Heme Superoxide Mimics: Is Ferryl the Key Intermediate? *J Am Chem Soc* **2020,** *142* (4), 1846-1856.

55. Sacramento, J. J. D.; Goldberg, D. P., Oxidation of an indole substrate by porphyrin iron(iii) superoxide: relevance to indoleamine and tryptophan 2,3-dioxygenases. *Chem Commun* **2020,** *56* (20), 3089-3092.

56. McCandlish, E.; Miksztal, A. R.; Nappa, M.; Sprenger, A. Q.; Valentine, J. S.; Stong, J. D.; Spiro, T. G., Reactions of superoxide with iron porphyrins in aprotic solvents. A high spin ferric porphyrin peroxo complex. *J Am Chem Soc* **1980,** *102* (12), 4268-4271.

57. Burstyn, J. N.; Roe, J. A.; Miksztal, A. R.; Shaevitz, B. A.; Lang, G.; Valentine, J. S., Magnetic and spectroscopic characterization of an iron porphyrin peroxide complex. Peroxoferrioctaethylporphyrin(1-). *J Am Chem Soc* **1988,** *110* (5), 1382-1388.

58. Friant, P.; Goulon, J.; Fischer, J.; Ricard, L.; Schappacher, M.; Weiss, R.; Momenteau, M., Structural investigation by EXAFS of peroxo-titanium (IV) and iron (III) porphyrinates. *Nouveau journal de chimie (1977)* **1985,** *9* (1), 33-40.

59. Goto, Y.; Wada, S.; Morishima, I.; Watanabe, Y., Reactivity of peroxoiron(III) porphyrin complexes: Models for deformylation reactions catalyzed by cytochrome P-450. *J Inorg Biochem* **1998,** *69* (4), 241-247.

60. Welborn, C. H.; Dolphin, D.; James, B. R., One-electron electrochemical reduction of a ferrous porphyrin dioxygen complex. *J Am Chem Soc* **1981,** *103* (10), 2869-2871.

61. Selke, M.; Sisemore, M. F.; Valentine, J. S., The Diverse Reactivity of Peroxy Ferric Porphyrin Complexes of Electron-Rich and Electron-Poor Porphyrins. *J Am Chem Soc* **1996,** *118* (8), 2008-2012.

62. Selke, M.; Sisemore, M. F.; Ho, R. Y. N.; Wertz, D. L.; Valentine, J. S., Dioxygen activation by iron complexes. The search for reactive intermediates. *J Mol Catal A: Chem* **1997,** *117* (1), 71-82.

63. Khenkin, A. M.; Shteinman, A. A., The mechanism of oxidation of alkanes by peroxo complexes of iron porphyrins in the presence of acylating agents: a model for activation of O2 by cytochrome P-450. *J Chem Soc, Chem Commun* **1984,** (18), 1219-1220.

64. Ohta, T.; Liu, J. G.; Nagaraju, P.; Ogura, T.; Naruta, Y., A cryo-generated ferrous-superoxo porphyrin: EPR, resonance Raman and DFT studies. *Chem Commun (Camb)* **2015,** *51* (62), 12407-10.

65. Duerr, K.; Olah, J.; Davydov, R.; Kleimann, M.; Li, J.; Lang, N.; Puchta, R.; Hubner, E.; Drewello, T.; Harvey, J. N.; Jux, N.; Ivanovic-Burmazovic, I., Studies on an iron(iii)-peroxo porphyrin. Iron(III)-peroxo or iron(II)-superoxo? *Dalton Trans* **2010,** *39* (8), 2049-56.

66. Tajima, K., A possible model of a hemoprotein-hydrogen peroxide complex. *Inorg Chim Acta* **1989,** *163* (1), 115-122.

67. Tajima, K.; Shigematsu, M.; Jinno, J.; Ishizu, K.; Ohya-Nishiguchi, H., Generation of Fe^{III}OEP-hydrogen peroxide complex (OEP = octaethylporphyrinato) by reduction of Fe^{II}OEP-O_2 with ascorbic acid sodium salt. *Journal of the Chemical Society. Chemical communications* **1990,** (2), 144-145.

68. Chang, C. J.; Chng, L. L.; Nocera, D. G., Proton-Coupled O−O Activation on a Redox Platform Bearing a Hydrogen-Bonding Scaffold. *J Am Chem Soc* **2003,** *125* (7), 1866-1876.

69. Liu, J. G.; Ohta, T.; Yamaguchi, S.; Ogura, T.; Sakamoto, S.; Maeda, Y.; Naruta, Y., Spectroscopic characterization of a hydroperoxo-heme intermediate: conversion of

a side-on peroxo to an end-on hydroperoxo complex. *Angew Chem Int Ed Engl* **2009,** *48* (49), 9262-9267.

70. Liu, J.-G.; Shimizu, Y.; Ohta, T.; Naruta, Y., Formation of an End-On Ferric Peroxo Intermediate upon One-Electron Reduction of a Ferric Superoxo Heme. *J Am Chem Soc* **2010,** *132* (11), 3672-3673.

71. Nagaraju, P.; Ohta, T.; Liu, J. G.; Ogura, T.; Naruta, Y., The secondary coordination sphere controlled reactivity of a ferric-superoxo heme: unexpected conversion to a ferric hydroperoxo intermediate by reaction with a high-spin ferrous heme. *Chem Commun (Camb)* **2016,** *52* (45), 7213-6.

72. Kim, H.; Rogler, P. J.; Sharma, S. K.; Schaefer, A. W.; Solomon, E. I.; Karlin, K. D., Heme-Fe(III) Superoxide, Peroxide and Hydroperoxide Thermodynamic Relationships: Fe(III)-O_2(*-) Complex H-Atom Abstraction Reactivity. *J Am Chem Soc* **2020,** *142* (6), 3104-3116.

73. Karlin, K. D.; Kim, H.; Rogler, P. J.; Sharma, S. K.; Schaefer, A. W.; Solomon, E. I., Ferric Heme Superoxide Reductive Transformations to Ferric Heme (Hydro)Peroxide Species: Spectroscopic Characterization and Thermodynamic Implications for H-atom Transfer (HAT). *Angew Chem Int Ed Engl* **2020**.

74. Mondal, P.; Ishigami, I.; Gerard, E. F.; Lim, C.; Yeh, S. R.; de Visser, S. P.; Wijeratne, G. B., Proton-coupled electron transfer reactivities of electronically divergent heme superoxide intermediates: a kinetic, thermodynamic, and theoretical study. *Chem Sci* **2021,** *12* (25), 8872-8883.

75. Brezny, A. C.; Johnson, S. I.; Raugei, S.; Mayer, J. M., Selectivity-Determining Steps in O_2 Reduction Catalyzed by Iron(tetramesitylporphyrin). *J Am Chem Soc* **2020,** *142* (9), 4108-4113.

76. Pegis, M. L.; Martin, D. J.; Wise, C. F.; Brezny, A. C.; Johnson, S. I.; Johnson, L. E.; Kumar, N.; Raugei, S.; Mayer, J. M., Mechanism of Catalytic O_2 Reduction by Iron Tetraphenylporphyrin. *J Am Chem Soc* **2019,** *141* (20), 8315-8326.

77. Bhunia, S.; Rana, A.; Roy, P.; Martin, D. J.; Pegis, M. L.; Roy, B.; Dey, A., Rational Design of Mononuclear Iron Porphyrins for Facile and Selective 4e(-)/4H(+) O_2 Reduction: Activation of O-O Bond by 2nd Sphere Hydrogen Bonding. *J Am Chem Soc* **2018,** *140* (30), 9444-9457.

78. Groves, J. T.; Watanabe, Y., Reactive iron porphyrin derivatives related to the catalytic cycles of cytochrome P-450 and peroxidase. Studies of the mechanism of oxygen activation. *J Am Chem Soc* **1988,** *110* (25), 8443-8452.

79. Nam, W.; Lim, M. H.; Oh, S.-Y.; Lee, J. H.; Lee, H. J.; Woo, S. K.; Kim, C.; Shin, W., Remarkable Anionic Axial Ligand Effects of Iron(III) Porphyrin Complexes on the Catalytic Oxygenations of Hydrocarbons by H_2O_2 and the Formation of Oxoiron(IV) Porphyrin Intermediates by m-Chloroperoxybenzoic Acid. *Angew Chem Int Ed* **2000,** *39* (20), 3646-3649.

80. Nam, W.; Lim, M. H.; Oh, S.-Y., Effect of Anionic Axial Ligands on the Formation of Oxoiron(IV) Porphyrin Intermediates. *Inorg Chem* **2000,** *39* (24), 5572-5575.

81. Balasubramanian, P. N.; Lee, R. W.; Bruice, T. C., Reaction of [meso-tetrakis(2,6-dimethyl-3-sulfonatophenyl)porphinato]iron(III) hydrate with various acyl and alkyl hydroperoxides in aqueous solution. *J Am Chem Soc* **1989,** *111* (23), 8714-8721.

82. Nam, W.; Han, H. J.; Oh, S.-Y.; Lee, Y. J.; Choi, M.-H.; Han, S.-Y.; Kim, C.; Woo, S. K.; Shin, W., New Insights into the Mechanisms of O−O Bond Cleavage of Hydrogen Peroxide andtert-Alkyl Hydroperoxides by Iron(III) Porphyrin Complexes. *J Am Chem Soc* **2000,** *122* (36), 8677-8684.

83. Traylor, T. G.; Tsuchiya, S.; Byun, Y. S.; Kim, C., High-yield epoxidations with hydrogen peroxide and tert-butyl hydroperoxide catalyzed by iron(III) porphyrins: heterolytic cleavage of hydroperoxides. *J Am Chem Soc* **1993,** *115* (7), 2775-2781.

84. Traylor, T. G.; Kim, C.; Richards, J. L.; Xu, F.; Perrin, C. L., Reactions of Iron(III) Porphyrins with Oxidants. Structure-Reactivity Studies. *J Am Chem Soc* **1995,** *117* (12), 3468-3474.

85. Wolak, M.; van Eldik, R., Mechanistic Studies on Peroxide Activation by a Water-Soluble Iron(III)–Porphyrin: Implications for O-O Bond Activation in Aqueous and Nonaqueous Solvents. *Chemistry – A European Journal* **2007,** *13* (17), 4873-4883.

86. Boaz, N. C.; Bell, S. R.; Groves, J. T., Ferryl protonation in oxoiron(IV) porphyrins and its role in oxygen transfer. *J Am Chem Soc* **2015,** *137* (8), 2875-85.

87. Casadei, C. M.; Gumiero, A.; Metcalfe, C. L.; Murphy, E. J.; Basran, J.; Concilio, M. G.; Teixeira, S. C. M.; Schrader, T. E.; Fielding, A. J.; Ostermann, A.; Blakeley, M. P.; Raven, E. L.; Moody, P. C. E., Neutron cryo-crystallography captures the protonation state of ferryl heme in a peroxidase. **2014,** *345* (6193), 193-197.

88. Groves, J. T.; Haushalter, R. C.; Nakamura, M.; Nemo, T. E.; Evans, B. J., High-valent iron-porphyrin complexes related to peroxidase and cytochrome P-450. *J Am Chem Soc* **1981,** *103* (10), 2884-2886.

89. Wołowiec, S.; Latos-Grażyński, L., Oxidation of Iron(III) Tetramesitylporphyrin with Dimethyldioxirane. *Inorg Chem* **1998,** *37* (12), 2984-2988.

90. Sugimoto, H.; Tung, H. C.; Sawyer, D. T., The formation, characterization, and reactivity of the oxene adduct of [tetrakis(2,6-dichlorophenyl)porphinato]iron(III) perchlorate in acetonitrile. Model for the reactive intermediate of cytochrome P-450. *J Am Chem Soc* **1988,** *110* (8), 2465-2470.

91. Costas, M., Selective C–H oxidation catalyzed by metalloporphyrins. *Coord Chem Rev* **2011,** *255* (23-24), 2912-2932.

92. Fujii, H., Effects of the electron-withdrawing power of substituents on the electronic structure and reactivity in oxoiron(IV) porphyrin .pi.-cation radical complexes. *J Am Chem Soc* **1993,** *115* (11), 4641-4648.

93. Bell, S. R.; Groves, J. T., A Highly Reactive P450 Model Compound I. *J Am Chem Soc* **2009,** *131* (28), 9640-9641.

94. Pan, Z.; Newcomb, M., Kinetics and Mechanism of Oxidation Reactions of Porphyrin−Iron(IV)−Oxo Intermediates. *Inorg Chem* **2007,** *46* (16), 6767-6774.

95. Cong, Z.; Kurahashi, T.; Fujii, H., Oxidation of chloride and subsequent chlorination of organic compounds by oxoiron(IV) porphyrin pi-cation radicals. *Angew Chem Int Ed Engl* **2011,** *50* (42), 9935-9.

96. Yokota, S.; Fujii, H., Critical Factors in Determining the Heterolytic versus Homolytic Bond Cleavage of Terminal Oxidants by Iron(III) Porphyrin Complexes. *J Am Chem Soc* **2018,** *140* (15), 5127-5137.

97. Cong, Z.; Yanagisawa, S.; Kurahashi, T.; Ogura, T.; Nakashima, S.; Fujii, H., Synthesis, characterization, and reactivity of hypochloritoiron(III) porphyrin complexes. *J Am Chem Soc* **2012,** *134* (51), 20617-20.

98. Cong, Z.; Kurahashi, T.; Fujii, H., Formation of iron(III) meso-chloro-isoporphyrin as a reactive chlorinating agent from oxoiron(IV) porphyrin pi-cation radical. *J Am Chem Soc* **2012,** *134* (10), 4469-72.

99. Weschler, C. J.; Hoffman, B. M.; Basolo, F., Synthetic oxygen carrier. Dioxygen adduct of a manganese porphyrin. *J Am Chem Soc* **1975,** *97* (18), 5278-5280.

100. Hoffman, B. M.; Weschler, C. J.; Basolo, F., The dioxygen adduct of meso-tetraphenylporphyrinmanganese(II), a synthetic oxygen carrier. *J Am Chem Soc* **1976,** *98* (18), 5473-5482.

101. Hoffman, B. M.; Szymanski, T.; Brown, T. G.; Basolo, F., The dioxygen adducts of several manganese(II) porphyrins. Electron paramagnetic resonance studies. *J Am Chem Soc* **1978,** *100* (23), 7253-7259.

102. Valentine, J. S.; Quinn, A. E., Reaction of superoxide with the manganese(III) tetraphenylporphine cation. *Inorg Chem* **1976,** *15* (8), 1997-1999.

103. VanAtta, R. B.; Strouse, C. E.; Hanson, L. K.; Valentine, J. S., Peroxo(tetraphenylporphinato)manganese(III) and chloro(tetraphenylporphinato)manganese(II) anions. Synthesis, crystal structures, and electronic structures. *J Am Chem Soc* **1987,** *109* (5), 1425-1434.

104. Groves, J. T.; Watanabe, Y.; McMurry, T. J., Oxygen activation by metalloporphyrins. Formation and decomposition of an acylperoxymanganese(III) complex. *J Am Chem Soc* **1983,** *105* (13), 4489-4490.

105. Jin, N.; Lahaye, D. E.; Groves, J. T., A "push-pull" mechanism for heterolytic o-o bond cleavage in hydroperoxo manganese porphyrins. *Inorg Chem* **2010,** *49* (24), 11516-24.

106. Groves, J. T.; Kruper, W. J.; Haushalter, R. C., Hydrocarbon oxidations with oxometalloporphinates. Isolation and reactions of a (porphinato)manganese(V) complex. *J Am Chem Soc* **1980,** *102* (20), 6375-6377.

107. Groves, J. T.; Stern, M. K., Synthesis, characterization, and reactivity of oxomanganese(IV) porphyrin complexes. *J Am Chem Soc* **1988,** *110* (26), 8628-8638.

108. Groves, J. T.; Lee, J.; Marla, S. S., Detection and Characterization of an Oxomanganese(V) Porphyrin Complex by Rapid-Mixing Stopped-Flow Spectrophotometry. *J Am Chem Soc* **1997,** *119* (27), 6269-6273.

109. Jin, N.; Groves, J. T., Unusual Kinetic Stability of a Ground-State Singlet Oxomanganese(V) Porphyrin. Evidence for a Spin State Crossing Effect. *J Am Chem Soc* **1999,** *121* (12), 2923-2924.

110. Nam, W.; Kim, I.; Lim, M. H.; Choi, H. J.; Lee, J. S.; Jang, H. G., Isolation of an Oxomanganese(V) Porphyrin Intermediate in the Reaction of a Manganese(III) Porphyrin Complex and H2O2 in Aqueous Solution. **2002,** *8* (9), 2067-2071.

111. Shimazaki, Y.; Nagano, T.; Takesue, H.; Ye, B.-H.; Tani, F.; Naruta, Y., Characterization of a Dinuclear Mn^{V}=O Complex and Its Efficient Evolution of O_2 in the Presence of Water. **2004,** *43* (1), 98-100.

112. Zhang, R.; Horner, J. H.; Newcomb, M., Laser Flash Photolysis Generation and Kinetic Studies of Porphyrin−Manganese−Oxo Intermediates. Rate Constants for Oxidations Effected by Porphyrin−Mn^{V}−Oxo Species and Apparent Disproportionation Equilibrium Constants for Porphyrin−Mn^{IV}−Oxo Species. *J Am Chem Soc* **2005,** *127* (18), 6573-6582.

113. Jin, N.; Ibrahim, M.; Spiro, T. G.; Groves, J. T., Trans-dioxo Manganese(V) Porphyrins. *J Am Chem Soc* **2007,** *129* (41), 12416-12417.

114. Liu, W.; Cheng, M.-J.; Nielsen, R. J.; Goddard, W. A.; Groves, J. T., Probing the C–O Bond-Formation Step in Metalloporphyrin-Catalyzed C–H Oxygenation Reactions. *ACS Catalysis* **2017,** *7* (6), 4182-4188.

115. Liu, W.; Groves, J. T., Manganese Catalyzed C-H Halogenation. *Acc Chem Res* **2015,** *48* (6), 1727-35.

116. Liu, W.; Groves, J. T., Manganese porphyrins catalyze selective C-H bond halogenations. *J Am Chem Soc* **2010,** *132* (37), 12847-9.

117. Li, G.; Dilger, A. K.; Cheng, P. T.; Ewing, W. R.; Groves, J. T., Selective C-H Halogenation with a Highly Fluorinated Manganese Porphyrin. *Angew Chem Int Ed Engl* **2018,** *57* (5), 1251-1255.

118. Anxolabéhère-Mallart, E.; Bonin, J.; Fave, C.; Robert, M., Small-molecule activation with iron porphyrins using electrons, photons and protons: some recent advances and future strategies. *Dalton Trans* **2019,** *48* (18), 5869-5878.

119. Anxolabéhère-Mallart, E.; Banse, F., Bioinspired molecular catalysts for homogenous electrochemical activation of dioxygen. *Current Opinion in Electrochemistry* **2019,** *15*, 118-124.

120. Creager, S. E.; Raybuck, S. A.; Murray, R. W., An efficient electrocatalytic model cytochrome P-450 epoxidation cycle. *J Am Chem Soc* **1986,** *108* (14), 4225-4227.

121. Creager, S. E.; Murray, R. W., Electrochemical reactivity of manganese(II) porphyrins. Effects of dioxygen, benzoic anhydride, and axial ligands. *Inorg Chem* **1987,** *26* (16), 2612-2618.

122. Sengupta, K.; Chatterjee, S.; Samanta, S.; Bandyopadhyay, S.; Dey, A., Resonance Raman and electrocatalytic behavior of thiolate and imidazole bound iron porphyrin complexes on self assembled monolayers: functional modeling of cytochrome P450. *Inorg Chem* **2013,** *52* (4), 2000-2014.

123. Collman, J. P.; Devaraj, N. K.; Decréau, R. A.; Yang, Y.; Yan, Y.-L.; Ebina, W.; Eberspacher, T. A.; Chidsey, C. E. D., A Cytochrome c Oxidase Model Catalyzes Oxygen to Water Reduction Under Rate-Limiting Electron Flux. *Science* **2007,** *315* (5818), 1565-1568.

124. Chatterjee, S.; Sengupta, K.; Mondal, B.; Dey, S.; Dey, A., Factors Determining the Rate and Selectivity of 4e(-)/4H(+) Electrocatalytic Reduction of Dioxygen by Iron Porphyrin Complexes. *Acc Chem Res* **2017,** *50* (7), 1744-1753.

125. Sengupta, K.; Chatterjee, S.; Samanta, S.; Dey, A., Direct observation of intermediates formed during steady-state electrocatalytic O_2 reduction by iron porphyrins. *Proc Natl Acad Sci U S A* **2013,** *110* (21), 8431-8436.

126. Mukherjee, M.; Dey, A., Electron Transfer Control of Reductase versus Monooxygenase: Catalytic C-H Bond Hydroxylation and Alkene Epoxidation by Molecular Oxygen. *ACS Cent Sci* **2019,** *5* (4), 671-682.

127. Wasylenko, D. J.; Rodriguez, C.; Pegis, M. L.; Mayer, J. M., Direct comparison of electrochemical and spectrochemical kinetics for catalytic oxygen reduction. *J Am Chem Soc* **2014,** *136* (36), 12544-7.

128. Pegis, M. L.; McKeown, B. A.; Kumar, N.; Lang, K.; Wasylenko, D. J.; Zhang, X. P.; Raugei, S.; Mayer, J. M., Homogenous Electrocatalytic Oxygen Reduction Rates Correlate with Reaction Overpotential in Acidic Organic Solutions. *ACS Cent Sci* **2016,** *2* (11), 850-856.

129. Pegis, M. L.; Wise, C. F.; Martin, D. J.; Mayer, J. M., Oxygen Reduction by Homogeneous Molecular Catalysts and Electrocatalysts. *Chem Rev* **2018,** *118* (5), 2340-2391.

130. Ching, H. Y. V.; Anxolabéhère-Mallart, E.; Colmer, H. E.; Costentin, C.; Dorlet, P.; Jackson, T. A.; Policar, C.; Robert, M., Electrochemical formation and reactivity of a manganese peroxo complex: acid driven H_2O_2 generation vs. O–O bond cleavage. *Chemical Science* **2014,** *5* (6), 2304.

131. El Ghachtouli, S.; Ching, H. Y.; Lassalle-Kaiser, B.; Guillot, R.; Leto, D. F.; Chattopadhyay, S.; Jackson, T. A.; Dorlet, P.; Anxolabéhère-Mallart, E., Electrochemical formation of Mn(III)-peroxo complexes supported by pentadentate amino pyridine and imidazole ligands. *Chem Commun (Camb)* **2013,** *49* (50), 5696-8.

132. Ségaud, N.; Anxolabéhère-Mallart, E.; Sénéchal-David, K.; Acosta-Rueda, L.; Robert, M.; Banse, F., Electrochemical study of a nonheme Fe(II) complex in the

presence of dioxygen. Insights into the reductive activation of O_2 at Fe(II) centers. *Chem Sci* **2015,** *6* (1), 639-647.

133. Oliveira, R.; Zouari, W.; Herrero, C.; Banse, F.; Schöllhorn, B.; Fave, C.; Anxolabéhère-Mallart, E., Characterization and Subsequent Reactivity of an Fe-Peroxo Porphyrin Generated by Electrochemical Reductive Activation of O_2. *Inorg Chem* **2016,** *55* (23), 12204-12210.

134. Helms, J. H.; Ter Haar, L. W.; Hatfield, W. E.; Harris, D. L.; Jayaraj, K.; Toney, G. E.; Gold, A.; Mewborn, T. D.; Pemberton, J. E., Effect of meso substituents on exchange-coupling interactions in .mu.-oxo iron(III) porphyrin dimers. *Inorg Chem* **1986,** *25* (14), 2334-2337.

135. D. Lexa, P. R., J.M. Savéant and F. Xu, Methods for investigating the mechanistic and kinetic role of ligand exchange reactions in coordination electrochemistry *J Electroanal Chem* **1985**, 253-279.

136. Zigah, D.; Wang, A.; Lagrost, C.; Hapiot, P., Diffusion of Molecules in Ionic Liquids/Organic Solvent Mixtures. Example of the Reversible Reduction of O2 to Superoxide. *J Phys Chem B* **2009,** *113* (7), 2019-2023.

137. Sacramento, J. J. D.; Goldberg, D. P., Oxidation of an indole substrate by porphyrin iron(iii) superoxide: relevance to indoleamine and tryptophan 2,3-dioxygenases. *Chem Commun (Camb)* **2020**.

138. Sato, T.; Hamada, Y.; Sumikawa, M.; Araki, S.; Yamamoto, H., Solubility of Oxygen in Organic Solvents and Calculation of the Hansen Solubility Parameters of Oxygen. *Industrial & Engineering Chemistry Research* **2014,** *53* (49), 19331-19337.

139. Baglia, R. A.; Zaragoza, J. P. T.; Goldberg, D. P., Biomimetic Reactivity of Oxygen-Derived Manganese and Iron Porphyrinoid Complexes. *Chem Rev* **2017,** *117* (21), 13320-13352.

140. Passard, G.; Dogutan, D. K.; Qiu, M.; Costentin, C.; Nocera, D. G., Oxygen Reduction Reaction Promoted by Manganese Porphyrins. *ACS Catalysis* **2018,** *8* (9), 8671-8679.

141. Shirazi, A.; Goff, H. M., Characterization of superoxide-metalloporphyrin reaction products: effective use of deuterium NMR spectroscopy. *J Am Chem Soc* **1982,** *104* (23), 6318-6322.

142. Savéant, J.-M., Molecular Catalysis of Electrochemical Reactions. Mechanistic Aspects. *Chem Rev* **2008,** *108* (7), 2348-2378.

143. Cofre, P.; Sawyer, D. T., Electrochemical reduction of dioxygen to perhydroxyl (HO2.cntdot.) in aprotic solvents that contain Brönsted acids. *Anal Chem* **1986,** *58* (6), 1057-1062.

144. Costentin, C.; Drouet, S.; Robert, M.; Savéant, J. M., Turnover numbers, turnover frequencies, and overpotential in molecular catalysis of electrochemical reactions. Cyclic voltammetry and preparative-scale electrolysis. *J Am Chem Soc* **2012,** *134* (27), 11235-42.

145. Meunier, B.; de Visser, S. P.; Shaik, S., Mechanism of Oxidation Reactions Catalyzed by Cytochrome P450 Enzymes. *Chem Rev* **2004,** *104* (9), 3947-3980.

146. Kostopoulos, N.; Achaibou, C.; Noël, J. M.; Kanoufi, F.; Robert, M.; Fave, C.; Anxolabéhère-Mallart, E., Electrocatalytic O_2 Activation by Fe Tetrakis(pentafluorophenyl)porphyrin in Acidic Organic Media. Evidence of High-Valent Fe Oxo Species. *Inorg Chem* **2020,** *59* (16), 11577-11583.

147. Izutsu, K., *Acid-base dissociation constants in dipolar aprotic solvents*. Blackwell Scientific Publications: Brookline Village, 1990; Vol. 35.

148. Franke, A.; Fertinger, C.; van Eldik, R., Axial Ligand and Spin-State Influence on the Formation and Reactivity of Hydroperoxo–Iron(III) Porphyrin Complexes. *Chemistry – A European Journal* **2012,** *18* (22), 6935-6949.

149. Achaibou, C. Approche électrochimique multiéchelle de l'activation réductrice de O_2 par un complexe de fer bioinspiré. PhD Thesis. Université de Paris, 2019. https://tel.archives-ouvertes.fr/tel-03199356/.

150. Bard, A. J.; Fan, F. R. F.; Kwak, J.; Lev, O., Scanning electrochemical microscopy. Introduction and principles. *Anal Chem* **1989,** *61* (2), 132-138.

151. Bard, A. J.; Faulkner, L. R., *Electrochemical Methods Fundamentals and Applications*. 2nd Edition ed.; John Wiley & Sons: 2001; p 165, 169, 669.

152. Polcari, D.; Dauphin-Ducharme, P.; Mauzeroll, J., Scanning Electrochemical Microscopy: A Comprehensive Review of Experimental Parameters from 1989 to 2015. *Chem Rev* **2016,** *116* (22), 13234-13278.

153. Mirkin, M. V.; Arca, M.; Bard, A. J., Scanning electrochemical microscopy. 22. Examination of thin solid silver(I) bromide films: ion diffusion in the film and heterogeneous kinetics at the film/solution interface. *The Journal of Physical Chemistry* **1993,** *97* (41), 10790-10795.

154. Stockmann, T. J.; Noël, J. M.; Ristori, S.; Combellas, C.; Abou-Hassan, A.; Rossi, F.; Kanoufi, F., Scanning electrochemical microscopy of Belousov-Zhabotinsky reaction: how confined oscillations reveal short lived radicals and auto-catalytic species. *Anal Chem* **2015,** *87* (19), 9621-30.

155. Nioradze, N.; Chen, R.; Kurapati, N.; Khvataeva-Domanov, A.; Mabic, S.; Amemiya, S., Organic Contamination of Highly Oriented Pyrolytic Graphite As Studied by Scanning Electrochemical Microscopy. *Anal Chem* **2015,** *87* (9), 4836-4843.

156. Tan, S.-y.; Zhang, J.; Bond, A. M.; Macpherson, J. V.; Unwin, P. R., Impact of Adsorption on Scanning Electrochemical Microscopy Voltammetry and Implications for Nanogap Measurements. *Anal Chem* **2016,** *88* (6), 3272-3280.

157. Yang, N.; Zoski, C. G., Polymer Films on Electrodes: Investigation of Ion Transport at Poly(3,4-ethylenedioxythiophene) Films by Scanning Electrochemical Microscopy. *Langmuir* **2006,** *22* (25), 10338-10347.

158. Kai, T.; Zhou, M.; Johnson, S.; Ahn, H. S.; Bard, A. J., Direct Observation of C_2O_4(*-) and CO_2(*-) by Oxidation of Oxalate within Nanogap of Scanning Electrochemical Microscope. *J Am Chem Soc* **2018,** *140* (47), 16178-16183.

159. Carver, C. T.; Matson, B. D.; Mayer, J. M., Electrocatalytic oxygen reduction by iron tetra-arylporphyrins bearing pendant proton relays. *J Am Chem Soc* **2012,** *134* (12), 5444-7.

160. Sengupta, K.; Chatterjee, S.; Dey, A., In Situ Mechanistic Investigation of O_2 Reduction by Iron Porphyrin Electrocatalysts Using Surface-Enhanced Resonance Raman Spectroscopy Coupled to Rotating Disk Electrode (SERRS-RDE) Setup. *ACS Catalysis* **2016,** *6* (10), 6838-6852.

161. Costentin, C.; Dridi, H.; Saveant, J. M., Molecular Catalysis of O_2 Reduction by Iron Porphyrins in Water: Heterogeneous versus Homogeneous Pathways. *J Am Chem Soc* **2015,** *137* (42), 13535-44.

162. Leroux, Y.; Schaming, D.; Ruhlmann, L.; Hapiot, P., SECM Investigations of Immobilized Porphyrins Films. *Langmuir* **2010,** *26* (18), 14983-14989.

163. Okunola, A. O.; Nagaiah, T. C.; Chen, X.; Eckhard, K.; Schuhmann, W.; Bron, M., Visualization of local electrocatalytic activity of metalloporphyrins towards oxygen reduction by means of redox competition scanning electrochemical microscopy (RC-SECM). *Electrochim Acta* **2009,** *54* (22), 4971-4978.

164. Mezour, M. A.; Cornut, R.; Hussien, E. M.; Morin, M.; Mauzeroll, J., Detection of Hydrogen Peroxide Produced during the Oxygen Reduction Reaction at Self-Assembled Thiol−Porphyrin Monolayers on Gold using SECM and Nanoelectrodes. *Langmuir* **2010,** *26* (15), 13000-13006.

165. Lexa, D.; Momenteau, M.; Savéant, J. M.; Xu, F., Electrochemistry of hanging-base basket-handle iron porphyrins. Coordination of iron(II) by the base and dioxygen. *Inorg Chem* **1986,** *25* (27), 4857-4865.

166. Atkins, P.; Paula, J. d., *Atkin's Physical Chemistry, Ninth edition*. Greek Translation: First ed.; Oxford University Press - Greek Translation: Panepistimiakes ekdoseis Kritis: Heraklion, 2014; p 877.

167. Ghiladi, R. A.; Kretzer, R. M.; Guzei, I.; Rheingold, A. L.; Neuhold, Y.-M.; Hatwell, K. R.; Zuberbühler, A. D.; Karlin, K. D., $(F_8TPP)Fe^{II}/O_2$ Reactivity Studies {F_8TPP = Tetrakis(2,6-difluorophenyl)porphyrinate(2−)}: Spectroscopic (UV−Visible and NMR) and Kinetic Study of Solvent-Dependent (Fe/O2 = 1:1 or 2:1) Reversible O_2-Reduction and Ferryl Formation. *Inorg Chem* **2001,** *40* (23), 5754-5767.

168. Noël, J. M.; Kostopoulos, N.; Achaibou, C.; Fave, C.; Anxolabéhère-Mallart, E.; Kanoufi, F., Probing the Activity of Iron Peroxo Porphyrin Intermediates in the Reaction Layer during the Electrochemical Reductive Activation of O_2. *Angew Chem Int Ed Engl* **2020,** *59* (38), 16376-16380.

169. Kadish, K. M.; Autret, M.; Ou, Z.; Tagliatesta, P.; Boschi, T.; Fares, V., Synthesis, Structure, and Electrochemistry of an Electron Deficient μ-Oxo Porphyrin

Dimer, [(TPPBr$_4$)Fe]$_2$O. *Inorg Chem* **1997**.

170. Lexa, D.; Momenteau, M.; Saveant, J. M.; Xu, F., Molecular environment effects on the reactivity of porphyrins. Influence of basket-handle superstructures on the formation of five-coordinated complexes of iron(II) with neutral nitrogen bases. *J Am Chem Soc* **1986,** *108* (22), 6937-6941.

171. Battioni, P.; Renaud, J. P.; Bartoli, J. F.; Reina-Artiles, M.; Fort, M.; Mansuy, D., Monooxygenase-like oxidation of hydrocarbons by hydrogen peroxide catalyzed by manganese porphyrins and imidazole: selection of the best catalytic system and nature of the active oxygen species. *J Am Chem Soc* **1988,** *110* (25), 8462-8470.

172. Li, F.; Van Heuvelen, K. M.; Meier, K. K.; Munck, E.; Que, L., Jr., Sc3+-triggered oxoiron(IV) formation from O2 and its non-heme iron(II) precursor via a Sc3+-peroxo-Fe3+ intermediate. *J Am Chem Soc* **2013,** *135* (28), 10198-201.

173. Getrey, L.; Krieg, T.; Hollmann, F.; Schrader, J.; Holtmann, D., Enzymatic halogenation of the phenolic monoterpenes thymol and carvacrol with chloroperoxidase. *Green Chem* **2014,** *16* (3), 1104-1108.

174. Spiro, T. G.; Strekas, T. C., Resonance Raman spectra of heme proteins. Effects of oxidation and spin state. *J Am Chem Soc* **1974,** *96* (2), 338-345.

175. Soldatova, A. V.; Ibrahim, M.; Spiro, T. G., Electronic structure and ligand vibrations in FeNO, CoNO, and FeOO porphyrin adducts. *Inorg Chem* **2013,** *52* (13), 7478-86.

176. Hashimoto, S.; Mizutani, Y.; Tatsuno, Y.; Kitagawa, T., Resonance Raman characterization of ferric and ferryl porphyrin .pi. cation radicals and the FeIV:0 stretching frequency. *J Am Chem Soc* **1991,** *113* (17), 6542-6549.

177. Burke, J. M.; Kincaid, J. R.; Peters, S.; Gagne, R. R.; Collman, J. P.; Spiro, T. G., Structure-sensitive resonance Raman bands of tetraphenyl and "picket fence" porphyrin-iron complexes, including an oxyhemoglobin analog. *J Am Chem Soc* **1978,** *100* (19), 6083-6088.

178. Cometto, C.; Chen, L.; Lo, P.-K.; Guo, Z.; Lau, K.-C.; Anxolabéhère-Mallart, E.; Fave, C.; Lau, T.-C.; Robert, M., Highly Selective Molecular Catalysts for the CO2-to-CO Electrochemical Conversion at Very Low Overpotential. Contrasting Fe vs Co Quaterpyridine Complexes upon Mechanistic Studies. *ACS Catalysis* **2018,** *8* (4), 3411-3417.

179. Park, M. J.; Lee, J. K.; Lee, B. S.; Lee, Y.-W.; Choi, I. S.; Lee, S.-g., Covalent Modification of Multiwalled Carbon Nanotubes with Imidazolium-Based Ionic Liquids: Effect of Anions on Solubility. *Chem Mater* **2006,** *18* (6), 1546-1551.

180. MacFarlane, D. R.; Choi, J.; Suryanto, B. H. R.; Jalili, R.; Chatti, M.; Azofra, L. M.; Simonov, A. N., Liquefied Sunshine: Transforming Renewables into Fertilizers and Energy Carriers with Electromaterials. *Adv Mater* **2020,** *32* (18), 1904804.

181. Maurin, A.; Robert, M., Noncovalent Immobilization of a Molecular Iron-Based Electrocatalyst on Carbon Electrodes for Selective, Efficient CO2-to-CO Conversion in Water. *J Am Chem Soc* **2016,** *138* (8), 2492-5.

182. Wang, M.; Chen, L.; Lau, T. C.; Robert, M., A Hybrid Co Quaterpyridine Complex/Carbon Nanotube Catalytic Material for CO_2 Reduction in Water. *Angew Chem Int Ed Engl* **2018,** *57* (26), 7769-7773.

183. Venegas, R.; Recio, F. J.; Riquelme, J.; Neira, K.; Marco, J. F.; Ponce, I.; Zagal, J. H.; Tasca, F., Biomimetic reduction of O_2 in an acid medium on iron phthalocyanines axially coordinated to pyridine anchored on carbon nanotubes. *Journal of Materials Chemistry A* **2017,** *5* (24), 12054-12059.

184. Dolby, L. J.; Booth, D. L., The Periodate Oxidation of Indoles1. *J Am Chem Soc* **1966,** *88* (5), 1049-1051.

185. Gueutin, C.; Lexa, D., Low temperature spectroelectrochemistry for the characterization of highly reduced σ-alkyl iron halogenated porphyrins. **1996,** *8* (11), 1029-1033.

186. Weingarth, D.; Foelske-Schmitz, A.; Wokaun, A.; Kotz, R., PTFE Bound Activated Carbon - A Quasi Reference Electrode for Ionic Liquids and Its Application. *ECS Transactions* **2013,** *50* (11), 111-117.

187. Thibon-Pourret, A.; Gennarini, F.; David, R.; Isaac, J. A.; Lopez, I.; Gellon, G.; Molton, F.; Wojcik, L.; Philouze, C.; Flot, D.; Le Mest, Y.; Reglier, M.; Le Poul, N.; Jamet, H.; Belle, C., Effect of Monoelectronic Oxidation of an Unsymmetrical Phenoxido-Hydroxido Bridged Dicopper(II) Complex. *Inorg Chem* **2018,** *57* (19), 12364-12375.

188. Teles, J. H.; Hermans, I.; Franz, G.; Sheldon, R. A., Oxidation. In *Ullmann's Encyclopedia of Industrial Chemistry*, Wiley-VCH Verlag GmbH & Co KGaA: 2015; pp 1-103.

189. Groves, J. T.; Nemo, T. E.; Myers, R. S., Hydroxylation and epoxidation catalyzed by iron-porphine complexes. Oxygen transfer from iodosylbenzene. *J Am Chem Soc* **1979,** *101* (4), 1032-1033.

190. Battioni, P.; Bartoli, J. F.; Leduc, P.; Fontecave, M.; Mansuy, D., A new and efficient biomimetic system for hydrocarbon oxidation by dioxygen using manganese porphyrins, imidazole, and zinc. *J Chem Soc, Chem Commun* **1987,** (10), 791-792.

191. Kim, H.; Rogler, P. J.; Sharma, S. K.; Schaefer, A. W.; Solomon, E. I.; Karlin, K. D., Ferric Heme Superoxide Reductive Transformations to Ferric Heme (Hydro)Peroxide Species: Spectroscopic Characterization and Thermodynamic Implications for H-Atom Transfer (HAT). *Angew Chem Int Ed* **2021,** *60* (11), 5907-5912.

192. Kostopoulos, N.; Banse, F.; Fave, C.; Anxolabéhère-Mallart, E., Modulating alkene reactivity from oxygenation to halogenation via electrochemical O_2 activation by Mn porphyrin. *Chem Commun* **2021,** *57* (10), 1198-1201.

Annex 3: Articles

Inorganic Chemistry

pubs.acs.org/IC Article

Electrocatalytic O_2 Activation by Fe Tetrakis(pentafluorophenyl)porphyrin in Acidic Organic Media. Evidence of High-Valent Fe Oxo Species

Nikolaos Kostopoulos, Célia Achaibou, Jean-Marc Noël, Frédéric Kanoufi, Marc Robert, Claire Fave, and Elodie Anxolabéhère-Mallart*

Cite This: *Inorg. Chem.* 2020, 59, 11577−11583 Read Online

ACCESS | Metrics & More | Article Recommendations | Supporting Information

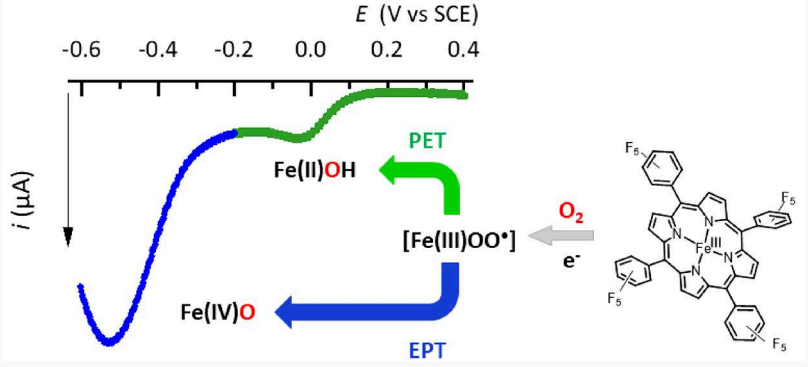

ABSTRACT: O_2 activation under mild conditions remains a weighty challenge for chemists. Herein we report a study of electrochemical O_2 reductive activation catalyzed by $Fe^{III}(F_{20}TPP)Cl$, by means of cyclic voltammetry and UV−vis spectroelectrochemistry in acidic solutions of *N*,*N*-dimethylformamide. Two parallel catalytic pathways have been evidenced occurring at different overpotentials. At high overpotential a classical electron−proton (EPT) pathway where protonation of Fe peroxo ultimately leads to the formation of high-valent Fe oxo species dominates. At low overpotential a proton−electron (PET) pathway involving a hydrosuperoxo species has been identified.

1. INTRODUCTION

Oxidation reactions are of fundamental importance not only in Nature but also in the chemical industry for the production of quantities of organic molecules. In order to successfully perform such processes, stoichiometric harmful oxidants, noble-metal catalysts, and/or high temperatures and pressures are generally required and large quantities of waste are generated.[1] The current economic, environmental, and climatic context demonstrates the need to urgently develop greener processes. In this framework, the ideal "green" oxidant is molecular oxygen (O_2) because it is abundant and environmentally benign (with H_2O as a byproduct).[2] However, the kinetic inertia of O_2 (triplet ground state) necessitates reductive activation steps. Highly efficient and selective oxidation reactions are achieved in Nature by metalloenzymes such as heme-containing CytP450, which unravel the O_2 potent oxidizing power under mild conditions through the so-called reductive activation.[3−6] This corresponds to partial ($2e^-$) and controlled reduction of O_2 bound at the Fe active site via sequential e^- and H^+ transfers to realize O−O bond cleavage. The $4e^-$ and $4H^+$ reduction of O_2 to H_2O (ORR), a key reaction in fuel cell technology, also occurs through activation of O_2 and breaking of O−O bonds at heme-containing active site of cytochrome *c* oxidase.[7,8]

Taking inspiration from the structure and efficient reactivity of these natural systems, researchers have carried out many chemical synthetic efforts over the past decades.[6,9−11] In order to achieve better control over proton and electron delivery, mechanistic studies and identification of reactive intermediates are necessary. Recently, the Mayer group obtained important insights into the kinetics of the ORR catalyzed by Fe porphyrins.[12,13] In a parallel effort, our own approach relies on controlling the production of some key postulated intermediate species such as $Fe^{III}OO^-$ (peroxo), $Fe^{III}OOH$ (hydroperoxo), and $Fe^{IV}O$ (oxo) (Scheme 1) and thus improving the understanding of the whole spectrum of

Received: May 12, 2020
Published: July 29, 2020

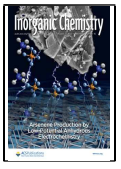

https://dx.doi.org/10.1021/acs.inorgchem.0c01379
Inorg. Chem. 2020, 59, 11577−11583

Scheme 1. Proposed Catalytic Cycle of O_2 Reductive Activation by $Fe^{III}(F_{20}TPP)Cl$[a]

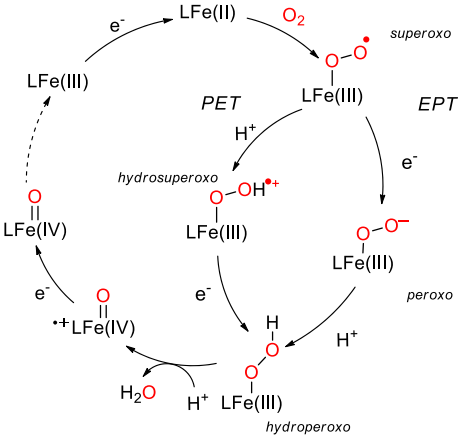

[a]Total charges of intermediates and axial ligands are omitted for clarity.

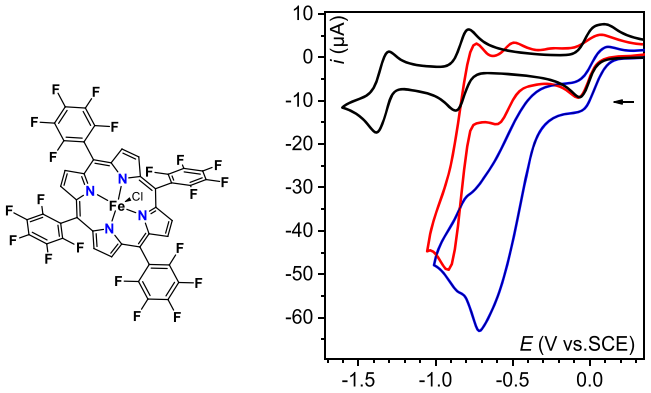

Figure 1. (left) Molecular structure of $Fe^{III}(F_{20}TPP)Cl$. (right) CVs at a glassy-carbon-disk electrode of a 1 mM solution of **1** in DMF + $TBAPF_6$ (0.1 M), with v = 0.1 V s^{-1} and T = 293 K: under argon (black trace); under O_2 (air saturated, 1 mM) (red trace); under O_2 with 10 mM $HClO_4$ (blue trace).

reductive activation of O_2 by Fe porphyrins, not only the ORR reaction.[6−11,14]

In this context, we recently reported the electrochemical generation of $Fe^{III}OO^-$ peroxo and $Fe^{III}OOH$ hydroperoxo species from organic solutions of the commercially available $[Fe^{III}(F_{20}TPP)Cl]$ (**1**; $F_{20}TPP$ = 5,10,15,20-tetrakis-(pentafluorophenyl)porphyrinate) and O_2 in an organic medium.[15] Using complementary techniques, i.e. cyclic voltammetry and low-temperature electronic absorption and EPR spectroscopy, we demonstrated that reductive activation of O_2 could be achieved using $Fe^{III}(F_{20}TPP)Cl$ through electrochemical reduction of the $Fe^{III}OO^•$ superoxo complex (at an electrolysis potential of −0.60 V vs SCE), leading to the formation of the $Fe^{III}OO^-$ peroxo complex (Scheme 1). In this paper, we report the effect of protons and of potential values on the generation and reactivity of such intermediates. This approach allowed us to identify and probe, in addition to the classical electron−proton transfer (EPT), a new and less demanding (occurring at more positive potential) proton−electron transfer (PET) pathway.

2. CYCLIC VOLTAMMETRY UNDER VARIOUS ACIDIC CONDITIONS

Figure 1 shows cyclic voltammograms (CVs) obtained for the iron porphyrin **1** under argon and O_2 and in the presence of acid. Under an argon atmosphere, CVs display three reversible monoelectronic waves corresponding to the successive Fe^{III}/Fe^{II} ($E_{1/2}$ = +0.02 V vs SCE), Fe^{II}/Fe^{I} ($E_{1/2}$ = −0.80 V vs SCE), and Fe^{I}/Fe^{0} ($E_{1/2}$ = −1.31 V vs SCE) reduction processes (Figure 1, black trace).[16] Upon O_2 saturation, a new monoelectronic wave appears at ca. E_{pc} = −0.60 V vs SCE (Figure 1, red trace) attributed to the reduction of $Fe^{III}O_2^•$ into the $Fe^{III}OO^-$ complex (Scheme 1).[15] The large peak at −0.85 V vs SCE in the red trace corresponds to the direct reduction of the excess O_2 in the diffusion layer that is not bound to the Fe. When a strong acid ($HClO_4$) is added, the signal at −0.60 V sharply increases, indicative of a catalytic process[17] (Figure 1, blue trace) attributed to the O_2 catalytic reduction[18] triggered by the protonation of the $Fe^{III}OO^-$ intermediate (Scheme 1). To describe this catalytic process, the direct reduction of O_2 on a glassy-carbon electrode in the presence of protons has to be subtracted. For this purpose, CVs of air-saturated DMF solutions in the absence of porphyrin with various concentrations of $HClO_4$ were recorded (Figure S1, left) and then subtracted from the traces shown in Figure 1. Figure 2A displays the current responses thus obtained at each concentration of $HClO_4$. Figure 2B,C shows the dependence of the peak potential of the $Fe^{III}OO^•/Fe^{III}OO^-$ couple ($E_{p,Fe^{III}OO^•/Fe^{III}OO^-}$) and of the normalized peak current (i_p/i^0) with the concentration of acid. With less than 2 equiv of $HClO_4$ the peak potential of the $Fe^{III}OO^•/Fe^{III}OO^-$ couple ($E_{p,Fe^{III}OO^•/Fe^{III}OO^-}$), initially centered at −0.60 V, slightly

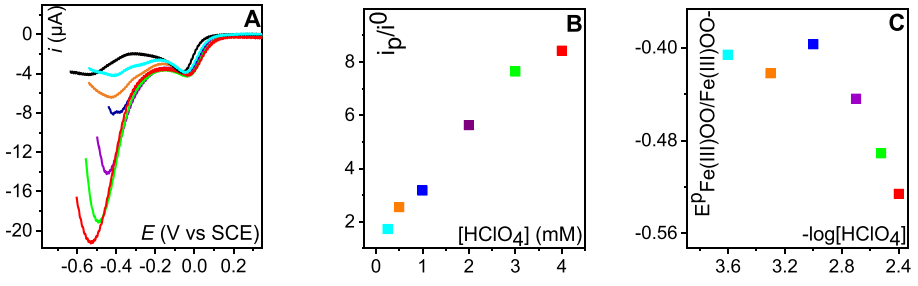

Figure 2. (A) CVs of **1** (0.5 mM) in DMF + $TBAPF_6$ (0.1 M) with v = 0.1 V s^{-1} and T = 293 K at a glassy-carbon electrode, under O_2 (air saturated, 1 mM) (black line) and in the presence of increasing concentrations of $HClO_4$ (0.025 mM/light blue, 0.5 mM/orange, 1 mM/blue, 2 mM/violet, 3 mM/green, and 4 mM/red), after subtraction of the current recorded in the absence of porphyrin (see Figure S1). For clarity only the forward scan is shown. Variation of (B) i_p/i^0 and (C) the peak potential for the $Fe^{III}OO^•/Fe^{III}OO^-$ redox couple with increasing concentrations of acid. The color codes are identical in (A)−(C).

https://dx.doi.org/10.1021/acs.inorgchem.0c01379
Inorg. Chem. 2020, 59, 11577−11583

shifts to a less negative potential, indicative of an electron transfer followed by a fast proton transfer (EC) process. Upon an increase in the acid concentration, the peak potential shifts toward more negative values and the increase of i_p/i^0 indicates a catalytic process. These experimental observations suggest that, in a CytP450-like behavior,[3] the protonation of the $Fe^{III}OO^-$ peroxo intermediate involves more than one proton before the O−O bond breaking occurs and the catalytic process starts. Full kinetic analysis of this catalytic process is beyond the scope of the present study.

In addition to this strong catalytic current, a slight increase in the current at the level of the Fe^{III}/Fe^{II} wave is also observed at +0.02 V vs SCE along with a modest anodic shift. Figure 3

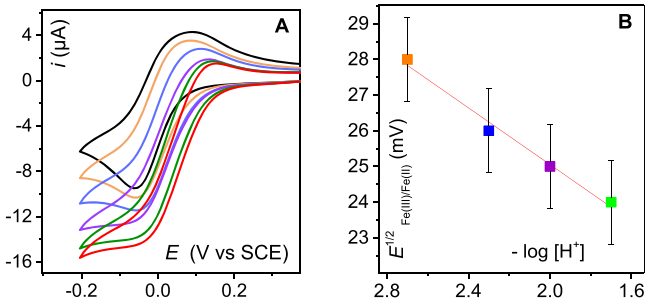

Figure 3. (A) CVs sof **1** (0.5 mM) in DMF + $TBAPF_6$ (0.1 M) with ν = 0.1 V s^{-1} and T = 293 K, at a glassy-carbon electrode under O_2 (air saturated) in the presence of increasing concentrations of $HClO_4$ (1 mM/orange, 2 mM/blue, 5 mM/violet, 10 mM/green, and 20 mM/red). (B) Variation of the half-wave potential of the Fe^{III}/Fe^{II} couple with increasing concentrations of acid. The color codes are identical in (A) and (B).

shows the half-wave potential evolution of this redox couple upon addition of increasing amounts of $HClO_4$ (up to 20 mM). In the absence of acid under argon (black trace) the CV exhibits a classical cathodic wave corresponding to the reduction of $Fe^{III}(F_{20}TPP)Cl$, with the anodic wave being a composite involving two overlapping waves (see the Supporting Information for details). Upon addition of $HClO_4$ in the presence of oxygen, an increase in the cathodic current occurs with a concomitant decrease in the anodic component until the wave becomes fully irreversible and plateaus, indicative of a kinetically controlled catalytic process (Figure 3).

Meanwhile, the addition of $HClO_4$ to a porphyrin solution in the absence of O_2 does not lead to any current variation (Figure S5). These observations indicate that a catalytic process involving both O_2 and protons is triggered at the Fe^{III}/Fe^{II} reduction wave. In this process, the Fe superoxo complex $Fe^{III}O_2^{\bullet}$ generated at the first reduction wave is further protonated in the presence of the strong acid ($HClO_4$) to give the hydrosuperoxo $Fe^{III}O_2^{\bullet}H^+$ species and then the reduced Fe^{III}OOH hydroperoxo intermediate upon one-electron transfer (Figure 4, PET green path). This PET pathway results in the overall O−O bond breaking at a remarkably weakly negative potential of only +0.02 V vs SCE. At this potential, the EPT pathway (Figure 4, blue path) is not thermodynamically accessible, since the $Fe^{III}OO^-$ peroxo species could not be formed.[15] The PET pathway lead to a smaller catalytic current yet occurs at a much lower cathodic potential in comparison to EPT, being energetically more favorable.

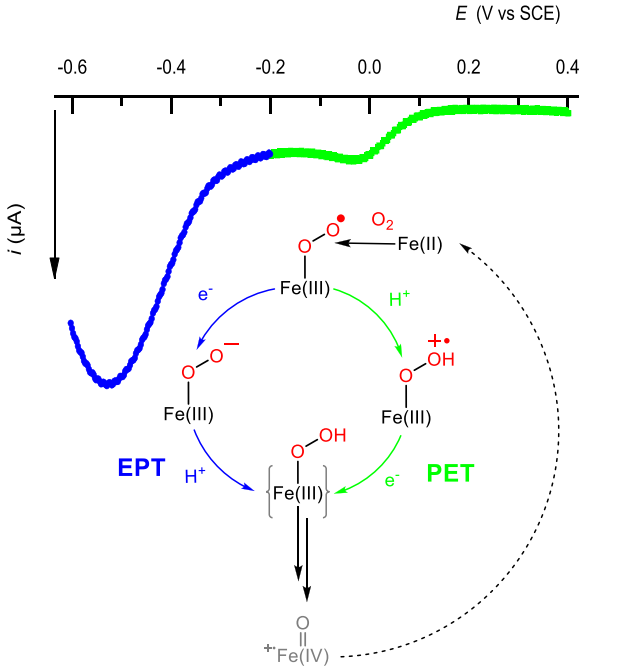

Figure 4. CV of **1** (1 mM) in DMF + $TBAPF_6$ (0.1 M) with ν = 0.1 V s^{-1} and T = 293 K, at a glassy-carbon electrode under O_2 (air saturated) in the presence of 10 mM $HClO_4$ (after subtraction of the current due to the direct reduction of O_2) and parallel catalytic pathways occurring at E_{elec} = −0.10 V vs SCE (green) and at E_{elec} = −0.60 V vs SCE (blue), respectively.

Addition of a weaker acid, fluoro-*tert*-butyl alcohol (pK_a(C-$(CF_3)_3$OH) in DMF = 11.8[19]), has no effect on the Fe^{III}/Fe^{II} wave, while catalytic activity is observed at the level of the peroxo wave (Figure S7), indicating that the superoxo $Fe^{III}O_2^{\bullet}$ is less basic than the peroxo $Fe^{III}OO^-$. The protonation of the Fe superoxo complex by a strong acid is also supported by the linear variation of the half-wave potential with log[$HClO_4$] (Figure 3). Protonation of a superoxo complex has been previously proposed in water with the iron tetrakis(*N*-methyl-4-pyridyl)porphyrin.[20] Recently Mayer et al. also put forward the formation of the hydrosuperoxo intermediate in organic solvents for the Fe tetrakis phenyl porphyrin.[13]

The present study provides new experimental proof and thermodynamic arguments for the accessibility of the PET pathway, the role of which has been recently taken into consideration for mechanistic analysis catalyzed by the ORR with Fe[13] and Co[21] porphyrins. Figure 4 summarizes the two different pathways that lead to the formation of Fe^{III}OOH species and to the subsequent O−O bond cleavage. The PET process occurs at a low overpotential (green path), while the EPT occurs at a higher overpotential (blue path). A change of the catalytic pathway upon modification of the medium has been evidenced in the case of the ORR catalyzed by ferrocene-decorated Fe porphyrins.[22] More recently, thermodynamic aspects of reduction and protonation pathways of a ferric superoxide have been also studied in detail.[23]

It may be noted that the breaking of the O−O bond is not the only possible reaction from Fe^{III}OOH; Fe−O bond breaking is also possible, leading to the formation of H_2O_2. Nevertheless, it has been shown that the production of H_2O_2 is unfavorable in the case of Fe porphyrins in organic solvents and it may be neglected in mechanistic analyses.[12]

https://dx.doi.org/10.1021/acs.inorgchem.0c01379
Inorg. Chem. 2020, 59, 11577−11583

The observed slow catalytic activity along the PET route offers favorable conditions for detecting intermediate species. To do so, we recorded low-temperature UV−vis spectra upon controlled applied potential (E_{elec}) under various acidic conditions.

3. UV−VIS SPECTROELECTROCHEMISTRY AND DETECTION OF INTERMEDIATES

Thin-layer UV−vis spectroelectrochemistry can provide useful information about the intermediate species that are formed in the reaction layer surrounding the electrode surface. Upon reduction of an air-saturated solution of **1** at E_{elec} = −0.20 V vs SCE in the presence of 1 equiv of $HClO_4$, the initial Fe^{III} spectrum (Soret band, λ = 414 nm and Q bands, λ = 500, 558, and 610 nm) evolves to a new spectrum showing a bathochromic shift of the Soret band a (λ = 420 nm) and two new Q bands centered at 530 and 550 nm, respectively (Figure 5A, blue trace). This spectrum is attributed to $Fe^{II}OH^-$ on the basis of a comparison with the spectrum of an electrochemically prepared $Fe^{II}OH^-$ in our own experimental configuration in an argon-saturated DMF solution in the presence of OH^- (see Figure S8). Hydroxo species of the porphyrin under study have been previously generated chemically and characterized by UV−vis spectroscopy in acetonitrile solution.[24] As partial reduction of O_2 to H_2O_2 has been reported as a minor pathway in organic media,[12] we propose that the formation of the OH^- ligand results from O−O bond cleavage (Scheme 2A) rather than an H_2O_2 disproportionation reaction.

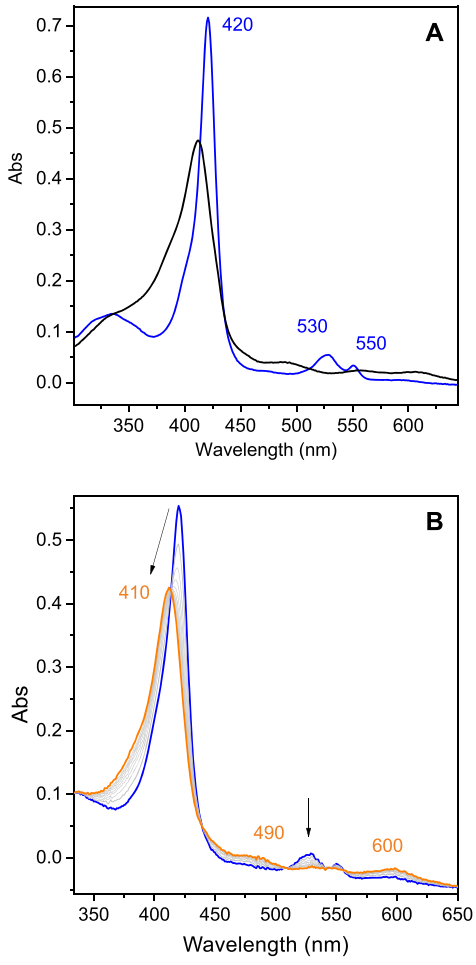

Figure 5. (A) UV−vis spectra of **1** (0.05 mM) in DMF + $TBAPF_6$ (0.2 M) at T = 258 K, under O_2 (air saturated) + $HClO_4$ 0.05 mM at open circuit (black trace) and at E_{elec} = −0.20 V vs SCE after 5 min (blue trace). (B) Spectral evolution of the same solution upon addition of $HClO_4$ 0.5 mM at E_{elec} = −0.20 V vs SCE after 5 min (orange trace).

Scheme 2. (A) Reactions Taking Place in the Catalytic Cycle Involving the $Fe^{II}OH^-$ and $Fe^{IV}O$ Species and (B) Disproportionation Reaction of $Fe^{IV}O$

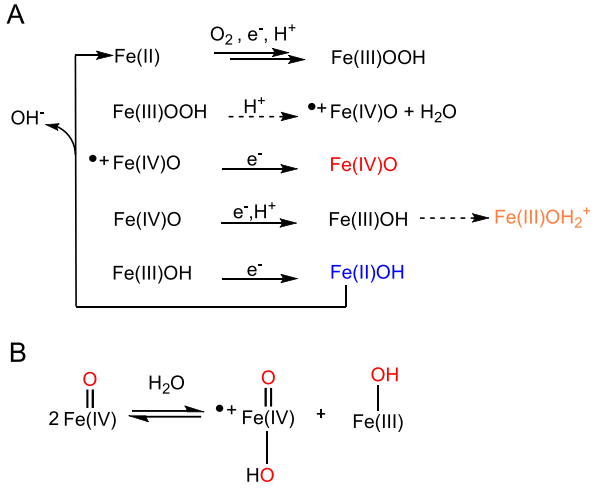

Upon addition of 10 equiv of protons at the same electrode potential (E_{elec} = −0.20 V vs SCE), the spectrum evolves to new features at 410 (Soret band) and 490, 555, and 605 nm (Figure 5B, orange trace) with isosbestic points. This spectrum is close to that of a chemically prepared ferric aquo species (see Figure S9). This new Fe^{III} species is less easily reducible than the initial $Fe^{III}Cl$, and its accumulation stops the catalysis. Once protons in the probed optical part of the spectroelectrochemical cell are consumed, the $Fe^{II}OH^-$ signature appears again (Figure S12).

Upon reduction of an air-saturated solution of **1** at more negative potential (−0.60 V vs SCE) in the presence of 1 equiv of acid, a characteristic Q band at 547 nm with a shoulder at 570 nm appears after ∼5 min (Figure 6, red trace). This spectral signature corresponds to the generation of the high-valent $Fe^{IV}O$ species. Indeed, the spectral signature of this electrochemically produced species matches well to that of a species prepared chemically using an excess of *m*-chloroperbenzoic acid (*m*-CPBA, see Figure S10) and is also in perfect accordance with data previously published.[25−27]

We propose that the $Fe^{IV}O$ π radical cation, resulting from the heterolytic breaking of the O−O bond (Scheme 2) in the $Fe^{III}OOH$ complex, can either react with the solvent or be further reduced to $Fe^{IV}O$ (Figure 4) (by the electrode or in solution by the electrogenerated Fe^{II}). We propose a heterolytic cleavage rather than a homolytic cleavage that could result directly in $Fe^{IV}O$ on the basis of recent studies by Fujii and co-workers, where it is shown that heterolytic cleavage prevails under acidic conditions.[28]

That $Fe^{IV}O$ accumulates under reductive conditions is supported by the disproportionation reaction that takes place between $Fe^{III}OH$ and $Fe^{IV}O$ π radical cation (Scheme 2B) and is known to favor $Fe^{IV}O$ formation in organic media.[23] Under

https://dx.doi.org/10.1021/acs.inorgchem.0c01379
Inorg. Chem. 2020, 59, 11577−11583

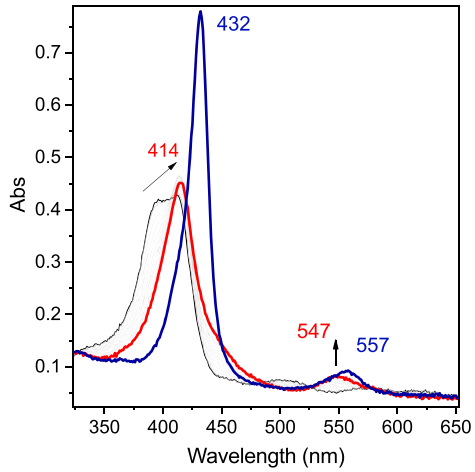

Figure 6. UV−vis spectra of **1** (0.05 mM) in DMF + $TBAPF_6$ (0.2 M), under O_2 (air saturated) + $HClO_4$ (0.05 mM), at T = 258 K (black trace), with E_{elec} = −0.60 V vs SCE after 5 min electrolysis (red trace), and after 20 min electrolysis (navy blue trace).

our conditions, the electrochemically generated $Fe^{III}OH$ species reacts with the $Fe^{IV}O$ π radical cation and leads to $Fe^{IV}O$. The formation of the $Fe^{IV}O$ is further favored by the electron-withdrawing substituents of the porphyrin ring.[25]

The possible involvement of H_2O_2 (obtained from direct O_2 reduction) in the generation of these high-valent Fe species was ruled out by control experiments (see Figure S11).

As shown in Figure 6 (blue trace), when a reductive potential (E_{elec} = −0.60 V vs SCE) is maintained, after about 20 min the $Fe^{IV}O$ signature fades and the characteristic spectral signature of the $Fe^{III}OO^-$ species appears (Soret band at 432 nm and Q band at 557 nm).[15] Such an evolution is attributed to the consumption of protons in the optical part of the spectroelectrochemical cell before diffusion of protons from the bulk solution compensates it, thus stopping the catalysis. Interestingly, the spectral evolution of $Fe^{III}OO^-$ at open circuit as a function of time (minutes scale) displays a signature corresponding to $Fe^{IV}O$ species (see Figure S13), as protons of the bulk solution diffuse to the electrode, supporting the proposition that this latter species originates from the O−O bond cleavage.

The signature of the $Fe^{IV}O$ species has been previously observed by resonance Raman spectroscopy among signatures of other species under electrocatalytic conditions, in the case of Fe porphyrins immobilized onto gold electrodes.[29,30] However, to the best of our knowledge, the present observation of accumulated high-valent species under reductive conditions has never been reported. This high-valent species can react with organic molecules such as cyclohexene and toluene. Preparative-scale electrolysis and analysis of the oxidation products are currently being performed and will be the subject of a future publication.

4. CONCLUSIONS AND PERSPECTIVES

Using the porphyrin $Fe^{III}F_{20}TPP$ as a catalyst for the electrochemical reduction of O_2 and a combination of CV and UV−vis spectroelectrochemistry, we have experimentally evidenced two catalytic pathways depending on the applied potential in acidic solutions of *N*,*N*-dimethylformamide. For the low-overpotential pathway (−0.20 V vs SCE) a proton−electron (PET) pathway involving a hydrosuperoxo species has been identified. At large overpotential (−0.60 V vs SCE) the electron−proton (EPT) pathway prevails where protonation of Fe^{III} peroxo ultimately leading to the formation of high-valent Fe^{IV} oxo species dominates. The observation that two different species are accumulated in each catalytic pathway suggests that the kinetics in the O−O bond cleavage differ. We thus propose that in the EPT case the more efficient catalysis likely favors the production of a larger amount of high-valent species. The unexpected observation of a high-valent Fe species under reductive conditions is quite remarkable and reminiscent of the O_2 reductive activation process observed in the Cyt P450 cycle. It opens the route to electrochemically triggered activity for oxidation processes using O_2 reductive activation.[31−33]

5. EXPERIMENTAL SECTION

5.1. Chemicals. All reagents and solvents were obtained commercially (Acros Organics and Aldrich). [$Fe^{III}(F_{20}TPP)Cl$] (**1**), tetrabutylammonium hexafluorophosphate ($TBAPF_6$) supporting electrolyte, tetrabutylammonium chloride (TBACl), *N*,*N*-dimethylformamide (DMF, anhydrous, 99.8%), silver perchlorate ($AgClO_4$), *m*-chloroperbenzoic acid 77% (m-CPBA), and perchloric acid 70% ($HClO_4$) were used without further purification.

5.2. Cyclic Voltammetry. Electrochemical experiments were run under an argon or O_2 atmosphere. A dry O_2 atmosphere was obtained by purging the solution with compressed air via a glass tube filled with $CaCl_2$. Cyclic voltammograms were recorded on a Metrohm potentiostat (AUTOLAB Model PGSTAT302N). For cyclic voltammetry, the counter electrode used was a Pt wire and the working electrode a glassy-carbon disk (3 mm diameter) carefully polished before each voltammogram with a 1 μm diamond paste, sonicated in an ethanol bath, and then washed with ethanol. The reference electrode used was an SCE (saturated calomel electrode), isolated from the rest of the solution with a fritted bridge. The supporting electrolyte had a concentration of 0.1 M (293 K) or 0.2 M (258 K). Low-temperature regulation was ensured by a Julabo circulation cryostat.

5.3. Low-Temperature UV−Visible Spectroelectrochemistry. Thin-cell spectroelectrochemical data were obtained using a combination of three electrodes in a thin cell (optical length 0.2 cm) mounted on a UV/vis Varian Cary 60 spectrophotometer, equipped with a transparent Dewar.[34] It consists of a 0.1 cm quartz UV−vis−NIR cell surmounted by a glass compartment. A homemade carbon-paper electrode was used as the working electrode, $Ag/AgNO_3$ as the reference electrode, and a platinum grid in a frit as the counter electrode. The entire solution was saturated with air (1 mM O_2), and the cell was cooled to 258 K by a Julabo circulation cryostat.

■ ASSOCIATED CONTENT

Supporting Information

The Supporting Information is available free of charge at https://pubs.acs.org/doi/10.1021/acs.inorgchem.0c01379.

CV analysis and simulation, including the CVs of an air-saturated DMF solution with increasing amounts of protons in the presence and absence of [$Fe^{III}(F_{20}TPP)$-Cl], CVs of [$Fe^{III}(F_{20}TPP)]^+$ (**1-DMF**) and [$Fe^{III}(F_{20}TPP)Cl$] (**1-Cl**) in DMF under argon, and [$Fe^{III}(F_{20}TPP)Cl$] (**1**) in DMF under argon in the presence of $HClO_4$, the variation of the i_p/i^0 ratio of the Fe^{III}/Fe^{II} wave potential of **1-Cl** with acid concentration under catalytic conditions, the effects of $C(CF_3)_3OH$, and CVs of chemically prepared Fe^{III} and $Fe^{IV}O$ species of $Fe(F_{20}TPP)$, UV−vis absorption spectra of chemically prepared Fe^{II} Fe^{III} and $Fe^{IV}O$ species of the $Fe(F_{20}TPP)$, Addition of H_2O_2 to an acidic [$Fe^{III}(F_{20}TPP)Cl$]

https://dx.doi.org/10.1021/acs.inorgchem.0c01379
Inorg. Chem. 2020, 59, 11577−11583

solution, and evolution of $Fe^{III}OH_2^+$ and $Fe^{III}OO^-$ species of Fe(F_{20}TPP) (PDF)

AUTHOR INFORMATION

Corresponding Author

Elodie Anxolabéhère-Mallart − *Université de Paris, Laboratoire d'Electrochimie Moléculaire, CNRS, F-75013 Paris, France;* orcid.org/0000-0002-8708-802X; Email: elodie.anxolabehere u-paris.fr

Authors

Nikolaos Kostopoulos − *Université de Paris, Laboratoire d'Electrochimie Moléculaire, CNRS, F-75013 Paris, France*

Célia Achaibou − *Université de Paris, Laboratoire d'Electrochimie Moléculaire, CNRS, F-75013 Paris, France*

Jean-Marc Noël − *Université de Paris, ITODYS, CNRS, F-75013 Paris, France*

Frédéric Kanoufi − *Université de Paris, ITODYS, CNRS, F-75013 Paris, France;* orcid.org/0000-0002-9784-2380

Marc Robert − *Université de Paris, Laboratoire d'Electrochimie Moléculaire, CNRS, F-75013 Paris, France; Institut Universitaire de France (IUF), F-75005 Paris, France;* orcid.org/0000-0001-7042-4106

Claire Fave − *Université de Paris, Laboratoire d'Electrochimie Moléculaire, CNRS, F-75013 Paris, France;* orcid.org/0000-0001-8146-8702

Complete contact information is available at: https://pubs.acs.org/10.1021/acs.inorgchem.0c01379

Notes

The authors declare no competing financial interest.

ACKNOWLEDGMENTS

We thank the LabEx MiChem part of French state funds managed by the ANR within the Investissements d'Avenir programme under reference ANR-11-IDEX-0004-02 (E.A.-M., C.A., C.F., F.K., and J.-M.N.). N.K. acknowledges funding from the French government for his Ph.D. Partial financial support to M.R. from the Institut Universitaire de France (IUF) is also gratefully acknowledged. E.A.-M. thanks Pr. Frédéric Banse (ICMMO, Université Paris Saclay) for fruitful discussions.

ABBREVIATIONS

PET proton electron transfer
EPT electron proton transfer
DMF *N*,*N*-dimethylformamide
ORR oxygen reduction reaction
CytP450 cytochrome P450 oxidase
SCE standard calomel electrode
CV cyclic voltammetry or cyclic voltammograms

REFERENCES

(1) Cavani, F. J. H.; Teles, J. H. Sustainability in catalytic oxidation: an alternative approach or a structural evolution? *ChemSusChem* **2009**, *2*, 508−534.

(2) Sheldon, R. A.; Arends, I. W. C. E.; Hanefeld, U. In *Green Chemistry and Catalysis*; Wiley-VCH: 2007; pp 133−221.

(3) Meunier, B.; De Visser, S. P.; Shaik, S. Mechanism of Oxidation Reactions Catalyzed by Cytochrome P450 Enzymes. *Chem. Rev.* **2004**, *104*, 3947−3980.

(4) Denisov, I. G.; Makris, T. M.; Sligar, S. G.; Schlichting, I. Structure and Chemistry of Cytochrome P450. *Chem. Rev.* **2005**, *105*, 2253−2278.

(5) Ortiz de Montellano, P. R. Hydrocarbon Hydroxylation by Cytochrome P450 Enzymes. *Chem. Rev.* **2010**, *110*, 932−948.

(6) Huang, X.; Groves, J. T. Oxygen Activation and Radical Transformations in Heme Proteins and Metalloporphyrins. *Chem. Rev.* **2018**, *118*, 2491−2553.

(7) Kaila, V. R. I.; Verkhovsky, M. I.; Wikström, M. Proton-Coupled Electron Transfer in Cytochrome Oxidase. *Chem. Rev.* **2010**, *110*, 7062−7081.

(8) Yoshikawa, S.; Shimada, A. Reaction mechanism of cytochrome c oxidase. *Chem. Rev.* **2015**, *115*, 1936−1989.

(9) Groves, J. T.; Han, Y.-Z. *Models and mechanisms of Cytochrome P450 Action*; Ortiz de Montellano, P. R., Ed.; Springer: Boston, MA, 1995.

(10) Tani, F.; Matsu-Ura, M.; Nakayama, S.; Naruta, Y. Synthetic models for the active site of cytochrome P450. *Coord. Chem. Rev.* **2002**, *226*, 219−226.

(11) Collman, J. P.; Boulatov, R.; Sunderland, C.; Fu, L. Functional Analogues of Cytochrome c Oxidase, Myoglobin, and Hemoglobin. *Chem. Rev.* **2004**, *104*, 561−588.

(12) Pegis, M. L.; McKeown, B. A.; Kumar, N.; Lang, K.; Wasylenko, D. J.; Zhang, X. P.; Raugei, S.; Mayer, J. M. Homogenous Electrocatalytic Oxygen Reduction Rates Correlate with Reaction Overpotential in Acidic Organic Solutions. *ACS Cent. Sci.* **2016**, *2*, 850−856.

(13) Pegis, M. L.; Martin, D. J.; Wise, C. F.; Brezny, A. C.; Johnson, S. I.; Johnson, L. E.; Kumar, N.; Raugei, S.; Mayer, J. M. Mechanism of Catalytic O_2 Reduction by Iron Tetraphenylporphyrin. *J. Am. Chem. Soc.* **2019**, *141*, 8315−8326.

(14) Anxolabéhère-Mallart, E.; Bonin, J.; Fave, C.; Robert, M. Small-molecule activation with iron porphyrins using electrons, photons and protons: some recent advances and future strategies. *Dalton Trans.* **2019**, *48*, 5869−5878.

(15) Oliveira, R.; Zouari, W.; Herrero, C.; Banse, F.; Schöllhorn, B.; Fave, C.; Anxolabéhère-Mallart, E. Characterization and Subsequent Reactivity of an Fe-Peroxo Porphyrin Generated by Electrochemical Reductive Activation of O_2. *Inorg. Chem.* **2016**, *55*, 12204−12210. In this study, the spectrum with λ_{max} = 420, 530, 550 nm has been mistakenly attributed to $Fe^{III}OO^{\bullet}$; according to our current knowledge this spectrum corresponds to the $Fe^{II}OH$ complex.

(16) Gueutin, C.; Lexa, D.; Savéant, J. M.; Wang, D. L. σ-Alkyl Iron Porphyrins from Sterically Encumbered Alkyl Halides and Iron ("0")Porphyrins. *Organometallics* **1989**, *8*, 1607−1613.

(17) Savéant, J.-M. In *Elements of Molecular and Biomolecular Electrochemistry*; Wiley-Interscience: New York, 2006.

(18) Wasylenko, D. J.; Rodríguez, C.; Pegis, M. L.; Mayer, J. M. Direct comparison of electrochemical and spectrochemical kinetics for catalytic oxygen reduction. *J. Am. Chem. Soc.* **2014**, *136*, 12544−12547.

(19) Izutsu, K., *Acid-Base Dissociation Constants in Dipolar Aprotic Solvents*, Blackwell Scientific Publications, Brookline Village, 1990, Vol. *35*, p 166.

(20) Costentin, C.; Dridi, H.; Savéant, J. M. Molecular Catalysis of O_2 Reduction by Iron Porphyrins in Water: Heterogeneous versus Homogeneous Pathways. *J. Am. Chem. Soc.* **2015**, *137*, 13535−13544.

(21) Wang, Y. H.; Schneider, P. E.; Goldsmith, Z. K.; Mondal, B.; Hammes-Schiffer, S.; Stahl, S. S. Bronsted Acid Scaling Relationships Enable Control Over Product Selectivity from O_2 Reduction with a Mononuclear Cobalt Porphyrin Catalyst. *ACS Cent. Sci.* **2019**, *5*, 1024−1034.

(22) Mittra, K.; Chatterjee, S.; Samanta, S.; Dey, A. Selective 4e-/4H + O_2 reduction by an iron(tetraferrocenyl)porphyrin complex: from proton transfer followed by electron transfer in organic solvent to proton coupled electron transfer in aqueous medium. *Inorg. Chem.* **2013**, *52* (24), 14317−25.

(23) Kim, H.; Rogler, P. J.; Sharma, S. K.; Schaefer, A. W.; Solomon, E. I.; Karlin, K. D. Heme-Fe(III) Superoxide, Peroxide and Hydroperoxide Thermodynamic Relationships: Fe^{III}-$O_2^{\bullet-}$ Complex H-Atom Abstraction Reactivity. *J. Am. Chem. Soc.* **2020**, *142* (6), 3104−3116.

(24) Franke, A.; Fertinger, C.; van Eldik, R. Axial Ligand and Spin-State Influence on the Formation and Reactivity of Hydroperoxo–Iron(III) Porphyrin Complexes. *Chem. - Eur. J.* **2012**, *18*, 6935–6949.
(25) Pan, Z.; Newcomb, M. Kinetics and Mechanism of Oxidation Reactions of Porphyrin-Iron(IV)-Oxo Intermediates. *Inorg. Chem.* **2007**, *46*, 6767–6774.
(26) Cong, Z.; Yanagisawa, S.; Kurahashi, T.; Ogura, T.; Nakashima, S.; Fujii, H. Synthesis, characterization, and reactivity of hypochloritoiron(III) porphyrin complexes. *J. Am. Chem. Soc.* **2012**, *134*, 20617–20620.
(27) Cong, Z.; Kurahashi, T.; Fujii, H. Oxidation of chloride and subsequent chlorination of organic compounds by oxoiron(IV) porphyrin pi-cation radicals. *Angew. Chem., Int. Ed.* **2011**, *50*, 9935–9939.
(28) Yokota, S.; Fujii, H. Critical Factors in Determining the Heterolytic versus Homolytic Bond Cleavage of Terminal Oxidants by Iron(III) Porphyrin Complexes. *J. Am. Chem. Soc.* **2018**, *140* (15), 5127–5137.
(29) Sengupta, K.; Chatterjee, S.; Samanta, S.; Dey, A. Direct observation of intermediates formed during steady-state electrocatalytic O_2 reduction by iron porphyrins. *Proc. Natl. Acad. Sci. U. S. A.* **2013**, *110*, 8431–8436.
(30) Sengupta, K.; Chatterjee, S.; Dey, A. In Situ Mechanistic Investigation of O_2 Reduction by Iron Porphyrin Electrocatalysts Using Surface-Enhanced Resonance Raman Spectroscopy Coupled to Rotating Disk Electrode (SERRS-RDE) Setup. *ACS Catal.* **2016**, *6* (10), 6838–6852.
(31) Minteer, S.; Baran, P. Electrifying Synthesis: Recent Advances in the Methods, Materials, and Techniques for Organic Electrosynthesis. *Acc. Chem. Res.* **2020**, *53* (3), 545–546.
(32) Anxolabéhère-Mallart, E.; Banse, F. Bioinspired molecular catalysts for homogenous electrochemical activation of dioxygen. *Current Opinion in Electrochemistry* **2019**, *15*, 118–124.
(33) Sengupta, K.; Chatterjee, S.; Samanta, S.; Bandyopadhyay, S.; Dey, A. Resonance Raman and electrocatalytic behavior of thiolate and imidazole bound iron porphyrin complexes on self assembled monolayers: functional modeling of cytochrome P450. *Inorg. Chem.* **2013**, *52* (4), 2000–14.
(34) Gueutin, C.; Lexa, D. Low temperature spectroelectrochemistry for the characterization of highly reduced σ-alkyl iron halogenated porphyrins. *Electroanalysis* **1996**, *8*, 1029–1033.

https://dx.doi.org/10.1021/acs.inorgchem.0c01379
Inorg. Chem. 2020, 59, 11577–11583

Molecular Electrochemistry Hot Paper

Zitierweise: *Angew. Chem. Int. Ed.* **2020**, *59*, 16376–16380
Internationale Ausgabe: doi.org/10.1002/anie.202004977
Deutsche Ausgabe: doi.org/10.1002/ange.202004977

Probing the Activity of Iron Peroxo Porphyrin Intermediates in the Reaction Layer during the Electrochemical Reductive Activation of O_2

Jean-Marc Noel, Nikolaos Kostopoulos, Célia Achaibou, Claire Fave, Elodie Anxolabéhère-Mallart,* and Frédéric Kanoufi**

Abstract: *Herein we report the first example of using scanning electrochemical microscopy (SECM) to quantitatively analyze O_2 reductive activation in organic media catalyzed by three different Fe porphyrins. For each porphyrin, SECM can provide in one single experiment the redox potential of various intermediates, the association constant of Fe^{II} with O_2, and the pK_a of the $Fe^{III}(OOH^-)$/ $Fe^{III}(OO^{2-})$ couple. The results obtained can contribute to a further understanding of the parameters controlling the catalytic efficiency of the Fe porphyrin towards O_2 activation and reduction.*

Oxidations are an important class of reactions in the chemical industry for the production of huge quantities of intermediate and final products. In the current economic and environmental context, the ideal oxidant is O_2 as it is abundant and benign (H_2O as by-product).[1] In nature, this O_2 activation is achieved through the so-called reductive activation and corresponds to a partial and controlled reduction of O_2 bound at a metal active site via sequential e^- and H^+ transfers. Cleavage of the O–O bond generates the reactive high-valent oxygen species. O_2 activation under mild conditions using earth-abundant-metal catalysts has thus become a major focus in heterogeneous, homogeneous, and biological catalysis.[2]

The use of Fe porphyrins (Figure 1 A) is an interesting biomimetic approach for O_2 activation, as Fe^{II} can reproduce the metabolic transformation catalyzed by Fe enzymes such as CytP450.[3,4] The first step of the catalytic cycle is the binding of O_2 to Fe^{II} to form an $Fe^{III}(OO^{\bullet-})$ (superoxo) intermediate which can be ultimately reduced to a $Fe^{III}(OO^{2-})$ (peroxo) intermediate (Figure 2 A). Due to their transient character, the isolation and spectroscopic characterization of such metal-bound reactive oxygen intermediates usually relies on their chemical generation and cryogenic trapping.[5] In the case of O_2 electrochemical activation, owing to the binding of the different O_2 reactive species at the metal active center, Fe porphyrins act as inner-sphere homogeneous catalysts, meaning that they serve as an electron shuttle (or a redox mediator) between the electrode and the metal-bound O_2 species.[6] Efficient electrocatalysis then engages the reactive intermediates in a thin layer adjacent the electrode, which impedes the direct observation of their (electro)chemical reactivity. Henceforth, the rational benchmarking of electrocatalysts, relying on structure–activity relationships regarding the formation or activity of such intermediates, is mostly based on thermodynamic arguments and at best DFT computations.[7]

Scanning electrochemical microscopy (SECM) offers an elegant approach to capture, quantify, and characterize short-lived intermediates,[8,9] including those in complex molecular homogeneous catalytic systems.[9] Here, the substrate generation–tip collection (SG/TC) mode is employed, as shown in Figure 1 B and detailed in Section 1 of the Supporting Information, SI. Briefly, the SECM is mounted inside a glove bag, allowing a controlled O_2 or Ar atmosphere and minimizing water contamination. A macroelectrode (a glassy carbon generator, G) is used to activate O_2 reduction by Fe porphyrin. The porphyrin in the Fe^{III} state, is reduced at G,

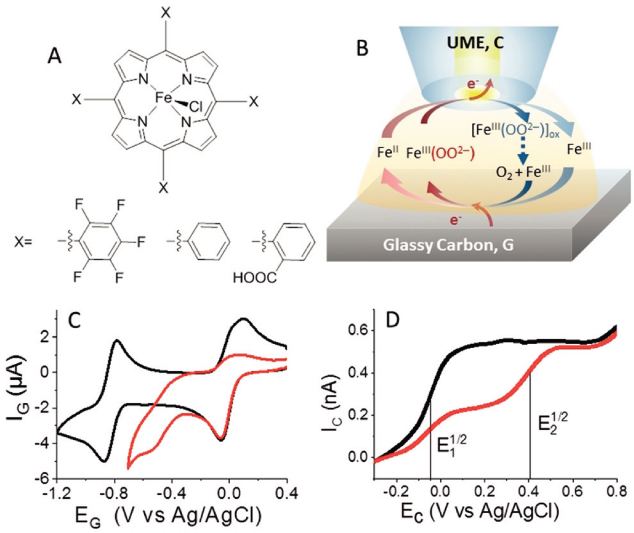

Figure 1. A) Various Fe porphyrins used in this work: $Fe^{III}(F_{20}TPP)Cl$, $Fe^{III}(TPP)Cl$, $Fe^{III}((2\text{-}CO_2H)_4TPP)Cl$; B) Setup used for a typical SECM investigation in the SG/TC mode of O_2 activation by Fe porphyrins. C) CVs recorded at GC electrode (G, 3 mm diameter) at $\nu = 0.1\ V s^{-1}$ and D) LSVs recorded at a gold UME (C, 25 µm diameter) at $\nu = 20\ mV s^{-1}$, in SG/TC mode, held at $d = 8 \pm 2$ µm from G, polarized at $E_C = -0.7$ V vs. Ag/AgCl, in DMF 0.1 M $TBAPF_6$ with 0.5 mM $[(FeF_{20}TPP)Cl]$ under argon (black trace) and with 1 mM O_2 (red trace).

[*] Dr. J.-M. Noel, Dr. F. Kanoufi
Université de Paris, ITODYS, CNRS
75006 Paris (France)
E-mail: jean-marc.noel@univ-paris-diderot.fr
frederic.kanoufi@univ-paris-diderot.fr
N. Kostopoulos, Dr. C. Achaibou, Dr. C. Fave,
Dr. E. Anxolabéhère-Mallart
Université de Paris, Laboratoire d'Electrochimie Moléculaire, CNRS
75006 Paris (France)
E-mail: elodie.anxolabehere@univ-paris-diderot.fr
Supporting information and the ORCID identification number(s) for the author(s) of this article can be found under: https://doi.org/10.1002/anie.202004977.

while, simultaneously the electrogenerated intermediates are collected that is, reoxidized at a 25 μm gold UME tip (collector, C) at controlled distance from G.

The activation of O_2 by Fe porphyrin had been previously studied in generation–collection configurations; however, this was mostly limited to the probing of final products (H_2O_2) at ring-disk electrodes.[10] SECM offers higher collection efficiency, at smaller and controllable generator–collector gap separation.[11] In the case SECM studies of porphyrin, surface charge transfer rates have been probed[12] and, during O_2 reduction, only final products have been detected.[13] Here it will allow deeper mechanistic insights through the real-time in situ probing of the metal-oxo intermediates formed during O_2 activation.

We focus here on the first intermediate produced in non-acidic medium, the $Fe^{III}(OO^{2-})$ (peroxo) adduct, for three porphyrins showing, based on earlier work,[7,14] different electronic density ($Fe(F_{20}TPP)Cl$, Fe(TPP)Cl, and $Fe((2\text{-}CO_2H)_4TPP)Cl$). New thermodynamic and kinetic parameters are experimentally obtained and related to earlier DFT calculations. This information, obtained in the absence of H^+, is then related to the efficiency of these catalysts for O_2 reduction in the presence of H^+.

Cyclic voltammograms (CVs) at G, for the reduction of $[(Fe^{III}F_{20}TPP)Cl]$ obtained under Ar and O_2, are shown in Figure 1C. Under Ar (black trace), the CV exhibits two successive reversible reductions steps: Fe^{III}/Fe^{II} with $E^0_{Fe^{III}/Fe^{II}} = -0.08$ V and Fe^{II}/Fe^{I} with $E^0_{Fe^{II}/Fe^{I}} = -0.9$ V. After introduction of O_2 in the solution (red trace), a new irreversible reduction, slightly less cathodic than the $O_2/O_2^{\bullet-}$ feature, appeared at $E^p_{Fe^{III}(OO^{\bullet-})/Fe^{III}(OO^{2-})} \approx -0.6$ V. In the absence of H^+, it is assigned to the reduction of the end-on superoxo adduct $Fe^{III}(OO^{\bullet-})$ into a side-on peroxo $Fe^{III}(OO^{2-})$. Indeed, upon reduction, significant electronic reshuffling occurs as well as a change of the coordination mode of the O_2 ligand from end-on to side-on.[5a,d,14]

In order to probe the reactivity of these Fe porphyrin–O_2 intermediates, SECM SG/TC experiments were performed holding the potential of G at $E_G = -0.7$ V, while sweeping anodically, in a LSV curve, the UME potential, E_C. Under Ar, the LSV at C probes a single oxidation event at the half-wave potential $E^{1/2}_{1,C} \approx -0.05$ V, attesting to the collection of Fe^{II} (black trace, Figure 1D). Under O_2, the LSV at C (red trace, Figure 1D) presents an additional second oxidation wave at $E^{1/2}_{2,C} \approx 0.4$ V. This new wave is attributed to the oxidation of $Fe^{III}(OO^{2-})$ probed directly in the diffusion layer of G corroborating its relative stability.[14] First, the absence of a collection current at the SECM tip for E_C close to $E^p_{Fe^{III}(OO^{\bullet-})/Fe^{III}(OO^{2-})}$ indicates that the reoxidation of $Fe^{III}(OO^{2-})$ does not yield $Fe^{III}(OO^{\bullet-})$, likely owing to the change in O_2 coordination within the porphyrin complex during the electron transfer steps.[5a,d,14] As a consequence, the $Fe^{III}(OO^{\bullet-})/Fe^{III}(OO^{2-})$ couple does not behave here as a reversible system, except at low temperature (210 K).[5d] Instead the oxidation of $Fe^{III}(OO^{2-})$ produces a different species, namely $Fe^{III}(OO^{2-})_{ox}$ at a much more anodic potential ca. 0.4 V than that at which it is generated. Hence, the formation and oxidation of $Fe^{III}(OO^{2-})$ involve two different irreversible redox couples, that is, $Fe^{III}(OO^{\bullet-})/Fe^{III}(OO^{2-})$ and $Fe^{III}(OO^{2-})_{ox}/Fe^{III}(OO^{2-})$; the former reductive formation is located at ca. −0.6 V while the latter oxidation is located at ca. 0.4 V.

Interestingly, under O_2, the sum of the current contributions corresponding to the oxidative collection of Fe^{II}, $I_{Fe^{II}}$, and to that of $Fe^{III}(OO^{2-})$, $I_{Fe^{III}(OO^{2-})}$, matches the current plateau for Fe^{II} collection under Ar (Figure 1D). The conservation of the faradaic balance suggests $Fe^{III}(OO^{2-})$ is oxidized at C, in a one-electron exchange, into $[Fe^{III}(OO^{2-})]_{ox}$ (Figure 2A), which dissociates to a Fe^{III}, maintaining the feedback loop at G. The decrease of $I_{Fe^{II}}$ at C agrees qualitatively with the loss of reversibility on the oxidation of Fe^{II} to Fe^{III} observed on the CV at G (Figure 1C).

Thin-layer UV/Vis spectroelectrochemistry experiments show that in a solution of electrochemically generated $Fe^{III}(OO^{2-})$, if a potential of 0.6 V is applied, a spectral signature similar to that of the starting Fe^{III} species appears (see SI, Section 2). We propose that the oxidation of the species is followed by chemical decomposition possibly by release of O_2 as suggested by the oxidation of chemically prepared non-heme $Fe^{III}(OO^{2-})$.[15] The SECM experiments corroborate a similar reaction scheme.

The relevance of the SECM probing of this reaction path was tested with COMSOL® simulations (see SI, Section 3). In the absence of a proton source, the simplified reaction scheme in Figure 2A was simulated. The irreversible reductive formation of $Fe^{III}(OO^{2-})$ and its irreversible oxidation are characterized by two different formal potentials, E^0_2 and E^0_3 ($E^0_2 < E^0_3$). The model also considers 1) the association between O_2 and Fe^{II} described by the equilibrium constant K_{O_2}, and 2) the chemical stability of the peroxo derivative, $Fe^{III}(OO^{2-})$, through a first-order decomposition rate constant, k_d. The first-order nature of k_d is confirmed spectroelectrochemically (see Figure S2C, SI). The influence of both parameters on the simulated LSVs at G and C is presented in Figure 2B–E.

In Figure 2B, the higher K_{O_2}, the higher and less cathodic the reduction peak of $Fe^{III}(OO^{\bullet-})$ is at G. Meanwhile at C, increasing K_{O_2} results in a drop of the collection of Fe^{II}, $I_{Fe^{II}}$ in favor of that of $Fe^{III}(OO^{2-})$, $I_{Fe^{III}(OO^{2-})}$ (overall decrease of the ratio $I_{Fe^{II}}/I_{Fe^{III}(OO^{2-})}$). Noteworthy, even for weak binding ($K_{O_2} < 1\,M^{-1}$) the $Fe^{III}(OO^{2-})$ intermediate could be collected at C, whereas its formation cannot be detected at G. Conversely for strong binding ($K_{O_2} > 100\,M^{-1}$) only $Fe^{III}(OO^{2-})$ is collected at C (though distance dependent) whereas the feature corresponding to the reduction of $Fe^{III}(OO^{\bullet-})$ to $Fe^{III}(OO^{2-})$ at G is still affected by K_{O_2}. However, absolute determination of K_{O_2} only from the LSV curves at G is delicate. It indeed requires prior knowledge about the $Fe^{III}(OO^{\bullet-})$ E^0 and is subject to baseline correction uncertainties owing to the nearby $O_2/O_2^{\bullet-}$ reduction feature (see the LSV in Figure 3). Figure 2B,C suggests the dual G and C responses remove such uncertainties.

The complexity in the mechanistic determination is further stressed by the chemical instability of the peroxo derivative, $Fe^{III}(OO^{2-})$. Thin-layer UV/Vis spectroelectrochemistry (Section 2, SI) revealed that the electrogenerated $Fe^{III}(OO^{2-})$ complex decomposes with time into Fe^{III}. This evolution was modeled by the rate constant k_d, (arrows

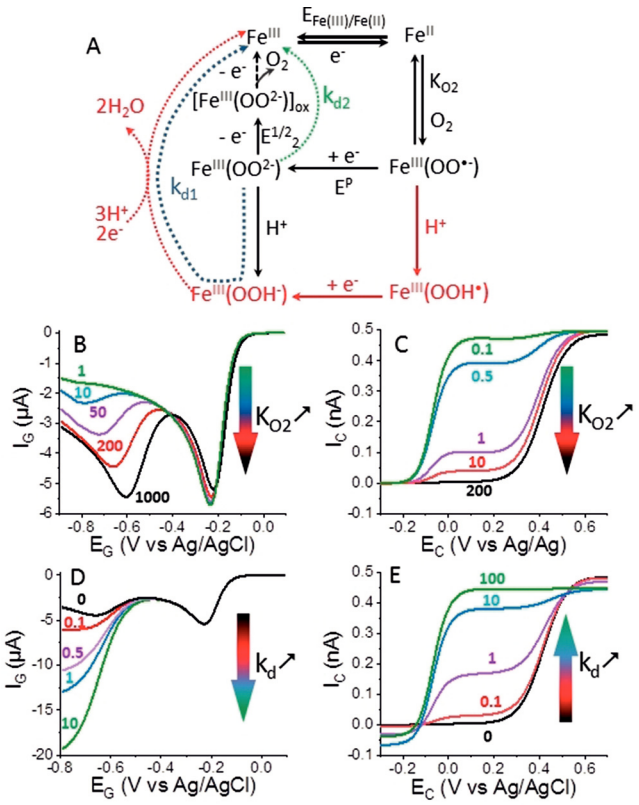

Figure 2. A) Mechanistic scheme: the black and green (k_{d2}) or blue (k_{d1}) parts correspond to the reaction cycle used for the simulations (see Section 3, SI,) whereas the red pathway (involving H^+) is related to the TOF of the $4e^-/4H^+$ reduction of O_2 to water determined in acidic medium. B–E) Influence of K_{O_2} and k_d on the simulated LSV curves at G (B, D) and at C in the SG/TC mode, $d = 8$ μm, (C, E) using parameters defined in Table S1, SI. B,C) $k_d = 0\ s^{-1}$ and B) $K_{O_2} = 1$–$1000\ M^{-1}$ and C) $K_{O_2} = 0.1$–$200\ M^{-1}$ from top to bottom. D,E) $K_{O_2} = 200\ M^{-1}$ and D) $k_d = 0$–$100\ s^{-1}$ from top to bottom and E) $k_d = 0$–$10\ s^{-1}$ from bottom to top.

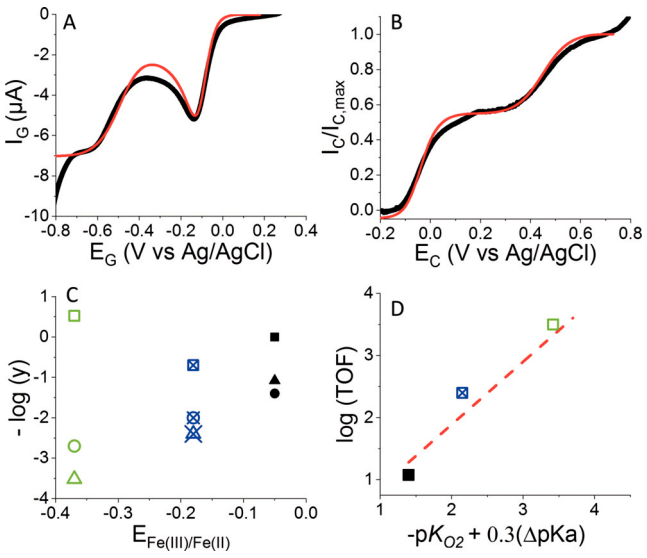

Figure 3. A) LSVs recorded at G and B) the dimensionless LSVs obtained subsequently at C and at a scan rate of 50 $mV s^{-1}$ in the SG/TC mode at $d = 8 \pm 2$ μm from G held at $E_G = -0.7$ V in 0.1 M $TBAPF_6$/DMF in the presence of 1 mM O_2 and 0.5 mM [($Fe^{III}F_{20}TPP$)Cl. Red lines are the corresponding simulated LSVs using $K_{O_2} = 25\ M^{-1}$ and $k_d = 1\ s^{-1}$. C) −log(γ), γ being k_d (■), K_{O_2} (●) and the TOF (▲) plotted versus $E^0_{Fe^{III}/Fe^{II}}$. D) Testing Eq. (1) for log (TOF) variations. Black solid, blue crossed, and green open symbols correspond to $Fe^{III}(F_{20}TPP)Cl$, $Fe^{III}(TPP)Cl$, and $Fe^{III}((2\text{-}CO_2H)_4TPP)Cl$, respectively.

labeled k_{d1} and k_{d2} in Figure 2 A). The simulated curves in Figure 2 D,E show the effect of k_d on the LSV at G and at C, respectively. At G, the superoxo reduction current in a catalytic fashion increases with higher k_d. Conversely, at C, Fe^{II} tends to be the predominant species (increase of $I_{Fe^{II}}/I_{Fe^{III}(OO^{2-})}$). Noteworthy, for $k_d = 100\ s^{-1}$ a small amount of $Fe^{III}(OO^{2-})$ can still be collected at C, meaning that in principle an intermediate species with a lifetime as low as 10 ms could be probed for the given UME size and G–C gap.

The opposite trends observed at C for K_{O_2} (decrease of $I_{Fe^{II}}/I_{Fe^{III}(OO^{2-})}$) and k_d (increase of $I_{Fe^{II}}/I_{Fe^{III}(OO^{2-})}$), combined with the LSV at G, allow K_{O_2} and k_d to be unequivocally determined from the fit of the LSVs at G and C. This strategy (Section 4, SI) is used to describe the activation of O_2 by three iron porphyrins. The main results obtained with the three porphyrins are summarized in Table 1.

The best fit of the experimental LSVs at G and the C UME for $Fe(F_{20}TPP)$ is obtained for $K_{O_2} = 25 \pm 10\ s^{-1}$, a value comparable but lower to previous estimate based only on the analysis of the CVs at G (see Section 4, SI),[14] and $k_d = 1 \pm 0.3\ s^{-1}$ as shown in Figure 3 A,B. k_d is 20 times higher than the apparent $Fe^{III}(OO^{2-})$ decomposition rate constant determined by the thin-layer spectroelectrochemical study at 253 K (Section 2, SI), a difference that could be accounted for by the 40 K temperature difference between the two experiments.

It is then extended to [$Fe^{III}(TPP)Cl$] and [$Fe^{III}((2\text{-}CO_2H)_4TPP)Cl$]. The LSVs recorded under O_2 at G for each porphyrin are shown in Figure S4-2 A,C. The change in $E^0_{Fe^{III}/Fe^{II}}$ toward more cathodic values (−0.18 and −0.37 V, respectively) when changing the phenyl rings substituents agrees with previous studies[7] and results from an increase in the electron density of the ligand, while it has little effect on the peak potential for $Fe^{III}(OO^{\bullet-})$ reduction:

Table 1: Redox potentials of catalysts and intermediates [V vs. Ag/AgCl], TOFs, association constants (K_{O_2}), and apparent dissociation rate constants of $Fe^{III}(OO^{2-})$ (k_d). The errors on the potentials were estimated based on three or four different experiments for each porphyrin.

Catalyst	$E^0_{Fe^{III}/Fe^{II}}$	$E^p_{[Fe^{III}(OO^{\bullet-})]/[Fe^{III}(OO^{2-})]}$	$E^{1/2}_{[[Fe^{III}(OO^{2-})]_{ox}]/[Fe^{III}(OO^{2-})]}$	TOF [s^{-1}]	K_{O_2} [M^{-1}]	k_d [s^{-1}]
$Fe^{III}(Fe_{20}TPP)Cl$	-0.05 ± 0.03	-0.58 ± 0.05	0.39 ± 0.04	12	25 ± 10	1 ± 0.3
$Fe^{III}(TPP)Cl$	-0.18 ± 0.01	-0.64 ± 0.01	0.18 ± 0.03	250	100 ± 40	5 ± 1
$Fe^{III}((2\text{-}CO_2H)_4TPP)Cl$	-0.37 ± 0.02	-0.62 ± 0.02	-0.07 ± 0.03	3300	500 ± 100	0.3 ± 0.1

$E^{p}_{Fe^{III}(OO^{\bullet-})/Fe^{III}(OO^{2-})} \approx -0.6$ V. The already reported[7] donating effect of the 2-COOH substituents is likely due to intraligand hydrogen-bond effects, which are expected to lower the COOH pK_a,[16] henceforth conferring it an +I effect.

On the LSVs recorded at C while the solution was electrolyzed at G ($E_G = -0.7$ V, Figure S4-2 B,D), two steps are probed and attributed, like for $Fe^{III}(F_{20}TPP)$, to the oxidation of Fe^{II} and $Fe^{III}(OO^{2-})$ (with $E^{1/2}_{[Fe^{III}(OO^{2-})]_{ox}/Fe^{III}(OO^{2-})} \approx 0.2$ and -0.05 V, respectively). K_{O_2} and k_d values were also extracted from the fit of the G and C LSVs. Noteworthy, the K_{O_2} value determined for $[Fe^{III}(TPP)Cl]$ is in excellent agreement with the DFT-calculated value,[7] strengthening the proposed methodology for accurately estimating the association constant K_{O_2}.

The experimental determination of K_{O_2} and k_d, as well as the reduction/oxidation potentials of new intermediates, provides access to structure–activity correlations within the iron porphyrin series. They are presented, in a logarithmic scale, in Figure 3 A relative to $E^0_{Fe^{III}/Fe^{II}}$. $\log(K_{O_2})$ varies linearly with $E^0_{Fe^{III}/Fe^{II}}$ with a slope of 60 mV per K_{O_2} decade, confirming experimentally the DFT-observed trend.[7] This shows in first instance the effect of decreasing ligand electron density which shifts $E^0_{Fe^{III}/Fe^{II}}$ to more positive values and lowers affinity to O_2.

In contrast, this decrease of ligand electron density should improve the stabilization of the reduced adduct ($Fe^{III}(OO^{2-})$) and should be reflected through either its stability rate constant k_d or the $Fe^{III}(OO^{\bullet-})$ reduction and $Fe^{III}(OO^{2-})$ oxidation potentials. If the latter ($E^{1/2}_{[Fe^{III}(OO^{2-})]_{ox}/Fe^{III}(OO^{2-})}$ determined at C for each porphyrin) varies linearly with $E^0_{Fe^{III}/Fe^{II}}$ with near-unity slope (Figure S5, Section 5, SI), there is a deviation for the other two.

Firstly, k_d should increase from $[Fe^{III}(F_{20}TPP)Cl]$ to $[Fe^{III}((2\text{-}CO_2H)_4TPP)Cl]$. If the trend is followed for $[Fe^{III}(F_{20}TPP)Cl]$ and $[Fe^{III}(TPP)Cl]$, the lowest k_d value was obtained for $[Fe^{III}((2\text{-}CO_2H)_4TPP)Cl]$, likely due to H-bond stabilization.

The $E^{1/2}_{[Fe^{III}(OO^{2-})]_{ox}/Fe^{III}(OO^{2-})} - E^0_{Fe^{III}/Fe^{II}}$ correlation suggests that electron transfer from the electrode to the Fe-O intermediates is controlled by the electron density of the porphyrin ligand, in agreement with the redox-mediating role of Fe porphyrin. From this argument one would expect that $E^{p}_{Fe^{III}(OO^{\bullet-})/Fe^{III}(OO^{2-})}$ shifts toward more cathodic potentials, as $E^0_{Fe^{III}/Fe^{II}}$ when the ligand electron density is increased. The relative insensitivity of $E^{p}_{Fe^{III}(OO^{\bullet-})/Fe^{III}(OO^{2-})}$ to the porphyrin ligand structure provides further mechanistic information. As shown from the simulated LSVs in Figure 2 B, increasing K_{O_2} also increases $E^{p}_{Fe^{III}(OO^{\bullet-})/Fe^{III}(OO^{2-})}$ by ca. 90 mV per K_{O_2} decade. However, considering the possible correlation $E^{p}_{Fe^{III}(OO^{\bullet-})/Fe^{III}(OO^{2-})} = E^0_{Fe^{III}/Fe^{II}} - 0.09\,pK_{O_2} + B$, where B is a constant term within the porphyrin series including standard potential differences between the two reductive steps $\Delta E^0 = E^0_{Fe^{III}/Fe^{II}} - E^0_{Fe^{III}(OO^{\bullet-})/Fe^{III}(OO^{2-})}$, a deviation from a unity slope is found (Section 6, SI). It means that K_{O_2} is not sufficient to explain the potential shift. Indeed owing to its stronger basic character, the electrogeneration of $Fe^{III}(OO^{2-})$ should be influenced by protonation (for example by residual water in the absence of added acid), which depends on the ligand porphyrin structure. As a first guess this protonation should be related to the pK_a of $Fe^{III}(OOH^-)/Fe^{III}(OO^{2-})$ and affect the LSV through an apparent E^0 varying as $E^0_{Fe^{III}(OO^{\bullet-})/Fe^{III}(OO^{2-})} + 0.06\,pK_a$. Thus, one expects $E^{p}_{Fe^{III}(OO^{\bullet-})/Fe^{III}(OO^{2-})} = E^0_{Fe^{III}/Fe^{II}} + 0.06\,pK_a - 0.09\,pK_{O_2} + B'$, where B' is a constant term along the porphyrin series. A ΔpK_a scale relative to the pK_a of $[Fe^{III}(F_{20}TPP)Cl]$, $\Delta pK_a = pK_a - pK_{aFeF_{20}TPP}$ as explained in Section S6, SI, can be evaluated experimentally (Figure S6). It yields $\Delta pK_a = 0.4$ for $[Fe^{III}(TPP)Cl]$ and $\Delta pK_a = 2.6$ for $[Fe^{III}((2\text{-}CO_2H)_4TPP)Cl]$. These values match the trend in ΔpK_a estimated by DFT within the parallel protonation of the superoxo couple $Fe^{III}(OOH^{\bullet})/Fe^{III}(OO^{\bullet-})$ (red path Figure 2 A).[7] It then suggests that the structure affects similarly the $Fe^{III}(OOH^-)/Fe^{III}(OO^{2-})$ and $Fe^{III}(OOH^{\bullet})/Fe^{III}(OO^{\bullet-})$ pK_as.

Both protonation steps are key in the tuning of the turnover catalytic frequency (TOF) during the electrochemical reduction of O_2, the prominence of each depending on the strength of the acid used. Thus the TOF for the electrochemical reduction of O_2 in acidic medium was determined for each porphyrin from the foot of the wave analysis (FOWA) as described by Savéant et al. (see Section 7, SI).[17] The TOF values found for the three porphyrins are slightly higher but on the same order of magnitude as the values reported for porphyrins having similar $E^0_{Fe^{III}/Fe^{II}}$, probably due to the higher dissociation of $HClO_4$ in DMF. Both log(TOF) and $\log(K_{O_2})$ vary linearly with $E^0_{Fe^{III}/Fe^{II}}$, showing a direct relationship between the catalytic efficiency and the O_2 binding. In order to predict the TOF of catalysts, it was shown, from transition state arguments and DFT estimates, that log(TOF) varies linearly with pK_{O_2} and the $Fe^{III}(OOH^{\bullet})/Fe^{III}(OO^{\bullet-})$ pK_a.[7] Considering the abovementioned similar structure effect on the pK_as of $Fe^{III}(OOH^{\bullet})/Fe^{III}(OO^{\bullet-})$ and $Fe^{III}(OOH^-)/Fe^{III}(OO^{2-})$, one then expects a similar trend [Eq. (1)],

$$\log(TOF) = -pK_{O_2} + \alpha\, pK_{a,Fe^{III}(OOH^-)/Fe^{III}(OO^{2-})} + B'' \qquad (1)$$

where B'' is a constant term within the series. This relationship is indeed verified here, in Figure 3 D, but with experimentally estimated thermodynamic parameters and using $\alpha = 0.3$, a value very similar to that obtained correlating TOF and the DFT-estimated $Fe^{III}(OOH^{\bullet})/Fe^{III}(OO^{\bullet-})$ pK_as.[7]

To summarize, we have demonstrated here all the potentiality of SECM in the SG/TC mode to decipher complex homogeneous catalytic systems based on the in situ probing of reaction intermediates. Particularly, with the help of simulations, we could quantitatively extract for the first time thermodynamic and kinetic parameters for such intermediates of complex processes in a single electrochemical experiment. It is exemplified here for probing the reductive activation of O_2 by iron porphyrins. Even in the absence of acid, the activity of intermediate oxo adducts, collected at the tip of a SECM, make it possible to draw pertinent structure–activity correlations to address the catalysis of O_2 reduction by such catalysts. The importance of O_2 binding and the peroxo protonation is highlighted through experimental estimates that correlate with catalysis TOF and earlier DFT calculations.[7] Moreover, in the absence of H^+, a decomposi-

tion path (k_d) of the peroxo intermediates has been evidenced. At that point, two mechanistic paths can be envisaged 1) $k_{d,1}$ is associated with the protonation of $Fe^{III}(OO^{2-})$ and participates in the TOF as it engages the two-electron reduction process of the $Fe^{III}OOH$ (dashed blue arrow in Figure 2A) and 2) $k_{d,2}$ is a concurrent path to the TOF (dashed green arrow), which, as suggested from the spectroelectrochemical experiments, corresponds to the homogeneous dissociation of peroxo. Even if its real effect is not clear, it raises interesting questions with implications for the catalytic process.

Finally, the determination by SECM of the exact location of the oxidation process opens electrochemical access to new highly oxidative intermediates. Particularly the increased interest in nanoelectrodes will draw unique opportunities in probing more unstable intermediates within thinner reaction layers. The proof of concept established here with O_2 activation can also be transposed to other relevant cases such as CO_2 reduction.

Acknowledgements

We are grateful for financial support by Labex MiChem, managed by ANR, within the Investissement d'Avenir program under reference ANR-11-IDEX-004-02.

Conflict of interest

The authors declare no conflict of interest.

Keywords: electrocatalysis · iron porphyrins · molecular electrochemistry · O—O activation · scanning electrochemical microscopy

[1] F. Cavani, J. H. Teles, *ChemSusChem* **2009**, *2*, 508 – 534.
[2] a) E. I. Solomon, S. S. Stahl, *Chem. Rev.* **2018**, *118*, 2299 – 2301; b) W. Zhang, W. Lai, R. Cao, *Chem. Rev.* **2017**, *117*, 3717 – 3797.
[3] D. Mansuy, *C. R. Chim.* **2007**, *10*, 392 – 413.
[4] E. Anxolabéhère-Mallart, F. Banse, *Curr. Opin. Electrochem.* **2019**, *15*, 118 – 124.
[5] a) J. G. Liu, T. Ohta, S. Yamaguchi, T. Ogura, S. Sakamoto, Y. Maeda, Y. Naruta, *Angew. Chem. Int. Ed.* **2009**, *48*, 9262 – 9267; *Angew. Chem.* **2009**, *121*, 9426 – 9431; b) A. Takahashi, T. Kurahashi, H. Fujii, *Inorg. Chem.* **2011**, *50*, 6922 – 6928; c) X. Huang, J. T. Groves, *Chem. Rev.* **2018**, *118*, 2491 – 2553; d) H. Kim, P. J. Rogler, S. K. Sharma, A. W. Schaefer, E. I. Solomon, J. D. Karlin, *J. Am. Chem. Soc.* **2020**, *142*, 3104 – 3116.
[6] J.-M. Savéant, *Chem. Rev.* **2008**, *108*, 2348 – 2378.
[7] M. L. Pegis, B. A. McKeown, N. Kumar, K. Lang, D. J. Wasylenko, X. P. Zhang, S. Raugei, J. M. Mayer, *ACS Cent. Sci.* **2016**, *2*, 850 – 856.
[8] *Scanning Electrochemical Microscopy*, 2nd ed. (Eds.: A. J. Bard, M. V. Mirkin), CRC, Boca Raton, FL, **2012**.
[9] a) T. Kai, M. Zhou, S. Johnson, H. S. Ahn, A. J. Bard, *J. Am. Chem. Soc.* **2018**, *140*, 16178 – 16183; b) T. J. Stockmann, J. M. Noël, S. Ristori, C. Combellas, A. Abou-Hassan, F. Rossi, F. Kanoufi, *Anal. Chem.* **2015**, *87*, 9621 – 9630.
[10] a) C. T. Carver, B. D. Matson, J. M. Mayer, *J. Am. Chem. Soc.* **2012**, *134*, 5444 – 5447; b) C. Costentin, H. Dridi, J.-M. Savéant, *J. Am. Chem. Soc.* **2015**, *137*, 13535 – 13544; c) K. Sengupta, S. Chatterjee, A. Dey, *ACS Catal.* **2016**, *6*, 6838 – 6852.
[11] a) C. Sánchez-Sánchez, J. Rodríguez-López, A. J. Bard, *Anal. Chem.* **2008**, *80*, 3254 – 3260; b) S. Cannan, J. Cervera, R. J. Steliaros, E. Bitziou, A. L. Whitworth, P. R. Unwin, *Phys. Chem. Chem. Phys.* **2011**, *13*, 5403 – 5412.
[12] Y. Leroux, D. Schaming, L. Ruhlmann, P. Hapiot, *Langmuir* **2010**, *26*, 14983 – 14989.
[13] a) A. O. Okunola, T. C. Nagaiah, X. Chen, K. Eckhard, W. Schuhmann, M. Bron, *Electrochim. Acta* **2009**, *54*, 4971 – 4978; b) M. A. Mezour, R. Cornut, E. M. Hussien, M. Morin, J. Mauzeroll, *Langmuir* **2010**, *26*, 13000 – 13006.
[14] R. Oliveira, W. Zouari, C. Herrero, F. Banse, B. Schöllhorn, C. Fave, E. Anxolabéhère-Mallart, *Inorg. Chem.* **2016**, *55*, 12204 – 12210.
[15] S. Bang, Y. M. Lee, S. Hong, K. B. Cho, Y. Nishida, M. S. Seo, R. Sarangi, S. Fukuzumi, W. Nam, *Nat. Chem.* **2014**, *6*, 934 – 940.
[16] S. Shan, D. Herschlag, *J. Am. Chem. Soc.* **1996**, *118*, 5515 – 5518.
[17] C. Costentin, S. Drouet, M. Robert, J.-M. Saveant, *J. Am. Chem. Soc.* **2012**, *134*, 11235 – 11242.

Manuscript received: April 6, 2020
Accepted manuscript online: June 15, 2020
Version of record online: July 16, 2020

ChemComm

ROYAL SOCIETY OF CHEMISTRY

COMMUNICATION

View Article Online
View Journal | View Issue

Cite this: *Chem. Commun.*, 2021, **57**, 1198

Received 17th November 2020,
Accepted 24th December 2020

DOI: 10.1039/d0cc07531k

rsc.li/chemcomm

Modulating alkene reactivity from oxygenation to halogenation *via* electrochemical O_2 activation by Mn porphyrin†

Nikolaos Kostopoulos, [a] Frédéric Banse, [b] Claire Fave [a] and Elodie Anxolabéhère-Mallart *[a]

Oxidation of organic substrates is achieved in nature under mild conditions thanks to metalloenzymes but remains a challenge for chemists. Herein we show by UV-Vis spectroelectrochemistry that when Mn^{III}TPPCl is electrochemically reduced to Mn^{II} in CH_2Cl_2 under O_2, a $Mn^{II}O_2^{\bullet}$ species is generated. Benzoic anhydride reacts with the latter triggering a catalytic current in cyclic voltammetry. Electrolysis on the catalytic wave in the presence of cyclooctene leads to its oxygenation or halogenation depending on the axial ligand present as reported here for the first time.

Oxidation and halogenation of hydrocarbons are reactions of great importance for the preparation of various organic molecules on an industrial scale. Regarding oxidation reactions (*i.e.* oxygenation and halogenation), hazardous chemical reagents and/or noble metal catalysts are often implemented. Despite its potent oxidizing power and renewable character, O_2 is scarcely used in synthetic chemistry under ambient conditions due to its kinetic inertness.[1] By contrast, in Nature, Fe oxygenases achieve highly efficient and selective oxidations by unravelling the O_2 potent oxidizing power through its partial and controlled reduction at the Fe active site, leading to O–O bond cleavage to generate the reactive high valent Fe–oxo (FeO).[2] Heme haloperoxidases formally generate their reactive species from the same Fe–oxo (FeO) in presence of Cl^- or Br^- leading to an Cl/BrFeO intermediate able to convert an aliphatic or aromatic C–H bond into a C–Cl/C–Br one.[3]

Fe and Mn porphyrin complexes have been extensively studied as models of the active site of these enzymes[4–6] and have for long been known to be able to oxidize and halogenate organic substrates with oxidizing agents such as H_2O_2, *m*-CPBA, PhIO and OCl^-. High valent Fe– or Mn–oxo species that are thus produced are responsible of such reactivity.

Since the first example of oxidation of organic molecules by PhIO catalyzed by a Fe porphyrin, reported by Groves[7] there has been numerous publications evidencing oxidation of organic substrates by chemically generated high valent Fe–oxo species.[8] Mn porphyrins are also able to catalyze the halogenation of various substrates with chemical oxidants and more precisely hypochlorite, as recently shown by Groves *et al.*[9,10] However, there are hardly any example of electrochemical oxidation of organic molecules catalyzed by Fe or Mn complexes that occurs by activation of O_2.[11]

Among the few examples of electrochemical oxidations by reductive activation of O_2 is the pioneering work of Murray[12,13] and the more recent work of Dey,[14] the latter focusing on Fe porphyrins immobilized on SAM. Murray showed that Mn^{III}(TPP) can induce epoxidation of cyclooctene under electrocatalytic conditions in good yields in presence of 1-methylimidazole (1-MeIm) and benzoic anhydride. In the present communication we show by means of spectroelectrochemistry that this oxidation process involves a $Mn^{II}O_2^{\bullet}$ adduct as proposed but not proven before. In addition, we show that under the same electrocatalytic conditions but using an excess of chloride instead of 1-MeIm, the oxidation process finally results in the halogenation of cyclooctene.

Fig. 1 displays representative cyclic voltammograms (CVs) of [Mn^{III}(TPP)Cl] (TPP = tetraphenylporphyrinate) under Ar and O_2 (air saturated) in a CH_2Cl_2 solution. Under Ar atmosphere (Fig. 1, black trace), the Mn^{III}/Mn^{II} wave is quasi reversible with $E_{1/2}$ = −0.35 V *vs.* SCE. Under O_2 (Fig. 1, red trace), the cathodic current increases and one additional new anodic peak appears at E_2^a = −0.16 V *vs.* SCE. The ratio between the two anodic peaks (E_1^a and E_2^a) varies with the scan rate and with the temperature as shown in the Fig. S1 and S2 (ESI†). These observations strongly suggest a chemical reaction between Mn^{II} species and O_2 and are in accordance with previous works.[12,13,15]

[a] *Université de Paris, Laboratoire d'Electrochimie Moléculaire UMR 7591, CNRS, F-75013 Paris, France. E-mail: elodie.anxolabehere@u-paris.fr*
[b] *Université Paris-Saclay, CNRS, Institut de Chimie Moléculaire et des Matériaux d'Orsay, 91405, Orsay, France*

† Electronic supplementary information (ESI) available. See DOI: 10.1039/d0cc07531k

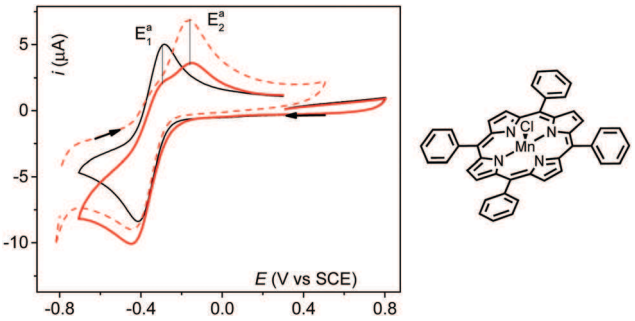

Fig. 1 (left) CVs of 0.5 mM Mn^{III}(TPP)Cl in a 0.1 M $TBAPF_6/CH_2Cl_2$ solution on a glassy carbon electrode, at 298 K; under Ar (black trace), under O_2 (red trace) and reverse scan under O_2 with 15 s delay time at $E_{app} = -0.85$ V (dashed red trace). (right) Schematic structure of Mn^{III}(TPP)Cl.

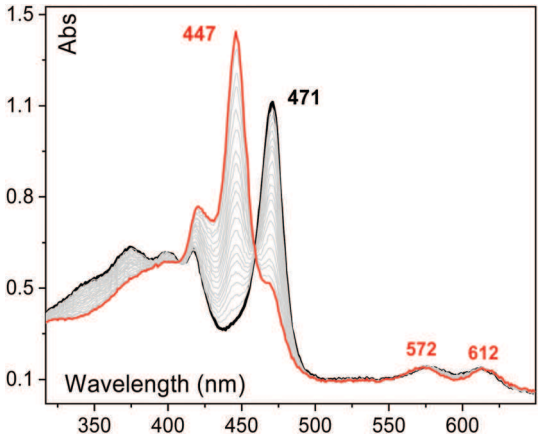

Fig. 2 UV-vis spectrum of 0.1 mM Mn^{III}(TPP)Cl, at 298 K, in 0.2 M $TBAPF_6/CH_2Cl_2$ under O_2 before applying potential (black trace) and after $E_{app} = -0.45$ V *vs.* SCE, (one spectrum per 20 s, grey traces with final spectrum red trace).

Murray and co-workers[12,13] proposed that O_2 binds on the Mn^{II}(TPP) generated at the electrode. This new adduct undergoes a one electron reduction, following an ECE mechanism as sketched in Table 1 (mechanism in CH_2Cl_2). The one electron reduced species thus formed is claimed to be oxidized at a more positive potential than the Mn^{II}(TPP) complex ($E_2^a = -0.16$ V *vs.* $E_1^a = -0.29$ V *vs.* SCE).[12,13,15] This proposition is consistent with the increase of the cathodic current of the Mn^{III}/Mn^{II} when O_2 is added in the solution, which excludes, indeed, a simple EC mechanism that would lead to a Mn^{III}–superoxo adduct in the diffusion layer.[16] However, to the best of our knowledge, no spectroscopic proof for the formation of the Mn^{II}–superoxo ($Mn^{II}O_2^{\bullet}$) or Mn^{III}–peroxo ($Mn^{III}OO^-$) intermediate has so far been provided to confirm the above interpretation. To gain further insight into the nature of this electrogenerated species we have performed UV-Vis spectroelectrochemistry.

These experiments were performed either at 298 K or at 258 K using a previously described set-up.[17] Spectra corresponding to Mn^{III} species in CH_2Cl_2 were recorded with the characteristic Soret band centered at 471 nm regardless of the atmosphere (Fig. 2, black trace and Fig. S3, ESI†). Under O_2 atmosphere upon reduction of a CH_2Cl_2 solution of Mn^{III}(TPP)Cl at $E_{app} = -0.45$ V *vs.* SCE, a new Soret band appears at 447 nm and simultaneously the Mn^{III} band at 471 fades as shown in Fig. 2 (red trace). The spectral characteristics of the species that accumulates (broad 397 nm, Soret 447 nm, and Q bands at 530, 572 and 612 nm) are identical to those reported for the sample prepared by addition of two equivalents of KO_2 in a Mn^{III}(TPP) solution in DMSO (broad 398 nm, Soret 446 nm, and Q bands at 530 nm, 572 and 614 nm).[18] A similar UV-Vis spectrum attributed to the formation of a Mn^{II}–superoxo species has also been obtained by addition of two equivalents of KO_2 in a Mn(TMP) solution (TMP = 5,10,15,20 tetramesitilporphyrinate) in CH_3CN.[19] We also propose that, in the present case, the electrochemically generated species is better formulated as a $Mn^{II}O_2^{\bullet}$ (Mn^{II}–superoxo) rather than a $Mn^{III}OO^-$ (Mn^{III}–peroxo). Indeed, the similarity between the UV-vis spectra obtained under O_2 and Ar at $E_{app} = -0.45$ V *vs.* SCE (Fig. S4 and S5, ESI†) suggests that the oxidation state of the metal in these species is the same, *i.e.* +II and not +III (Table 1).

In order to gain further insight into the characteristics of this key intermediate, experiments in DMF, a dissociating solvent, have also been performed. CV of the Mn(TPP)Cl recorded in a DMF solution with 0.1 M $TBAPF_6$ under Ar (Fig. S6, ESI†) shows an important positive shift of the $E_{1/2}$ for the Mn^{III}/Mn^{II} wave compared to those recorded in CH_2Cl_2 ($E_{1/2}$ (DMF) = −0.18 V *vs.* $E_{1/2}$ (CH_2Cl_2) = −0.35 V).

This behaviour indicates that the $[Mn^{III}(TPP)(DMF)]^+$ form is prominent in this solvent[18] the latter being reduced at more positive potentials. The observed difference in the UV-Vis spectra in DMF and in CH_2Cl_2 is also significant and indicative of a change in the coordination sphere (Table 1). Interestingly,

Table 1 Potential values and spectroscopic characteristics of the species generated electrochemically. Proposed mechanisms for the formation of the Mn^{II} superoxo adduct

	CH_2Cl_2	DMF		
$E_{1/2}(Mn^{III}/Mn^{II})^a$	−0.347	−0.178	Mechanism 1: CH_2Cl_2	Mechanism 2: DMF
$Mn^{III b}$	471, 575 and 612	471, 566 and 601		
$Mn^{II b}$	444, 576 and 616	437, 569 and 609	$\mathbf{E_1}$ $Mn^{III} \xrightarrow{e^-} Mn^{II}$ k_1	$\mathbf{E_1}$ $Mn^{III} \xrightarrow{e^-} Mn^{II}$ k_1'
$[Mn^{III}/Ar/E_{app} = -0.45]^b$	444, 576 and 616	437, 569 and 609	$\mathbf{C}$ $Mn^{II} \xrightarrow{O_2} Mn^{III}O_2^{\bullet}$ K	$\mathbf{E_2}$ $O_2 \xrightarrow{e^-} O_2^{-\bullet}$ k_3
$[Mn^{III}/O_2/E_{app} = -0.45]^b$	447, 570 and 612	437, 569 and 609	$\mathbf{E_2}$ $Mn^{III}O_2^{\bullet} \xrightarrow{e^-} Mn^{II}O_2^{\bullet}$ k_2	$\mathbf{C}$ $Mn^{II} + O_2^{-\bullet} \rightarrow Mn^{II}O_2^{\bullet}$ K′
$[Mn^{III}/O_2/E_{app} = -1.1]^b$	—	447, 570 and 612		

[a] In V *vs.* SCE. [b] In nm.

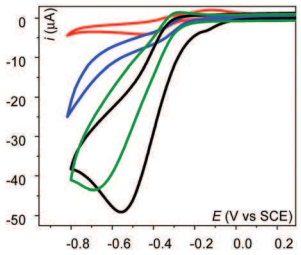

Fig. 3 CVs of 0.5 mM Mn^{III}(TPP)Cl in 0.1 M $TBAPF_6/CH_2Cl_2$ solution on a glassy carbon electrode at 298 K with 0.44 M benzoic anhydride under O_2 (black trace) and with addition of 20 mM 1-MeIm (blue trace) or with 5 mM TBACl (green trace). For comparison CV under O_2 without benzoic anhydride has been added (red trace).

the CV of the Mn^{III}(TPP) complex under O_2 atmosphere remains unchanged in DMF (see the Mn^{III}/Mn^{II} wave in Fig. S6, ESI†) contrary to what was observed in CH_2Cl_2. If more negative potentials are scanned, after the $O_2/O_2^{\bullet-}$ wave (−0.85 V *vs.* SCE), a shoulder at the foot of the O_2 reduction wave is observed (Fig. S7A (ESI†), red trace) suggesting a chemical reaction between Mn^{II} and $O_2^{\bullet-}$.[20,21]

Moreover, on the reverse scan, two anodic peaks are observed at −0.78 V and at −0.08 V *vs.* SCE. The former one corresponds to oxidation of free superoxide generated by reduction of excess O_2 at the electrode, while the additional peak appearing at a potential close to the one observed in CH_2Cl_2 can be ascribed to oxidation of a $Mn^{II}O_2^{\bullet}$ intermediate (Fig. S7B, ESI†). The intensity of this wave suggests a two-electron process as expected for the oxidation of $Mn^{II}O_2^{\bullet}$ to give Mn^{III} and O_2. The hypothesis that this key species is formed in DMF following the mechanism 2 (Table 1) is confirmed by spectroelectrochemistry. When a potential of −0.45 V *vs.* SCE is applied in a Mn^{III} solution (Fig. S8A, ESI†), spectra similar to that attributed to the Mn^{II} species are recorded regardless of the atmosphere (Ar or O_2).[18] In contrast, when a potential of −1.1 V *vs.* SCE is applied under O_2, the spectrum of the Mn^{II}(TPP) complex evolves towards a spectroscopic signature identical to the one obtained in CH_2Cl_2 and attributed to the $Mn^{II}O_2^{\bullet}$ adduct (Fig. S8B, ESI†). These observations strongly suggest two different mechanisms for the Mn^{II}–superoxo formation depending on the solvent. In DMF, the solvent binds the Mn ion (in line with the shift of the Soret and Q bands of the Mn^{II} and of the cathodic peak of the Mn^{III} complex, Table 1) preventing the coordination of the weak donor O_2 on the Mn^{II} center, while allowing that of the better donor $O_2^{\bullet-}$ ion (mechanism 2). In the non-coordinating solvent CH_2Cl_2, such a competition for the coordination of dioxygen does not occur. As depicted in mechanism 1 (Table 1), it can easily bind to the Mn^{II} center which results in its reduction and formation of the $Mn^{II}O_2^{\bullet}$ intermediate.

Taken into account that the $Mn^{II}O_2^{\bullet}$ intermediate can be generated at a less negative potential in CH_2Cl_2 than in DMF (−0.45 *vs.* −1.1 V *vs.* SCE), thus avoiding the concomitant generation of superoxide radicals, we have decided to study the electrocatalytic reactivity of the system for substrate oxidation in CH_2Cl_2.

Fig. 3 displays the CV of Mn^{III}(TPP)Cl in CH_2Cl_2 under O_2 in absence (red trace) or in presence of excess benzoic anhydride (880 eq., black trace) (CV under argon, in presence of benzoic anhydride is shown in Fig. S9B, red trace, ESI†). The presence of O_2 and benzoic anhydride triggers an increase of the current, indicating a catalytic activity occurring at the onset of the Mn^{III}/Mn^{II} wave. This observation indicates that benzoic anhydride reacts with the $Mn^{II}O_2^{\bullet}$ adduct formed in the diffusion layer. In accordance with the literature, we propose that the catalytic current is due to the O–O bond cleavage[12] *via* the transient generation of an acylperoxo species evolving to a $Mn^{V}O$ species. The $Mn^{V}O$ intermediate can be reduced at the electrode or eventually react with a substrate. In both cases, regeneration of the Mn^{III} species will end the cycle.

Preparative electrolyses under O_2 atmosphere at 298 K were first carried out at E_{app} = −0.45 V *vs.* SCE of Mn^{III}(TPP)Cl (0.5 mM) in 0.1 M $TBAPF_6/CH_2Cl_2$ solution with excess of benzoic anhydride, and in presence of 1-MeIm (40 equivalents *vs.* Mn) and cyclooctene as substrate (20 equivalents *vs.* Mn). Under these conditions (entry 1, Table 2), cyclooctene oxide was detected with a TON of *ca.* 7.3 after 4 hours electrolysis (see details in ESI†). This result is in accordance with those of Murray *et al.* who used a similar system.[12] It is noteworthy that even though the addition of the 1-MeIm axial base diminished the catalytic current in our case (Fig. 3, blue trace) it is known to significantly improve the yield of the oxidation reactions catalyzed by Mn porphyrins, with H_2O_2 as oxidant, by promoting the formation of the $Mn^{V}O$.[22] Indeed that was also the case in the present system (see Table 2, entries 1 and 2). The faradaic yield of the reaction was 81% as calculated from the current *vs.* time plot (Fig. S10A, ESI†).

Then, a preparative electrolysis was performed in presence of 10 eq. of TBACl instead of 1-MeIm (Fig. 3, green trace). In that case, trace amounts of cyclooctene oxide was detected, and chloro-cyclooctene was observed in the chromatogram (Table 2, entry 3 and Fig. S11 for a representative chromatogram, ESI†)

Table 2 Results of preparative scale electrolysis at 298 K under O_2. Conditions: 0.5 mM Mn^{III}(TPP)Cl, 10 mM alkene and 440 mM benzoic anhydride in 0.1 M $TBAPF_6/CH_2Cl_2$ at E_{app} = −0.45 V *vs.* SCE for 4 h. TON = mole of product/mole of catalyst

Entry	Substrate	Solvent	1-MeIm	TBACl	Cyclooctene-oxide	Chlorocyclooctene
0	Cyclooctene	CH_2Cl_2			Traces	Not detected
1	Cyclooctene	CH_2Cl_2	20 mM	—	TON = 7.3	Not detected
2	Cyclooctene	CH_2Cl_2	20 mM	5 mM	TON = 7.1	Not detected
3	Cyclooctene	CH_2Cl_2	—	5 mM	Traces	TON = 4.8
4	Cyclooctene	CH_2Cl_2	—	40 mM	Traces	TON = 1.6
5	Cyclooctene	DMF	—	40 mM	Not detected	Not detected

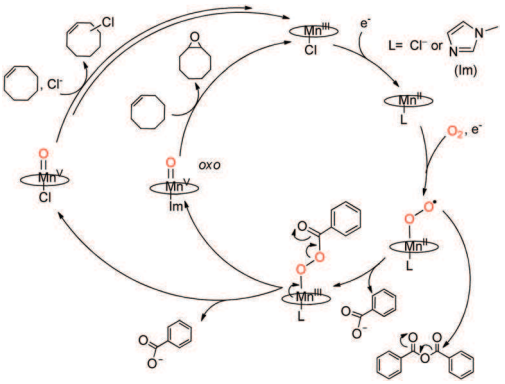

Scheme 1 Activation of O_2 catalyzed by Mn(TPP)Cl in CH_2Cl_2, in the presence of benzoic anhydride, and 1-MeIm or Cl^- leading to oxygenation or chlorination of cyclooctene, respectively.

with TON = 7.1. When the same solution was subjected to a second preparative electrolysis after addition of 1-MeIm, cyclooctene was produced but no more chlorinated compound (Fig. S11, blue trace, ESI†). The faradaic yield calculated from Fig. S10B (ESI†) was 53%. An increase of TBACl concentration did not induce any increase of the yield but rather a slight decrease (Table 2, entry 4). This observation can be ascribed to a coordination of Cl^- to the Mn center in competition with O_2, in accordance with the decreased catalytic current observed in the presence of Cl^- (compare black and green traces in Fig. 3). Along the same line, the nature of the solvent plays an important role as one could anticipate from the cyclic voltammetry study (*vide supra*). Replacing CH_2Cl_2 by DMF (Table 2, entry 5) leads to a total inhibition of the reactivity, as the result of the coordination of DMF.

Scheme 1 summarizes a proposed mechanism for the observed reactivity which emphasizes the role of the exogenous ligand, *i.e.* 1-methylimidazole or chloride. When neither of the two is in solution, almost no reaction takes place (Table 2, entry 0). If 1-MeIm is added (with or without chloride in solution), the oxygenation reaction is favored with formation of epoxide.[9] When chloride is added (without 1-MeIm), only chlorination reaction takes place. To rationalize these observations, we propose two different mechanistic pathways depending on the nature of the 6th ligand (Scheme 1). As shown above, a $Mn^{II}O_2^{\bullet}$ is formed at the electrode polarized at −0.45 V which further reacts with benzoic anhydride to generate a Mn^{III}–acylperoxo intermediate. The presence of the *trans* 1-MeIm ligand promotes the heterolytic cleavage to give a $Mn^{V}O$ species responsible for the oxygenation of cyclooctene. In the presence of excess Cl^- instead of 1-MeIm, the selectivity of the reaction is completely changed towards halogenation of the substrate. While a systematic study of this reaction has not yet been performed, it is tempting to propose that the $Mn^{V}O$ active intermediate would preferentially react with the anion rather the olefin to yield a chlorinating agent (Cl radicals and $Mn^{IV}O$ or Mn^{III}–OCl).

In conclusion, in this communication we bring insights into the mechanism of O_2 reductive activation by a Mn porphyrin, and explore new routes of reactivity under electrocatalytic conditions. We provide the first spectroscopic evidences that a $Mn^{II}O_2^{\bullet}$ adduct is formed in the Mn^{III}/Mn^{II} wave ($E_{1/2}$ = −0.35 V *vs.* SCE) in presence of O_2 in CH_2Cl_2. In DMF the formation of the same intermediate occurs *via* the interaction of Mn^{II} ion with electrochemically generated $O_2^{\bullet-}$ at a more negative potential ($E_{1/2}(O_2/O_2^{\bullet-})$ = −0.75 V *vs.* SCE). We then also show that oxidative transformation of cyclooctene is possible under electrocatalytic conditions at the Mn^{III}/Mn^{II} wave in CH_2Cl_2 in presence of benzoic anhydride: when an excess of Cl^- is added the reaction is directed towards chlorination of the substrate, whereas cyclooctene-oxide is selectively formed when 1-MeIm is used. We have now in hands a simple way to direct the reaction pathway from oxygenation to halogenation by simple swapping of the exogenous ligand.

NK acknowledges the French government for his PhD fellowship. NK thanks Martin Kientz for his help during the acquisition and the analysis of the GC/MS data. Support from GDR MAPYRO and GIS FrenchBic is acknowledged.

Conflicts of interest

There are no conflicts to declare.

Notes and references

1 F. Cavani and J. H. Teles, *ChemSusChem*, 2009, **2**, 508–534.
2 I. G. Denisov, T. M. Makris, S. G. Sligar and I. Schlichting, *Chem. Rev.*, 2005, **105**, 2253–2278.
3 J. Latham, E. Brandenburger, S. A. Shepherd, B. R. K. Menon and J. Micklefield, *Chem. Rev.*, 2018, **118**, 232–269.
4 X. Huang and J. T. Groves, *Chem. Rev.*, 2018, **118**, 2491–2553.
5 R. A. Baglia, J. P. T. Zaragoza and D. P. Goldberg, *Chem. Rev.*, 2017, **117**, 13320–13352.
6 S. Sahu and D. P. Goldberg, *J. Am. Chem. Soc.*, 2016, **138**, 11410–11428.
7 J. T. Groves, T. E. Nemo and R. S. Myers, *J. Am. Chem. Soc.*, 1979, **101**, 1032–1033.
8 W. Nam, *Acc. Chem. Res.*, 2007, **40**, 522–531.
9 W. Liu and J. T. Groves, *J. Am. Chem. Soc.*, 2010, **132**, 12847–12849.
10 G. Li, A. K. Dilger, P. T. Cheng, W. R. Ewing and J. T. Groves, *Angew. Chem., Int. Ed.*, 2018, **57**, 1251–1255.
11 E. Anxolabéhère-Mallart and F. Banse, *Curr. Opin. Electrochem.*, 2019, **15**, 118–124.
12 S. E. Creager, S. A. Raybuck and R. W. Murray, *J. Am. Chem. Soc.*, 1986, **108**, 4225–4227.
13 S. E. Creager and R. W. Murray, *Inorg. Chem.*, 1987, **26**, 2612–2618.
14 M. Mukherjee and A. Dey, *ACS Cent. Sci.*, 2019, **5**, 671–682.
15 G. Passard, D. K. Dogutan, M. Qiu, C. Costentin and D. G. Nocera, *ACS Catal.*, 2018, **8**, 8671–8679.
16 J.-M. Savéant, *Chem. Rev.*, 2008, **108**, 2348–2378.
17 N. Kostopoulos, C. Achaibou, J. M. Noel, F. Kanoufi, M. Robert, C. Fave and E. Anxolabéhère-Mallart, *Inorg. Chem.*, 2020, **59**, 11577–11583.
18 J. S. Valentine and A. E. Quinn, *Inorg. Chem.*, 1976, **15**, 1997–1999.
19 J. T. Groves, Y. Watanabe and T. J. McMurry, *J. Am. Chem. Soc.*, 1983, **105**, 4489–4490.
20 R. Oliveira, W. Zouari, C. Herrero, F. Banse, B. Schöllhorn, C. Fave and E. Anxolabéhère-Mallart, *Inorg. Chem.*, 2016, **55**, 12204–12210.
21 N. Ségaud, E. Anxolabéhère-Mallart, K. Sénéchal-David, L. Acosta-Rueda, M. Robert and F. Banse, *Chem. Sci.*, 2015, **6**, 639–647.
22 P. Battioni, J. P. Renaud, J. F. Bartoli, M. Reina-Artiles, M. Fort and D. Mansuy, *J. Am. Chem. Soc.*, 1988, **110**, 8462–8470.